Calcul intensif en simulation de frittage à l'échelle des particules.

Daniel Pino Muñoz

Ecole Nationale Supérieure des Mines
SAINT-ETIENNE

NNT : 2012 EMSE 0669

THÈSE

présentée par

Daniel Humberto PINO MUÑOZ

pour obtenir le grade de
Docteur de l'École Nationale Supérieure des Mines de Saint-Étienne

Spécialité : Mécanique et Ingénierie

HIGH-PERFORMANCE COMPUTING OF SINTERING PROCESS AT PARTICLE SCALE

soutenue à Saint-Etienne, le 26 octobre 2012

Membres du jury

Président :	M. Thierry COUPEZ	Pr., CEMEF – ENSMP, Sophia-Antipolis
Rapporteurs :	M. Jingzhe PAN	Pr., University of Leicester, Leicester
	M. Jean-François MOLINARI	Pr, LSMS – EPFL, Lausanne
Examinateurs :	M. Didier BOUVARD	Pr, SIMAP - INPG, Grenoble
	M. Thierry COUPEZ	Pr., CEMEF – ENSMP, Sophia-Antipolis
Directeur de thèse :	M. Sylvain DRAPIER	Pr., ENSMSE, Saint-Étienne
Co-directeur de thèse :	M. François VALDIVIESO	Dr., ENSMSE, Saint-Étienne
Co-encadrant de thèse :	M. Julien BRUCHON	Dr., ENSMSE, Saint-Étienne

Spécialités doctorales :	Responsables :
SCIENCES ET GENIE DES MATERIAUX	K. Wolski Directeur de recherche
MECANIQUE ET INGENIERIE	S. Drapier, professeur
GENIE DES PROCEDES	F. Gruy, Maître de recherche
SCIENCES DE LA TERRE	B. Guy, Directeur de recherche
SCIENCES ET GENIE DE L'ENVIRONNEMENT	D. Graillot, Directeur de recherche
MATHEMATIQUES APPLIQUEES	O. Roustant, Maître-assistant
INFORMATIQUE	O. Boissier, Professeur
IMAGE, VISION, SIGNAL	JC. Pinoli, Professeur
GENIE INDUSTRIEL	A. Dolgui, Professeur
MICROELECTRONIQUE	Ph. Collot, Professeur

EMSE : Enseignants-chercheurs et chercheurs autorisés à diriger des thèses de doctorat (titulaires d'un doctorat d'État ou d'une HDR)

AVRIL	Stéphane	MA	Mécanique & Ingénierie	CIS
BATTON-HUBERT	Mireille	MA	Sciences & Génie de l'Environnement	Fayol
BENABEN	Patrick	PR 1	Sciences & Génie des Matériaux	CMP
BERNACHE-ASSOLLANT	Didier	PR 0	Génie des Procédés	CIS
BIGOT	Jean-Pierre	MR	Génie des Procédés	SPIN
BILAL	Essaïd	DR	Sciences de la Terre	SPIN
BOISSIER	Olivier	PR 1	Informatique	Fayol
BORBELY	Andras	MR	Sciences et Génie des Matériaux	SMS
BOUCHER	Xavier	MA	Génie Industriel	Fayol
BRODHAG	Christian	DR	Sciences & Génie de l'Environnement	Fayol
BURLAT	Patrick	PR 2	Génie industriel	Fayol
COLLOT	Philippe	PR 1	Microélectronique	CMP
COURNIL	Michel	PR 0	Génie des Procédés	SPIN
DARRIEULAT	Michel	IGM	Sciences & Génie des Matériaux	SMS
DAUZERE-PERES	Stéphane	PR 1	Génie industriel	CMP
DEBAYLE	Johan	CR	Image, Vision, Signal	CIS
DELAFOSSE	David	PR1	Sciences & Génie des Matériaux	SMS
DESRAYAUD	Christophe	MA	Mécanique & Ingénierie	SMS
DOLGUI	Alexandre	PR 1	Génie Industriel	Fayol
DRAPIER	Sylvain	PR 1	Mécanique & Ingénierie	SMS
FEILLET	Dominique	PR 2	Génie Industriel	CMP
FOREST	Bernard	PR 1	Sciences & Génie des Matériaux	CIS
FORMISYN	Pascal	PR 1	Sciences & Génie de l'Environnement	Fayol
FRACZKIEWICZ	Anna	DR	Sciences & Génie des Matériaux	SMS
GARCIA	Daniel	MR	Sciences de la terre	SPIN
GIRARDOT	Jean-Jacques	MR	Informatique	Fayol
GOEURIOT	Dominique	MR	Sciences & Génie des Matériaux	SMS
GRAILLOT	Didier	DR	Sciences & Génie de l'Environnement	Fayol
GROSSEAU	Philippe	MR	Génie des Procédés	SPIN
GRUY	Frédéric	MR	Génie des Procédés	SPIN
GUY	Bernard	MR	Sciences de la Terre	SPIN
GUYONNET	René	DR	Génie des Procédés	SPIN
HAN	Woo-Suck	CR		SMS
HERRI	Jean-Michel	PR 2	Génie des Procédés	SPIN
INAL	Karim	PR 2	Microélectronique	CMP
KLÖCKER	Helmut	DR	Sciences & Génie des Matériaux	SMS
LAFOREST	Valérie	CR	Sciences & Génie de l'Environnement	Fayol
LERICHE	Rodolphe	CR CNRS	Mécanique et Ingénierie	SMS
LI	Jean-Michel	EC (CCI MP)	Microélectronique	CMP
MALLIARAS	George Grégory	PR 1	Microélectronique	CMP
MOLIMARD	Jérôme	PR2	Mécanique et Ingénierie	SMS
MONTHEILLET	Frank	DR 1 CNRS	Sciences & Génie des Matériaux	SMS
PERIER-CAMBY	Laurent	PR 2	Génie des Procédés	SPIN
PIJOLAT	Christophe	PR 1	Génie des Procédés	SPIN
PIJOLAT	Michèle	PR 1	Génie des Procédés	SPIN
PINOLI	Jean-Charles	PR 0	Image, Vision, Signal	CIS
ROUSTANT	Olivier	MA		Fayol
STOLARZ	Jacques	CR	Sciences & Génie des Matériaux	SMS
SZAFNICKI	Konrad	MR	Sciences & Génie de l'Environnement	Fayol
TRIA	Assia		Microélectronique	CMP
VALDIVIESO	François	MA	Sciences & Génie des Matériaux	SMS
VIRICELLE	Jean-Paul	MR	Génie des procédés	SPIN
WOLSKI	Krzysztof	DR	Sciences & Génie des Matériaux	SMS
XIE	Xiaolan	PR 1	Génie industriel	CIS

ENISE : Enseignants-chercheurs et chercheurs autorisés à diriger des thèses de doctorat (titulaires d'un doctorat d'État ou d'une HDR)

FORTUNIER	Roland	PR	Sciences et Génie des matériaux	ENISE
BERGHEAU	Jean-Michel	PU	Mécanique et Ingénierie	ENISE
DUBUJET	Philippe	PU	Mécanique et Ingénierie	ENISE
LYONNET	Patrick	PU	Mécanique et Ingénierie	ENISE
SMUROV	Igor	PU	Mécanique et Ingénierie	ENISE
ZAHOUANI	Hassan	PU	Mécanique et Ingénierie	ENISE
BERTRAND	Philippe	MCF	Génie des procédés	ENISE
HAMDI	Hédi	MCF	Mécanique et Ingénierie	ENISE
KERMOUCHE	Guillaume	MCF	Mécanique et Ingénierie	ENISE
RECH	Joël	MCF	Mécanique et Ingénierie	ENISE
TOSCANO	Rosario	MCF	Mécanique et Ingénierie	ENISE
GUSSAROV Andrey	Andrey	Enseignant contractuel	Génie des procédés	ENISE

Glossaire :

PR 0	Professeur classe exceptionnelle	Ing.	Ingénieur
PR 1	Professeur 1ère classe	MCF	Maître de conférences
PR 2	Professeur 2ème classe	MR(DR2)	Maître de recherche
PU	Professeur des Universités	CR	Chargé de recherche
MA(MDC)	Maître assistant	EC	Enseignant-chercheur
DR	Directeur de recherche	IGM	Ingénieur général des mines

Centres :

SMS	Sciences des Matériaux et des Structures
SPIN	Sciences des Processus Industriels et Naturels
FAYOL	Institut Henri Fayol
CMP	Centre de Microélectronique de Provence
CIS	Centre Ingénierie et Santé

Dernière mise à jour le : 02 avril 2012

Life is like riding a bicycle. To keep your balance you must keep moving.

by Albert Einstein

Acknowledgements

I would like to express my gratitude to my supervisors, Prof. Sylvain Drapier, Dr. Julien Bruchon and Dr. François Valdivieso for their continuous guidance and support during this study. Various difficulties in the present work were overcome through numerous discussions with them. Above all without their skills and their right guidance this thesis could not be framed. I owe a debt of gratitude to Dr. Julien Bruchon for his involvement and support in different aspects of my research project.

I would like to thank Prof. Jean-François Molinari and Prof. Jingzhe Pan for accepting to review this manuscript. It was a great honor to me to defend this thesis in front of them as well as Prof. Didier Bouvard and Prof. Thierry Coupez.

Most of the work carried out during this thesis was related to numerical simulations, therefore I would like to thank Dr. Nicolas Moulin, Mr. Olivier Breuil, Mr. Thierry Louvancourt and the other members of the staff of the Numerical Platform for their help during the last three years and for the computing facilities which they managed to keep always in excellent conditions.

In particular, I would also like to thank the past and present members of the Mechanics and Material Processing Department for creating such a great atmosphere for work. I am sure this work would have been way more difficult without their constant support.

I would also like to thank my friends at the Ecole Nationale Supérieure des Mines de Saint-Etienne: Carlos, Abdellah, Benjamin, Fey, Edgar, Yolanda, Canan, Yves, Renata, Marc, Arnaud, Howatchinou, Vincent, Baroudi, Jean-Baptiste, Greg, Daniel, Pierre-Yves, Alex, Nico, Julie (both), Laura, Aaron, Manu and Baptiste. I will always keep great memories of our coffee breaks and our countless soirées. I would like to thank Toñita for her understanding and her unfailing encouragement, specially during the tough moments of this thesis.

Lastly, but not leastly, to my parents, Rubén Darío and Ligia Stella, I dedicate this thesis, they made of me the person I am today, and for that I will always be thankful.

Muchas gracias!

Contents

List of Figures

List of Tables

Chapter 1

Introduction

Sintering process is, nowadays, a very important industrial process used for the manufacturing of countless materials and solid parts. Understanding, and therefore, modeling the underlying physical mechanisms that drive the evolution of a consolidated ceramic or metallic powder is important for controlling the material properties of the finished product or material.

Accordingly, considerable attention has been given to the understanding of the physical mechanisms responsible of the morphological changes that occur during sintering. The microstructural evolution during sintering is known to be influenced by many factors, e.g., compacting pressure, heating rate, particle size distribution, sintering temperature, etc. Because of the complex combination of these numerous factors onto the sintering process, it may be somehow difficult to extract pertinent information from experimental data. Numerical simulations can help in providing meaningful information about the phenomena controlling sintering.

The numerical simulations of industrial or natural processes are often carried out at two different scales: microscopic and macroscopic scale. Regarding the sintering and other phenomena involving microstructure evolutions, the connection between the two scales is not yet well known, and the macroscopic behavior is usually approximated by using phenomenological models. Within the framework of continuum mechanics of the sintering process at the macroscopic scale, the strains taken into account in the phenomenological models are related the evolution of the structure at the microscopic scale. Therefore, a better understanding of the mechanisms that are involved in the sintering process at the microscopic scale could help to develop more realistic macroscopic models, provided hundreds of particles can be investigated to establish micro-macro scale transitions.

A consolidated powder is a porous packing of particles. This consolidated powder presents a surface free energy excess, directly related to the specific surface of the compact, and its reduction is the sintering driving force. The reduction of this free energy excess is achieved by diffusional transport between the particles, leading to a reduction of the surface. The complexity of the geometry of a consolidated powder combined with the topological changes that can appear during sintering and with all the physical phenomena, make of the simulation

of sintering process at the microscopic scale a very challenging task.

In the present work, the sintering of ceramic materials is modeled and investigated numerically at the microscopic scale. The main underlying physical mechanisms responsible of the microstructural evolution during solid state sintering process are surface diffusion, volume diffusion and grain boundary diffusion. Several challenges have to be addressed in order to integrate those physical mechanisms into a continuum formulation leading to a numerical approach capable of simulating the sintering process. In this work the solid state sintering by surface and volume diffusion will be studied. There are several unanswered questions about the underlying physical phenomena on sintering, this work represents a step toward a better understanding on the sintering process of the effect of surface and volume diffusions, and to a least extent the effects of the grain boundary diffusion.

This approach at the local scale is conceivable also because the frame of high performance computing was considered from the onset. This development could be the starting point for embedding microstructural evolution into macroscopic models. Moreover, a Eulerian level set approach is used to integrate the diffusion mechanisms into a finite element continuum mechanics framework. It specially permits to deal, simultaneously, with severe topological changes which characterize powder sintering. All this is possible because of the power of computers has dramatically been increased by parallel computing techniques allowing the simulation of larger systems.

The generalities of the sintering process will be presented along with the Fick's laws used to describe the diffusion phenomena in Chapter 2. Concerning the sintering simulation at the particles scale, different numerical approaches are available in literature. Among those models there are some analytical laws which allow to predict the growth of the neck between two particles. Those analytical models as well as more elaborated numerical approaches will be presented in Chapter 3. The lack of a numerical strategy able to handle simulation of sintering in 3D by different diffusion mechanism is evident. For this reason a numerical approach for the simulation of sintering at the particles scale will be proposed. The computational framework, based on the level set method, will be set in Chapter 4. Next, a method allowing to simulate sintering by surface diffusion will be presented in Chapter 5. In order to introduce the volume diffusion into the numerical approach proposed, the pressure field inside the particles has to be computed (Chapter 6). Taking into account this pressure computation, the numerical strategy for the sintering simulation for volume diffusion will be presented in Chapter 7. Finally the coupling between the volume diffusion and the surface diffusion will be presented in Chapter 8, as well as the bases for the grain boundary diffusion.

Chapter 2

Sintering and diffusion phenomena

Contents

The technique of forming parts from powders by pressing and sintering dates back to the beginning of human civilization. Almost every metal or ceramic material was initially made by using powders [Exner *et al.* 1996]. It was only after the 1940s that sintering was studied scientifically. Since then, a large number of scientific publications have appeared, but several questions about the underlying physical phenomena remain unanswered.

Even though remarkable developments in sintering science have been achieved as much as from the practical point of view, today's challenge is to produce sintered parts with reproducible and controlled microstructure through the control of the process variables.

In Section 2.1 a general introduction to the manufacturing process by sintering of consolidated powder is presented. This manufacturing process presents several stages, but this work will be concerned about the sintering stage. Therefore, the sintering phenomenon is also introduced in this section and it will be shown that the diffusion phenomena control this stage. The microstructural evolution that takes place during sintering process is due to the diffusion phenomena, for this reason the theory related to the diffusion phenomena is developed in Section

2.2. Finally the conclusions are presented in Section 2.3.

2.1 Sintering process

From the physcical point of view, sintering is a thermally activated phenomenon driven by the excess of free energy of the system and which allows the passage from a consolidated powder to a coherent material. From a practical point of view, this industrial process can be described as an operation where a powder compact changes its structure to obtain a solid density-controlled body with some specific mechanical properties. Today, sintering is a widely used fabrication process, and its applications are widespread: high performance structural parts, porous materials for multiple applications, carbides for cutting tools, biocompatibles materials and medical devices are some examples of such applications.

It is possible to identify different kind of sintering processes such as Hot Isostatic Pressing Sintering (HIP), microwave sintering, Spark Plasma Sintering (SPS), free sintering. Their applications as well as their modeling are very different. The present research is concerned by the free sintering that is presented below in Section 2.1.1.

2.1.1 Sintering of consolidated powder process

Even if in this work the emphasis will be placed on the study of the sintering stage itself, it is important to know the preliminary stages. Indeed, several studies in literature show that the preliminary operations have an important impact on the properties of the finished part or material [Rahaman 1995]. The general stages of the production of a part by sintering of consolidated powders are shown in the flow chart in Figure 2.1.

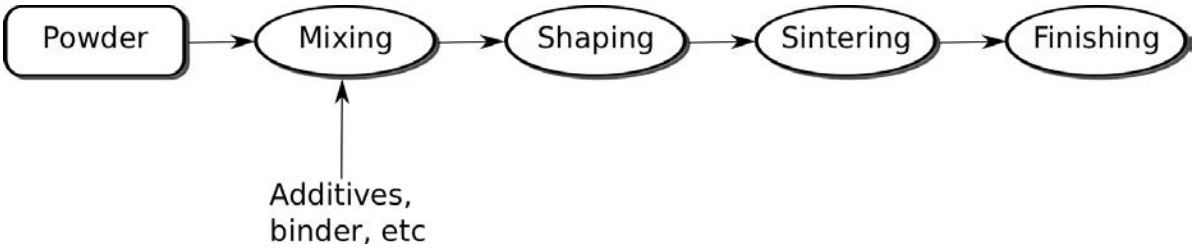

Figure 2.1: General flow chart of the sintering process.

In order to produce a sintered part it is necessary to follow the stages presented in Figure 2.1. A brief description of each stage can be proposed:

1. *Powder preparation*

The powder characteristics of greatest interest are the size, size distribution, shape, degree of agglomeration, chemical composition and purity. Those characteristics highly depend on the preparation method used. There exist two main methods for the preparation of powders: mechanical and chemical methods. Within the mechanical methods, milling processes are the most used and they can be used for the production of powder with a particle size ranging from 0.1μm to 100μm. Regarding the chemical methods, three main categories can be differentiated: solid-state reactions, preparation from liquid solutions and preparation by vapor-phase reactions (see [Rahaman 1995] for further information).

2. *Mixing*

   The powder is dispersed into a liquid to create a colloidal suspension. Colloidal suspension are used for the consolidation of ceramic powder rather than the powder on its dry state because of the better uniformity that can be achieved with the suspension. Furthermore, a better uniformity of the consolidated powder leads to a better control of the microstructure. During the preparation of the suspension, it is very important to avoid flocculation. That occurs when the particles stick between them due to attractive forces. To avoid flocculation, the colloidal suspension should be stabilized mainly in two ways. The electrostatic stabilization aims to create a repulsion between the particles by using electrostatic charges. And the polymeric stabilization is done by adding some organic polymer molecules. All this mixing process should be performed trying to keep the viscosity of the suspension as low as possible, which will be favorable for the shaping step. Other additive products such as solvents, dispersants, binders, plasticizers, etc. can be added to the solution in order to improve specific characteristics mainly related to the solution homogeneity and the strength of the green body. Those additives (that are generally of organic nature) are removed from the green body (pressed) after the shaping stage. Usually, additives are removed by heating the green body at temperatures around 500°C or by dissolution in a solvent.

3. *Shaping*

   This stage, also known as *forming*, is used to shape the powder into a particular geometry. The body obtained from this operation is referred to as the *green body*. There are many methods that can be used for the forming, the choice of the method will depend on shape and the size of the part. One of the most important variables to be controlled in this stage is the packing density that can be defined as:

$$\text{Packing density} = \frac{\text{Volume of the particles}}{\text{Total volume: particles + voids}} \tag{2.1}$$

A high packing density is favorable to the fabrication of fully dense materials and requires a smaller sintering time. This packing density depends on multiple parameters such as the forming pressure [1], the particle size and the particle size distribution, etc.

4. *Sintering*
   The main goal of this stage is to heat the consolidated powder to obtain the desired packing density and microstructure. Raise on temperature triggers some diffusion mechanisms that are responsible for the microstructural evolution of the structure. Two main sintering categories can be identified: solid state and liquid phase sintering. The solid state sintering occurs when the sintering process is carried out at a temperature such that the whole consolidated powder remains in a solid state. On the other hand, if the temperature is high enough to achieve the fusion of at least one of the components of the powder, then it is called liquid phase sintering. The present work is limited to the study of the solid state sintering at the particle scale and will focus on this specific stage of sintering of consolidated powders that will be further discussed in Section 2.1.2.
5. *Finishing*
   According to the application, additional operations are performed to get the final product. Those operations are very variable and its study is beyond the scope of this work.

The fabrication by sintering of consolidated powder is a very complex process, and in order to obtain the desired properties, it is necessary to set all the process variables that have been presented. Furthermore, in the fabrication of advanced material or parts, other steps should be added, introducing in this way, additional variables that should also be controlled. Those complementary stages will not be detailed in this work.

There are two possible approaches attempting to provide a better understanding of the microstructural evolution, the empirical one which consists in making measurements under controlled conditions and the theoretical approach which is based on the modeling of the process. A theoretical approach will be used in this work, and the fundamentals of the sintering process are presented below in Section 2.1.2.

2.1.2 Sintering phenomena

As a function of the packing density, it is possible to identify three sequential stages during the sintering process (see Figure 2.2):

1. In the first stage, the neck bridging the particles is rapidly created and the particles of the

1. In the case of shaping by pressing.

powder system are still distinguishable. This stage is supposed to last until the radius of the neck between the particles has reached a value about $0.4 - 0.5$ of the particle radius. From the macroscopic point of view, this is equivalent to a packing density of about 0.65 [Ashby 1974, Rahaman 1995].

2. At the beginning of this intermediate stage the porosity is still open, which means that the pores are interconnected and their shape is roughly cylindrical. As the different diffusion paths take place, the porosity shrinks, some isolated pores appear and the packing density continues raising up to a value of about 0.92. It is important to highlight that this stage covers the major part of the sintering process.

3. This final stage leads to the final microstructure of the material. The pores, which are isolated and spherical, are supposed to continue shrinking to finally end up by almost disappearing. The final relative density of the material can raise up to 0.999.

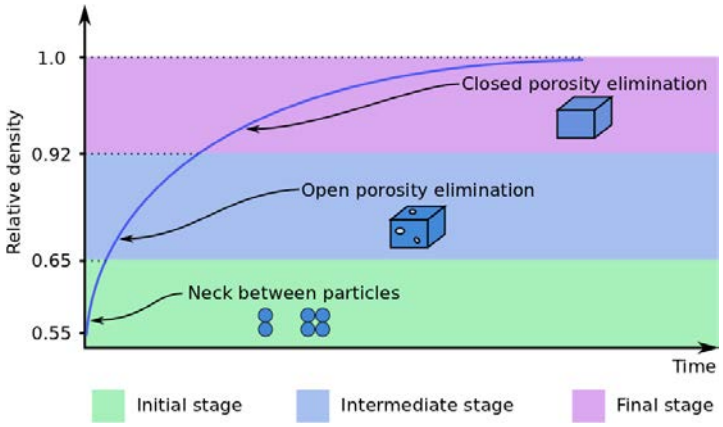

Figure 2.2: Packing density during the sintering stages.

During the sintering process, matter is transported to the contact points between the particles through multiple mechanisms involving diffusion phenomena [Ashby 1974]. This matter transport contributes to the development of necks between the particles. As the matter is transported the porosity between the particles is filled, the density of the compact increases and as a consequence, the powder packing shrinks. Figure 2.3 shows the neck formed between the particles.

Surface energy provides the driving force for the evolution of the structure during pressureless sintering. Depending on the size distribution of the powder particles and the porosity of the consolidated powder, the total excess of free energy of the surface reaches to 0.1-100$\frac{\text{J}}{\text{mol}}$, where the smaller number applies to coarse consolidated powders ($\sim 100\mu$m) with low porosity and

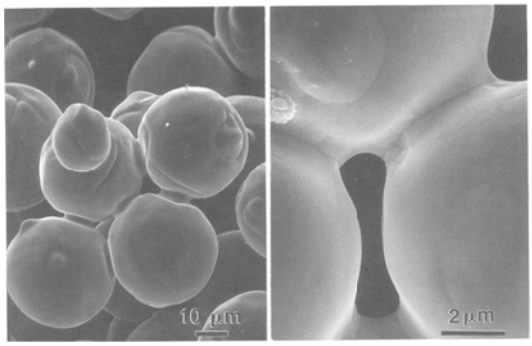

Figure 2.3: Neck between the particles created during sintering ([German 1996] page 71).

the larger number to sub-micron powders or highly dispersed porosity [Exner *et al.* 1996, Herring 1951].

It is possible to distinguish at least six mechanisms leading to the necks growing and/or the densification of the solid. They will be described in detail In Chapter 3. Those six matter transport paths shown in Figure 2.4, have a common driving force: the reduction of the total free surface area which is directly related to the surface free energy of the system. The six diffusion mechanisms shown in Figure 2.4 correspond to surface diffusion (1), volume diffusion (2, 5 and 6), grain boundary diffusion (4) and vapor transport (3). As the diffusion phenomena take place, the total free surface is reduced, but at the same time, the surface of the solid-solid interfaces increases (the grain boundary surface). The grain boundary energies usually are lower than surface energies. However the matter transport can stop because of the establishment of local equilibrium between grain boundary and surface energy [Exner *et al.* 1996, Hoge & Pask 1977].

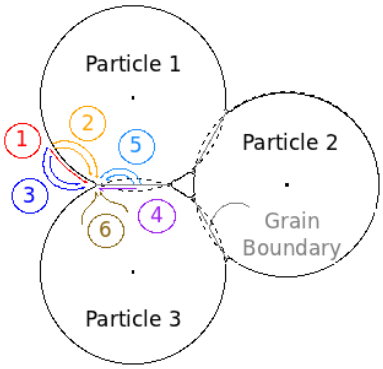

Figure 2.4: Six different diffusion paths.

All the paths presented in Figure 2.4 contribute simultaneously to the neck growth, but only some of them lead to densification. At the particle scale, the densification is defined as the rate at which the particles centers approach each other. Considering an atom or a mole of material, according with its position on the solid (surface, volume or grain boundary) an associated *chemical potential* can be defined and the matter flux is proportional to the gradient of this chemical potential. This will be further detailed in Chapter 2.2.

Table 2.1 shows the sources and the sink of matter for each diffusion path presented in Figure 2.4. The "Densifying" column indicates if the diffusion path leads whether or not to densification.

	Diffusion Path	Source	Sink	Densifying
1	Surface diffusion	Surface	Neck	
2	Volume diffusion	Surface	Neck	
3	Vapor transport	Surface	Neck	
4	Grain boundary diffusion	Grain boundary	Neck	✓
5	Volume diffusion	Grain boundary	Neck	✓
6	Volume diffusion	Dislocations	Neck	✓

Table 2.1: Matter transport paths

In the next section, the theory to study the diffusion phenomena will be introduced. As it has been outlined before, the matter flux can be estimated, under some specific hypotheses, by using the chemical potential. Therefore the corresponding expressions for these potentials will be developed.

2.2 Diffusion phenomena

As presented in the previous section, diffusion is responsible of sintering. The *Fick's laws* describe the movement of chemical species as a function of the gradient of concentration. In cases where the concentration is independent on the time, the diffusion process can be described by using Fick's first law [Howard & Lidiard 1964], which states that the flux of diffusing species is proportional to the gradient of concentration as follows:

$$\underline{j} = -D\underline{\nabla C} \tag{2.2}$$

where D is the diffusion coefficient and is assumed to be independent on the concentration [Rahaman 1995]. In Equation (2.2) the diffusion coefficient can be replaced by the diffusion

coefficient tensor $\underline{\underline{D}}$ in cases where the diffusion is not the same in all directions. However in this work diffusion is considered to be isotropic, and therefore D is a scalar value.

It is very important to recall that diffusion is thermally activated. This means that an *activation energy* should be supplied to the system to trigger diffusion. For example, consider the three (a. b. and c.) states presented in Figure 2.5. In order to induce the change in position of the interstitial atom shown in Figure 2.5a to Figure 2.5c, the lattice should be distorted in the intermediate position (Figure 2.5b). As the energy in the intermediate state is higher than in the initial one, this distortion can only be achieved by supplying some supplementary energy to the system. As the level of energy of the atoms is different, only a certain fraction of atoms will have sufficient energy to be able to move from one position to another. Considering this fact, the diffusion coefficient D is expected to depend on the temperature as follows [Rahaman 1995, Howard & Lidiard 1964]:

$$D = D_0 \exp \frac{-Q}{RT} \tag{2.3}$$

where Q is the activation energy, R is the gas constant and T is the temperature.

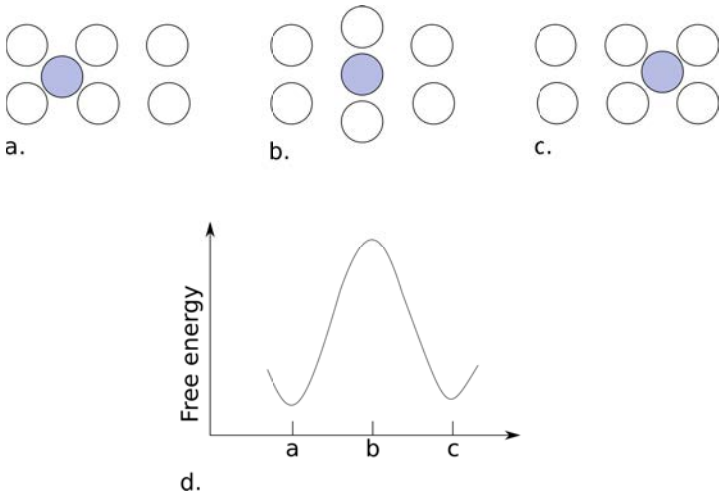

Figure 2.5: Schematic diagram showing the configuration of a set of atoms when one of them changes its position (a. b. and c.) and the corresponding free energy of the lattice (d.).

As outlined earlier, the diffusion phenomena during sintering can be studied by using Fick's first law (Equation (2.2)) where the matter flux is proportional to the concentration gradient. However in literature [Kuczynski 1949, Herring 1951, Howard & Lidiard 1964, Ashby 1974, Exner *et al.* 1996, Rahaman 1995], sintering is considered as a *chemical diffusion process* and it

is usually studied in terms of *chemical potential*. Instead of using the concentration gradient for modeling the matter flux, this flux is considered to be proportional to the chemical potential gradient as detailed below in Section 2.2.1.

2.2.1 Chemical potential

In the same way as the temperature measures the feeling of cold or hot and the heat flux goes downward the temperature, the chemical potential measures the tendency to diffuse of a substance and the matter flux goes downward the chemical potential. This kind of laws are often called *first gradient law*.

In order to introduce the *chemical potential*, consider a pure solid substance in which vacancies are the only kind of point defect present. If the local equilibrium between vacancies and atoms is assumed, the *Gibbs-Duhem* relation is satisfied [Herring 1951, Rahaman 1995]:

$$G = \mu_a N_a + \mu_v N_v \tag{2.4}$$

where μ_a is the chemical potential of the atoms, μ_v the chemical potential of the vacancies, N_a is the number of atoms, N_v is the number of vacancies and G is the Gibbs free energy which is defined as a function of temperature T, pressure p and internal energy U as follows:

$$G = U + pV - TS \tag{2.5}$$

where V is the volume and S is the entropy.

The chemical potentials which represent the energy brought by an atom, μ_a, and by a vacancy, μ_v can be derived from the previous equation:

$$\mu_a = \left(\frac{\partial G}{\partial N_a}\right)_{N_v,T,p} \tag{2.6}$$

$$\mu_v = \left(\frac{\partial G}{\partial N_v}\right)_{N_a,T,p} \tag{2.7}$$

The change in internal energy U can be written as a function of the change of the extensive quantities [2] S, V, N_a and N_v:

$$dU = TdS - pdV + \mu_a dN_a + \mu_v dN_v \tag{2.8}$$

2. that depend on the amount of material of the system.

temperature T, pressure p, chemical potential of the atoms μ_a and vacancies μ_v, are the intensive quantities of the system (that do not depend on the amount of material).

Equation (2.8) tells that the energy of a system can change in different ways: by changing its entropy S, its volume V, the amount of atoms N_a or the amount of vacancies N_v. The intensive quantities (T, p, μ_a, μ_v) determine the magnitude of the energy change related to the change of the corresponding extensive quantities (S, V, N_a, N_v). For example, given a change of the system entropy dS, the energy increase is large if the temperature is high, and is small if the temperature is low [Job & Herrmann 2006]. Indeed, the change of the free energy of the system is given by the sum of two contributions, the change in internal energy δU and the change of the surface free energy.

Finally a set of thermodynamical expressions that will be useful for future reference are presented:

$$\left(\frac{\partial \mu_a}{\partial p}\right)_{N_v,T} = \left(\frac{\partial^2 G}{\partial p \partial N_a}\right)_{N_v,T} = \Omega \tag{2.9}$$

$$\left(\frac{\partial \mu_v}{\partial p}\right)_{N_a,T} = \left(\frac{\partial^2 G}{\partial p \partial N_v}\right)_{N_a,T} = f\Omega \tag{2.10}$$

where the volume of a vacancy is supposed to be the fraction f of the atomic volume Ω [Herring 1951, Garikipati *et al.* 2001]. Figure 2.6 shows how the lattice is distorted because of the presence of a vacancy.

In addition, the change in chemical potentials μ_a and μ_v with respect to the change in vacancies concentration C_v is mainly due to the entropy mixing of atoms and vacancies [Herring 1951]. The vacancies concentration is defined as a function of the number of atoms N_a and the number of lattice sites N_L in a given volume: $C_v = (N_L - N_a)/N_L$ and since $C_v \ll 1$, it is possible to write:

$$\left(\frac{\partial \mu_v}{\partial C_v}\right)_{p,T} = \frac{kT}{C_v} + \mathcal{O}(1) \tag{2.11}$$

$$\left(\frac{\partial \mu_a}{\partial C_v}\right)_{p,T} = -kT + \mathcal{O}(C_v) \tag{2.12}$$

The diffusional transport can take place only by migration of interstitial atoms or lattice vacancies and neither of these processes changes the number of lattice sites in the region. In other words the number of atoms N_a and the number of vacancies N_v change by equal and

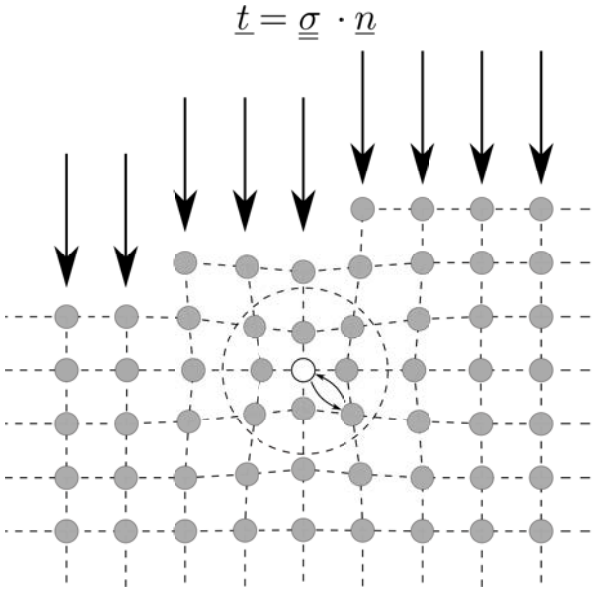

Figure 2.6: Schematic diagram showing the rearrangement of the lattice around a vacancy.

opposite amounts [Herring 1951]. Under those conditions, the change of the free energy of a region is therefore equal to the number of atoms entering or leaving it multiplied by the difference of chemical potential involved in the atom-vacancies switching ($\mu_a - \mu_v$). Moreover, the diffusional flux is given by:

$$\underline{j} = -\frac{D}{kT\Omega}\left(\nabla\underline{\mu_a} - \nabla\underline{\mu_v}\right) \tag{2.13}$$

The previous expressions will be used in the following sections in order to find the chemical potential beneath a surface (2.2.2), on the volume (2.2.3) and over the grain boundary (2.2.4).

2.2.2 Surface diffusion

In order to introduce the chemical potential beneath a curved surface, consider the Figure 2.7a, where a solid with a concave and a convex surface is presented.

The *specific surface free energy*[3] (γ_{sf}) of a crystalline solid is defined as the increase of energy when the area of the free surface $\partial\omega$ of the crystal is increased by a unit amount. It comes that the surface free energy E_s of the system is given by:

3. sometimes also known as *surface tension coefficient* or for the sake of simplicity just *surface tension*.

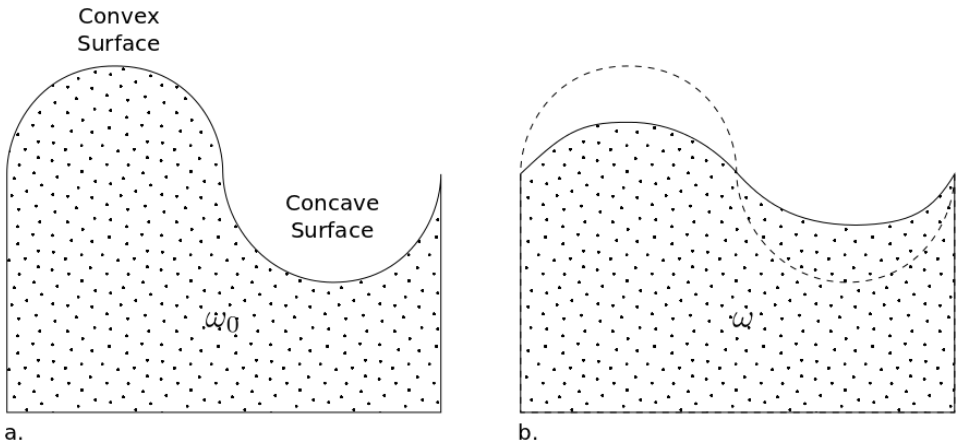

Figure 2.7: Schematic diagram showing a solid ω with a concave and a convex surface. a. Initial shape ω_0. b. Final shape ω (the dashed line represents the initial shape).

$$E_s = \int_{\partial\omega} \gamma_{sf} dA \tag{2.14}$$

$\partial\omega$ is the free surface of the solid ω. In this work γ_{sf} is considered to be constant along the surface.

By considering Equation (2.14), it is possible to show that the solid in Figure 2.7a has a higher surface free energy than the solid presented in Figure 2.7b. Therefore a way to reduce the energy is to reduce the total surface of the solid, and this can be achieved by transporting matter from the convex region to the concave region or globally to tend toward a surface of lower curvature.

An expression of the chemical potential can be found by establishing that the free energy is a minimum with respect to any infinitesimal virtual change in which the local shape of the surface is altered by removing atoms from the interior and placing them on the surface [Gibbs 1928, Herring 1951], or vice versa (see Figure 2.8).

Considering a smoothly curved surface as shown in Figure 2.8, the change of the surface free energy is given by:

$$\delta\left(\int_{\partial\omega} \gamma_{sf} dA\right) = \int_{\partial\omega_0} \delta\left(\gamma_{sf}\right) dA_0 + \int_{\partial\omega} \gamma_{sf} \delta\left(dA\right) \tag{2.15}$$

where δ represents a small change of the quantity, dA_0 is the area of an element of the original surface and $dA_0 + \delta dA$ the area of the element of the final surface. The term $\delta\gamma_{sf}$ is equal to zero because γ_{sf} is considered to be constant.

Considering Figure 2.8, $\delta\left(dA\right)$ is given by:

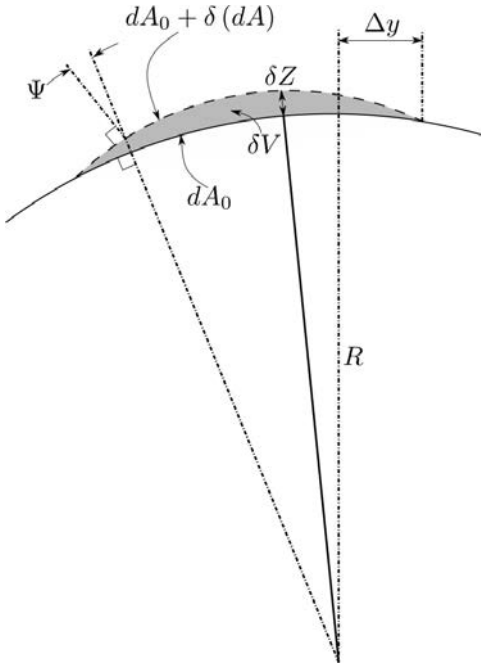

Figure 2.8: Infinitesimal hump formed building up a curved surface. Full line: original surface. Dashed line: built-up surface [Herring 1951].

$$\delta(dA) = \left(\frac{1}{\cos\Psi} - 1\right) dA_0 + \delta Z \left(\frac{1}{R_1} + \frac{1}{R_2}\right) dA_0 \tag{2.16}$$

where R_1 and R_2 are the two principal radii of curvature at dA_0. A principal radius of curvature is considered to be positive for convex surface, e.g. $R_1 = R_2 = R$ for a sphere of radius R. If Δy (Figure 2.8) is small, then R_1 and R_2 may be taken constant in the hump and $(1/\cos\Psi - 1) \simeq 0$. Finally Equation (2.15) can be simplified as follows:

$$\delta\left(\int_{\partial\omega} \gamma_{sf} dA\right) = \gamma_{sf}\left(\frac{1}{R_1} + \frac{1}{R_2}\right)\delta V \tag{2.17}$$

with δV the volume of the hump: $\delta V = \int_{\partial\omega} \delta Z dA_0$.

From Equation (2.8) and considering an isothermal process where only a vacancy is brought (no change on the number of atoms), the change of the volume term of the free energy due to the creation of the hump is:

$$\delta U = -p\delta V + \mu_v \frac{\delta V}{\Omega} \tag{2.18}$$

where p is the hydrostatic pressure beneath the surface element being considered and $\frac{\delta V}{\Omega}$

represents the number of atoms which must me brought into this portion of the crystal to build up the hump. As the shape of the surface should be in equilibrium with respect to the creation or annihilation of small humps, the internal and external energies variations (sum of Equations (2.18) and (2.15)) must vanish [Gibbs 1928, Herring 1951, Rahaman 1995]:

$$\begin{aligned} \delta U + \delta\left(\int_{\partial\omega} \gamma_{sf} dA\right) &= 0 \\ \Rightarrow \qquad -p\delta V + \mu_v \frac{\delta V}{\Omega} + \gamma_{sf}\left(\frac{1}{R_1} + \frac{1}{R_2}\right)\delta V &= 0 \end{aligned} \tag{2.19}$$

From Equation (2.19), the vacancies chemical potential beneath a curved surface can be written as:

$$\mu_v = p\Omega - \gamma_{sf}\left(\frac{1}{R_1} + \frac{1}{R_2}\right)\Omega = p\Omega - \gamma_{sf}\kappa\Omega \tag{2.20}$$

where κ is the mean curvature. In order to get an expression of the diffusional flux on surface $\underline{j^s}$, the atoms chemical potential should be computed. Since the vacancies concentration C_v is always $\ll 1$, Equation (2.12) shows that variations in μ_a due to variations of C_v will be negligible compared to the corresponding variation of μ_v (Equation (2.11)) [Herring 1951]. Therefore by using Equation (2.9) one can write:

$$\mu_a = \mu_{a_0} + p\Omega \tag{2.21}$$

where μ_{a_0} is the atoms chemical potential under no stress.

Finally, the surface atoms flux $\underline{j^s}$ is given by:

$$\underline{j^s} = -\frac{D_s \gamma_{sf}}{kT} \underline{\nabla_s \kappa} \tag{2.22}$$

where D_s is teh surface diffusion coefficient and κ is the mean curvature of the surface and it is also positive for a convex surface. As the chemical potential is defined along the surface of the particles, the gradient presented in Fick's law should be a gradient computed along the surface of the particles (∇_s).

2.2.3 Volume diffusion

Consider the solid presented in Figure 2.6 (page 13) where the lattice is deformed because of the presence of a vacancy. The deformation of the lattice due to the presence of a vacancy is supposed to be isotropic. This means that a vacancy that has been brought into a portion

of the crystal will induce a virtual change of the volume δV. The number of vacancies required to generate that volume change is given by $\delta V / f\Omega$.

Furthermore, as the system should be in equilibrium with respect to this virtual volume change, the change of the internal energy δU must be equal to zero:

$$\delta U = -p\delta V + \mu_v \frac{\delta V}{f\Omega} = 0 \tag{2.23}$$

From the previous Equation (2.23), it is possible to find an expression for the vacancies chemical potential μ_v inside the volume:

$$\mu_v = f\, p\Omega \tag{2.24}$$

Like in the previous Section 2.2.2, the atoms chemical potential μ_a is considered not to depend on the vacancies concentration C_v as $C_v \ll 1$. Therefore the atoms chemical potential μ_a will be, again, given by Equation (2.21). And the volume atoms flux can be written as follows:

$$\underline{j^v} = -\left(1 - f\right) \frac{D_v}{kT} \underline{\nabla p} \tag{2.25}$$

where D_v is the volume diffusion coefficient.

2.2.4 Grain boundary diffusion

Even if this work is mainly concerned by surface and volume diffusion, the grain boundary diffusion is a very important path of sintering and the theory related to the matter transport by this mechanism is presented. As in Section 2.2.2, the change of the free energy of the system is given by the sum of two contributions, the change in internal energy δU and the change of the surface free energy. The main difference is related to the internal energy that can be lowered by the migration of matter from one particle to its neighbor. If the internal energy of one of the particles forming the grain boundary is higher than the internal energy of its neighbor, matter will migrate and the particle of lower energy will grow at the expense of the other particle.

By making the same kind of development as those presented in Sections 2.2.2 and 2.2.3, it is possible to show that the chemical potential at the grain boundary between the particles can be written as a function of the normal stress σ_{nn} [Herring 1951, Pan & Cocks 1995, Wakai & Brakke 2011]:

$$\underline{j^{gb}} = -\frac{D_{gb}}{kT}\underline{\nabla_{gb}\sigma_{nn}} \tag{2.26}$$

where D_{gb} is the grain boundary diffusion coefficient. Like in the surface diffusion, ∇_{gb} corresponds to a gradient computed along the grain boundary.

2.2.5 Diffusion induced velocity

According to the path followed by the diffusion flux, the induced velocity should be computed in a different way. In the case of the surface and grain boundary diffusions, matter is transported along the interfaces. For the surface diffusion, the flux follows the free surface and for the case of the grain boundary, the flux appears along the grain boundary between the particles. Those transport paths result in a deposition or removal of material over the corresponding interface (whether it is a free surface or a grain boundary), which gives raise to a displacement rate assumed to be normal to the interface: $\underline{v_n} = v_n\underline{n}$.

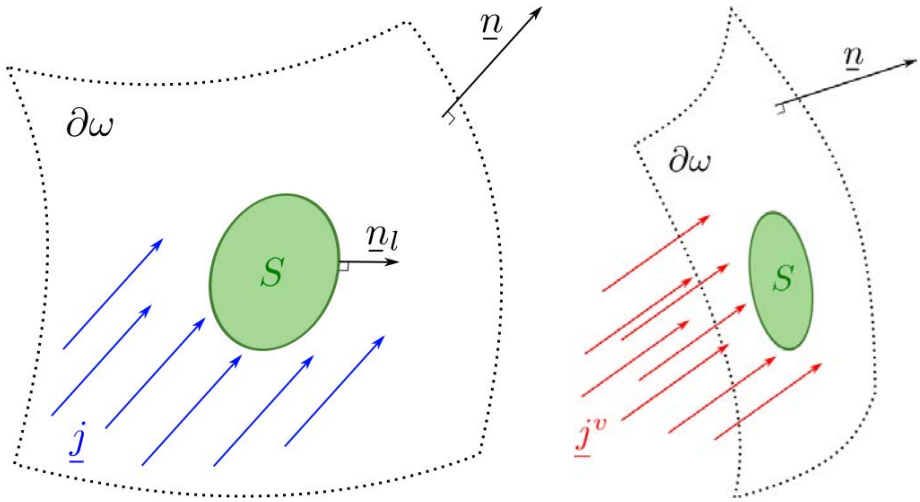

a. Surface or Grain boundary diffusion b. Volume diffuion

Figure 2.9: Elementary surface S under a matter flux due to: a. Surface diffusion $\underline{j} = \underline{j^s}$ or grain boundary diffusion $\underline{j} = \underline{j^s}$ b. Volume diffusion $\underline{j^v}$.

In order to find an expression for the normal velocity v_n, consider either a surface diffusion flux or a grain boundary diffusion flux $\underline{j}$. A matter balance is considered over the region $S \subset \partial\omega$ shown in Figure 2.9a. As the density of the material is constant, then it is possible to say that the matter transported by the induced velocity $\underline{v_n}$ is equal to $\underline{v_n}/\Omega$. Since matter is transported along the surface, the balance of matter is given by:

$$\int_{\partial S} \underline{j} \cdot \underline{n}_l dL = -\int_S \frac{1}{\Omega} \underline{v_n} \cdot \underline{n} dS$$
$$\int_{\partial S} \underline{j} \cdot \underline{n}_l dL = -\int_S \frac{v_n}{\Omega} dS \tag{2.27}$$

where $\underline{n}_l$ is the outward-pointing normal to ∂S (e.i. $\underline{n}_l$ is tangent to the surface S, see Figure 2.9a). By using the divergence theorem, Equation (2.27) becomes:

$$\int_S \left(\underline{\nabla_s} \cdot \underline{j} + \frac{1}{\Omega} \underline{v_n} \cdot \underline{n} \right) dS = 0$$
$$\int_S \left(\underline{\nabla_s} \cdot \underline{j} + \frac{v_n}{\Omega} \underline{n} \cdot \underline{n} \right) dS = 0 \tag{2.28}$$

where $\underline{\nabla_s \cdot}$ is the surface divergence operator. Since Equation (2.28) holds for any arbitrary surface $S \subset \partial\omega$, the integrand must be equal to zero. In this way, it is possible to find some expressions for the diffuion induced velocity for surface diffusion $\underline{v^s}$ and grain boundary diffusions $\underline{v^{gb}}$:

$$\underline{v^s} = v^s \underline{n} \qquad ; \qquad v^s = -\Omega \underline{\nabla_s} \cdot \underline{j^s} \tag{2.29}$$
$$\underline{v^{gb}} = v^{gb} \underline{n} \qquad ; \qquad v^{gb} = -\Omega \underline{\nabla_{gb}} \cdot \underline{j^{gb}} \tag{2.30}$$

with $\underline{\nabla_{gb} \cdot}$ is the surface divergence operator over the surface defined by the grain boundary.

In contrast with the surface and grain boundary diffusions, matter flux due to volume diffuion is not transported along the interfaces. In fact, this matter comes from the lattice (see Figure 2.9b), and therefore the balance of matter has to be established in a different way:

$$\int_S \underline{j^v} \cdot \underline{n} = \int_S \frac{1}{\Omega} \underline{v^v} \cdot \underline{n} dS \tag{2.31}$$

where $\underline{v^v}$ is the volume diffusion velocity.

Again, as Equation (2.31) holds for any arbitrary surface $S \subset \partial\omega$, the normal velocity induced by volume diffusion $\underline{v^v}$ is given by:

$$\underline{v^v} = v^v \underline{n} \qquad ; \qquad v^v = \Omega \underline{j^v} \cdot \underline{n} \tag{2.32}$$

2.3 Conclusions

From a macroscopic point of view, it is very difficult to develop a model taking into account all the different variables that have an impact on the evolution of the structure during sintering. The complexity of the sintering process makes very difficult the understanding of the underlying physical phenomena and experimental approaches very often do not allow to gather enough information.

The diffusion phenomena are responsible for the microstructural evolution of the structure. The *Fick*'s laws, which relate the matter flux to the gradient of the chemical potential, can be used for the modeling of these phenomena. The different expression for the chemical potential in surface, volume and grain boundary were developed and their corresponding velocities were also found.

The study of the sintering at the particle scale seems to be a very interesting way to enhance the understanding of the underlying physical phenomena. At this point the numerical approaches become a powerful tool that could clear several questions.

2.4 Résumé en français : Le frittage et les phénomènes de diffusion

Dans ce chapitre les généralités du procédé d'élaboration de matériaux par frittage ainsi que les équations utilisées pour la modélisation de la diffusion de matière sont présentées. Le frittage est un procédé très ancien utilisé pour l'élaboration par métallurgie des poudres des matériaux métalliques et céramiques depuis le début de la civilisation humaine. Les différentes étapes élémentaires du processus de frittage sont donc présentées. Même si ce procédé est d'une très grande importance du point de vue industriel, ce n'est que dans les années 40 que des études approfondies des différents phénomènes physiques présents dans ce procédé ont débuté. Avec ces recherches, la compréhension des différents phénomènes responsables de l'évolution microstructurale du système pendant le frittage a commencé à se développer. Malgré ces efforts, un grand nombre des questions concernant ces phénomènes physiques reste sans réponse. Pour cette raison, ce travail vise à étudier le procédé de frittage à échelle des grains.

Le frittage des matériaux est un procédé très complexe dans lequel des interactions multiphysiques ont lieu. La diffusion de matière est responsable de l'évolution du système et la prise en compte des phénomènes de diffusion à cette échelle est indispensable pour améliorer la compréhension du procédé. La loi de Fick est décrite en termes de potentiels chimiques afin de modéliser les différents chemins de diffusion présents pendant le frittage.

Chapter 3

Sintering modeling

Contents

In this chapter a general overview of different numerical simulations of the sintering process at the particle-size scale is presented. The first computer simulations of sintering appeared between 1955 and 1965. Those early attempts to simulate the sintering process were developed to predict the evolution of the neck and the shrinkage of two particles as a function of time. With the development of computers, more complex models of sintering appeared and the simulation of more realistic powder packing became possible.

First in Section 3.1, some power laws used to study the growth of the neck between to particles are presented. Even if this kind of laws is limited to the study of the sintering between only two particles, they represent a very useful tool concerning the validation of more complex models. Furthermore, kinetics of the different diffusion mechanisms is considered to be well represented by this kind of models (at least during the first stages of sintering). In Section 3.2, more elaborated numerical approaches are presented into two main categories: stochastic and deterministic approaches. Finally the conclusions are discussed in Section 3.3

3.1 Analytical models

As presented in the previous section, matter transport by diffusion is the underlying physical phenomenon during sintering. The main idea behind the analytical models is to solve a differential equation of matter transport by making some hypotheses mainly related to the geometry of the particles and the stress distribution.

Usually those models are developed to study the diffusion phenomena between two spherical particles or between a spherical particle and a plane by just one diffusion path. Even in those simple cases, the exact quantitative description of the geometry of the contact area presents some analytical difficulties, therefore multiple geometrical hypotheses should be made. In general, the geometry of the bodies is assumed to remain unchanged and the real shape of the contact area is replaced by a geometry were the curvature of the neck is constant. The most used geometrical parameters needed to develop this kind of models are shown in Figure 3.1. All those geometrical approaches are complemented with some hypotheses related to the diffusion path that is being modeled. Nevertheless, those simplifications are generally accepted [Uskoković & Exner 1977].

3.1.1 Grain boundary diffusion

In order to introduce the analytical models, the grain boundary diffusion will be considered. Grain boundary diffusion is assumed to occur over a constant thickness δ_{gb} and as it has been shown in Table 2.1, it is a densifying path.

The diffusion of atoms from the grain boundary into the neck [1] is given by the following Equation:

$$\underline{j}_{gb} = -D\underline{\nabla C} \tag{3.1}$$

where D is the atom diffusion coefficient and C is the atoms concentration. By making the hypothesis that the matter flux is parallel to the outward normal at the triple line, the volume of matter transported by unit of time into the neck is given by:

$$\frac{dV_{neck}}{dt} = D\|\underline{\nabla C}\|\, A_{gb}\Omega \tag{3.2}$$

where Ω is the molar volume and A_{gb} is the area of the grain boundary surface at the triple point and can be computed as $A_{gb} = 2\pi\, X\delta_{gb}$. The system is considered to be axisymmetric

1. Diffusion path number 4 in Figure 2.4 (page 8).

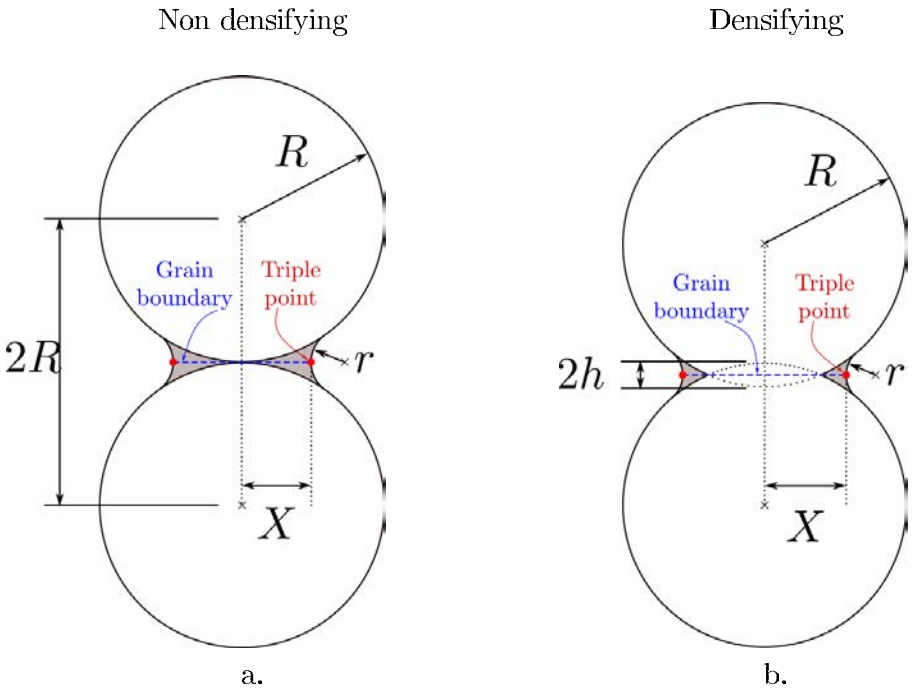

Figure 3.1: Geometrical parameters of two particles. a. Geometry for two particles without densification. b. Geometry of two particles with densification.

with respect to the axis formed by the centers of the two particles. Equation (3.2) becomes one-dimensional and can be simplified as follows:

$$\frac{dV_{neck}}{dt} = 2\pi\,\Omega D\,X\delta_{gb}\,\frac{dC}{dr} \tag{3.3}$$

At this point, another important hypothesis should be made concerning the concentration gradient dC/dr. The derivative of the concentration (C) with respect to the radius (r) is considered to be constant [Kuczynski 1949, Rahaman 1995], therefore dC/dr can be simplified as:

$$\frac{dC}{dr} = \frac{\Delta C}{\Delta r} = \frac{C - C_0}{X} = -\frac{\gamma_{sf}}{kT\,X}\left(\frac{1}{r_1} + \frac{1}{r_2}\right) \tag{3.4}$$

where C_0 is a reference concentration value, usually corresponding to the concentration under a flat surface. γ_{sf} is the surface tension coefficient of the solid-vapor interface, k is the Boltzmann's constant, T is the temperature and r_1 and r_2 are the two principal radii of curvature, which according to Figure 3.1, are equal to $r_1 = -r$ and $r_2 = X$, and it is assumed that $X \gg r$.

From Figure 3.1, it is possible to find simple geometrical expressions to compute the volume of matter transported into the neck (V_{neck}), the area of the surface of the neck (A_{neck}) and the main radii of curvature (r) can be computed as a function of the neck radius X and the particle radius R (see Figure 3.1). It is important to highlight that those expressions are different if the diffusion path lead whether or not to densification. Table 3.1 shows the expressions for V_{neck}, A_{neck}, r and for the cases with the densification, the expression for the centers approach h.

Parameter	No Densifying	Densifying
h	0	$X^2/4R$
r	$X^2/2R$	$X^2/4R$
A_{neck}	$\pi X^3/R$	$\pi X^3/2R$
V_{neck}	$\pi X^4/2R$	$\pi X^4/8R$

Table 3.1: Expressions for V_{neck}, A_{neck}, r and h for the geometries shown in Figures 3.1a and 3.1b.

The expressions shown in Table 3.1 are accurate up to $X \sim R/3$, and it can be shown that the hypothesis used to obtain those expressions can lead to serious deviations from the real values beyond this value of the neck radius (see [Uskoković & Exner 1977] for further details).

By replacing r and V_{neck} from Table 3.1 for a densifying mechanism and introducing Equation (3.4) into (3.3), a differential equation of the neck growth as a function of time can be obtained:

$$\begin{aligned} \frac{dV_{neck}}{dt} &= \frac{d}{dt}\left(\frac{\pi X^4}{8R}\right) = & 2\,\Omega D \pi\, X \delta_{gb} \frac{dC}{dr} \\ &= \frac{X^3}{2R}\frac{dX}{dt} = & 2\,\Omega D_{gb}\delta_{gb}\,\frac{\gamma_{sf}}{kT\,r} \\ &= \frac{X^3}{2R}\frac{dX}{dt} = & 8\,\Omega D_{gb}\delta_{gb}\,\frac{R\gamma_{sf}}{kT\,X^2} \end{aligned}$$

$$\Rightarrow \quad X^5 dX = \frac{16\,\Omega D_{gb}\delta_{gb}\,R^2\gamma_{sf}}{kT} dt \tag{3.5}$$

where D_{gb} is the grain boundary diffusion coefficient given by $D_{gb} = D\,C_0$.

Finally, by integrating and using the boundary condition of $X = 0$ at $t = 0$, Equation (3.5) becomes:

$$X^6 = \left(\frac{96\,\Omega D_{gb}\delta_{gb}\,R^2\gamma_{sf}}{kT} \right) t \tag{3.6}$$

In order to be able to establish some comparisons between the different models of two particles sintering by different diffusion paths, Equation (3.6) will be rewritten in a more convenient way:

$$\left(\frac{X}{R} \right)^6 = \frac{96\,\Omega D_{gb}\delta_{gb}\,\gamma_{sf}}{kT}\,R^{-4}\,t \tag{3.7}$$

3.1.2 Other diffusion paths

By using the same procedure, it is possible to obtain expressions for the neck growth as a function of time for the other diffusion paths. According to the hypothesis made different results for the same diffusion mechanism can be found. However those models are generally of power-law type:

$$\left(\frac{X}{R} \right)^n = BR^{-m}t \tag{3.8}$$

where R is the radius of the particles, t is time and n, m and B are constants. The value of those constants depends on the hypotheses used to obtain the model. Table 3.2 lists the range of values for m and n that can be found in literature and a plausible set of values for the three constants presented by [Exner *et al.* 1996].

The previous equations are based on some strong simplifications and their validity is limited to neck radii: $X < 0.3\,R$, and limited to the study of the sintering of two particles. As the computational capabilities increased, the interest in performing more elaborated sintering simulation became an important research field. A trend toward the simulation of more realistic powders sintering is present in several works, in Section 3.2 different approaches of sintering simulation over more complex particles packings will be presented.

3.2 Numerical modeling of the sintering process

Concerning the numerical modeling of the sintering process at the particles scale, it is possible to distinguish two main categories. From one side the deterministic models try to study the evolution of the compact powder under some specific conditions by modeling the underlying physical phenomena. This kind of approaches always produce the same output given a set of specific initial conditions. In the other hand, stochastic models are based in

Diffusion path	Values range		Plausible set of Values from [Exner *et al.* 1996]		
	n	m	n	m	B*
Surface diffusion	3-7	2-4	7	4	$\frac{23\gamma_{sf}D_s\delta_s\Omega}{kT}$
Volume diffusion from surface	4-5	3	4	3	$\frac{20D_v\gamma_{sf}\Omega}{kT}$
Vapor transport	3-7	2-4	3	2	$3\sqrt{\frac{2}{\pi}}\frac{\upsilon\gamma_{sf}p_g\Omega^{3/2}\rho^{1/2}}{(kT)^{3/2}}$
Grain boundary diffusion	6	4	6	4	$\frac{96\,\Omega D_{gb}\delta_{gb}\,\gamma_{sf}}{kT}$
Volume diffusion from grain boundary	4-5	3	5	3	$\frac{16D_v\gamma_{sf}\Omega}{kT}$
Volume diffusion from dislocations	2	1	2	1	$\frac{3\gamma_{sf}}{2\eta}$

*where the symbols in the expression of B: D_s, D_v and D_{gb} are the diffusion coefficients for surface, volume and grain boundary, respectively. γ_{sf} is the surface tension of the solid-vapor interface, δ_s and δ_{gb} are the thickness of the surface and grain boundary diffusion layers, Ω is the molar volume, k is the Boltzmann's constant, T is the absolute temperature, υ is an accommodation constant for gas transport, p_g is the gas pressure, ρ is the specific density and η is the viscosity.

Table 3.2: Constants appearing in Equation (3.8) and a set of plausible values [Exner *et al.* 1996].

probabilistic considerations, this means that given a specific configuration of the structure, its evolution is obtained in a random way by following a probability distribution. Therefore it is possible to obtain several different solutions out of the same initial set of conditions.

Compared to the analytical methods presented previously, deterministic and stochastic approaches are used to study the sintering of more complex sets of particles. Regardless the numerical approach, a trend toward the simulation of sintering over more realistic powder compacts is exhibited. However most of those simulations are performed in 2D.

3.2.1 Stochastic approaches

This kind of approaches are based on probabilistic considerations and the Kinetic Monte-Carlo method is the main method used. This method has been used to study the grain growth and the microstructural evolution of structures [Wu 1983, Weaire *et al.* 1986, Holm *et al.* 1991, Hassold *et al.* 1990, Chen *et al.* 1990, Tikare *et al.* 2003, Braginsky *et al.* 2005, Qiu *et al.* 2008,

Tikare *et al.* 2010]. Among those works, the Potts' model [Wu 1983] is used to simulate sintering of particles.

The idea is to create a grid of grain sites which contains the particles and the surrounding medium (pores). A particle is built-up of several grid sites and each site can assume any of Q distinc states. The state of a given site of a particle is given by a value of the q: $q_{\text{particle}} = [1, 2, 3, \ldots, Q]$ and a grid site corresponding the surrounding medium is given by a value of q: $q_{\text{pore}} = -1$.

The computational domain is given by a square in 2D or by a cube in 3D. the particles are mapped on the grid sites, each particle corresponding to a single state q. Contiguous grid sites of the same state q ($q > 0$) form a particle and contiguous empty sites ($q = -1$) form a pore. Grain boundaries exist between neighboring particles sites of different states, q, and pore-grain interfaces exist between neighboring pore and particles sites. The total energy of the system is the sum of the surface and grain boundary contributions. For a system of N grid sites, the total energy is given by:

$$E = \frac{1}{2} \sum_{i}^{N} \sum_{j}^{N} J(q_i, q_j) w_{i,j} [1 - \delta(q_i, q_j)] \tag{3.9}$$

where the term $\delta(q_i, q_j)$ is the Kronecker delta function such that $\delta(q_i, q_j) = 1$ if $q_i = q_j$ and $\delta(q_i, q_j) = 0$ if $q_i \neq q_j$. This means that the term $[1 - \delta(q_i, q_j)]$ is only different from 0 where an interface is present (a free surface or a grain boundary). $J(q_i, q_j)$ is the energy between the states q_i and q_j. $w_{i,j}$ is a weigthening term for the nearest neighbors and the next-nearest neighbors:

$$\begin{aligned} w_{i,j} &= w_f = 1 && i, j \text{ nearest neighbors} \\ w_{i,j} &= w_s && i, j \text{ next-nearest neighbors} \\ w_{i,j} &= 0 && \text{otherwise} \end{aligned} \tag{3.10}$$

in some works ([Tikare *et al.* 2003, Braginsky *et al.* 2005, Tikare *et al.* 2010]), the weigth of the next-nearest neighbors is not considered ($w_s = 0$).

The value of the states energy $J(q_i, q_j)$ is given by:

$$J(q_i, q_j) = \begin{cases} J & \text{if } q_i\, q_j < 0 \\ \varrho J & \text{if } q_i\, q_j > 0 \end{cases} \tag{3.11}$$

where J corresponds to the energy of the free surface interface and ϱJ corresponds to the energy of the grain-boundary.

The effect of different phenomena is taken into account in different ways. Concerning the grain-growth, a particle site ($q > 0$) is chosen at random from the computational domain and then a new state q is chosen from the Q possible states in the system. Before the new state q was assigned the total energy of the system (Equation (3.9)) was E_i, after the state q was changed, the total energy of the system can be different (E_f). The energy change is given by: $\Delta E = E_f - E_i$. Next the standard Metropolis algorithm is used to perform the grain growth step based in Boltzmann statistics. A random number between 0 and 1 is generated. The transition probability (P) is calculated using the following equation:

$$P(\Delta E) = \begin{cases} \exp \frac{-\Delta E}{k_B T} & \text{if } \Delta E > 0 \\ 1 & \text{if } \Delta E \leq 0 \end{cases} \tag{3.12}$$

where k_B is the Boltzmann constant and T is the temperature. If a random number R is lower than $P(\Delta E)$, then the new state q is accepted otherwise the original state is restored.

Other phisical phenomena such as the surface diffusion is considered by performing another procedure, this time an empty grid site ($q = -1$) is chosen randomly, if this site has a neighbor with a state $q \neq 0$, then the sites are temporarily exchanged. The exchange can lead to a change of the total energy of the system. Again, the Metropolis algorithm is used and the corresponding transition probability is computed by using Equation (3.9) [2]. After generating a random number R between 0 and 1, if $R \leq P$ the exchange is accepted otherwise the origial states are restored.

By using similar methods, other physical phenomena are introduced into the Monte-Carlo simulation. Time (t) is usually set in terms of Monte-Carlo Steps (MCS) such that 1 MSC corresponds to N attempted exchanges or changes, where N is the total number of grid sites of the computational domain.

Figure 3.2 shows the sintering of a set of about 20 particles of different size at different time steps. The significant feature of this result is the disappearance of some of the initially

2. The Boltzmann constant (k_B) present in this equation can be different for each physical phenomena, therefore it is a parameter that has to be set.

presented particles and the increase in the average size of the remaining particles.

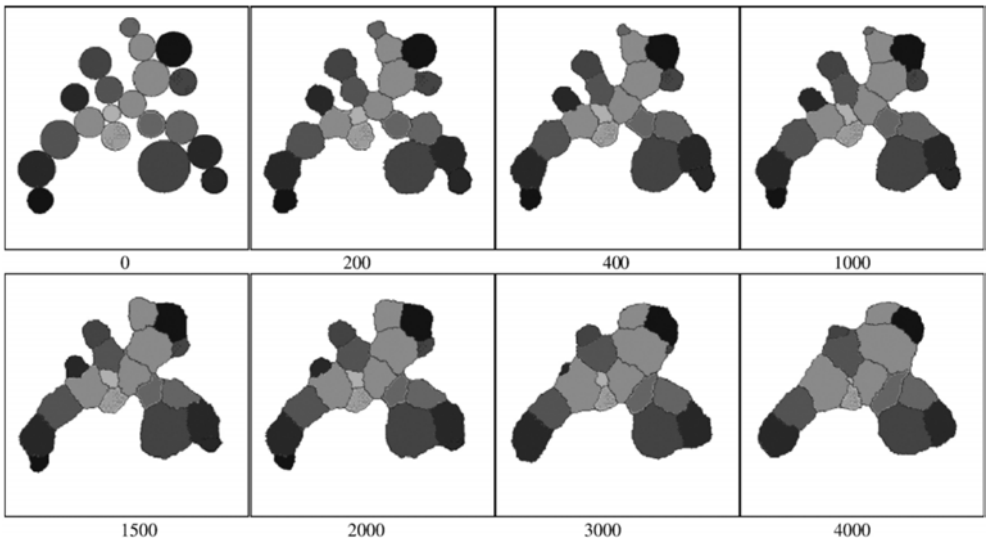

Figure 3.2: Sintering of a set of particles at different time steps. Using: $k_BT/J = 0.5$, $K_BT/\varrho J = 1$ and $w_s = 0.5$ [Qiu *et al.* 2008].

The main drawback of this kind of approaches is related to the high number of parameters that has to be set and very often comparisons with experimental results are required. Additionally, it is very complex to modify the parameters of the model in order to take into account different mechanical behaviors or different materials.

3.2.2 Deterministic approaches

Within the deterministic approaches, it is possible to find the finite element methods, finite difference methods, phase field methods, etc. Very often, those methods are used to simulate the sintering of a set of particles by multiple diffusion mechanisms at the same time [Pan & Cocks 1995, Chen 2002, Wakai & Brakke 2011]. Even if almost all approaches developed are supposed to be used over an arbitrary number of particles, many of them are only used within the framework of the sintering of two particles. Furthermore, most of them are limited to simulations in 2D.

These numerical methods have been used to study the underlying physical phenomena during the sintering process by many research team around the world. An early attempt to simulate the sintering process by coupled surface and grain boundary diffusion at the particles scale was presented by Bross and Exner [Bross & Exner 1979] in 1979. This work, based in the model developed by Nichols [Nichols & Mullins 1965], uses the finite difference method. The

results obtained in [Bross & Exner 1979] opened the way toward the simulation of the sintering of more complex powder compacts, and at the same time, greatly enhanced the understanding of sintering processes. However, this model was limited to 2D simulations and to rather simple geometries.

Until recently, the simulation of processes involving microstructural evolutions, such as sintering and recrystallization, of large systems was not possible because of the computational power limitations. Nowadays, the power of computers has significantly increased and with the development of parallel computing techniques, the simulation of this kind of problems is becoming possible.

As an important remark, the chemical potential associated with the volume and grain boundary diffusions is related to stress, specifically pressure p and normal stress σ_{nn}. However most of the studies concerning the sintering simulation by either of those mechanisms do not take into account the mechanical behavior of the particles. Instead, the stress is supposed to evolve following a known distribution [Riedel *et al.* 1994, Wakai & Brakke 2011] which is then used to compute the matter flux. To the author's knowledge, there exists only one study where the matter flux is computed by explicitly taking into account the mechanical behavior of the material [Djohari *et al.* 2009, Djohari & Derby 2009].

Some important works concerning the sintering simulations will be presented in the following Sections.

3.2.2.1 Pan & Cocks model [Pan & Cocks 1995]

In that work, the surface and the grain boundary diffusions are coupled to study the microstructural evolution involving these two diffusion paths. A rigorous treatment of the continuity conditions at the junction between the surface and the grain boundary is presented. This method has been successfully applied to simulate the microstructural evolution in 2D systems.

The computational domain is shown in Figure 3.3. Grain boundaries are assumed to be formed by straight lines and the grains are supposed to be rigid. The matter flux is modeled by using the Fick law presented in Chapter 2 (Equations (2.22) and (2.26) for surface and grain boundary diffusions, respectively).

The mass conservations at a triple point formed by two free surfaces and a grain boundary (as in Figure 3.4) is written as a function of the grain boundary matter flux $\underline{j_{gb}}$ and matter fluxes at the free surfaces $\underline{j_s}$:

$$\underline{j_{gb}} = -(\underline{j_s^+}) + (\underline{j_s^-}) \tag{3.13}$$

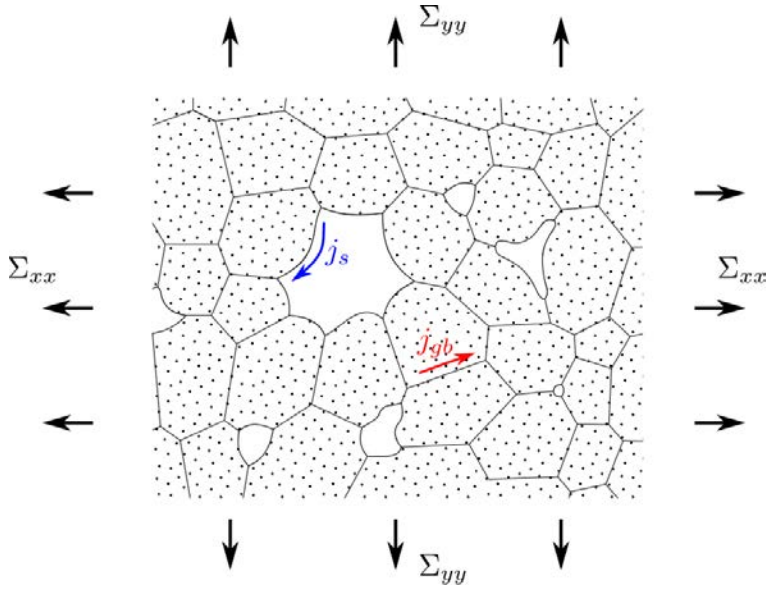

Figure 3.3: Polycrystalline material with pores [Pan & Cocks 1995].

where + and - indicate the two free surfaces at the triple point and the sign convention for these fluxes is defined in Figure 3.4.

If the triple point is formed by n grain boundaries, the mass conservation impose:

$$\sum_{i=1}^{n} \underline{j_{gb,i}} \cdot \underline{t_i} = 0 \tag{3.14}$$

where t_i is a unit vector pointing away from the i*th* grain boundary.

Concerning the momentum conservation, another condition can be written. The surface tension γ_{sf} and the grain boundary tension γ_{ss} lead to a discontinuity of the tangent at the triple point which is referred to as the dihedral angle 2θ (Figure 3.4):

$$\cos\theta = \frac{\gamma_{ss}}{2\gamma_{sf}} \tag{3.15}$$

Finally, the chemical potential should be continuous and therefore a relationship between the normal stress σ_{nn} and the "curvature" at the triple point κ^{tp} is established:

$$\sigma_{nn}^{tp} = \gamma_{sf}\kappa^{tp} \tag{3.16}$$

It is important to say that the curvature κ is undefined at the triple point. Therefore, it is considered as an additional unknown of the problem.

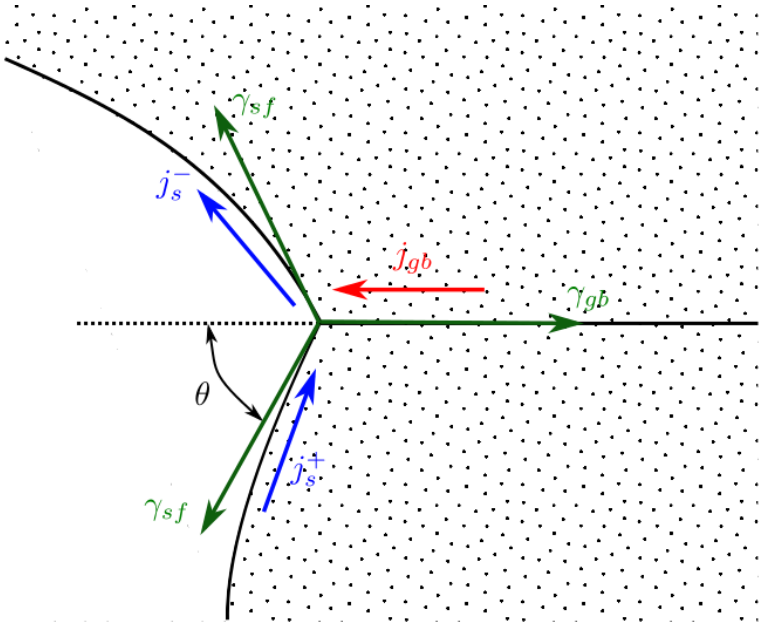

Figure 3.4: A triple point: junction between a grain boundary and a free surface. [Pan & Cocks 1995].

The finite element method is used to compute the matter flux by grain boundary diffusion and the matter flux by surface diffusion is computed by using a finite differences approach. In order to compute the matter flux by grain boundary diffusion, consider the following functional Π:

$$\Pi = \Pi_0 - \sum_{\text{tp}} \left(\lambda \sum_{i=1}^{n} \underline{t}^i \cdot \underline{j}_{gb}^i \right)$$

$$\Rightarrow \quad \Pi = \frac{1}{2} \int_{\Gamma_{gb}} \underline{j_{gb}} \cdot \underline{j_{gb}} dA + \sum_{tp} \sigma_{tp} \underline{t} \cdot \underline{j_{gb}} - \int_{S_T} \underline{T} \cdot \underline{V} dS$$
$$+ \sum_{tp} \gamma_{sf} \parallel \underline{v_{gb}} \parallel \sin\theta - \sum_{\text{tp}} \left(\lambda \sum_{i=1}^{n} \underline{t}^i \cdot \underline{j}_{gb}^i \right) \tag{3.17}$$

where $\sum_{tp}$ is a summation performed over all the triple points, $\sum_{i=0}^{n}$ corresponds to the n grain boundaries that meet at a given triple point, $\underline{t}$ is the unit vector along the grain boundary toward the triple point, S_T is the surface where the traction $\underline{T}$ is applied, $\underline{V}$ is the velocity of S_T, θ is the dihedral angle and λ represents a set of Lagrange multipliers introduced to ensure the mass conservation at the triple points.

Among all the kinematically admissible fields $\underline{j_{gb}}$ the true field makes the functional Π_0 minimum [Pan & Cocks 1995, Pan *et al.* 1997].

Concerning the surface diffusion, since all the simulations performed were in 2D, the free surface is discretized by using straight segments. From the coordinates of the nodes of the surface and from Equation (3.16), the curvature on each node is computed. Next the matter flux and the associated velocity is computed in the same way.

The coupling between the grain boundary and the surface diffusion is established by using the mass conservation at the triple points (Equation (3.13)). Figure 3.5 shows the evolution of two particles during sintering.

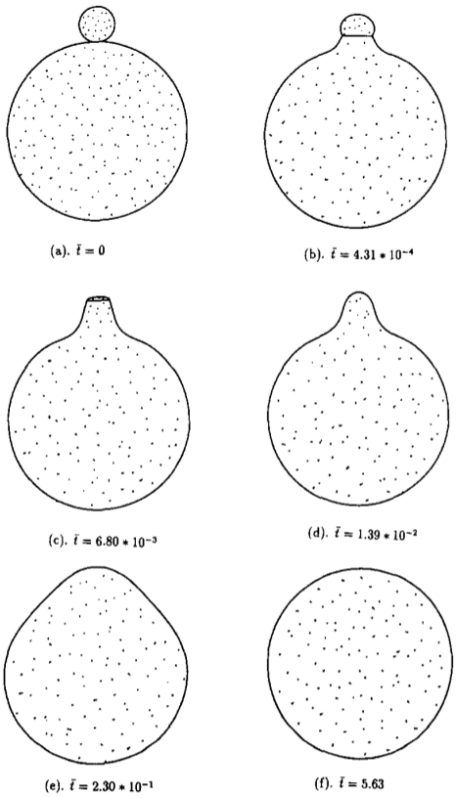

Figure 3.5: Sintering of two cylinders of different radii [Pan & Cocks 1995].

Several works using this approach have been presented by the team of J. Pan [Pan *et al.* 1997, Pan *et al.* 1998, Kucherenko *et al.* 2000, Ch'ng & Pan 2004, Ch'ng & Pan 2005, Pan *et al.* 2005].

In [Pan *et al.* 1997], a fully finite element formulation is used to solve the variational principle presented in Equation (3.17). All the simulations are performed in 2D, therefore the computational domain is discretized by using straight line elements. Concerning the surface diffusion and in contrast with the finite differences approach used in [Pan & Cocks 1995], a

finite element approach is used to compute the surface flux and the induced velocity. In this case, special elements are used to establish the junction between the free surfaces and the grain boundary.

An enhancement to the coupled finite element formulation presented in [Pan *et al.* 1997] is developed in [Ch'ng & Pan 2004]. The main idea is to represent the structure by using classical cubic spline elements. One of the advantages of this method is related to the smoothness of the interface that is enforced in such a way that second order derivatives are continuous at any point of the interface. This smoothness allows to reduce the high frequency oscillations of the interface during their migration and focuses the numerical solution on the global evolution of the microstructure.

3.2.2.2 Phase field model [Wang 2006]

When using finite element methods or finite differences methods within a Lagrangian continuum mechanics framework, the free surfaces of the system as well as the grain boundaries are used to apply boundary conditions to the problem. This kind of approaches are very useful when dealing with 2D problems and very often are used to validate the hypotheses made. Nevertheless, it is very complicated to enhance that kind of models in order to deal with 3D problems over complex geometries.

Alternative methods allowing to describe microstructural evolutions over complex geometries have been developed. The phase field methods is among those alternative methods and has been used by Wang in [Wang 2006] within the context of sintering simulation.

The phase field model uses several field functions (the so-called phase fields) which correspond to well-defined physical parameters such as the composition. In the case of the sintering simulation, the field functions take specific values in each particle and change smoothly but rapidly across the interfaces (the so-called diffuse interfaces) [Wang 2006, Chen 2002]. Figure 3.6 shows a field function F, equal to F_0 inside the particles and equal to 0 outside the particles. The bottom of Figure 3.6 shows the evolution of the field function along the horizontal line $A-A$ shown in the top. As it can be seen, there is smooth transition of F across the interfaces.

The total free energy of the system is a functional of the field functions and the microstructural evolution is driven by the reduction of the total free energy. In [Wang 2006], a parameter field η_i is defined to describe each particle, η_i is equal to 1 inside the ith particle and equal to 0 outside. An additional mass density field ρ is defined, this field allows to identify the particles from the surrounding media.

The change in the structure is given by the mass conservation equation:

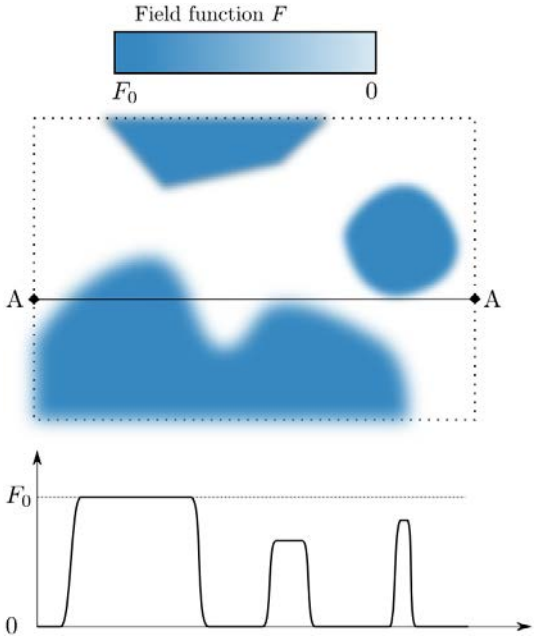

Figure 3.6: Diffuse interface of the field function F: on top a field function F is plotted over a square domain and at bottom the value of the field function across the line A-A is shown.

$$\frac{\partial \rho}{\partial t} + \underline{\nabla} \cdot (\rho \underline{v}) \tag{3.18}$$

where $\underline{v}$ is the local instantaneous velocity. Let define a mass flux density $\underline{p} = \rho \underline{v}$. The flux can be written as a sum of the contribution of two distinct processes:

$$\underline{p} = \underline{p}_{dif} + \underline{p}_{adv} \tag{3.19}$$

where $\underline{p}_{dif}$ and $\underline{p}_{adv}$ are the diffusion and advection [3] flux densities, respectively.

The advection flux is supposed to be induced by a rigid body motion characterized by a translation and a rotation of each particle. Those translations and rotations are computed in such a way that the mass is conserved. All the details of its computations are presented in [Wang 2006].

The diffusion flux takes into account all the diffusion paths at the same time and is computed as a function of a global chemical potential:

3. This kind of flux path is considered in order to ensure the mass conservation, because if only the diffusion paths are considered, the mass could, in some cases, not be conserved [Wang 2006, Wakai & Brakke 2011].

$$\underline{p}_{dif} = -D_{gl}\underline{\nabla\mu_{gl}} = -D_{gl}\underline{\nabla}\frac{\delta F}{\delta\rho} \tag{3.20}$$

where D_{gl} is the diffusion coefficient function of the phase fields ρ and η_i because its value depends on the region of the solid being considered (surface, grain boundary, volume, etc.). F is the total free energy of the system also computed by using the field functions ρ and η_i as follows:

$$F = \int_{\omega}\left(f\left(\rho,\{\eta_i\}\right) + \frac{1}{2}\beta_\rho \parallel \underline{\nabla\rho} \parallel^2 + \sum_i \frac{1}{2}\beta_\eta \parallel \underline{\nabla\eta_i} \parallel^2\right) dV \tag{3.21}$$

where β_ρ and β_η are constant coefficients of the model, $f\left(\rho,\{\eta_i\}\right)$ corresponds to the energy associated with the volume and the last two terms correspond to the energy at the free surface and the grain boundaries, respectively.

Equations (3.18) to (3.21) are solved by using a finite difference method. Figure 3.7 shows the evolution of a compact powder during sintering.

3.3 Conclusions

Sintering is a very complex process and several challenges should be handled in order to simulate the sintering process at the particles scale. However, important developments have been proposed and today it is possible to think about the simulation of the sintering of a packing of particles in 3D.

The analytical models presented at the beginning of this chapter are limited to very simple cases. Nevertheless, they represent the most useful way to validate the results of more complex numerical approaches because it is still very complicated to use experimental setups to validate those results. Furthermore, analytical models allow to study the kinetics of the process that is mainly based on the driving force selected for a given sintering mechanism.

More complex approaches allowing to simulate the sintering of more complex particles packs are usually limited to 2D and even if the numerical methods should work in 3D, none of them are used to perform simulations of sintering over realistic sets of particles in 3D.

As it has been presented in Chapter 2, the chemical potential in volume and grain boundary is computed as a function of the state of stress state of the particles. However, the mechanical response of the material to the external loading and the surface tension acting on free surface is usually neglected. A numerical approach taking into account the mechanical behavior of the particles and allowing to perform simulations in 3D is to be developed.

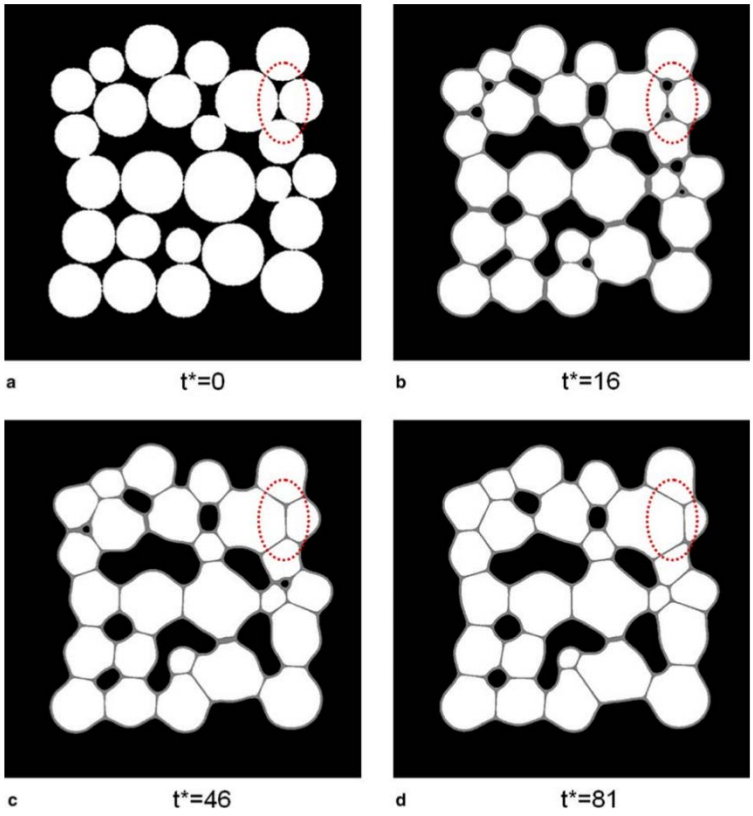

Figure 3.7: Simulated microstructure evolution in a powder compact during sintering. (a) initial green compact. (b-d) Typical snapshots of the simulated sintering process. The highlighted area shows the removal of two pores and the subsequent grain boundary migration [Wang 2006].

3.4 Résumé en français : Modélisation du frittage

Dans ce chapitre différents modèles numériques pour la simulation du frittage sont présentés. Dans un premier temps, des modèles concernant le frittage de deux particules par un seul mécanisme de diffusion sont discutés. Ces modèles sont très simples et la quantité d'information qui peut être obtenue est très limitée. Néomoins, ils représentent un outil très puissant pour la validation des approches plus complexes. Ces types de modèles, appelés modèles analytiques, sont toujours présentés sous la forme d'une loi puissance qui permet de relier la taille du cou formé entre deux particules au temps, donc en condition isotherme.

Au delà de ces modèles analytiques, un grand nombre de travaux concernant la simulation du frittage à l'échelle des particules est disponible. Ces modèles sont classés en deux grandes catégories, les modèles stochastiques et les modèles déterministes. Ici l'attention est portée sur ces derniers. Les modèles déterministes peuvent aussi être classés en deux grandes catégories : des approches Lagrangiennes et des approches Eulériennes. Différents travaux dans ces deux catégories sont présentés, et il peut être constaté que les approches existantes ne permettent pas de simuler le frittage à l'échelle des particules en 3D en tenant compte des différents mécanismes de diffusion sur des empilements granulaires proches de la réalité.

Une approche permettant de simuler le frittage à l'échelle des particules en 3D avec la prise en compte des différents mécanismes de diffusion ainsi que du comportement mécanique du matériau sera donc présentée par la suite.

Chapter 4

Numerical strategy

Contents

The numerical simulation of processes involving strong topological changes is an important field of research and different approaches have been developed to cope with these processes. Sintering, as it was presented in Chapter 3, is one of these processes and considering its simulation at the particles scale, numerical approaches must handle this challenge. Considering this, a classification of the numerical methods can be made depending on the nature of the computational grid for spatial discretization: (1) deformable grids and (2) fixed grids, where an additional strategy is needed to describe the internal change in the structure.

The use of deformable grids leads to an explicit description of the compact powder, and therefore the boundary conditions at the surface of the particles can be represented in a more accurate way. In counterpart, when representing the strong topological changes that can appear during the process, large deformations of the grid can occur. To deal with those large deformations, complete re-meshing is required which is very complex from the computational point of view and is usually quite expensive, especially for 3D problems. For those reasons, the evolution of the structure will be handled by using a fixed grid.

The use of a fixed grid adds a second phase to the problem modeling because the surrounding medium must be considered. In this way, the interface between the two phases (the compact powder and the surrounding medium which in this case is the air) should be described in a separate way. According to the method used to describe the interfaces, the numerical approaches can be divided into two different categories. The "Front tracking" methods and the "Front capturing" methods. Front tracking methods are based on a Lagrangian description of the interface where some markers are used to locate and follow the interface over the time. On the other hand, in front capturing methods the interface is implicitly represented by a phase function discretized on the fixed grid. This phase function allows to identify to which phase a given point belongs and the interface is defined by using the phase function.

In this chapter, some front tracking and front capturing methods are presented in Section 4.1 and 4.2, respectively. The choice of the Level-Set method is also supported in Section 4.2. All the generalities of the Level-Set (LS) method are discussed in Section 4.3. The LS approach used in this work is slightly different from the classical LS method. The modified LS approach as well as a mesh adaptation strategy backed on this modified LS approach are presented in Section 4.4. Finally the conclusions of the chapter are discussed in Section 4.5.

4.1 Front tracking methods

Front tracking methods are based on the use of markers which make a Lagrangian description of the interface. The main advantage of this kind of approaches is the straightforward interface definition. A high degree of accuracy can be achieved by extracting the interface geometry with high-order polynomial interpolations [Popinet & Zaleski 1999, Coyajee 2007]. Nevertheless, as for deformable grids, front tracking methods require regular redistribution of the markers on the interface to ensure a proper representation of the moving front. Within this category the "Volume tracking" and the "Surface tracking" are the most common methods.

4.1.1 Volume tracking

The earliest numerical technique developed to deal with problems involving two phases was the well-known marker and cell (MAC) method and was initially used within the framework of free surface flow [Harlow *et al.* 1965]. This technique uses marker particles that are advected with the local fluid velocity and the markers distribution allows the current fluid configuration to be known. Figure 4.1 shows a set of markers distributed over a fixed grid where each black point is a marker. The position of the i*th* marker is given by the vector $\underline{x}_i$ and the motion of the markers is given by the following equation:

$$\frac{d\underline{x}_i}{dt} = \underline{v}_i\left(\underline{x}_i, t\right) \tag{4.1}$$

where $\underline{v}_i$ is the velocity field interpolated at the point $\underline{x}_i$ using the fixed grid velocity values.

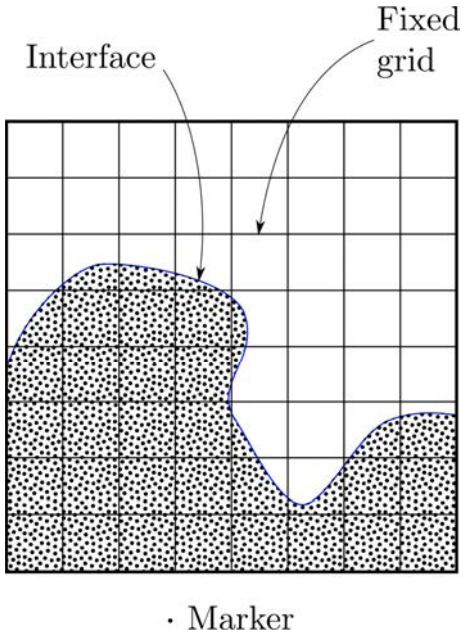

Figure 4.1: MAC technique representing a region over a fixed grid.

Although the MAC method allows to represent an arbitrary region over a fixed grid, it is difficult to obtain good quantitative information on interface orientation or partial cell volume from markers. Furthermore, boundary conditions at the interface are problematic and therefore are applied in an approximated way which very often lead to instability of the free surface [Rudman 1997]. This problem can be improved by ensuring that each cell contains a large number of markers, but this solution is computationally very expensive. Another drawback of this

technique is related to the distribution of the markers which can be very high in certain regions and very low in others following the physics of the problem. In this case some redistribution algorithms must be used periodically in order to avoid a significant loss of information.

4.1.2 Surface tracking

This method was proposed by Daly and Pracht in 1968 [Daly & Pracht 1968], the main idea is to use markers only over the interface instead of having them all over the concerned region. The motion of the interface is simply computed by moving the marker using Equation (4.1) again by using the velocity $\underline{v}_i$ interpolated from the fixed grid velocities. The interface is found by interpolating a curve (2D) or a surface (3D) across the markers as it is shown in Figure 4.2.

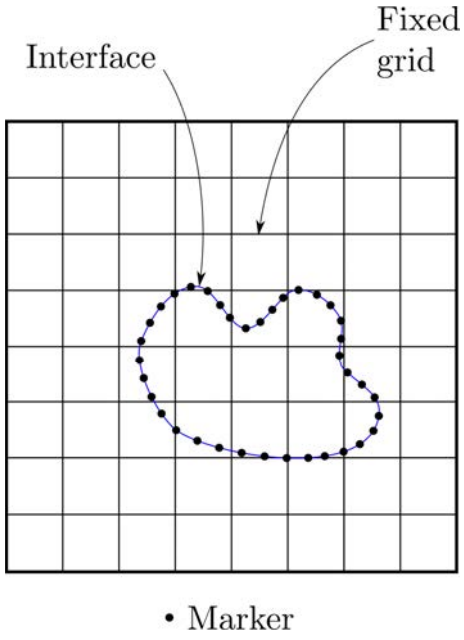

Figure 4.2: Front markers method.

The explicit representation of the interface is the most important advantage of this method. However it still has the inconvenient of the distribution of the markers over the interface, as the simulation goes on, some regions of the interface will be defined by much more markers compared to other regions where its density could be very low. Again some algorithms of redistribution of the markers are required. Additionally the connectivity between the markers is needed in order to reconstruct the interface.

The fixed grids approaches are supposed to handle topological changes with ease. However,

in this case the coalescence or detachment of a section of the surface can be very difficult to represent. In fact, concerning the coalescence of two non-connected interfaces, some surface markers will be placed in the middle of the two regions and therefore they should be removed, which is achieved by performing an additional operation. The removing operation should be applied under some criteria that should be manually defined. The same kind of procedure must be applied to deal with the detachment of a section of the interface. Additionally those criteria are much more complex when dealing with 3D problems. Figure 4.3 shows a schematic example of the coalescence and detachment of a region of the interface. Figure 4.3a shows two different interfaces that should be merged, the markers that are shown on the dashed gray ellipse should be removed to obtain a single interface as in Figure 4.3b. In the same way, the connectivity between the markers is modified of obtain the detachment a part of the interface, Figure 4.3c shows an interface that should be split into two separated interfaces (Figure 4.3d).

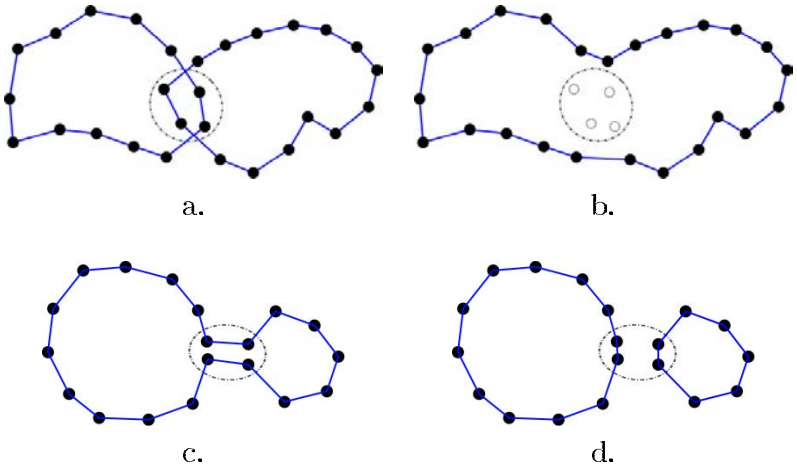

Figure 4.3: Surface markers coalescence (a. and b.) and detachment (c. and d.).

4.2 Front capturing methods

In this category of methods the interface is implicitly described within a fully Eulerian approach. here an additional phase function is required and the motion of the interface is studied by solving the advection problem under a given velocity field (this will be further discussed in the next Section 4.3). The main advantage of these approaches is that all the topological changes are taken into account naturally by the numerical technique. However, the computation of integrals over the interface is usually more complicated compared to the front

tracking methods, because the interface is neither defined by markers or by the computational grid. The most common numerical methods are the Volume-Of-Fluid (VOF) and the Level-Set (LS) methods.

4.2.1 Volume-Of-Fluid method

The method was first introduced by Hirt and Nichols in 1981 [Hirt & Nichols 1981]. The main idea behind this kind of methods is that a fractional volume or "color" function C is defined. This function indicates the fraction of a mesh cell that is filled with a particular phase. In this case this color would represent the fraction of the mesh cell that is filled. In particular, VOF methods have been developed to solve the advection Equation (4.2) in such a way that interfaces remain sharp [Rudman 1997]:

$$\frac{\partial C}{\partial t} + \underline{\nabla} \cdot (\underline{v} C) = 0 \tag{4.2}$$

Geometry of the interface can be reconstructed from the values of the color function C and there are many schemes allowing to perform this interface reconstruction. Several reconstruction schemes have been reviewed by Rider and Kothe in [Rider & Kothe 1998]. Here only the most common schemes are presented: the "Simple Line Interface Calculation (SLIC)" presented by Noh and Woodward [Noh & Woodward 1976], the "Hirt-Nichols" presented in [Hirt & Nichols 1981] and the "Y-VOF" method presented by Youngs in [Youngs 1982]. A brief description of each of those three schemes will be presented next.

SLIC: This method reconstructs the interface using straight lines in 2D or planes in 3D aligned with one of the coordinate directions. In this algorithm a sweep direction is chosen and only cell neighbors in the sweep direction are used to reconstruct the interface.

Hirt-Nichols: Like the SLIC method, the interface is reconstructed using straight lines in 2D (planes in 3D) parallel to the coordinate directions. The difference is that the interface is computed by considering a nine cells neighborhood.

Y-VOF: This method is more accurate than first presented previously, an orientation β of a line segment (or the plane in 3D) is computed by using the gradient of the color function $\underline{\nabla C}$. Then the position of the interface on a given cell is computed in such a way that the value of the color function does not change.

Figure 4.4 shows a schematic representation of different interface reconstructions of the actual geometry shown in Figure 4.4a. Figures 4.4b and 4.4c show the reconstruction obtained by using SLIC method for $x-$ and $y-$sweep directions, respectively. Figure 4.4d represents the

interface configuration obtained using Hirt-Nichols scheme and finally Figure 4.4e shows the interface obtained with the Y-VOF method.

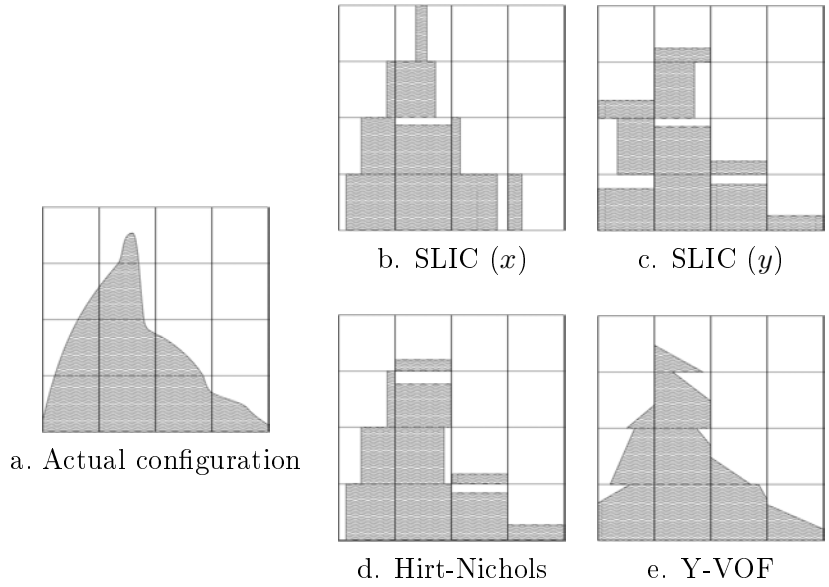

Figure 4.4: Schematic representation of interface reconstructions of the actual phase configuration shown in a. : (b., c.) SLIC (x- and y-sweep respectively); d. Hirt-Nichols' VOF; e. Y-VOF method [Rudman 1997].

The main advantages of VOF approaches are related to the simplicity of the method and the volume conservation capability. Considering its application to the sintering simulation at the particles scale, the main drawback concerns the description of the interface which is not reconstructed in a very accurate way. Also the computation of the curvature of the interface and high order derivatives if the color function can be difficult and, very often, introduces numerical noise as the color function is constant within each cell.

4.2.2 Level-Set method

The Level-Set method was first introduced by Osher and Sethian in 1988 [Osher & Sethian 1988]. Initially the method was presented to study fronts propagating with curvature-dependent velocity. Since its introduction it has been used in wide range of applications such as multiphase flow, Stefan problems, kinetic crystal growth, etc [Osher & Fedkiw 2001]. The main idea behind the method is to represent the interface Γ as the zero iso-value of a smooth function $\phi(\underline{x}, t)$:

$$\Gamma(t) = \{\underline{x} \ \in \mathcal{R}^n, \phi(\underline{x}, t) = 0\} \tag{4.3}$$

ϕ is usually computed as a signed distance function to the interface Γ (positive from one side of the interface and negative from the other one). One of the main advantages of the method is related to the ease of computation of geometrical quantities such as the curvature and the normals. Additionally, it has been shown that the approach allows to treat problems in 3D with ease and its implementation is simple [Peng *et al.* 1999, Osher & Fedkiw 2001]. The goal of the LS method is to represent the motion of an interface Γ under a velocity field $\underline{v}$ which can depend on position, time, geometry of the interface, and external physical laws [Osher & Fedkiw 2001]. Its main drawback is related to the volume conservation which can not be ensured just by transporting ϕ (see Section 4.3 for further details).

4.2.3 Choice of the method

As it has been presented previously in Chapters 2 and 3, during the simulation of the sintering process at the particles scale strong topological changes must be handled. Therefore fixed grid methods are chosen because they are more likely to handle this kind of structural evolution.

The diffusion phenomena play the main role on the structural evolution of the system. The direct simulation of these phenomena require a very accurate interface representation as the result highly depends on geometrical quantities such as the normal and, even more importantly, the curvature. The curvature computation is very important for the computation of the matter flux by surface, volume and grain boundary diffusion, therefore the curvature computation is a key point in the choice of the numerical method. Additionally, one of the goals of this work is to carry out simulations in 3D, hence the numerical method must allow to perform simulations in 2D and 3D with ease.

VOF approaches do not allow to have a precise description of the interface, moreover, it is difficult to have a good estimation of the curvature and the normals and 3D simulations seem to be carry out. On the other hand, the Level-Set method allows to have an accurate description of the interface and both curvature and normal can be directly computed with this approach. For these reasons, the Level-Set methods represent a better option. A general introduction to this method is presented in the next Section 4.3.

4.3 Classical Level-Set method

The classical Level-Set method will be discussed in the section. The level set function ϕ will be presented in Section 4.3.1. The equations concerning the motion of ϕ are discussed in

Section 4.3.3. The necessity of the reinitialization step as well as the equations used to perform this operation will be presented in Section 4.3.4.

4.3.1 Level set function

Let Γ be the boundary of a bounded region $\omega \subset \mathcal{R}^n$ which can deform along the time. At each time t, the description of ω and its boundary Γ is done through a function $\phi : \mathcal{R}^n \times \mathcal{R}^+ \rightarrow \mathcal{R}$ which has the following properties:

$$\phi(\underline{x}, t) \begin{cases} < 0 & \text{if } \underline{x} \in \omega \\ > 0 & \text{if } \underline{x} \notin \omega \\ = 0 & \text{if } \underline{x} \in \Gamma \end{cases} \tag{4.4}$$

with $\underline{x}$ the point in R^n where ϕ is being evaluated and t is time.

In the classical LS method, the level set function ϕ is a smooth function given by Equation (4.5).

$$\phi(\underline{x}, t) = \begin{cases} -\text{dist}(\underline{x}, \Gamma) & \text{if } \underline{x} \in \omega \\ \text{dist}(\underline{x}, \Gamma) & \text{if } \underline{x} \notin \omega \\ 0 & \text{if } \underline{x} \in \Gamma \end{cases} \tag{4.5}$$

where $\text{dist}(\underline{x}, \Gamma)$ is the Euclidean distance from the point $\underline{x}$ to the interface Γ. Contrary to the color function used with a VOF-like method, the level set function ϕ is smooth: at least continuous and with $\| \underline{\nabla \phi} \| = 1$ where this gradient exists. These properties allow the use of continuous finite elements for solving the transport equation (see Section 4.3.3), which represent an advantage in terms of numerical developments. At this point, it should be noted that the computation of the LS function for a given geometry is not a trivial problem, but this will be further discussed later.

Figure 4.5 shows the LS function corresponding to a circle of radius $R = 0.3$ centered in $x = 0.5$ and $y = 0.5$. The Z axis represents the value of ϕ.

4.3.2 Level-Set features

One of the main advantages of this method is its capability of computing some geometrical quantities such as the curvature κ and the normal $\underline{n}$. It is also possible to compute with ease other functions that will be very useful regarding the sintering simulation. The outward normal

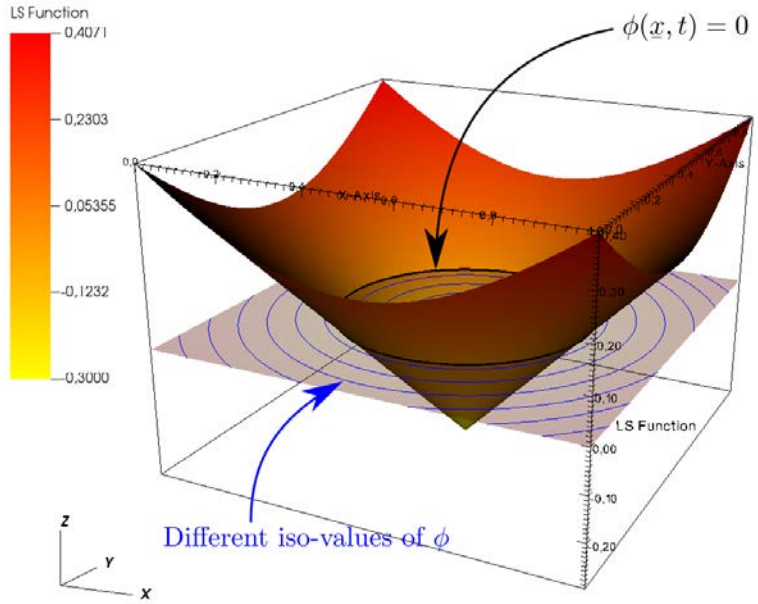

Figure 4.5: LS function ϕ of a circle. The black line represents the zero iso-value of ϕ.

$\underline{n}$ and curvature κ can be computed by using Equations (4.6) and (4.7), respectively.

$$\underline{n} = \frac{\underline{\nabla\phi}}{\| \underline{\nabla\phi} \|} \tag{4.6}$$

$$\kappa = \underline{\nabla} \cdot \underline{n} \tag{4.7}$$

As presented previously, when a front capturing method (e.g. the level method) is used, a second phase is introduced into the problem modeling. In the case of the sintering simulation, the computational domain Υ will be composed of two different phases: the compact powder and the surrounding medium. It is also possible to compute the Heaviside functions [1] H corresponding to each phase (H^s for the compact powder and H^f for the surrounding medium):

$$H^s(\phi) = \begin{cases} 1 & \text{if } \phi \leq 0 \\ 0 & \text{if } \phi > 0 \end{cases} \quad ; \qquad H^f = 1 - H^s \tag{4.8}$$

Those Heaviside functions H are used to compute a volume (3D problems) or surface (2D problems) integrals over just a region of the computational domain Υ. For example the integral

1. Also known as characteristic functions.

of the function $p(\underline{x},t)$ over the solid phase (the compact powder) can be computed as follows:

$$\int_{\Upsilon} p(\underline{x},t)H^s(\phi)dV \tag{4.9}$$

note here, that the computational domain Υ contains both the compact powder and the surrounding medium, but by introducing the heaviside function H^s into the integral, the above integral corresponds to the integral of a function $p(\underline{x},t)$ over the compact powder only.

4.3.3 Convection

As stated previously, the goal of the LS method is to represent the motion of an interface Γ under a velocity field $\underline{v}$. The motion of the interface Γ (defined by the zero iso-value of ϕ) is given by the result of the advection equation:

$$\frac{\partial\phi}{\partial t} + \underline{v}\cdot\underline{\nabla\phi} = 0 \tag{4.10a}$$

$$\phi(\underline{x},t=0) = \phi_0(\underline{x}) \tag{4.10b}$$

$$\phi(\underline{x},t) = g^{\text{inflow}} \qquad \text{if } \underline{x}\in\partial\omega^- \tag{4.10c}$$

where Equation (4.10c) corresponds to the inflow boundary. This equation sets the value of the level set funtion ϕ over the inflow boundary $\partial\omega^-$ to be equal to g^{inflow}. The inflow boundary is defined as: $\partial\omega^- = \{\underline{x}\in\partial\omega, \underline{v}(\underline{x})\cdot\underline{n}<0\}$.

When solving Equation (4.10) by the finite element method, the convected quantity (ϕ) remains smooth when using a distance function (Equation (4.5)). Furthermore, the smoothness of the gradient is very important regarding the stability of the finite element scheme used [Ville *et al.* 2011].

The solution of Equation (4.10) does not ensure that the norm of the gradient of ϕ remains equal to one: $\parallel\underline{\nabla\phi}\parallel = 1$ [Osher & Sethian 1988, Peng *et al.* 1999, Osher & Fedkiw 2001]. In fact, according to the velocity $\underline{v}$ the LS function ϕ can become very flat or very steep at the interface Γ. A procedure, usually called *reinitialization*, is used to reset the LS function ϕ to be a signed distance function to Γ, this procedure will be presented in the next section.

4.3.4 Reinitialization

The reinitialization procedure can be described simply as the process of replacing the function $\phi(\underline{x},t)$ by another function $\tilde{\phi}(\underline{x},t)$ that has the same zero iso-value but behaves better.

Then the new function $\tilde{\phi}(\underline{x},t)$ is used until the next round of reinitialization.

A way to find this new function $\tilde{\phi}(\underline{x},t)$ is to find the location of the interface Γ with some interpolation technique and then compute a signed distance function out from the interpolation, as presented in [Merriman *et al.* 1994]. Some drawbacks of this approach are related to the computational cost and the noise that is introduced during the reinitialization that can have an important impact on some geometrical quantities such as the curvature [Peng *et al.* 1999]. An alternative strategy has been presented by Sussex et al. in [Sussman *et al.* 1994]. A Hamilton-Jacobi equation is implemented to reconstruct the LS function from the zero iso-value of $\phi(\underline{x},t)$. A virtual time τ is introduced:

$$\frac{\partial\tilde{\phi}}{\partial\tau}+\operatorname{sgn}\left(\tilde{\phi}_0\right)\left(\parallel\underline{\nabla\tilde{\phi}}\parallel-1\right)=0 \tag{4.11a}$$

$$\tilde{\phi}\left(\underline{x},0\right)=\tilde{\phi}_0\left(\underline{x}\right)=\phi\left(\underline{x},t\right) \tag{4.11b}$$

where the signed function $\operatorname{sgn}(\alpha)$ is defined below, but usually approached by $\hat{\operatorname{sgn}}(\alpha)$:

$$\operatorname{sgn}(\alpha)=\begin{cases}1 & \text{if } \alpha>0\\ -1 & \text{if } \alpha<0\\ 0 & \text{if } \alpha=0\end{cases}\quad;\quad \hat{\operatorname{sgn}}(\alpha)=\frac{\alpha}{\sqrt{\alpha^2+\epsilon^2}} \tag{4.12}$$

where ϵ is a parameter related to the spatial discretization size.

For practical purposes Equation (4.11) can be rewritten as an advection equation and can be solved by using the same numerical method used to solve Equation (4.10):

$$\frac{\partial\tilde{\phi}}{\partial\tau}+\underline{v}_r\cdot\underline{\nabla\tilde{\phi}}=\hat{\operatorname{sgn}}\left(\tilde{\phi}_0\right) \tag{4.13a}$$

$$\tilde{\phi}_0\left(\underline{x}\right)=\tilde{\phi}\left(\underline{x},0\right)=\phi\left(\underline{x},t\right) \tag{4.13b}$$

since $\underline{\nabla\tilde{\phi}}\cdot\underline{\nabla\tilde{\phi}}=\parallel\underline{\nabla\tilde{\phi}}\parallel^2$, the reinitialization velocity $\underline{v}_r$ is given by:

$$\underline{v}_r=\hat{\operatorname{sgn}}\left(\tilde{\phi}_0\right)\frac{\underline{\nabla\tilde{\phi}}}{\parallel\underline{\nabla\tilde{\phi}}\parallel} \tag{4.14}$$

In contrast with the transport Equation (4.10), there is no inflow boundary condition. When using the level-set method, the computational domain is usually given by a cube (3D) or a square (2D) which contains the interface that is being tracked. In this case, the reinitialization

velocity is always pointing out of the computational domain, and therefore the inflow boundary is empty: $\partial\omega^- = \emptyset$.

To summarize, the standard LS method resolution scheme is presented in Algorithm 1.

Algorithm 1 Classical LS method

$t \leftarrow 0$
$\phi_0(\underline{x}, t=0) \leftarrow$ Equation (4.5) from a given geometry ω_0 at $t=0$
while $t < t_f$ **do**
  $\underline{v} \leftarrow$ From physical phenomena, e.g. Equations (2.29), (2.30) and (2.32)
  $\phi(\underline{x}, t+\Delta t) \leftarrow$ From Equation (4.10)
  $\tilde{\phi}(\underline{x}, \tau) \leftarrow$ From Equation (4.13) with $\tilde{\phi}_0(\underline{x}, \tau=0) = \phi(\underline{x}, t+\Delta t)$
  $\phi(\underline{x}, t+\Delta t) \leftarrow \tilde{\phi}(\underline{x}, \tau)$
  $t \leftarrow t + \Delta t$
end while

Equation (4.13) should be solved until the steady state is reached. When the steady state is reached $\partial\tilde{\phi}/\partial\tau = 0$ and therefore $\| \underline{\nabla\tilde{\phi}} \| = 1$. The terms involving $\hat{\text{sgn}}\left(\tilde{\phi}_0\right)$ are introduced to ensure that the zero isovalue of $\tilde{\phi}$ is exactly the same than $\phi\left(\underline{x}, t\right)$.

An important point should be highlighted concerning the value of the physical velocity $\underline{v}$. Consider a point that is away from the interface $\underline{x}^{away}$. The value level set function ϕ at this point $\underline{x}^{away}$ changes after the transport is performed (Equation (4.10)) and, in the general case, the level set function does not satisfy anymore the property of $\| \underline{\nabla\phi} \| = 1$, therefore the reinitialization procedure has been performed. Then the value of ϕ at the point $\underline{x}^{away}$ is replaced by the result obtained from the reinitialization procedure (Equation (4.13)). This means that the value of the level set function at a point away from the interface ($\phi(\underline{x}^{away}, t)$) is mainly set by the reinitialization velocity. Finally it can be conclude that the physical velocity $\underline{v}$ is only required near to the interface.

In fact, the reinitialization procedure is an additional problem that should be solved which leads to an increase of the computational time. For this reason an alternative procedure allowing to perform both the convection and the reinitialization in a single step will be presented in the next section.

4.4 Local level-Set approach and mesh adaptation strategy

One of the main drawbacks of the LS method is related to its computational cost. By embedding the interface as the zero iso-value of a higher dimensional function, a one dimensional interface problem is transformed into a two dimensional problem. In three dimensions,

considerable computational labor is required per time step [Adalsteinsson & Sethian 1995]. Additionally, the reinitialization procedure is computationally expensive. For those reasons, in this sections some numerical approaches aiming to reduce the computation time are presented.

4.4.1 Convective reinitialization

The main idea is to couple the reinitialization procedure with the convection step [Coupez 2006]. Let define a parameter λ relating the virtual time τ and the real time t such that:

$$\lambda = \frac{\partial \tau}{\partial t} \tag{4.15}$$

Additionally, it is possible to write:

$$\frac{\partial \tilde{\phi}}{\partial t} = \frac{\partial \tilde{\phi}}{\partial \tau}\frac{\partial \tau}{\partial t} = \lambda \frac{\partial \tilde{\phi}}{\partial \tau} \tag{4.16}$$

By replacing Equation (4.16) into the reinitialization Equation (4.13), the following expression can be found:

$$\frac{\partial \tilde{\phi}}{\partial t} + \lambda\, \underline{v}_r \cdot \underline{\nabla \tilde{\phi}} = \lambda\, \hat{\text{sgn}}\left(\tilde{\phi}_0\right) \tag{4.17}$$

The previous Equation (4.17) corresponds to the reinitialization step over the real time. Now if $\tilde{\phi}$ is considered to evolve under the physical velocity $\underline{v}$ (Equation (4.10)) and the initial condition of the reinitialization step establishes that $\tilde{\phi}(\underline{x}, \tau = 0) = \phi(x, t)$, then Equation (4.17) can be rewritten as the convection-reinitialization equation for ϕ:

$$\frac{\partial \phi}{\partial t} + \underline{v} \cdot \underline{\nabla \phi} + \lambda\, \underline{v}_r \cdot \underline{\nabla \phi} = \lambda\, \hat{\text{sgn}}\left(\phi\right) \tag{4.18}$$

the term $\underline{v} \cdot \underline{\nabla \phi}$ comes from the fact that ϕ evolves within an Eulerian context.

Now, consider a time marching scheme of physical time step Δt associated with the virtual time step $\Delta \tau$ evaluated as $\| \underline{v}_r \| \Delta \tau \approx h$, with h being the element size. Since the gradient reinitialization velocity $\underline{v}_r$ (Equation (4.14)) is close to one: $\| \underline{v}_r \| \approx 1$ then the parameter λ will be chosen equal to $h/\Delta t$. Finally, the convected reinitialization equation can be written as follows:

$$\frac{\partial \phi}{\partial t} + (\underline{v} + \lambda \underline{v}_r) \cdot \underline{\nabla \phi} = \lambda \hat{\text{sgn}}(\phi) \tag{4.19a}$$

$$\phi(\underline{x}, t = 0) = \phi_0(\underline{x}) \tag{4.19b}$$

As stated previously, in practice the physical velocity $\underline{v}$ is only necessary over a region close to the interface (the zero isovalue of the level set function ϕ) since it is responsible for the motion of the interface. Away from the interface, the physical velocity $\underline{v}$ is no longer required because the value of the level set function is controlled by the reinitialization velocity $\underline{v}_r$ which also ensures that the gradient of ϕ remains equal to one: $\| \underline{\nabla \phi} \| = 1$.

4.4.2 Local level set function

One of the drawbacks of the LS method stems from the required computational effort [Adalsteinsson & Sethian 1995]. Considering that all the geometrical useful information (the interface itself, the curvature and the normal) of the LS function is present in a narrow band close to the interface, the advection of the LS function is not necessary over all the computational domain Υ. Furthermore, it could be the cause of numerical instabilities [Ville *et al.* 2011]. A way to reduce the computational cost and avoid numerical instabilities is to cut off the LS function at a thickness E using for example a sinusoidal filter [Coupez 2006, Ville *et al.* 2011].

A sinusoidal filter is applied to the LS function ϕ given by Equation (4.4) to obtain the filtered LS function $\breve{\phi}(\phi)$:

$$\breve{\phi}(\phi) = \begin{cases} \frac{2E}{\pi} & \text{if } \phi > E \\ \frac{2E}{\pi} \sin \frac{\pi}{2E} \phi & \text{if } -E \leq \phi \leq 0 \\ -\frac{2E}{\pi} & \text{if } \phi < E \end{cases} \tag{4.20}$$

The advantage of using this function is that its derivative is continuous:

$$\frac{\partial \breve{\phi}}{\partial \phi} = \cos \frac{\pi}{2E} \phi \tag{4.21}$$

and thus, the re-distanciation condition that has to be satisfied is not any more $\| \underline{\nabla \phi} \| = 1$, but:

$$\| \underline{\nabla \breve{\phi}} \| = \sqrt{1 - \left(\frac{\pi}{2E} \breve{\phi} \right)^2} \tag{4.22}$$

For simplicity, the notation ϕ will be used from now on instead of $\breve{\phi}$. By using this modified LS function, the reinitialization equation presented in Section 4.3.4 must be also modified. As a result the convective-reinitialization Equation (4.19) is transformed into the following expression:

$$\frac{\partial \phi}{\partial t} + (\underline{v} + \lambda\, \underline{v}_r) \cdot \underline{\nabla \phi} = \lambda\, \hat{\mathrm{sgn}}\,(\phi) \sqrt{1 - \left(\frac{\pi}{2E}\phi\right)^2} \tag{4.23a}$$

$$\phi(\underline{x}, t = 0) = \phi_0(\underline{x}) \tag{4.23b}$$

It is important to highlight that Equation (4.23) is non-linear as the reinitialization velocity $\underline{v}_r$ is a function of the LS function ϕ and the right hand side term also depends on ϕ. But it is linearized by computing $\underline{v}_r$ at the previous time step. This linearization is valid as the goal of the convection-reinitialization step is to perform the advection of the LS function ϕ under the physical velocity $\underline{v}$, while keeping the smoothness of ϕ. However, the time step must remain small in order to ensure the numerical stability of the method. Fortunately, this condition is often satisfied because the time step needed to compute the physical velocity is small enough to guarantee the stability of the convection-reinitialization step [Ville *et al.* 2011].

The sinusoidal filter applied in Equation (4.20) is not the only filter that can be used. In fact, there are several filters that can be used. For example a hyperbolic tangent filter can be used and in this case the filter would be given by:

$$\breve{\phi}(\phi) = E \tanh \frac{\phi}{E} \tag{4.24}$$

It is important to recall that the reinitialization equation (4.13) has to be modified in order take into account that the value of the level set filtered function gradient $\underline{\nabla \breve{\phi}}$ is different according the filter used. As a consequence, the convective-reinitialization equation (4.19) also has to be modified. Figure 4.6 shows a comparison between a sinusoidal filter (Equation (4.20)) and a hyperbolic tangent filter (Equation (4.24)). The value of the thickness E is 0.1 for both filters.

4.4.3 Finite element discretization

The computational domain Υ is discretized by using an unstructured mesh $\mathcal{T}_h(\Upsilon)$ built up of simplex elements K (triangles in 2D and tetrahedra in 3D). The discretized domain is given by Υ_h:

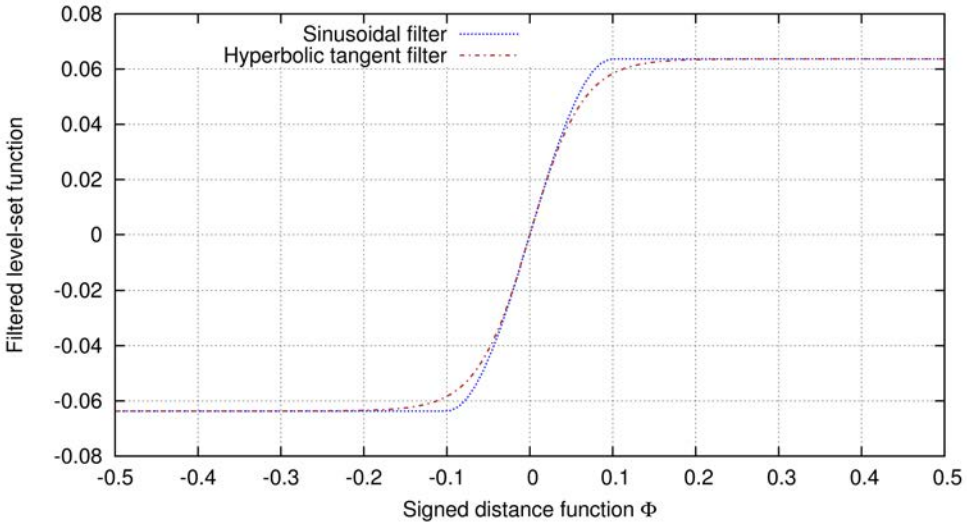

Figure 4.6: Two different filters of the signed distance level set funcion ϕ over a thickness $E = 0.1$. The blue dotted line corresponds to a sinusoidal filter (Equation (4.20)) and the red dashed line corresponds to a hyperbolic tangent filter (Equation (4.24))

$$\bar{\Upsilon}_h = \bigcup_{K \in \mathcal{T}_h(\Upsilon)} K \tag{4.25}$$

Within a finite element context Equation (4.23) is solved by using the following Galerkin weak formulation:

$$\begin{gathered}\int_{\Upsilon_K} \frac{\partial \phi_h}{\partial t} w_h dV + \int_{\Upsilon_K} (\underline{v}_h + \lambda\, \underline{v}_{h\,r}) \cdot \underline{\nabla \phi_h} w_h dV = \int_{\Upsilon_K} \lambda\, \hat{\text{sgn}}\,(\phi_h) \sqrt{1 - \left(\frac{\pi}{2E}\phi_h\right)^2} w_h dV \\ \phi_h(\underline{x}, t = 0) = \phi_0(\underline{x})\end{gathered} \tag{4.26}$$

where w is the weighting function, the level set function ϕ and the physical velocity $\underline{v}$ are approximated by w_h, ϕ_h and $\underline{v}_h$, respectively, using continuous and piecewise linear functions belonging to the functional space defined as:

$$\mathcal{W}_h = \{w_h \in \mathcal{C}^0(\Upsilon_h), w_h \in \mathrm{P}^1(K),\, \forall K \in \mathcal{T}_h(\Upsilon)\} \tag{4.27}$$

where $\mathcal{C}^0$ is the espace of continuous over Υ_h.

The finite element method uses a spatial discretization and a weighted residual formulation to establish an algebraic form of the set of partial differential equations. The solution of the

problem is an approximation of solution of the original boundary value problem. In the Galerkin formulation, which very often used, the weighting and interpolation functions are from the same class of functions. When dealing with problems involving convection, the matrix associated with the convection term is non-symmetric which often leads to numerical oscillations of the solution (See [Brooks & Hughes 1982] and [Hughes 1987] for further information).

A way to avoid those numerical oscillations of the solution is to use a stabilization technique. A well known stabilization technique is the "Streamline Upwind/Petrov-Galerkin" (SUPG) method, presented in 1982 by Brooks and Hughes [Brooks & Hughes 1982]. The main idea is to add a diffusion term acting along the direction of the convection velocity $\underline{v}$. This is achieved by choosing the weighting functions in a functional space different from the one of the shape functions (Petrov-Galerkin method). The stabilization is performed by using the SUPG method and the weighting function $\tilde{w}_h$ is given by:

$$\tilde{w}_h = \{\tilde{w}_h, \tilde{w}_h|_K = w_h + \tau_{SUPG}\, \underline{v} \cdot \underline{\nabla w}_h, \forall K \in \mathcal{T}_h(\Upsilon)\} \tag{4.28}$$

where the coefficient τ_{SUPG} is given by [Ville *et al.* 2011]:

$$\tau_{SUPG} = \frac{1}{M\,|\underline{v} \cdot \underline{\nabla w}_h|} \simeq \frac{1}{2}\frac{h_K}{\| \underline{v} \|} \tag{4.29}$$

where M is the number of nodes per element ($M = n + 1$ in R^n), $|\bullet|$ is the absolute value operator and h_K is the element size.

The weak formulation presented in Equation (4.26) is stabilized by using the SUPG method and the formulation obtained is by replacing the weighting function w_h by $\tilde{w}_h$ as defined in Equation (4.28):

$$\begin{aligned}
&\int_{\Upsilon_K} \frac{\partial \phi_h}{\partial t} \underbrace{(w_h + \tau_{SUPG}(\underline{v}_h + \lambda \underline{v}_{hr}) \cdot \underline{\nabla w}_h)}_{\text{SUPG stabilization}} dV + \\
&\int_{\Upsilon_K} (\underline{v}_h + \lambda\, \underline{v}_{hr}) \cdot \underline{\nabla \phi_h} \underbrace{(w_h + \tau_{SUPG}(\underline{v}_h + \lambda \underline{v}_{hr}) \cdot \underline{\nabla w}_h)}_{\text{SUPG stabilization}} dV = \\
&\int_{\Upsilon_K} \lambda\, \hat{\text{sgn}}\,(\phi_h) \sqrt{1 - \left(\frac{\pi}{2E}\phi_h\right)^2} \underbrace{(w_h + \tau_{SUPG}(\underline{v}_h + \lambda \underline{v}_{hr}) \cdot \underline{\nabla w}_h)}_{\text{SUPG stabilization}} dV \\
&\phi_h(\underline{x}, t = 0) = \phi_0(\underline{x})
\end{aligned} \tag{4.30}$$

It is important to highlight that a validation of the method and its implementation in the

finite element library *CimLib*® [Digonnet *et al.* 2007] has been performed by Ville et al. in [Ville *et al.* 2011]. In that work, several benchmark problems were considered, including the advection of a circle in 2D and a sphere in 3D, the Zalesak's problem in 2D and 3D, and multiple applications to the jet buckling problem also in 2D and 3D.

4.4.4 Mesh adaptation strategy

The LS approach presented in Sections 4.4.1 and 4.4.2 should be combined with an appropriate mesh adaptation strategy in order to have a better description of the interface Γ. In this work an anisotropic mesh adaptation is used. This strategy has been developed by the team of Coupez [Mesri *et al.* 2008]. The idea is to create a mesh with different element sizes in each spatial direction.

Very often, discontinuities must be handled across the interface: different mechanical properties, different mechanical behaviors, normal stress discontinuities, etc. Regarding those discontinuities, a way to cope with those problems is to solve them by using an adapted mesh in such a way that an error estimation is minimized. The mesh adaptation is performed by refining and coarsening the mesh based on a metric which is a positive defined tensor of order n in $\mathcal{R}^n$. This metric specifies the stretching in the space directions and is computed by using *a posteriori* error estimation. The error estimation is based on the Hessian (second-order spatial derivatives) of a given field. This mesh adaptation strategy allows to capture discontinuities in a more accurate way while keeping a -rather- reasonable number of nodes and elements [Mesri *et al.* 2008].

In the present work the filtered LS function (Equation (4.20)) is chosen to compute the metric used for the mesh adaptation. In fact, by using the filtered LS function for the computation of the metric (error estimation), the obtained mesh is adapted with respect to the geometry of the interface, allowing to describe the interface in a very precise way. Furthermore, the framework for the treatment of the discontinuities for mechanical properties and normal stress (due to the surface tension) is set.

As an example, consider two particles connected with a neck, embedded in a computational square domain of side 1 in 2D. The radius R of both particles is equal to 0.2 and the neck radius between them to 10% of R: $r = 0.1R$. The particles are centered respectively in $\underline{c}_1 = [0.3\,,\,0.5]'$ and $\underline{c}_2 = [0.7\,,\,0.5]'$. This geometry is shown in Figure 4.7a.

The classical LS function is initialized from Equation (4.5) and is shown in Figure 4.7b along with the initial mesh. The solid black line corresponds to the zero iso-value of the LS function and the other iso-values shown allow to see how the classical LS function changes over

all the computational domain. Then, the classical LS function is filtered by using Equation (4.20) with $E = 0.01$ and it is shown in Figure 4.7c. As previously, the black line corresponds to the zero iso-value, but this time all the other iso-values are packed together near to the interface (narrow band of width $2E = 0.02$). It is important to highlight, that the interface is not modified when the filter is applied. The mesh adaptation strategy presented is applied using the filtered LS function to compute the metric. From this metric the mesh is adapted and the result can be seen in 4.7e. Finally, a close-up of the inter-particular region is shown in Figures 4.7d and 4.7f.

The initial mesh is made up of 19,800 triangles and the adapted mesh has 17,654 triangles. Even if the adapted mesh has less elements than the initial one, from Figures 4.7d and 4.7f it is clear that the interface representation is much more smooth when the LS function is interpolated over the adapted mesh. This more precise representation is obtained because the element size near to the interface on the adapted mesh is about $h_K \approx 0.001$ compared to $h_K = 0.006$ on the initial mesh. If an isotropic mesh was to be built with the equivalent element size of the adapted mesh, it would have about one million of elements. Even if the remeshing process may take an important amount of time, it will be shown later that the total computational time is reduced by using mesh adaptation.

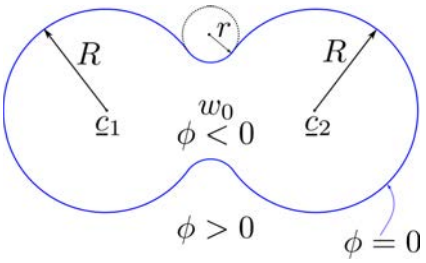

a. Initial geometry

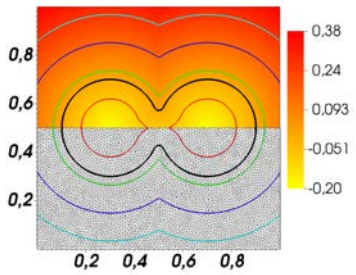

b. Classical LS function (Initial mesh)

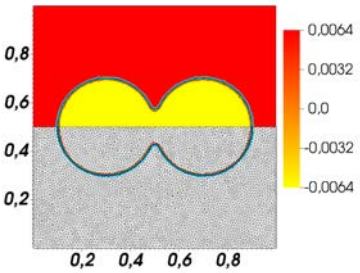

c. Filtered LS function (Initial mesh)

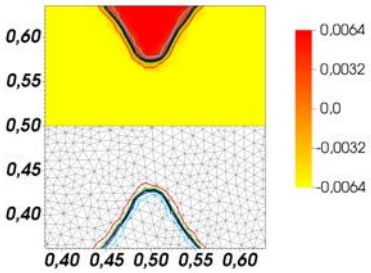

d. Inter-particular zone from c.

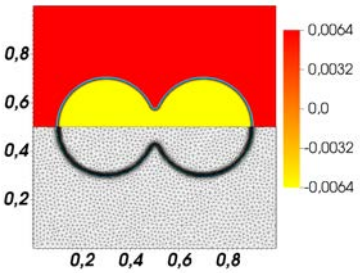

e. Filtered LS function (Adapted mesh)

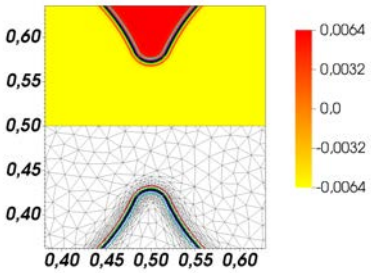

f. Inter-particular zone from e.

Figure 4.7: Mesh adaptation strategy: a. Geometry description; b. Classical LS function over the initial mesh; c. Filtered LS function over the initial mesh; d. Inter-particular region from c; e. Filtered LS function over the adapted mesh; f. Inter-particular region from e.

4.5 Conclusions

Different numerical strategies allowing to deal with problems involving topological changes have been presented. Among those numerical strategies, fixed grids are more suitable to be used for the sintering simulation at the particles scale. Within the fixed grids approaches, the LS method and multiple VOF techniques were considered. Eventually, the LS method has been chosen over the VOF approaches due to its capability of handling strong topological changes while having a good description of the interface. Also, the computation of some geometrical quantities is easier within a LS context. The main drawback of the LS approach is related to its computational cost, therefore some strategies allowing to reduce the computational time were presented.

First, a modified LS approach, which allows to couple the convection to the reinitialization step, is used. Furthermore, a filtered LS functions is used instead of a classical distance signed function which avoids unnecessary convection of the LS function away from the interface. Secondly, a mesh adaptation strategy is combined in order to have a good accuracy of the solution while keeping a reduced number of nodes.

In the next chapter, the simulation of sintering at the particles scale by surface diffusion is presented.

4.6 Résumé en français : Stratégie numérique

Le manque d'outil numérique capable de traiter le frittage par différents mécanismes de diffusion, sur des géométries complexes et avec des forts changements topologiques en 2D et 3D est évident. Pour cette raison, différentes stratégies numériques permettant de pallier à ce problème ont été présentées. Parmi ces stratégies numériques, les approches avec des domaines fixes (approches Eulériennes) se sont avérées plus appropriées pour la simulation du frittage à l'échelle des particules. La méthode Level-Set permet de traiter des problèmes avec de forts changements topologiques et fournit une très bonne description de la surface des particules. Additionnellement, cette méthode permet de calculer certaines quantités telles que la normale et la courbure d'une interface.

L'interface entre les particules et le milieu environnant est donc représentée par l'isovaleur zéro de la fonction Level-Set. Cette interface, qui représente la surface des particules, évolue sous l'effet d'un champ de vitesses induit par les différents chemins de diffusion. Le transport de cette fonction level-set sous l'effet du champ de vitesses peut mener à la perte de certaines propriétés liées au calcul des propriétés géométriques. Afin de récupérer ces propriétés, une procédure appelée réinitialisation est utilisée. Cette méthode est coûteuse du point de vue computationnel. Plusieurs méthodes pour réduire le temps de calcul ont donc été testées (réinitialisation convective, fonction level-set filtrée, adaptation de maillage, etc)

Chapter 5

Sintering by surface diffusion

Contents

In this chapter the numerical strategy developed to simulate sintering by surface diffusion is presented and validated. It is important to highlight that, in this chapter, only the surface diffusion will be taken into account. The particles are considered to be spheres and are set to be tangent at the beginning of the simulation. Furthermore, no grain-boundary between the particles is considered. The final results and the numerical framework have already been published in [Bruchon *et al.* 2010] and [Bruchon *et al.* 2011].

The level-set method will be used, therefore it is necessary to initialize the level-set function on every node of the mesh. The algorithm used for the initialization of the level-set function is presented in Section 5.1. Starting from the level-set function obtained with this algorithm, the strategy for surface diffusion is described in Section 5.2. Then different benchmark cases are considered to validate the numerical approach and some simulation of sintering are presented in Section 5.3. Finally the conclusions of this chapter are presented in Section 5.4.

5.1 Initial geometry

The first step toward the simulation of the sintering process at the particles scale consists in the definition of the initial geometry of the compact powder. One of the main advantages of level-set approaches is related to its capacity to deal with complex geometries. However the initial step can be tricky as the level-set function must be initialized over each node of the mesh and this initialization can be difficult if the geometry is very complex.

According to the mechanical properties of the powder and the shaping method used, the particles can whether or not be considered to remain spherical. The deformation induced into the ceramic particles during the shaping step is very low because of their high stiffness. Therefore it seems to be safe to state that the particles remain spherical after the shaping step. The fact of considering the particles to remain spherical simplify the task of the level-set function initialization.

5.1.1 Two particles

One of the main tools used to validate the numerical simulation of sintering at this scale consists in performing sintering simulations between two particles of the same radius. The growth of the neck between the particles is then compared with the analytical expressions previously presented in Section 3.1.

As a simple example, the level-set value function on a node of coordinates $\underline{x}$ corresponding to two tangent spheres of radius R and centered at $\underline{C_1}$ and $\underline{C_2}$ can be computed with ease as follows:

$$\phi(\underline{x}) = \min_i \left[\| \underline{x} - \underline{C_i} \| - R \right] \qquad \text{For } i = 1, 2 \tag{5.1}$$

The level-set function obtained by using Equation (5.1) is next filtered by using Equation (4.20) to reduce the computation cost (filtered level-set as presented in the previous Chapter 4). Figure 5.1 shows a level-set function obtained by using Equation (5.1) with $\underline{C_1} = [0.3\,,\, 0.5]'$, $\underline{C_2} = [0.7\,,\, 0.5]'$ and $R = 0.2$.

It is important to say that the level-set function can be ill-defined close to the contact point between the two particles as it can be seen in the close-up zoom in Figure 5.1. This problem comes from the interpolation of the level-set function. Near to the contact point, when the distance between the surfaces of the two particle is close to the element size h, the interpolation is not accurate. In fact, even if the element size is reduced, the problem will not be solved since the contact point is a singularity and can not be properly caught by refining the mesh.

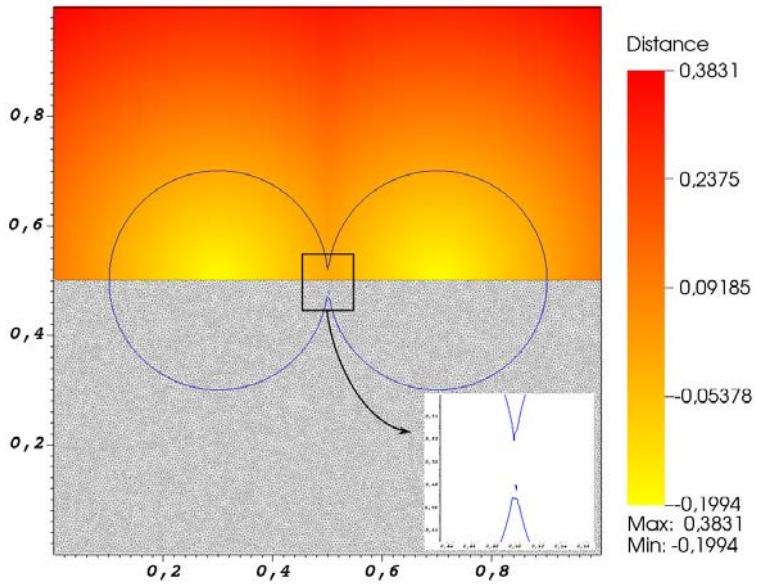

Figure 5.1: Level-set function ϕ computed as a signed distance function using Equation (5.1) over a non structured mesh with element size $h = 0.005$.

As it will be shown in Section 5.3.2, this singularity does not represent a problem regarding the simulation of sintering by surface diffusion. However, it can indeed become a problem regarding the volume diffusion path, because the mechanical problem (Chapter 6) is very sensitive to slight variations of the curvature.

A way to overcome this problem consists in creating a neck of radius r between the particles as shown in Figure 5.2. In this case the initialization of the level-set function is different and is presented in Equation (5.2).

$$\phi(\underline{x}) = \begin{cases} \min_i \left[\| \underline{x} - \underline{C_i} \| - R_i \right] & \text{For } i = 1,2 \quad ; \quad \text{if } \underline{x} \notin \text{Region A} \\ \min_i \left[r - \| \underline{x} - \underline{N_i} \| \right] & \text{For } i = 1,2 \quad ; \quad \text{if } \underline{x} \in \text{Region A} \end{cases} \tag{5.2}$$

where $\underline{N_1}$ and $\underline{N_2}$ are the centers of the neck that can be easily computed as a function of the neck radius r, the particles radii R_1 and R_2 and the particles centers $\underline{C_1}$ and $\underline{C_2}$. Finally the "Region A" corresponds to the quadrilateral defined by the points $\{\underline{C_1}, \underline{N_2}, \underline{C_2}, \underline{N_1}\}$. Figure 5.2a shows a diagram of two particles with a neck and the shaded region corresponds to the "Region A".

It is important to recall that the neck is added in order to remove the singularity at the contact point between two particles, therefore the value of r should be high enough to remove the singularity but low enough to avoid any strong change in the initial geometry. Considering

this, it seems that a neck radius equal to the element size is a good choice: $r = h$. Figure 5.2b shows a comparison of the geometry of two tangent spherical particles with different neck radii.

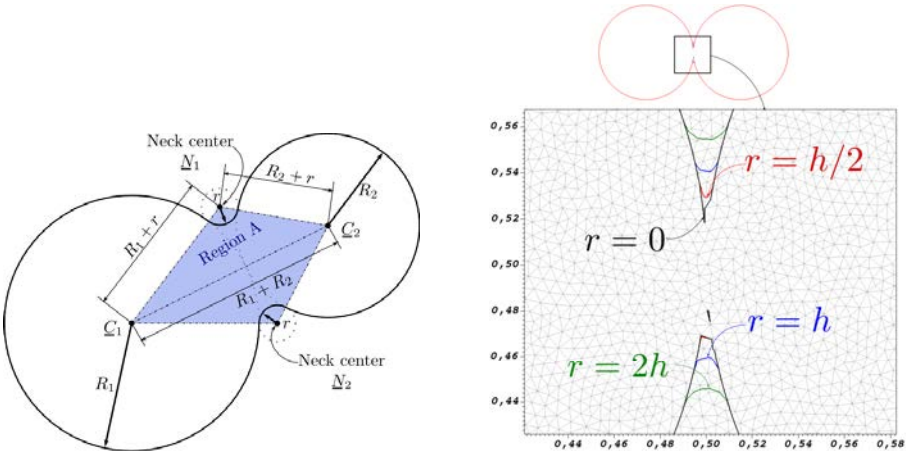

a. Two particles with a neck of radius r.

b. Two particles with different neck radii r.

Figure 5.2: Geometry of two particles with a neck of radius r: a. Diagram of two particles with a neck of radius r; b. Geometry of the neck between two particles for different values of r.

The examples shown in this section are in 2D. However the method can be used for a 3D case without any further development. If two particles with a neck in 3D are intersected with the plane[1] formed by the two particles centers ($\underline{C_1}$ and $\underline{C_2}$) and the point $\underline{x}$, then the 3D problem is reduced to a 2D problem and Equation (5.2) can be used to initialize the level-set function $\phi(\underline{x})$.

Sintering of two particles is very important for the validation of the numerical approach, however this work aims at performing simulation over more realistic powder compacts where more than two particles must be considered. In the next section some examples of more realistic powder packing will be presented.

1. If the point $\underline{x}$ is aligned with axis formed by $\{\underline{C_1}, \underline{C_2}\}$ the solution is still the same as any plane passing by the two centers can be used.

5.1.2 Multiple particles

Within the level-set context presented in this work, the computational domain Υ is given by a square (2D) or a cube (3D) where the powder packing is contained. The packing of spheres or circles of different sizes is a research field itself and many works can be found in literature [Han *et al.* 2005, Siiriä & Yliruusi 2007, Jerier *et al.* 2010, Al-Raoush & Alsaleh 2007, Hitti 2011, Hitti *et al.* 2011]. For this reason the methods used to generate a powder packing will not be described in detail here.

In this work the developments presented by Hitti et al. in [Hitti 2011, Hitti *et al.* 2011] will be used to generate a set of M particles. The particles are generated in such a way that the particles radii follow a given distribution which is chosen according to the powder size distribution. The set of particles consists in a set of centers and radii: $[\underline{C_i}, R_i]$ for $i = 1, 2, \ldots M$. Figure 5.3 shows a set of 2031 particles packed in a cube of unit size.

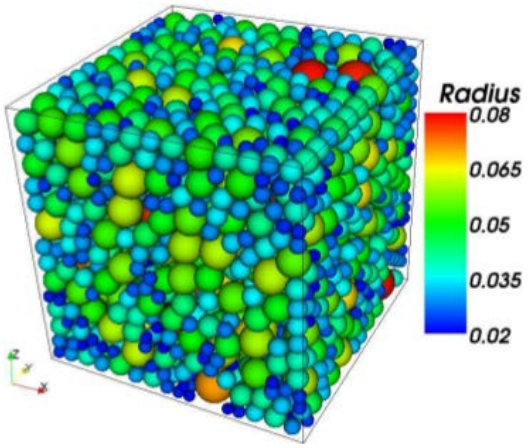

Figure 5.3: A set of 2031 spheres in a unit cube modelling a 3D powder [Hitti 2011].

Given a set of particles, the corresponding level set function has to be initialized. As the particles are set initially to be tangent, the i_{th} particle will have N^i neighbor particles. As in the previous Section 5.1.1, a singularity appears on each contact point between two particles, therefore the i_{th} particle will have N^i singularities that should be regularized. Then there are N^i necks that will be created on the i_{th} particle following the corrections previously proposed. This time the initialization of the level-set function is slightly more complicated, but it can still be performed by using Equation (5.2). In this case the procedure to compute the value of the level-set function $\phi(\underline{x})$ at a node of coordinates $\underline{x}$ is presented in Algorithm 2.

Algorithm 2 Initialization of the level-set function at a node of coordinates $\underline{x}$ for a set of M particles given by $\left[\underline{C_i}\,,\, R_i\right]$. N^i is the number of neighbors (also called coordination number) of the i_{th} particle.

for $j = 1 \rightarrow M$ **do**
  $\phi_j(\underline{x}) = \| \underline{x} - \underline{C_j} \| - R_j$
  for $k = 1 \rightarrow N^i$ **do**
    $\phi_k(\underline{x}) \leftarrow$ From Equation (5.2) with $r = h$ and $i = j, k$.
    if $\phi_k < \phi_j$ **then**
      $\phi_j \leftarrow \phi_k$
    end if
  end for
end for
$\phi(\underline{x}) = \min_j \left[\phi_j(\underline{x})\right] \quad j = 1, 2, \ldots M$

5.2 Surface diffusion within a Level-Set context

As it has been presented previously in Chapter 2, the surface diffusion can be modeled by using the *Fick*'s first law which relates the matter flux to the surface gradient of the curvature (Equation (2.22)):

$$\underline{j^s} = -\frac{D_s \gamma_{sv}}{kT} \underline{\nabla_s \kappa} \tag{5.3}$$

The surface gradient operator $\underline{\nabla_s}$ is the tangent component of the classical gradient and is defined as a function of the normal $\underline{n}$. In this work, the normal $\underline{n}$ corresponds to the outward normal to the surface Γ:

$$\underline{\nabla_s \kappa} = \underline{\nabla \kappa} - \left(\underline{\nabla \kappa} \cdot \underline{n}\right) \underline{n}$$

For simplicity the projection tensor $\underline{\underline{\mathcal{P}}}$ will be introduced:

$$\underline{\underline{\mathcal{P}}} = \underline{\underline{\mathcal{I}}} - \underline{n} \otimes \underline{n} \tag{5.4}$$

where $\underline{\underline{\mathcal{I}}}$ is the identity tensor of order n in $\mathcal{R}^n$ and $\otimes$ is the tensorial product operator. By using the projection operator, the curvature surface gradient can be written as follows:

$$\underline{\nabla_s \kappa} = \underline{\underline{\mathcal{P}}} \cdot \underline{\nabla \kappa} \tag{5.5}$$

At this point it is important to highlight that the accuracy of the numerical approach highly depends on the good approximation of the projection operator $\underline{\underline{\mathcal{P}}}$. Fortunately, as it will

be shown later, the chosen level-set approach allows to obtain a good approximation of this operator [Bruchon *et al.* 2011].

The matter flux given by Equation (5.3) induces a normal velocity that is given by the surface divergence of the matter flux (Equation (2.29)):

$$\underline{v^s} = v^s \underline{n} = \left(-\Omega \underline{\nabla} \cdot \underline{j^s}\right) \underline{n} \qquad \Rightarrow \qquad v^s = \frac{D_s \gamma_{sv} \Omega}{kT} \Delta_s \kappa \tag{5.6}$$

where Δ_s is the surface Laplacian operator, which can be seen as the classical Laplacian operator but computed along the surface of the particles. This operator is also called the Laplace-Beltrami's operator.

Another key point is related to the volume conservation. Since each particle is considered to fully dense and there is no chemical reactions during the sintering process then the density of the material remains constant and as the mass of the compact powder is also constant, the volume of the solid phase must be conserved throughout the whole simulation. This volume conservation is not systematically guaranteed by the direct simulation of the diffusion paths. For example in the case of the grain-boundary diffusion, a change of the total volume of the particles is induced by this diffusion path, therefore a rigid body velocity is added in order to ensure the volume conservation [Pan *et al.* 1997, Kucherenko *et al.* 2000, Wakai & Brakke 2011]. This will be discussed later in Chapter 7.

However in the particular case of the surface diffusion, the velocity induced by this mechanism leads to volume conservation. Indeed, a way to validate a numerical approach of surface diffusion consists in measuring the variation of the volume of the powder compact. Furthermore, the stability of this problem has been studied from the mathematical point of view (see [Bernoff *et al.* 1998, Escher *et al.* 1998]).

From the previous Equations (5.2) and (5.6), it is clear that the normal $\underline{n}$ and the curvature κ are very important considering the simulation of sintering by surface diffusion. By using the expressions presented in Chapter 4, the normal and the curvature can be computed as functions of ϕ:

$$\underline{n_\phi} = \frac{\underline{\nabla \phi}}{\| \underline{\nabla \phi} \|} \tag{5.7}$$

$$\kappa_\phi = \nabla \cdot \frac{\underline{\nabla \phi}}{\| \underline{\nabla \phi} \|} \tag{5.8}$$

Both curvature and normal are some geometrical quantities related to the surface of the particles ($\{\phi = 0\}$). But within a level-set context, κ and $\underline{n}$ are defined over all the computational domain Υ as the level-set function ϕ is also defined over Υ. However, κ and $\underline{n}$ vanish outside the narrow band $[-E\,,\,E]$ when the local level-set approach presented in Section 4.4.2 is used. Within a level-set context, the surface diffusion velocity can be rewritten as follows:

$$\underline{v^s} = v^s \frac{\underline{\nabla \phi}}{\| \underline{\nabla \phi} \|} \tag{5.9}$$

and

$$v^s = A_0 \frac{1}{\| \underline{\nabla \phi} \|} \underline{\nabla} \cdot \left(\| \underline{\nabla \phi} \| \underline{\underline{\mathcal{P}_\phi}} \cdot \underline{\nabla \kappa_\phi} \right) \tag{5.10}$$

with $A_0 = D_s \gamma_{sv}/kT$ a characteristic parameter of the diffusion mechanism and the projection operator within the level-set context $\underline{\underline{\mathcal{P}_\phi}}$ given by:

$$\underline{\underline{\mathcal{P}_\phi}} = \underline{\underline{\mathcal{I}}} - \frac{\underline{\nabla \phi}}{\| \underline{\nabla \phi} \|} \otimes \frac{\underline{\nabla \phi}}{\| \underline{\nabla \phi} \|} \tag{5.11}$$

The velocity obtained from Equations (5.9) and (5.10) corresponds to the surface diffusion velocity in the vicinity of the surface of the particles ($\{\phi = 0\}$).

The spatial discretization presented in the previous Chapter 4 is used. The computational domain $\Upsilon \subset \mathcal{R}^n$ is discretized by a simplex mesh $\mathcal{T}_h(\Upsilon)$. In this way, variables ϕ, κ and v^s are approximated by ϕ_h, κ_h and v_h^s, respectively, chosen to be continuous and piecewise linear over Υ. In the same way a temporal discretization of the time interval $[0, t_f]$ is used $0 = t_0 < t_1 < t_2 < \ ... \ < t_f$. in the following, a variable Y evaluated at the time t is denoted Y^t.

5.2.1 Explicit formulation

At first glance it seems that numerical implementation of the surface diffusion mechanism within the level-set context is straightforward. By using the level-set function ϕ_h, it is possible to compute the curvature κ_h, and then from this curvature, a normal velocity v_h^s could be deduced. However some difficulties must be handled:

- The velocity v_h^s depends on the fourth spatial derivative of the level-set function ϕ_h which is piecewise linear. This means that the gradient $\underline{\nabla \phi_h}$ is piecewise constant and $\underline{\nabla^{(n)} \phi_h} \equiv 0$ for $n \geq 2$. Therefore Equations (5.8) and (5.10) must be considered in a week sense to be properly handled (see [Bänsch *et al.* 2005, Burger *et al.* 2007]).

– The non linear coupling between the level-set function ϕ, the curvature κ and the surface diffusion velocity $\underline{v^s}$.

This work aims at simulating sintering process by considering the three main diffusion paths (surface, volume and grain-boundary diffusions). For this reason it is necessary to develop a strategy that allows to take into account the contributions of the different diffusion mechanisms. Considering the surface diffusion mechanism, the surface diffusion velocity is computed in an explicit way in the transport of the level-set function (Equation (4.10)):

$$\frac{\partial \phi}{\partial t} + \underline{v_h^s} \cdot \underline{\nabla \phi} = 0$$

this means that $\phi_h^{t+\Delta t}$ is computed by solving Equation (4.10) with the velocity $v_h^{s\,t}$ evaluated at time t corresponding to ϕ_h^t.

As a first approach, Equations (4.10) (level-set transport), (5.7) (normal), (5.8) (curvature) and (5.10) (surface diffusion velocity) are solved successively in an explicit way. In order to avoid some oscillation of the computation of κ_h and v_h^s, an elliptic regularization is used (see [Miller 1997]). In this regularization, the terms $\epsilon_\kappa \Delta\kappa$ and $\epsilon_{v^s}\Delta v^s$ are respectively added to the left hand side of Equations (5.8) and (5.10) where ϵ_κ and ϵ_{v^s} are two regularization parameters. The regularized weak form of the surface flux (Equation (5.3)) writes as:

$$\int_\Upsilon \kappa_h^t \psi_h dV + \epsilon_\kappa \int_\Upsilon \underline{\nabla \kappa_h^t} \cdot \underline{\nabla \psi_h} dV = -\int_\Upsilon \frac{\nabla \phi_h^t}{\| \underline{\nabla \phi_h^t} \|} \cdot \underline{\nabla \psi_h} dV \tag{5.12}$$

for any continuous test function ψ_h piecewise linear on Υ. The effect of the regularization parameter ϵ_κ is shown in Figure 5.4. In this example ϕ_h^t is computed as the filtered signed distance function to a circle of radius $R = 0.2$. The curvature obtained by using Equation (5.12) is defined over all the computational domain Υ and should be equal to the circle curvature $\kappa_h^t = 1/R = 5$ near to the surface of the circle $\{\phi_h^t = 0\}$. When no regularization is considered ($\epsilon_\kappa = 0$) the iso-value $\{\kappa_h^t = 5\}$ is scattered over a wide band around the interface, as shown in Figure 5.4a. However if a small regularization parameter is considered, then the iso-value $\{\kappa_h^t = 5\}$ is superimposed with the surface of the circle ($\{\phi_h^t = 0\}$), as it can be seen in Figure 5.4b. An additional circle of the iso-value $\{\kappa_h^t = 5\}$ can be seen inside the circle. This second iso-value is a result of the discontinuity of the second order derivative of the level-set function ϕ_h^t that comes from the filtering step. However, this discontinuity appears far from the interface and therefore does not represent a problem.

The regularization term added for the computation of the curvature allows to improve its computation. However this curvature should be used again to compute the surface diffusion

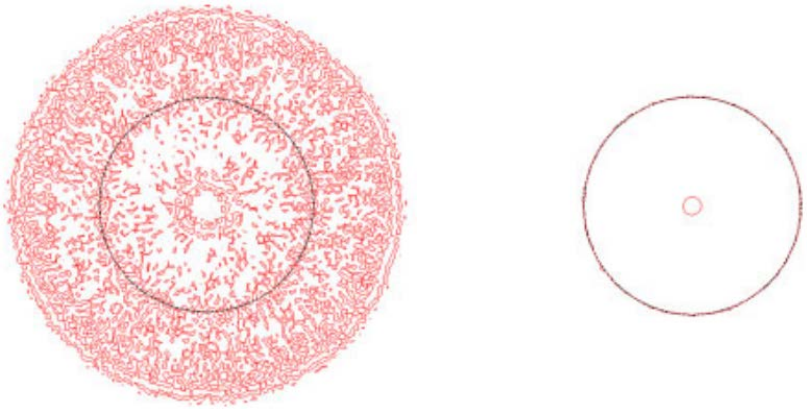

a. $\epsilon_\kappa = 0$. b. $\epsilon_\kappa = 10^{-4}$.

Figure 5.4: The zero iso-value of the Level-set function $\{\phi_h = 0\}$ of a circle of radius $R = 0.2$ (black line) and iso-value of the curvature $\{\kappa_h = 5 = 1/R\}$ (red line). Influence of the parameter ϵ_κ: a. $\epsilon_\kappa = 0$ and b. $\epsilon_\kappa = 10^{-4}$ [Bruchon *et al.* 2011].

velocity and this time the elliptic regularization is much more complex. If the regularization parameter ϵ_{v^s} is "too large" (compared with the velocity), the solution is stable but the velocity is underestimated (see Section 5.3.1). On the other hand, if ϵ_{v^s} is "small", then the formulation leads to an accurate computation of the velocity during the first time steps, but then some spurious oscillations of the curvature appear as shown in Figure 5.5. These oscillations can be prevented by using a "small" time step.

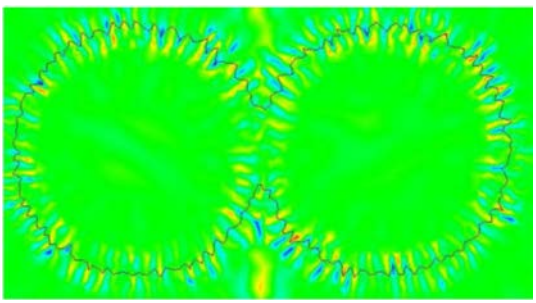

Figure 5.5: Zero iso-value of the level-set function $\{\phi_h^t = 0\}$ (black line) and the curvature field κ_h^t computed by using $\epsilon_{v^s} = \epsilon_\kappa = 10^{-4}$ [Bruchon *et al.* 2011].

In order to perform a simulation of sintering by surface diffusion with this explicit approach, it is necessary to set the values of the two stabilization parameters (ϵ_κ and ϵ_{v^s}) and a small time step should be used. This can represent a problem as the parameters are sometimes,

difficult to tune, therefore another formulation will be presented in the next Section 5.2.2 to avoid those complications.

5.2.2 Mixed $\kappa/\Delta_s\kappa$ formulation

Assuming that the level-set function ϕ_h^t is known at time t, the idea consists in building a coupled system where the unknowns are the curvature κ_h^t and the velocity v_h^{st}. From Equation (5.6), the velocity v_h^{st} is equal to $A_0\Delta_s\kappa_h^t$, then this is equivalent to write a mixed formulation $\kappa_h^t/\Delta_s\kappa_h^t$.

In order to introduce an implicit regularization, a first-order Taylor's expansion is considered at intermediate time $t < t + 1/2 < t + \Delta t$:

$$\phi_h^{t+\frac{1}{2}} \equiv \phi_h^t + \frac{\partial \phi_h^t}{\partial t}\Delta t = \phi_h^{t+\Delta t} + \mathcal{O}\left(\Delta t\right)$$

hence, $\phi_h^{t+\frac{1}{2}}$ is the first-order approximation of $\phi_h^{t+\Delta t}$. Since the level-set function is solution of the transport Equation (4.10), $\partial\phi_h^t/\partial t = -\underline{v_h^{st}} \cdot \underline{\nabla\phi_h^t}$, the previous expression can be rewritten as follows:

$$\phi_h^{t+\frac{1}{2}} = \phi_h^t - \underline{v_h^{st}} \cdot \underline{\nabla\phi_h^t}\,\Delta t$$

Finally by replacing teh surface velocity (Equation (5.9)), the following expression can be found:

$$\phi_h^{t+\frac{1}{2}} = \phi_h^t - v_h^{st} \parallel \nabla\phi_h^t \parallel \Delta t \tag{5.13}$$

The coupled system $\kappa_h^t/\Delta_s\kappa_h^t$ can be now constructed by considering $\phi^{t+\frac{1}{2}}$ instead of ϕ_h^t in the curvature expression (Equation (5.8)). Since ϕ_h^t is supposed to be known at time t, the coupled system can be written as follows:

$$\kappa_h^t + \underline{\nabla} \cdot \left(\frac{\Delta t}{B}\underline{\nabla v_h^{st}}\right) = \underline{\nabla} \cdot \left(\frac{1}{B}\underline{\nabla\phi_h^t}\right) \tag{5.14a}$$

$$v_h^{st} \parallel \underline{\nabla\phi_h^t} \parallel - A_0\underline{\nabla} \cdot \left(\parallel \underline{\nabla\phi_h^t} \parallel \underline{\underline{\mathcal{P}_{\phi_h^t}}} \cdot \underline{\nabla\kappa_h^t}\right) = 0 \tag{5.14b}$$

the term denoted B corresponds to $\parallel \underline{\nabla\phi_h^{t+\frac{1}{2}}} \parallel$. However, to avoid dealing with non-linearities, the computations presented in this work are performed by computing as $B = \parallel \underline{\nabla\phi_h^t} - \Delta t\underline{\nabla v_h^{st-\Delta t}} \parallel$.

An important point should be highlighted, since ϕ_h^t is a distance function near the surface ($\{\phi_h^t = 0\}$) then $\parallel \underline{\nabla \phi_h^t} \parallel$ is approximatively equal to 1 near to the surface. This is why $\parallel \underline{\nabla \phi_h^t} \parallel$ does not appear in the second term [2] on Equation (5.14a).

The key point of this approach is that using $\phi_h^{t+\frac{1}{2}}$ instead of ϕ_h^t to compute the curvature introduces an additional term in the left-hand side of Equation (5.14a). This additional coupling term κ/v^s is equivalent to a regularization term Δv^s with the regularization parameter equal to $\Delta t/B$. In this way, only one regularization term is necessary to compute the curvature and the surface diffusion velocity, in contrast with the explicit approach where two regularization parameters were needed. Furthermore, the value of this parameter appears naturally and is directly related with the time step.

The mixed formulation (5.14) shows strong similarities with the one developed by Bänsch et al. within the context of a Lagrangian description of the particles in [Bänsch *et al.* 2005]. The stability of this formulation (5.14) will not be proven strictly in this work, but numerical experiments demonstrate a very good behavior (see numerical result in Section 5.3).

The mixed formulation (5.14) is solved within a finite element framework. As previously, the computational domain Υ is discretized by a simplex mesh $\mathcal{T}_h(\Upsilon)$, and variables ϕ_h^t, κ_h^t and v_h^{st} are chosen to belong to a space of piecewise linear continuous functions, denoted $\mathcal{V}_h$. The mixed weak formulation of (5.14) consists in finding $(\kappa_h^t, v_h^{st}) \in (\mathcal{V}_h \times \mathcal{V}_h)$ solution of:

$$\begin{aligned} \int_\Upsilon \kappa_h^t \psi_h dV - \Delta t \int_\Upsilon \frac{1}{B} \underline{\nabla v_h^{st}} \cdot \underline{\nabla \psi_h} dV = -\int_\Upsilon \frac{1}{B} \underline{\nabla \phi_h^t} \cdot \underline{\nabla \psi_h} dV \\ \int_\Upsilon \parallel \underline{\nabla \phi_h^t} \parallel v_h^{st} \psi_h dV + \int_\Upsilon A_0 \parallel \underline{\nabla \phi_h^t} \parallel \left(\underline{\underline{\mathcal{P}_{\phi_h^t}}} \cdot \underline{\nabla \kappa_h^t} \right) \cdot \underline{\nabla \psi_h} dV = 0 \end{aligned} \tag{5.15}$$

for any $\psi_h \in \mathcal{V}_h$. Note that only one single type of weighting functions ψ_h is used for both equations, curvature and velocity, as κ_h^t and v_h^{st} belong to the same functional space $\mathcal{V}_h$. Furthermore, the previous weak formulation does not require any Dirichlet's boundary condition: since ϕ_h^t is constant near the boundary of the computational domain $\partial\Upsilon$, κ_h^t and v_h^{st}, which depend on its derivatives, vanish over $\partial\Upsilon$.

5.2.3 Surface diffusion time stepping algorithm

Algorithm 3 presents the procedure used to perform the simulation by surface diffusion.

It is important to notice that the initial mesh adaptation and the remeshing step are performed by using the method described in Section 4.4.4 . After each remeshing step, the level-set function ϕ_h^t is projected from the "old" mesh onto the new one by P1 interpolation

2. It will be shown later that this term is only a regularization term.

Algorithm 3 Time stepping algorithm for the surface diffusion strategy developed.

$\phi_h^t \leftarrow$ From Algorithm 2 for a given geometry at $t = 0$.
$\mathcal{T}_h(\Upsilon)$: Initial mesh adaptation by using ϕ_h^t at $t = 0$
for $t = 0 \rightarrow (t_f - \Delta t)$ with ϕ_h^t known at t **do**
  $v_h^{s\,t} \leftarrow$Solution of the system (5.15)
  $\underline{v_h^{s\,t}} \leftarrow$From Equation (5.9)
  $\phi_h^{t+\Delta t} \leftarrow$From the resolution of the convective-reinitialization Equation (4.19)
  $t \leftarrow t + \Delta t$
  $\mathcal{T}_h(\Upsilon) \leftarrow$Remeshing step every f_{rem} time steps.
end for
$\phi_h^{t_f} \rightarrow$ Output of the simulation at $t = t_f$.

(see [Ville *et al.* 2011] for further details). The effect of this projection will be analyzed in Section 5.3.1.

5.3 Numerical results

As presented in the previous Section 5.2.3, the mesh adaptation strategy introduced in Section 4.4.4 is used. Therefore, before performing any simulation of surface diffusion, a simulation proposed in [Chopp & Sethian 1999] will be used to see the impact of the mesh adaptation and the remeshing steps on a evolution by surface diffusion of a given geometry. Figure 5.6 shows a star shape flowing under Laplacian of curvature driving force. In this example, the star shape is composed of 3 ellipses with a ratio between the major and minor axes equal to 10. Parameter A_0 gathering the diffusion physical characteristics (Equation (5.10)) is taken equal to $2 \cdot 10^{-3}$, while the time step for this calculation is $\Delta t = 5 \cdot 10^{-4}$. The shape becomes roughly circular within 5000 iterations (Figure 5.6d). Hence, two different simulations are compared, the first one (dashed-line in Figure 5.6) has been obtained by using an unstructured mesh with a uniform element size $h = 6.25 \cdot 10^{-3}$ without any remeshing step; the second simulation (black solid-line in Figure 5.6) uses the mesh adaptation strategy described in Section 4.4.4 with a minimal element size of $h_{min} = 6.25 \cdot 10^{-3}$ and a maximal element size $h_{max} = 8.0 \cdot 10^{-2}$. The remeshing step is applied with a frequency of three time steps (which is a very high remeshing frequency considering this problem). The evolution of the star shape is shown to be similar in both cases. Hence, perturbation in the free surface evolution due to the remeshing steps, seems to be acceptable. In fact, the remeshing step works well when considering adaptation with respect to the distance function, because this function can be assumed to be nearly linear in the vicinity of the free surface (if this last one is smooth enough). In this case, P1 interpolation

from mesh to mesh is then exact. Further finite element simulations involving very accurate descriptions of free surfaces with mesh adaptation can be found in [Ville *et al.* 2011].

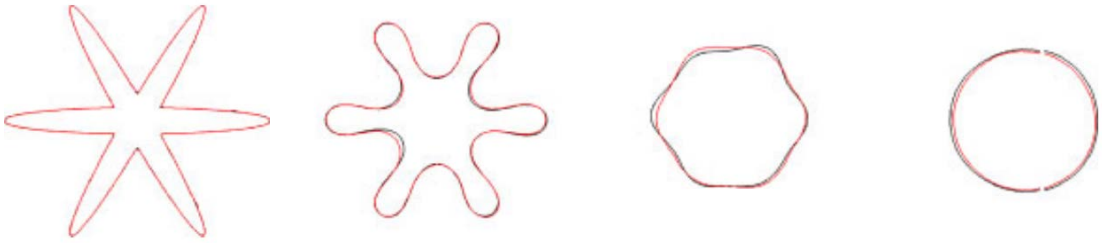

a. $t = 0$ b. $t = 0.3$ c. $t = 1.25$ d. $t = 2.5$

Figure 5.6: Evolution of star shape (at times t = 0, 0.3, 1.25, and 2.5): without mesh adaptation (black solid-line) and with mesh adaptation and remeshing (dashed-line) [Bruchon *et al.* 2011].

As the perturbations due to the mesh adaptation combined with the remeshing steps are very low, this meshing strategy will be used from now on to perform the simulations of sintering by surface diffusion with a frequency adapted to the considered case.

5.3.1 Evolution of an ellipse

The analytical solution of the evolution of a structure by surface diffusion is only available for very simple cases. This benchmark case aims at asserting the methodology presented by comparing the results obtained from numerical simulations to the results predicted by an analytical model. The computational domain Υ is an unit square (2D).

First, the evolution of an ellipse by surface diffusion is considered (as in [Chopp & Sethian 1999]). As the motion by surface diffusion tends to minimize the surface energy while the volume is conserved, this example can be used to evaluate the convergence and the conservation properties of the approach. The initial geometry is given by an ellipse with a ratio between the major and the minor axis equal to 4, $A_0 = 2 \cdot 10^{-6}$ and $\Delta t = 5 \cdot 10^{-4}$. The level-set function ϕ_h is initialized as the signed distance function to an ellipse and then is filtered by using Equation (4.20). The interface (the zero iso-value of the level-set function $\{\phi_h = 0\}$) evolves toward a circular shape.

Figure 5.7 points out the convergence properties of this strategy by showing the zero level set of ϕ_h obtained after 5000 time steps with different space discretizations. Several structured

meshes have been used (80×80, 160×160, and 320×320 meshes), as well as two unstructured meshes with a mesh size of $6.25 \cdot 10^{-3}$ and $1 \cdot 10^{-3}$ ($h = 6.25 \cdot 10^{-3}$ corresponds to the mesh size of the 160×160 mesh). Beside the convergence in shape, the convergence in the area conservation property can also be observed in Figure 5.7. The area loss is equal to 40%, 2.8%, and 0.9% of the initial area respectively for the three structured meshes, while it is equal to 2.4% for the unstructured mesh having a uniform mesh size of $6.25 \cdot 10^{-3}$ (without mesh adaptation, 34 000 nodes), and to 6% when the remeshing technique is applied with $h_{min} = 6.25 \cdot 10^{-3}$ (approximatively 2200 nodes). However, when using the mesh adaptation method with $h_{min} = 10^{-3}$ (12 000 nodes), the area loss drops to 1%.

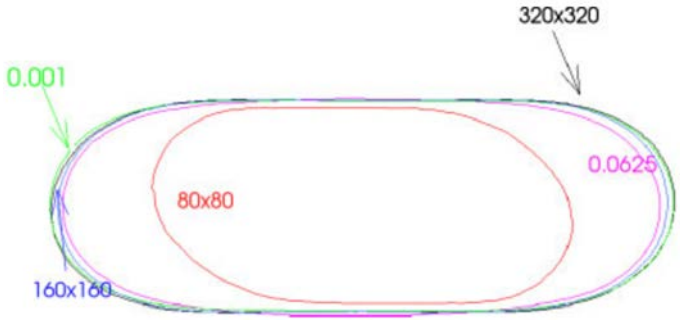

Figure 5.7: Geometries obtained at $t = 2.5$ of the surface diffusion of an ellipse for different spatial resolutions (Number of elements for structured meshes or minimal element size for unstructured meshes) [Bruchon *et al.* 2011].

In this way, another validation of the mesh adaptation and remeshing step is achieved. Even if the mesh adaptation introduces an additional numerical diffusion which can lead to a gain or loss in mass, the previous simulations (star shape (Figure 5.6) and oval shape (Figure 5.7)) show that convergence in shape as well as in mass conservation is obtained when using the proposed remeshing technique.

Another simulation concerning the evolution by surface diffusion of an ellipse of axes 0.3 and 0.2 was performed. This time $A_0 = 10^{-3}$, $\Delta t = 10^{-3}$ and a mesh with $h_{min} = 6.25 \cdot 10^{-3}$ close to the interface and $h_{max} = 3.0 \cdot 10^{-2}$ far from the interface. Figure 5.8 shows the interface as a black solid-line, which evolves toward a circular shape. The curvature is plotted over a narrow band around the interface [3] in Figures 5.8a and 5.8b. As the area of the ellipse should be conserved by surface diffusion, it is possible to compute the analytical value of the final circular shape at the equilibrium. Furthermore, it can be seen that the curvature κ_h^t converges toward its expected value $\kappa_{final} = 4.08$ (Figure 5.8b) and the area, that can not be seen in this

3. The region where $\kappa_h^t \neq 0$.

figure, is preserved. Figure 5.8c shows the surface diffusion velocity field close to the interface at time $t = 0$, this velocity is, as expected, higher in the regions where the surface gradient of the curvature $\underline{\nabla_s \kappa_h^t}$ is larger.

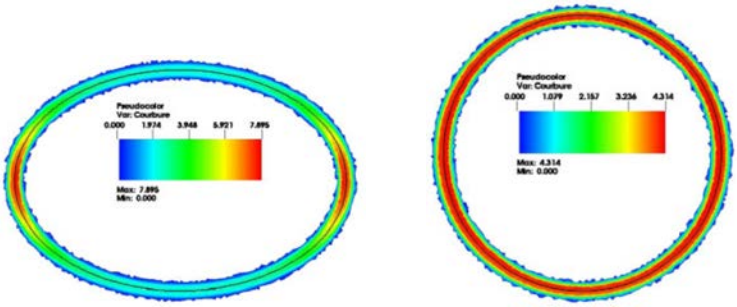

a. κ_h^t at $t = 0$. b. κ_h^t at $t = 1$.

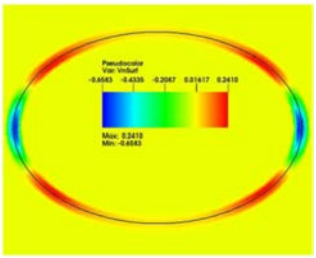

c. v_h^{st} at $t = 0$.

Figure 5.8: Evolution of the interface $\{\phi_h = 0\}$ (black line) of an ellipse: a. κ_h^t at $t = 0$; b. κ_h^t at $t = 1$; c. v_h^{st} at $t = 0$ [Bruchon *et al.* 2011].

The final shape of the ellipse has been compared with success to the analytical circle of radius $R_{final} \approx 0.245 = 1/\kappa_{final}$. Moreover, it is possible to compare the shape of the ellipse obtained numerically with the predicted one given by an analytical model all along the simulation. Let $a(t)$ and $b(t)$ be the major and the minor axes of the ellipse at the time t, with $a(0) = 0.3$ and $b(0) = 0.2$. The surface laplacian of the ellipse curvature can be computed with ease and the velocity of the major axis of ellipse at the point $[a(t)\,,\,0]$ is given by:

$$v_{\text{axis}_a} = A_0 \frac{3\left(b^2 - a^2\right) a}{b^6} \tag{5.16}$$

Hence, the length of the axis a at time $t + \Delta t$ can be computed by an explicit Eulerian scheme: $a(t + \Delta t) = a(t) + v_{\text{axis}_a} \Delta t$. As the area of the ellipse must be conserved, the length

of the minor axis is given by $b(t+\Delta t) = a(0)\,b(0)/a(t+\Delta t)$.

Figure 5.9 presents a comparison over time between the values of a and b obtained by three different ways: from the analytical model, from the level-set approach when system $\kappa_h/\Delta\kappa_h$ (5.14) is solved (red lines), and from the fully explicit formulation (blue lines, with $\epsilon_{v^s} = \epsilon_\kappa = 10^{-3}$ and still $\Delta t = 10^{-3}$). The results provided by the mixed method show a good behavior of the interface, with a maximal error on both major and minor axes lower than 3%. The fully explicit method does not exhibit such a behavior, with an important error on the interface position. Furthermore, as already mentioned, this method appears to be unstable when, for instance, $\epsilon_{v^s} = \epsilon_\kappa = 10^{-4}$ and $\Delta t = 10^{-3}$, or when $\epsilon_{v^s} = \epsilon_\kappa = 10^{-4}$ and $\Delta t = 10^{-4}$. Finally, note that 1000 time steps have been carried out with the mixed approach for a CPU time of approximatively 600 s on one processor of 2.2 GHz and with a mesh of approximatively 4800 nodes.

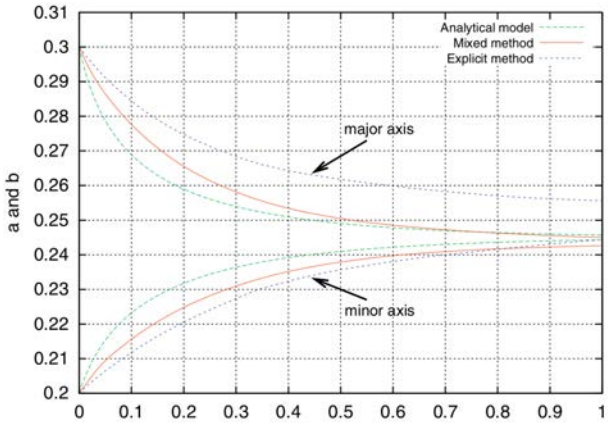

Figure 5.9: Change in the major and minor axes of the interface over time: analytical model, simulation with the mixed approach, and simulation with the fully explicit approach ($\epsilon_{v^s} = \epsilon_\kappa = 10^{-3}$) [Bruchon *et al.* 2011].

5.3.2 Growth of the neck between two particles of the same size

This example aims at establishing a comparison between the numerical approach developed and the analytical model of surface diffusion presented in Section 3.1 fot two particles of the same size. The first case involves two particles of radii R as shown in Figure 5.10. The initialization of the level-set function ϕ_h is carried out by using Equation (5.2) with a neck radius $r = 0$, this is equivalent to two tangent particles as described in Section (5.1.1). This level-set function is next filtered as usual by using Equation (4.20). It is important to note that the zero iso-value obtained from two tangent particles is ill-defined (as presented previously in

Section 5.1). However, despite the initial "roughness" of the contact area between the particles, and due to the matter diffusion, this area becomes quickly smooth as shown in Figure 5.10. Furthermore, it has to be pointed out that there is no special algorithm here to deal with the singularities near to the contact point. Those singularities will represent a problem concerning the sintering by volume diffusion, as it will be shown in Chapter 6.

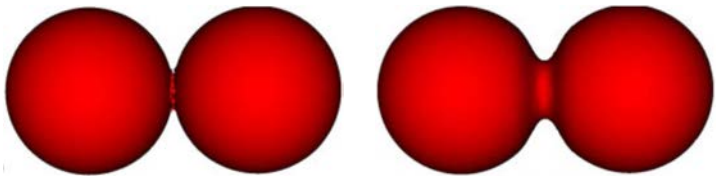

a. $t = 0$. b. $t = 10^{-2}$.

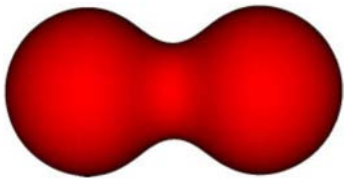

c. $t = 3$.

Figure 5.10: Change of the interface $\{\phi_h = 0\}$ during the sintering of two particles of equal size (radius $R = 0.1$) at different time: a. $t = 0$; b. $t = 10^{-2}$; c. $t = 3$ [Bruchon *et al.* 2011].

This simple simulation allows to see how the neck between the particles is naturally developed, and according to Table 5.1, the change of the volume of the particles is very low. As stated previously, this change of the volume highly depends on the element size and the time step, but for the numerical parameter used for this simulation ($A_0 = 10^{-6}$, $\Delta t = 10^{-3}$ and $h_{min} = 8.0 \cdot 10^{-3}$) the volume change is limited 0.8% after 1000 time steps.

Time	0	0.02	0.06	0.1	0.4	0.6	1
Volume Change (%)	0	+0.023	+0.0005	-0.011	-0.18	-0.44	-0.79

Table 5.1: Change in volume during the sintering of two particles of $R = 0.2$ [Bruchon *et al.* 2011].

Free sintering is a very slow process, sometimes it may take several hour. Therefore, if

the real values of the diffusion coefficients for the different diffusion mechanisms were used, the appropiate time step would be very high which could lead to some instabilities of the numerical approaches. In order to use a small time step, the diffusion related properties of the materials were taken to be about 20,000 times higher than they are in reality. This is equivalent to change time unit and since the coupling with the thermal problem is not considered, the results obtained with this approach still represent the kinetics of the surface diffusion. The diffusion coefficients used for the volume diffusion (Chapter 7) are also chosen in such a way that a "small" time step can be used.

The analytical model for the growth of the neck between the particles presented in Chapter 3 (Table 3.2) can be rewritten as follows:

$$\frac{x(t)}{R} = \left(\frac{23\gamma_{sv}D_s\delta_s\Omega}{kT}\frac{t}{R^4}\right)^{1/7} = \left(\frac{23\,A_0}{R^4}t\right)^{1/7}$$
$$\frac{x(t)}{R} = 1.57\,t'^{\,1/7} \tag{5.17}$$

where t' is an adimensional time, defined by $t' = (A_0/R^4)t$. Figure 5.11 shows the evolution of the adimensional neck radius x/R obtained by using the numerical approach presented for different particles radii, ranging from 0.1 to 2.5.

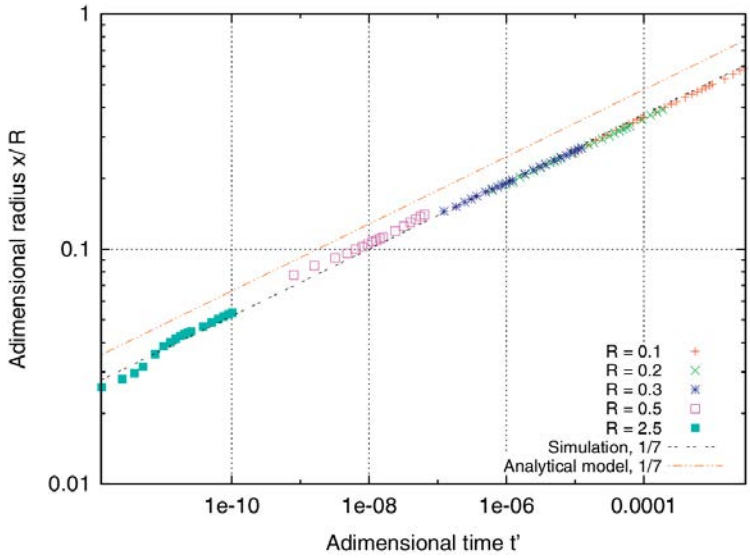

Figure 5.11: Evolution of the adimensional neck radius x/R over the adimensional time t' (logarithmic scale) for different values of R [Bruchon *et al.* 2011].

As predicted by Equation (5.17), this evolution over t' does not depend on the particle radius

R, and behaves as $t'^{1/7}$. Hence, despite an initial contact surface between the particles which is not well defined as already mentioned, the neck radius x/R provided by each simulation tends quickly toward a same curve of power law form (5.17). Instead of the coefficient 1.57 given by the analytical model, simulations provide a coefficient equal to 1.3. The curves corresponding to these two values are denoted in Figure 5.11 by "Analytical model, 1/7" and "Simulation, 1/7", respectively. It has to be underlined that this result is shown to be stable with respect to the time step (ranging from 10^{-6} to 10^{-2}), with respect to the mesh size (ranging from 10^{-4} to 10^{-2}, with isotropic or anisotropic remeshing), and thus with respect to the initial neck radius: in all the investigated cases, the neck radius x/R obtained by direct simulation tends quickly toward a "master curve" of the type given in Equation (5.17) with a coefficient approximatively equal to 1.3. It also has to be highlighted that the two key parameters that characterize the surface diffusion from the particle surface toward the neck in Equation (5.17) are, on one hand the power 1/7, and on the other hand, the power 4 applied to R in the denominator (see [Rahaman 1995]). The differences between the simulations and the analytical model can be explained by the geometrical approximations made in the former one.

5.3.3 Particle packing sintering

A sintering simulation by surface diffusion of a set of 154 spherical particles is presented. As discussed in Chapter 2, surface diffusion does not lead to shinkage of the compact powder. Figure 5.12a shows the inital geometry of a powder compact of 154 particles, as it can be seen a mesh adaptation strategy is used and the element size near to the particles surface is smaller ($h_{min} = 0.001$) than the element size far from the interface ($h_{max} = 0.1$). After $170\Delta t$ the neck between the particles has developed up to 50% of the radius of some particles, however it can be seen in Figure 5.12b that the cluster of particles has not shrunk.

One of the main advantages of numerical approaches is that it is possible to measure and quantify some variables which would not be possible with an experimental setup. Concerning the sintering at the particles scale, it is very hard measure experimentally the total surface or the specific surface [4] of a compact powder during sintering. Figure 5.12c shows (dashed green line) the evolution of the total free surface of the compact powder over time.

4. The specific surface is the ratio between the total free surface of the compact powder and its mass.

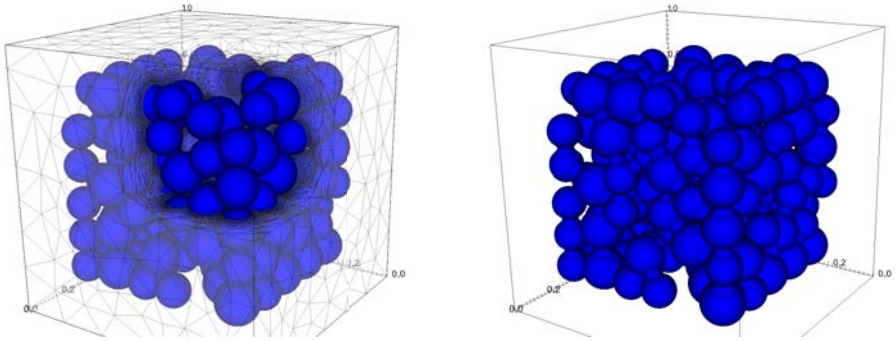

a. $t = 0$.

b. $t = 170\Delta t$.

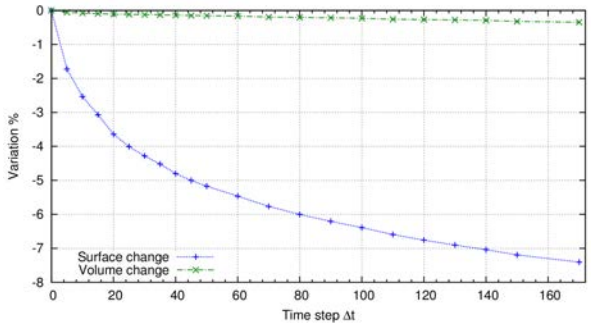

c.

Figure 5.12: Sintering simulation by surface diffusion of a set of 154 particles at the initial time (a. $t = 0$) and after $170\Delta t$ (b. $t = 105\Delta t$). Variation of the volume (green dased line in c.) and total surface reduction (blue line in c.)

5.4 Conclusions

A finite element level set formulation of the surface diffusion problem has been proposed. The numerical approach developed in this work is based on a linear interpolation of the level set function. Nevertheless, the surface diffusion physical phenomenon establishes that the velocity induced by this diffusion path depends on the fourth-order spatial derivative of the level set function. In order to overcome this difficulty, a mixed system in curvature/surface Laplacian of the curvature has been developed. This formulation induces implicitly a stabilization term with an associated stabilization parameter depending on the time step.

The stability of the method has been shown through many numerical experiments. First, the convergence of the method is studied by considering the volume conservation (or the area

conservation in 2D) over different structured and unstructured meshes. There exists different analytical models allowing to study the geometrical evolution of a structure by surface diffusion for simple geometries, such as an ellipsoid or two particles of the same size. Considering those analytical models, the results obtained from the numerical approach presented here were successfully compared with those analytical models. Even if these kind of simulation are very important for the validation of the numerical approach, this work aims at the simulation of more realistic particles packing. For this reason some examples considering the sintering of more complex powder compacts were also studied.

In the next Chapters 6 and 7 a numerical approach allowing to introduce the volume diffusion into the same framework used for the surface diffusion will be presented.

5.5 Résumé en français : Frittage par diffusion surfacique

Une fois le cadre numérique de travail fixé, dans ce chapitre, une formulation éléments finis basée sur la méthode Level-Set est proposée pour traiter le problème de diffusion surfacique. Le domaine de calcul est discrétisé à l'aide des simplexes (i.e. des triangles à trois nœuds en 2D ou bien des tetraèdres à quatre nœuds en 3D). Cette discrétisation mène à une interpolation linéaire des différents champs, et, en particulier, de la fonction level-set. Cependant, la vitesse induite par la diffusion surfacique est proportionnelle à la dérivée seconde de la courbure. La courbure est donnée elle-même par la dérivée seconde de la fonction level-set. Par conséquent, la vitesse de diffusion surfacique est proportionnelle à la dérivée quatrième de la fonction level-set. Afin de pouvoir résoudre ce problème, une formulation mixte courbure/Laplacien surfacique de la courbure a été développée. Cette formulation mixte introduit, implicitement, un terme de stabilisation avec un paramètre de stabilisation lié au pas de temps.

Plusieurs cas test ont montré la stabilité de la méthode ainsi que sa capacité à simuler le phénomène de diffusion surfacique. Les résultats obtenus en utilisant cette approche ont été comparés avec succès aux prédictions données par les modèles analytiques pour le frittage entre deux particules. Cette validation permet de conclure que l'approche développée décrit bien la cinématique du phénomène de diffusion surfacique. Comme un premier pas vers la simulation du frittage en 3D, quelques exemples de frittage en 3D ont été présentés.

Chapter 6

Mechanical problem

Contents

Sintering simulation by surface diffusion has been introduced in previous Chapter 5. Aiming to integrate the volume diffusion mechanism into the same framework, the matter flux given by the following expression (Equation (2.25)) must be computed:

$$\underline{j^v} = -A_1 \underline{\nabla p}$$

where A_1 is a parameter related to the diffusion properties and temperature. This equation illustrates the most important fact: the volume matter flux $\underline{j^v}$ is proportional to the gradient of pressure $\underline{\nabla p}$. Therefore, a numerical strategy must be developed to properly compute the pressure inside and outside the particles, which is equivalent to solve the whole fluid/particles mechanical problem.

Considering this diffusion mechanism, in this chapter numerical methods for simulating fluid - elastic solid interaction with surface tension are presented. A Level-Set method presented in Chapter 4 is used to capture the interface between the solid bodies and the surrounding fluid. A mixed velocity - pressure variational formulation is established for the global coupled mechanical problem and discretized using a continuous linear approximation in both velocity and pressure (Section 6.1). This kind of problems leads to the occurrence of some unphysical spurious oscillations. Those oscillations are the result of the numerical resolution of the system and it is possible to identify two different sources of oscillations. On the one hand, when the stokes incompressible problem or the linear (slightly compressible) elasticity problem are treated by using a mixed finite element formulations if the Babušca-Brezzi condition is not satisfied, then unphysical oscillations of the pressure appear. Different solutions can be considered: one solution consists in using a compatible set of elements as the elements $P2/P1$ or the $P1+/P1$. Another solution is to modify the discrete weak formulation in order to stabilize it (multiscale methods). On the other hand, unphysical oscillations also come from the discontinuity of the mechanical properties of the materials, from the discontinuity of the the normal stress and from the computation of the curvature for the surface tension term. Again, it is necessary to use stabilization techniques in order to cope with this problem. Therefore, three ways are investigated to reduce the spurious oscillations of the pressure which appear at the fluid - solid interface (Section 6.2). First, two stabilized finite element methods are used: the MINI-element and the Algebraic Sub-Grid method. Second, the contribution of the surface tension is accounted for the Continuum Surface Force technique and surface local reconstruction (SLR) algorithm. Secondly, and besides the direct evaluation method proposed by Bruchon et al. [Bruchon *et al.* 2011], an alternative method is proposed to avoid the explicit computation of the surface curvature which may be a source of difficulty. The numerical strategy presented in this chapter will be available very soon in [Pino Muñoz *et al.* 2012].

6.1 Governing equations

Let Ψ be an open region, $\Psi \subset \mathcal{R}^d$, where d is the spatial dimension. The computational domain Ψ contains two inmiscible phases: a set of elastic solids, denoted Ψ_s, embedded into a surrounding fluid Ψ_f, $\bar{\Psi} = \bar{\Psi}_s \cup \bar{\Psi}_f$ is the closure of Ψ. Furthermore, Ψ_s is assumed to be completely contained in Ψ, *i.e.* $\partial\bar{\Psi}_s \cap \partial\bar{\Psi} = \emptyset$. The outer boundary of Ψ, $\Sigma_f = \partial\bar{\Psi}$, is divided into Σ_t and Σ_v where the Neumann and Dirichlet boundary conditions [1] are respectively

1. Dirichlet boundary conditions are those where the velocity is imposed and Neumann boundary conditions consist in imposing the stress vector.

applied. Finally, the interface between the two phases is denoted by $\Gamma_{s/f} = \bar{\Psi}_s \cap \bar{\Psi}_f$ (see Figure 6.1).

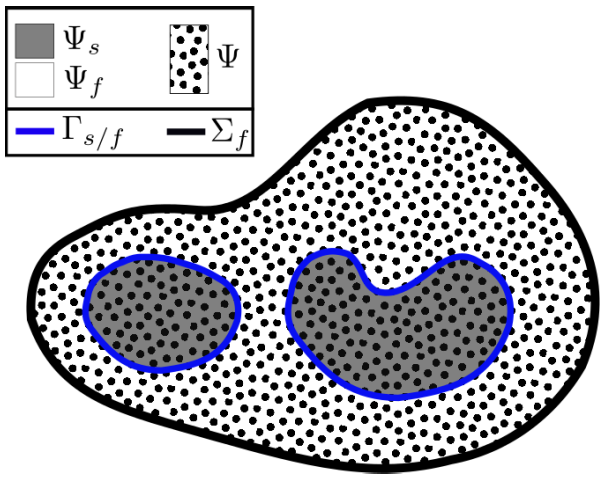

Figure 6.1: Computational domain Ψ divided into Ψ_s and Ψ_f by the interface $\Gamma_{s/f}$.

In this work, the inertia terms and the volume forces are neglected. The momentum conservation can be expressed as follows:

$$\begin{aligned} \underline{\nabla} \cdot \underline{\underline{\sigma}} &= \underline{0} && \text{in } \Psi, \\ \underline{\underline{\sigma}} \cdot \underline{n} &= -p_e \, \underline{n}^f && \text{in } \Sigma_t, \\ \underline{v} &= \underline{v_c} && \text{in } \Sigma_v \end{aligned} \tag{6.1}$$

where $\underline{\underline{\sigma}}$ is the *Cauchy* stress tensor for the solid or the fluid, as detailed in Sections 6.1.1 and 6.1.2. p_e is the pressure applied on the outer boundary Σ_t, $\underline{n}^f$ is the outward normal to Σ_t and velocity $\underline{v}$ is equal to $\underline{v_c}$ over Σ_v. Since the formulation proposed is a mixed formulation, the momentum conservation equation should be complemented with the mass conservation equation for each phase.

6.1.1 Incompressible Newtonian fluid Ψ_f

The *Cauchy* stress tensor $\underline{\underline{\sigma}}^f$ and the mass conservation for an incompressible Newtonian fluid are given by Equations (6.2) and (6.3) respectively.

$$\underline{\underline{\sigma}}^f(\underline{v}) = 2\eta \underline{\underline{\dot{\epsilon}}}(\underline{v}) - p \underline{\underline{\mathcal{I}}} \tag{6.2}$$

$$\operatorname{div} \underline{v} = 0 \tag{6.3}$$

with p the pressure, $\underline{v}$ the velocity, η the viscosity, $\underline{\underline{\dot{\epsilon}}}(\underline{v}) = (\nabla \underline{v} + {}^t\nabla \underline{v})/2$ the strain rate tensor and $\underline{\underline{\mathcal{I}}}$ the second order identity tensor.

6.1.2 Isotropic linear elastic solid Ψ_s

The *Cauchy* stress tensor $\underline{\underline{\sigma}}^s$ and the mass conservation for an isotropic linear elastic solid are given by Equations (6.4) and (6.5) respectively:

$$\underline{\underline{\sigma}}^s(\underline{u}) = 2\mu \underline{\underline{\epsilon}}(\underline{u}) - \left(1 - \frac{2}{3}\frac{\mu}{K}\right) p \underline{\underline{\mathcal{I}}} \tag{6.4}$$

$$\operatorname{div} \underline{u} + \frac{p}{K} = 0 \tag{6.5}$$

with $\underline{u}$ the displacement, μ the shear modulus, $\underline{\underline{\epsilon}}(\underline{u}) = (\nabla \underline{u} + {}^t\nabla \underline{u})/2$ the linearized strain tensor and K the bulk modulus.

6.1.3 Laplace's law

Coupling between fluid and solid is expressed through the surface tension acting over the interface $\Gamma_{s/f}$. The jump of the stress vector $\underline{\underline{\sigma}} \cdot \underline{n}$ is given by [Landau & Lifshits 1959]

$$\left[\left(\underline{\underline{\sigma}} \cdot \underline{n} \right) \right] |_{\Gamma_{s/f}} = \gamma_{sf} \kappa \underline{n} + \underline{\nabla}_s \gamma_{sf} \tag{6.6}$$

Here $[\cdot]|_{\Gamma_{s/f}}$ denotes the jump across the interface $\Gamma_{s/f}$, $\underline{n}$ is the unit vector normal to the interface $\Gamma_{s/f}$ (pointing outward Ψ_f or Ψ_s), γ_{sf} is the surface tension coefficient at the interface between the particles and the surrounding fluid, $\underline{\nabla}_s = \left(\underline{\underline{\mathcal{I}}} - \underline{n} \otimes \underline{n}\right) \cdot \underline{\nabla}$ is the surface gradient operator and κ is the surface mean curvature. In this work the surface tension coefficient γ_{sf} is assumed constant and previous Equation (6.6) writes:

$$\left[\left(\underline{\underline{\sigma}} \cdot \underline{n} \right) \right] |_{\Gamma_{s/f}} = \gamma_{sf} \kappa \underline{n} \tag{6.7}$$

Because of mass conservation across the interface, the normal velocity has to be continuous across this interface:

$$[\underline{v} \cdot \underline{n}]|_{\Gamma_{s/f}} = 0 \tag{6.8}$$

6.1.4 Mixed variational formulation

Consider the momentum conservation Equation (6.1) for the fluid domain and the solid domains. Multiplying this equilibrium by the appropriate trial functions and integrating by part, the integral of the stress vector $\underline{\underline{\sigma}} \cdot \underline{n}$ over the boundary of each domain appears naturally in the weak formulation. The coupled system is then obtained by adding both formulations.

The following functional spaces are first defined for any bounded region $A \subset \mathcal{R}^d$:

$$
\begin{aligned}
Q(A) = \mathcal{L}^2(A) &= \left\{ q : A \mapsto \mathcal{R} \,;\, \int_A q^2 \, dA \, < \, +\infty \right\} \\
V(A) = \mathcal{H}^1(A) &= \left\{ q \, \in \, \mathcal{L}^2(A) \,;\, \nabla q \, \in \, (\mathcal{L}^2(A))^d \right\} \\
V_\Gamma(A) = \mathcal{H}^1_\Gamma(A) &= \left\{ q \, \in \, \mathcal{H}^1(A) \,;\, q_{|\Gamma} = 0 \text{ with } \Gamma \subset \partial\Psi \right\}
\end{aligned}
$$

The mixed variational formulation of Equation (6.1) for an elastic solid consists in finding $(\underline{u}, p)$ in $(V(\Psi_s)^d \times Q(\Psi_s))$ such that:

$$
\int_{\Psi_s} 2\mu \underline{\underline{\epsilon}}(\underline{u}) : \underline{\underline{\epsilon}}(\underline{w}) \, dV - \int_{\Psi_s} \left(1 - \frac{2}{3}\frac{\mu}{K}\right) p \, \mathrm{div}(\underline{w}) \, dV = \underbrace{\int_{\Gamma_{s/f}} (\underline{\underline{\sigma}}^s \cdot \underline{n}^s) \cdot \underline{w} \, dS}_{\text{Stress vector at } \Gamma_{s/f}} \tag{6.9}
$$

$$
\int_{\Psi_s} \mathrm{div}(\underline{u}) q \, dV + \int_{\Psi_s} \frac{p}{K} q \, dV = 0 \tag{6.10}
$$

for any trial functions $\underline{w} \in V(\Psi_s)^d$ and $q \in Q(\Psi_s)$. The unit normal vector $\underline{n}^s$ is pointing outward the solid part.

The mixed variational formulation of Equation (6.1) for an incompressible fluid consists in finding $(\underline{v}, p)$ in $(V(\Psi_f)^d \times Q(\Psi_f))$, with $\underline{v}_{|\Sigma_v} = \underline{v_c}$ such that:

$$
\int_{\Psi_f} 2\eta \underline{\underline{\dot{\epsilon}}}(\underline{v}) : \underline{\underline{\epsilon}}(\underline{w}) \, dV - \int_{\Psi_f} p \, \mathrm{div}(\underline{w}) \, dV = \int_{\Sigma_t} (-p_e \underline{n}^f) \cdot \underline{w} \, dS + \underbrace{\int_{\Gamma_{s/f}} (\underline{\underline{\sigma}}^f \cdot \underline{n}^f) \cdot \underline{w} \, dS}_{\text{Stress vector at } \Gamma_{s/f}} \tag{6.11}
$$

$$
\int_{\Psi_f} \mathrm{div}(\underline{v}) \, q \, dV = 0 \tag{6.12}
$$

for any trial functions $\underline{w} \in V_{\Sigma_v}(\Psi_f)^d$ and $q \in Q(\Psi_f)$. The unit normal vector $\underline{n}^f$ is pointing outward the fluid part.

Equations (6.9) and (6.11) have both an integral surface defined over $\Gamma_{s/f}$. When adding

those two variational formulations, the Laplace's coupling conditions appears naturally as a jump of the stress vector:

$$\begin{aligned}\int_{\Gamma_{s/f}} \left((\underline{\underline{\sigma}}^s \cdot \underline{n}^s) \cdot \underline{w} + (\underline{\underline{\sigma}}^f \cdot \underline{n}^f) \cdot \underline{w} \right) dS &= \int_{\Gamma_{s/f}} \left[(\underline{\underline{\sigma}} \cdot \underline{n}) \right] \cdot \underline{w}\, dS \\ &= \int_{\Gamma_{s/f}} \gamma_{sf} \kappa \underline{n} \cdot \underline{w}\, dS \end{aligned} \tag{6.13}$$

because $\underline{n}^s = -\underline{n}^f$, and with $\underline{n} = \underline{n}^s$ or $\underline{n} = \underline{n}^f$.

Finally by adding the variational formulation of the solid (Equations (6.9) and (6.10)) and the variational formulation of the fluid (Equations (6.11) and (6.12)), the mixed coupled variational formulation consists in finding $(\underline{u}, \underline{v}, p)$ in $(V(\Psi_s)^d \times V(\Psi_f)^d \times Q(\Psi))$, with $\underline{v}_{|\Sigma_v} = \underline{v_c}$ such that:

$$\begin{aligned} \int_{\Psi_s} 2\mu \underline{\underline{\epsilon}}(\underline{u}) : \underline{\underline{\epsilon}}(\underline{w})\, dV + \int_{\Psi_f} 2\eta \dot{\underline{\underline{\epsilon}}}(\underline{v}) : \underline{\underline{\epsilon}}(\underline{w})\, dV - \\ \int_{\Psi_s} \left(1 - \frac{2}{3}\frac{\mu}{K}\right) p \operatorname{div}(\underline{w})\, dV - \int_{\Psi_f} p \operatorname{div}(\underline{w})\, dV = \\ \int_{\Gamma_{s/f}} \gamma_{sf} \kappa \underline{n} \cdot \underline{w}\, dS + \int_{\Sigma_f} (-p_e \underline{n}^f) \cdot \underline{w}\, dS \end{aligned} \tag{6.14}$$

$$\int_{\Psi_s} \operatorname{div}(\underline{u}) q\, dV + \int_{\Psi_s} \frac{p}{K} q\, dV = 0 \tag{6.15}$$

$$\int_{\Psi_f} \operatorname{div}(\underline{v})\, q\, dV = 0 \tag{6.16}$$

for any trial functions $\underline{w} \in V_{\Sigma_v}(\Psi)^d$ and $q \in Q(\Psi)$.

Additionally, velocity $\underline{v}$ can be writen as the derivative of the displacement with respect to time: $\underline{v} = d\underline{u}/dt$, and within a Eulerian context, it is given by:

$$\underline{v} = \frac{d\underline{u}}{dt} = \frac{\partial \underline{u}}{\partial t} + \underline{v} \cdot \underline{\underline{\nabla u}} \tag{6.17}$$

which is a non linear expression as the velocity $\underline{v}$ depends on the velocity itself.

6.2 Numerical strategy

The computational domain Ψ is divided into two different phases Ψ_s and Ψ_f separated by an interface $\Gamma_{s/f}$, as shown in Figure 6.1 (page 91). A Level-Set method [Osher & Fedkiw 2001, Peng *et al.* 1999, Sussman *et al.* 1994] presented in Chapter 4 is used to capture the interface $\Gamma_{s/f}$. In this case the classical level-set function ϕ is computed as follows:

$$\phi(\underline{x}) = \begin{cases} -\text{dist}\left(\underline{x}, \Gamma_{s/f}\right) & \text{if } \underline{x} \in \Psi_s \\ \text{dist}\left(\underline{x}, \Gamma_{s/f}\right) & \text{if } \underline{x} \in \Psi_f \\ 0 & \text{if } \underline{x} \in \Gamma_{s/f} \end{cases}$$

where $\text{dist}\left(\underline{x}, \Gamma_{s/f}\right)$ is the distance from any point $\underline{x}$ to the interface $\Gamma_{s/f}$. In this way, $\Gamma_{s/f}$ is described by the iso-surface $\{\phi(\underline{x}) = 0\}$.

One of the most important steps in the computation of the surface tension term is the estimation of the mean curvature κ [Smolianski 2005, Hysing 2011]. Both normal vector $\underline{n}$ and curvature κ can "easily" be derived from the level-set function:

$$\underline{n} = \frac{\nabla\phi}{\| \nabla\phi \|}, \quad \kappa = \nabla \cdot \underline{n} \tag{6.18}$$

However this procedure, as it has been shown in the previous Chapter 5, leads to a significant loss of accuracy on the curvature computation. To avoid this problem two alternative methods to deal with the curvature are used. The first one is the mixed curvature/curvature-laplacian ($\kappa/\Delta_s\kappa$) method presented for the surface diffusion. In the second method, the curvature is replaced by a tensorial product [Fortin *et al.* 1998, Lafaurie *et al.* 1994]. Those methods will be presented in section 6.2.3.

6.2.1 Time discretization

The constitutive law of the fluid (Equation (6.2)) is a function of both pressure p and velocity $\underline{v}$. Nevertheless the mechanical behavior of the solid (Equation (6.4)) classically depends on displacement $\underline{u}$ and pressure p. The velocity is obviously the derivative of the displacement with respect to time. By neglecting the convection term in Equation (6.17), the velocity can be approached by: $\underline{v} = \partial\underline{u}/\partial t$. In order to be able to link both phases in a single monolithic approach where the only unknowns are $\underline{v}$ and p, Equation (6.4) is written as a function of the velocity $\underline{v}$ by using a Euler scheme:

$$\underline{v} = \frac{\underline{u} - \underline{u}^{t-\Delta t}}{\Delta t} \tag{6.19}$$

where $\underline{u}$ and $\underline{v}$ are the displacement and velocity fields at the current time t, $\underline{u}^{t-\Delta t}$ is the displacement field at time $t - \Delta t$ and Δt is the time step. The displacement $\underline{u}^{t-\Delta t}$ is known at the current time t.

By introducing this time discretization into the variational formulations (6.14), (6.15) and (6.16), one of the unknowns of the problem is eliminated (a similar time discretization has been presented by Papadakis [Papadakis 2008]). Assuming that the displacement $\underline{u}^{t-\Delta t}$ is known at time t, the variational formulation then consists in finding $(\underline{v}, p)$ in $(V(\Psi_f)^d \times Q(\Psi_f))$ such that:

$$\int_\Psi 2\left(H_s(\phi)\mu\Delta t + H_f(\phi)\eta\right) \underline{\underline{\dot{\epsilon}}}(\underline{v}) : \underline{\underline{\dot{\epsilon}}}(\underline{w})\, dV - \int_\Psi \left(H_s(\phi)\left(1 - \frac{2}{3}\frac{\mu}{K}\right) + H_f(\phi)\right) p\, \mathrm{div}(\underline{w})\, dV =$$

$$\underbrace{\int_{\Gamma_{s/f}} \gamma_{sf}\kappa\underline{n} \cdot \underline{w}\, dS}_{\text{Surface tension term}} + \int_{\Sigma_f} (\underline{\underline{\sigma}}^f \cdot \underline{n}^f) \cdot \underline{w}\, dS - \int_\Psi 2H_s(\phi)\mu\underline{\underline{\epsilon}}(\underline{u}^{t-\Delta t}) : \underline{\underline{\epsilon}}(\underline{w})\, dV \tag{6.20}$$

$$\int_\Psi \mathrm{div}(\underline{v}) q\, dV + \int_\Psi H_s(\phi)\frac{p}{K\Delta t} q\, dV = -\int_\Psi \frac{H_s(\phi)}{\Delta t}\mathrm{div}(\underline{u}^{t-\Delta t}) q\, dV \tag{6.21}$$

where H_s and H_f are some Heaviside function defined in Chapter 4 and recalled below.

Note that the time discretization scheme (6.19) is the simplest scheme that can be used. In particular, it involves a minimum of additional terms in mixed variational formulations (6.20) and (6.21). However, this scheme is of the first order in time and is not so accurate. Consequently, when the elastic body is not in a quasi-equilibrium state and deforms under the velocity (or the displacement) solution of the mechanical problem (6.20)-(6.21), a more accurate scheme should be considered, as the Crank-Nicolson scheme used in [Papadakis 2008]. It is important to remind that this mixed formulation for the mechanical problem is developed aiming to integrate the volume diffusion path into the Eulerian numerical strategy presented. Considering this diffusion phenomenon, the evolution of the structure is given by the matter transport rather than the motion induced by the mechanical deformation. For this reason, the Euler's scheme (6.19) can be used without perturbing significantly the simulations.

In order to discretize these equations by a finite element method using one single unstructured mesh, integrals involved in Equations (6.20) and (6.21) are valid on the whole computational domain Ψ. This extension has been performed thanks to the solid and fluid Heaviside functions H_s and H_f introduced in Chapter 4, and here defined again as:

$$H_s(\phi) = \begin{cases} 1 & \text{if } \phi \leq 0 \\ 0 & \text{if } \phi > 0 \end{cases} \tag{6.22}$$

$$H_f(\phi) = 1 - H_s(\phi) \tag{6.23}$$

where ϕ is the level set function.

6.2.2 Stabilized finite element method

The finite element discretization is done by restricting the variational formulation (6.20) and (6.21) to the finite - dimensional space $(V_h^d \times Q_h)$, where $V_h \subset V$ and $Q_h \subset Q$ are the approximation spaces for velocity and pressure, respectively. In the present work, both velocity and pressure are approximated by continuous and piecewise linear functions ($P1/P1$ approximation), ($\underline{v}_h$ and p_h) respectively, defined on a mesh made up of triangular elements when $d = 2$ and tetrahedrons when $d = 3$.

It is well known that the $P1/P1$ approximation for the Stokes problem does not satisfy the Babušca-Brezzi condition, this leads to an unstable formulation [Roberts & Thomas 1987, Arnold *et al.* 1984]. To stabilize the previous $P1/P1$ formulation, two methods have been implemented and compared. The first one is the well-known MINI-element. It can be seen as an enrichment of the velocity field by a bubble function, which for the $P1+/P1$ here is linear per sub-element (see [Arnold *et al.* 1984] for further details). The second method, called Algebraic Subgrid Scale (ASGS) method, can be cast in the variational multiscale framework [Hughes & Sangalli 2007]. This method is detailed in [Badia & Codina 2009] for the Stokes - Darcy coupling problem. The basic idea of such methods is to approximate the effect of the component of the continuous solution which can not be captured by the finite element mesh on the discrete solution [Chiumenti *et al.* 2002]. Let V be the velocity space (omitting Ψ_s, Ψ_f or Ψ and the superscript "d"). V is then approximated by $V_h \oplus \tilde{V}$, where $\tilde{V}$ is an approximation to the complement of V_h in V. Similarly, V_{Σ_v} is approximated by $V_{\Sigma_{vh}} \oplus \tilde{V}_{\Sigma_v}$, where $\tilde{V}_{\Sigma_v}$ is an approximation to the complement of $V_{\Sigma_{vh}}$ in V_{Σ_v}. The space $\tilde{V}_{\Sigma_v}$ is called the velocity space of subscales, which are assumed to be zero on the element boundaries. Thus, $\tilde{V}_{\Sigma_v} = \tilde{V}$. Velocity

and trial functions can then be decomposed as $\underline{v} = \underline{v}_h + \tilde{\underline{v}}$ and $\underline{w} = \underline{w}_h + \tilde{\underline{w}}$.

The variational formulation of the subscale problem associated with Equation (6.20) is obtained by considering trial functions that belong to $\tilde{V}$, it writes:

$$\sum_K \left(< a_1 \underline{\underline{\dot{\epsilon}}}(\underline{v}_h), \underline{\underline{\dot{\epsilon}}}(\tilde{\underline{w}}) >_K + < a_1 \underline{\underline{\dot{\epsilon}}}(\tilde{\underline{v}}), \underline{\underline{\dot{\epsilon}}}(\tilde{\underline{w}}) >_K - < a_2 p_h, \mathrm{div}(\tilde{\underline{w}}) >_K \right) = L(\tilde{\underline{w}}) \tag{6.24}$$

where $< ., . >_K$ denotes the inner product of $L^2(K)$, $\sum_K$ stands for the summation over all the mesh elements K, $a_1 = 2(H_s \mu \Delta t + H_f \eta)$, $a_2 = H_s(1 - 2\mu/3K) + H_f$ and $L(\tilde{\underline{w}})$ is the right hand side term in Equation (6.20). Because $\underline{v}_h$ and $\underline{u}_h$ are piecewise linear and $\tilde{\underline{w}}$ vanishes on the element boundaries, the first term and the right-hand side term of the previous subscale problem equate zero. Consequently, by integrating the subscale problem by parts, Equation 6.24 reduces to:

$$\sum_K < \mathrm{div}(a_1 \underline{\underline{\dot{\epsilon}}}(\tilde{\underline{v}})), \tilde{\underline{w}} >_K = \sum_K < a_2 \underline{\nabla p_h}, \tilde{\underline{w}} >_K$$

This relation can be rewritten with the projection operator $\underline{\underline{\tilde{\mathcal{P}}_K}}$ onto the subscale space, and restricted to an element K:

$$\underline{\underline{\tilde{\mathcal{P}}_K}} \cdot (\mathrm{div}(a_1 \underline{\underline{\dot{\epsilon}}}(\tilde{\underline{v}})) = \underline{\underline{\tilde{\mathcal{P}}_K}} \cdot (a_2 \underline{\nabla p_h})$$

It can be infered that for smooth physical properties variations a_1 and a_2 will little vary. Therefore the differential operator $\frac{a_1}{a_2}\mathrm{div}(.)$ can be expressed, it is approximated by an algebraic operator $\tau_K^{-1} \underline{\underline{\mathcal{I}}}$, to finally obtain

$$\tilde{\underline{v}} = \tau_K \underline{\underline{\tilde{\mathcal{P}}_K}} \cdot \underline{\nabla p_h} \tag{6.25}$$

and therefore the problem is to approximate the projection operator $\underline{\underline{\tilde{\mathcal{P}}_K}}$. As explained in [Cervera *et al.* 2010], the simplest choice is to take $\underline{\underline{\tilde{\mathcal{P}}_K}}$ as the identity when applied to the pressure gradient, which is equivalent to the finite element residual. Finally, this stabilization term, $\tau_K \underline{\nabla p_h}$, does not appear in the finite element scale Equation (6.20) (which corresponds to $\underline{w} = \underline{w}_h$), since the products between the first derivatives of $\tilde{\underline{v}}$ and $\underline{w}_h$ are equal to zero.

In Equation (6.21), the subscale velocity appears through the divergence term:

$$\int_\Psi \mathrm{div}(\underline{v}_h + \underline{\tilde{v}})\, q\, dV = \int_\Psi \mathrm{div}(\underline{v}_h)\, q\, dV - \sum_K \int_K \tau_K \underline{\tilde{v}} \cdot \underline{\nabla q}\, dV$$

Consequently, the ASGS methods consists in adding the stabilization term

$$\sum_K \int_K \tau_K \underline{\nabla p_h} \cdot \underline{\nabla q_h}\, dV \tag{6.26}$$

to the mass conservation equation (6.21). In the present case (Stokes and elasticity equations), the derived term acts as a pressure diffusion term. Such stabilization term has also been derived from the bubble stabilization in [Puaux *et al.* 2010] and is used in [Ausas *et al.* 2010].

Finally, the stabilization parameter τ_K can be approximated through an adequate Fourier analysis of the initial problem (in a one-dimensional form, and by considering that the Fourier transform of $\mathrm{div}(\underline{\tilde{v}})$ is dominated by wave numbers of order $1/h_K$, where h_K is the size of element K). Using the same procedure as in [Badia & Codina 2010], τ_K can be related to h_K and to the material properties: $\tau_K = h_K^2/(2H_s\mu\Delta t + 2H_f\eta)$. In the simulations, continuous expressions of H_f and H_s are replaced by smoothed Heaviside functions [2] of the solid and the fluid [Gerlach *et al.* 2006]:

$$\hat{H}_s(\phi_h) = \begin{cases} 1 & \text{if } \phi_h < -E \\ \frac{1}{2E}\left(E - \phi_h - \frac{E}{\pi}\sin\frac{\pi\phi_h}{E}\right) & \text{if } -E \le \phi_h \le E \\ 0 & \text{if } \phi_h > E \end{cases} \tag{6.27}$$

$$\hat{H}_f(\phi_h) = 1 - \hat{H}_s(\phi_h) \tag{6.28}$$

where ϕ_h is the discrete piecewise linear level-set function, and E is the width of the transition zone where the mechanical behavior is a mixture of the mechanical behavior of both phases, solid and fluid.

6.2.3 Discretization and computation of the surface tension integral

The Laplace's law (6.7), that expresses the fluid - solid coupling, appears in Equation (6.20) as an integral over the interface $\Gamma_{s/f}$. However, the implementation of this surface integral is not straightforward within a Eulerian context. Indeed, surface $\Gamma_{s/f}$ is not known explicitly (it is not a set of mesh element faces), but it is defined by the zero level set of the function ϕ_h, which

2. As presented in Chapter 4.

passes through the mesh elements. To overcome this situation, two strategies are proposed here: the Continuum Surface Force (CSF) method and the surface local reconstruction (SLR) method (Section 6.2.3.1). Additionally, two methods for the computation of the curvature are discussed (Section 6.2.3.2).

6.2.3.1 Surface integration methods

Two different methods for the numerical computation of a surface integral within a Eulerian framework are presented. In particular, the surface integration approaches are used to compute the surface tension term appearing in Equation (6.20). The first method is the Continuum Surface Force (CSF) and the second one is the Surface Local Reconstruction (SLR) method.

Continuum Surface Force (CSF) method:

The surface tension term in Equation (6.20) has been widely studied [Brackbill *et al.* 1992, Lafaurie *et al.* 1994, Williams *et al.* 1998, Renardy & Renardy 2002, Smolianski 2005, Aulisa *et al.* 2007, Gerlach *et al.* 2006, Hysing 2006, Groß & Reusken 2007, Bordère *et al.* 2010, Hysing 2011]. Most of those works uses the CSF method, where the surface integral is approximated by a volume integral. The transformation from the surface integral to the volume integral is achieved by multiplying the original function by a *Dirac* function $\delta(\phi)$:

$$\int_{\Gamma_{s/f}} \gamma_{sf}\kappa\underline{n}\cdot\underline{w}dS = \int_{\Psi} \gamma_{sf}\kappa\underline{n}\cdot\underline{w}\delta(\phi)\,dV \tag{6.29}$$

The Dirac function $\delta(\phi)$ is computed by differentiating a smooth characteristic function [3] $\hat{c}(\underline{x})$ that allows to identify the phase which the point $\underline{x}$ belongs to:

$$c(\underline{x}) = \begin{cases} c_1 & \text{if } \underline{x} \in \Psi_s \\ c_2 & \text{if } \underline{x} \in \Psi_f \\ \frac{c_1+c_2}{2} & \text{if } \underline{x} \in \Gamma_{s/f} \end{cases}$$

$$\hat{c}(\underline{x}) = \mathbf{K} * c(\underline{x}) = \int_{\Xi_K} c(\underline{x}')\mathbf{K}(\underline{x}'-\underline{x})d\underline{x}' \tag{6.30}$$

where Ξ_K is the compact support of the kernel $\mathbf{K}$ (see [Williams *et al.* 1998] for further details). The performance of this kind of methods highly depends on the choice of the kernel $\mathbf{K}$ and its

3. An example of a characteristic function is the Heaviside function approximation presented in Equation (6.27).

support Ξ_K. The numerical computation of this function requires many integration points in order to guarantee the accuracy of the computation of Equation (6.29).

The characteristic function used in the CSF version considered in the present work is given by Equation (6.28). The Dirac function in Equation (6.29) can be found by differentiating $\hat{H}_f(\phi_h)$:

$$\begin{aligned}
\delta(\phi_h) &= \frac{\partial \hat{H}^f(\phi_h)}{\partial \phi_h} \\
&= \frac{\partial}{\partial \phi_h} \underbrace{\left(\frac{1}{2E} \left(E + \phi_h + \frac{E}{\pi} \sin \frac{\pi \phi_h}{E} \right) \right)}_{\text{Characteristic function}} \\
&= \frac{1}{2E} \left(1 + \cos \left(\frac{\pi \phi_h}{E} \right) \right)
\end{aligned} \tag{6.31}$$

The corresponding support is given by the region $\Xi_K : -E \leq \phi_h \leq E$. One of the disadvantages of this method is that the kernel $\mathbf{K}$ depends on a numerical parameter, here the width of the transition zone E, which has to be chosen with respect to the mesh size [Williams *et al.* 1998]. The performance of the method highly depends on this choice.

Surface Local Reconstruction (SLR) method:

An alternative method to integrate the surface tension term in Equation (6.20) is proposed: here, the interface $\Gamma_{s/f}$ is given by the zero isosurface of the level-set function, $\{\phi = 0\}$, since it allows to locally reconstruct the interface, then the surface tension term can then be explicitly computed over this reconstructed surface.

This method consists, for each element cut by the interface, in approximating linearly this surface by a segment in 2D or a plane in 3D. This approximation is possible thanks to the metric properties of the level-set function. Once the interface has been locally reconstructed, the contribution of the element to the surface integral can be explicitly computed by Gaussian integration [4]: the integration points used to compute the integral are placed over this surface. It has to be pointed out that this approach is local to each element, and can be implemented in the assembly loop of a finite element code. In particular, the whole surface is never reconstructed. The first advantage of this method is that it does not require to choose any numerical parameter contrary to the CSF method. Furthermore, the accuracy of the numerical results are shown to be slightly improved using this technique, as described in Section 6.3.

4. An analytical integration can also be carried out.

From a practical point of view, the linear approximation of the surface is given by the plane (or the segment in 2D) where the level-set function vanishes. The points where the level-set function is equal to zero are referred to as vertices in the following. In an element crossed by the interface, the vertices define the plane or the segment approximating this interface. These vertices can then be placed over the edges of the element, when the level-set function ϕ is positive in one node of this edge and negative in the other one; in special cases, they correspond to a node of the element (when $\phi = 0$ on that node). The different possibilities of intersections between the interface and an element are given in Figure 6.2 for the 2D case, and in Figure 6.3 for the 3D case. In the general case, the coordinates of the vertex are function of the coordinates of the two nodes forming the edge as well as the value of the level-let function on these nodes. The coordinates of the vertex $\underline{x}_{vertex}$ placed on the edge formed by the nodes m and n are given by:

$$\underline{x}_{vertex} = \underline{x}_m + (\underline{x}_n - \underline{x}_m)\frac{\parallel \phi(\underline{x}_m) \parallel}{\parallel \phi(\underline{x}_m) \parallel + \parallel \phi(\underline{x}_n) \parallel} \tag{6.32}$$

where $\underline{x}_m$ and $\underline{x}_n$ are, respectively, the coordinates of nodes m and n, and $\phi(\underline{x}_m)$ and $\phi(\underline{x}_n)$ are the values of the Level-Set function at these nodes, which should have opposite signs.

Note that in 3D cases, the intersection of the interface with an element can be a quadrilateral (Figure 6.3g) if the level-set function is positive in two nodes and negative in the two other nodes. In this case, the quadrilateral is divided into two triangles, and the contribution of the element to the surface integral is the sum of the contribution of both triangles. Furthermore, special attention has to be paid to particular cases described in Figures 6.2 and 6.3. First, in the cases presented in Figures 6.2a and 6.3a-b, the element is not intersected by the interface, and its contribution to the surface integral is therefore zero. Next, Figures 6.2b and 6.3c show configurations where the interface can be shared by two neighboring elements. The contribution of each of these elements to the surface integral has consequently to be divided by two. Finally, in Figures 6.2c and 6.3d-e, the level-set function is equal to zero in at least one node of the element. In this case, the integration is carried out as for a regular element cut by the interface.

6.2.3.2 Curvature computation strategies

As indicated previously, the performance of the present method highly depends on the accuracy of the computation of the curvature κ. The first method has been introduced in the previous Chapter 5 within the context of sintering by surface diffusion. One of the unknowns of the the mixed formulation curvature-surface laplacian of the curvature ($\kappa/\Delta_s\kappa$) presented

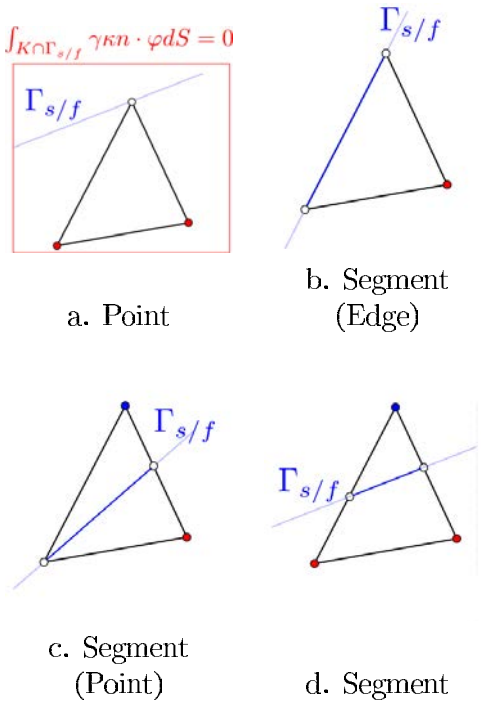

Figure 6.2: Intersection between the interface $\Gamma_{s/f}$ and an element in 2D.

in Section 5.2.2 is the curvature κ, then this method can also be used here. Indeed, since the simulation of sintering by multiple diffusion mechanisms constitutes the aim of this work, the curvature obtained from the surface diffusion step, can be introduced into the mechanical solver to obtain the pressure field needed for the volume diffusion. This explicit curvature computation is referred to as "Direct" method.

An alternative method can be adopted to avoid the explicit computation of the curvature. Let $\underline{w}$ be a vector in $\mathcal{R}^d$. The surface gradient of $\underline{w}$ with respect to $\Gamma_{s/f}$ is defined as the tangential part of the gradient of $\underline{w}$: $\underline{\underline{\nabla_s w}} = \underline{\underline{\nabla w}} - \left(\underline{\underline{\nabla w}}\cdot\underline{n}\right)\otimes\underline{n} = \left(\underline{\underline{\mathcal{I}}} - \underline{n}\otimes\underline{n}\right)\cdot\underline{\underline{\nabla w}}$, where $\underline{n}$ is the outward normal to $\Gamma_{s/f}$. The surface divergence of $\underline{w}$ is defined as the trace of the surface gradient operator:

$$\nabla_s\cdot\underline{w} = \nabla\cdot\underline{w} - \left(\underline{\underline{\nabla w}}\cdot\underline{n}\right)\cdot\underline{n} = \left(\underline{\underline{\mathcal{I}}} - \underline{n}\otimes\underline{n}\right) : \underline{\underline{\nabla w}} \tag{6.33}$$

Furthermore, since $\underline{\underline{\mathcal{I}}} - \underline{n}\otimes\underline{n}$ is the operator of projection onto the tangent space of $\Gamma_{s/f}$, the vector $(\underline{\underline{\mathcal{I}}} - \underline{n}\otimes\underline{n})\cdot\underline{w}$ is tangent to $\Gamma_{s/f}$. Consequently, and because $\Gamma_{s/f}$ is a closed surface, the following relation holds [Fortin *et al.* 1998]:

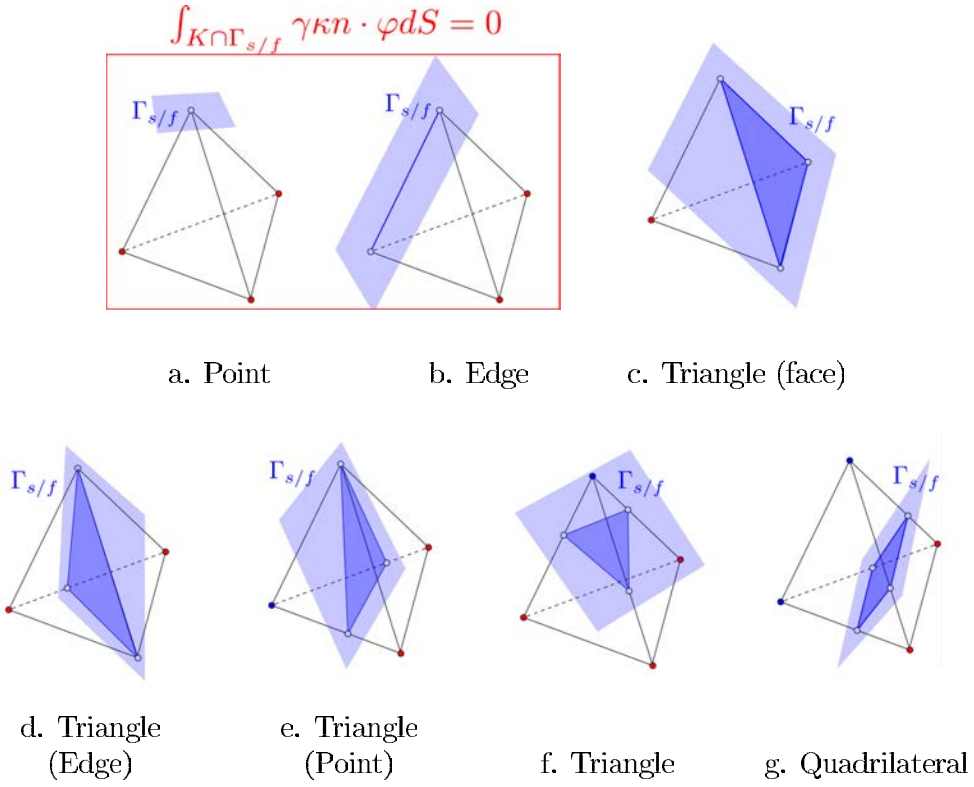

a. Point b. Edge c. Triangle (face)

d. Triangle (Edge) e. Triangle (Point) f. Triangle g. Quadrilateral

Figure 6.3: Intersection between the interface $\Gamma_{s/f}$ and an element in 3D.

$$\int_{\Gamma_{s/f}} \gamma_{sf} \underline{\nabla_s} \cdot \left[(\underline{\underline{\mathcal{I}}} - \underline{n} \otimes \underline{n}) \cdot \underline{w} \right] dS = 0 \tag{6.34}$$

where γ_{sf} is assumed to be a constant.

By using the definition of the surface divergence (Equation (6.33)), the above relationship (Equation (6.34)) writes:

$$\int_{\Gamma_{s/f}} \gamma_{sf} \left[\underline{\underline{\mathcal{I}}} - \underline{n} \otimes \underline{n} \right] : \underline{\underline{\nabla w}} dS = \int_{\Gamma_{s/f}} \gamma_{sf} \left(\underline{\underline{\mathcal{I}}} - \underline{n} \otimes \underline{n} \right) : \underline{\nabla} (\underline{n} \otimes \underline{n} \cdot \underline{w}) dS$$

Finally, it can be shown that the right hand term in the previous equation is equal to the

surface tension term that is to be computed in Equation (6.20):

$$\begin{aligned}
\int_{\Gamma_{s/f}} \gamma_{sf} \left(\underline{\underline{\mathcal{I}}} - \underline{n} \otimes \underline{n}\right) : \underline{\nabla}(\underline{n} \otimes \underline{n} \cdot \underline{w}) dS &= \int_{\Gamma_{s/f}} \gamma_{sf} \left(\underline{\underline{\mathcal{I}}} - \underline{n} \otimes \underline{n}\right) : \left[\underline{\underline{\nabla n}} \left(\underline{n} \cdot \underline{w}\right) + \underline{n} \otimes \left(\underline{\underline{\nabla n}} \cdot \underline{w}\right)\right. \\
&\quad \left. + \underline{n} \otimes \left(\underline{\underline{\nabla w}} \cdot \underline{n}\right)\right] dS \\
&= \int_{\Gamma_{s/f}} \gamma_{sf} \left(\underline{\nabla} \cdot \underline{n} \left(\underline{n} \cdot \underline{w}\right) + \underline{n} \cdot \left(\underline{\underline{\nabla n}} \cdot \underline{w}\right) + \underline{n} \cdot \left(\underline{\underline{\nabla w}} \cdot \underline{n}\right)\right. \\
&\quad \left. - (\underline{n} \otimes \underline{n}) : \underline{\underline{\nabla n}} \left(\underline{n} \cdot \underline{w}\right) - \underline{n} \cdot \left(\underline{\underline{\nabla n}} \cdot \underline{w}\right) - \underline{n} \cdot \left(\underline{\underline{\nabla w}} \cdot \underline{n}\right)\right) dS \\
&= \int_{\Gamma_{s/f}} \gamma_{sf} \left(\underline{\nabla} \cdot \underline{n} - \left(\underline{n} \otimes \underline{n} : \underline{\underline{\nabla n}}\right)\right) \underline{n} \cdot \underline{w} dS \\
&= \int_{\Gamma_{s/f}} \gamma_{sf} \underline{\nabla_s} \cdot \underline{n} \left(\underline{n} \cdot \underline{w}\right) dS
\end{aligned}$$

The mean curvature can be defined as the divergence of the outward unit normal along the surface because $\underline{\nabla} \cdot \underline{n} = \underline{\nabla}_s \cdot \underline{n}$. Therefore the last expression in the previous equation is equal to the surface tension term in Equation (6.20).

$$\int_{\Gamma_{s/f}} \gamma_{sf} \left[\underline{\underline{\mathcal{I}}} - \underline{n} \otimes \underline{n}\right] : \underline{\underline{\nabla w}} dS = \int_{\Gamma_{s/f}} \gamma_{sf} \kappa \underline{n} \cdot \underline{w} dS \tag{6.35}$$

By substituting the surface tension term of Equation (6.20) by the left hand side term of Equation (6.35), the explicit computation of curvature κ can be avoided. This approach was inspired by [Fortin *et al.* 1998], and also discussed in [Lafaurie *et al.* 1994].

6.3 Results and Discussion

Again, all the simulations presented in the forthcoming section have been performed by using the finite element library *CimLib*, a fully parallel C++ scientific code, mainly developed at the CEMEF, MinesParisTech [Digonnet *et al.* 2007].

6.3.1 Parasitic Current (two-phase incompressible flow)

As a first validation of the approach, a benchmark case is considered that has been widely studied to check the accuracy of the different methods introduced so far. The test consists in computing the mechanical equilibrium of an incompressible fluid bubble placed inside another incompressible fluid, with the stress vector set to $-p_{out}\underline{n}$ over the boundary of the computational domain. The analytical solution of this problem is a zero velocity field and a pressure field p equal to p_{out} outside the bubble and jumping to $p_{in} = p_{out} + \gamma_{sf}\kappa$ inside the bubble.

It has to be highlighted that the formulation of the mechanical problem (Equations (6.20) and (6.21)) holds for a problem where the phase 1 (Ψ_s) presents a linear elastic behavior. Hence, in order to perform this two-fluid test case, the formulation has to be slightly modified. Both phases will be assumed to respond as Newtonian fluids presented in Equations (6.2) and (6.3). Even if the analytical solution of this problem is a zero velocity field, some nonphysical *parasitic currents* are generated as a result of the numerical simulation [Brackbill *et al.* 1992, Lafaurie *et al.* 1994, Williams *et al.* 1998, Renardy & Renardy 2002, Smolianski 2005, Aulisa *et al.* 2007, Gerlach *et al.* 2006, Hysing 2006, Groß & Reusken 2007, Bordère *et al.* 2010, Hysing 2011]. These parasitic currents are used to assert the convergence and the performance of the different approaches presented below to calculate the surface tension integral.

The dependence of the maximum velocity $\underline{v}_{max}$ to the surface tension / viscosity ratio (γ_{sf}/η) is first investigated. Table 6.1 shows the value of $C = \underline{v}_{max}/(\frac{\gamma_{sf}}{\eta})$ obtained for a wide range of values of γ_{sf}/η, from 10 to 10^5. C is found to be constant. This result confirms the proposition in [Lafaurie *et al.* 1994] and [Smolianski 2005]: $\underline{v}_{max}$ depends linearly on γ_{sf}/η.

γ_{sf}/η		10^1	10^2	10^3	10^4	10^5
C	[Smolianski 2005]	$9.1 \cdot 10^{-3}$	$9.0 \cdot 10^{-3}$	$8.8 \cdot 10^{-3}$	$9.1 \cdot 10^{-3}$	$9.4 \cdot 10^{-3}$
	Pino Muñoz et al.	$3.7 \cdot 10^{-3}$	$3.7 \cdot 10^{-3}$	$3.7 \cdot 10^{-3}$	$3.7 \cdot 10^{-3}$	$3.7 \cdot 10^{-3}$

Table 6.1: Values of $C = v_{max}\eta/\gamma_{sf}$ two-fluid simulation.

Figure 6.4 shows how the parasitic currents are mainly concentrated around the interface $\Gamma_{s/f}$. The simulations have been performed over a structured mesh with an element size of 1/64 (Figure 6.4 left), using the direct computation of the curvature [5]. Complementary tests showed that the maximum velocity $\underline{v}_{max}$ does not depend on the element size, and consequently, the results quality depends mostly on the method used for prescribing the surface tension. Additionally, those tests showed that the result did neither change when the surface integral was computed using CSF or SLR.

Next, the dependence of the finite element error on the bubble mean pressure is evaluated versus the mesh size. The simulation is performed in a structured 2D mesh of N nodes over a square domain of side length 1m. The parameters of the simulation are a bubble radius of $R = 0.2\,\text{m}$, a surface tension coefficient $\gamma_{sf} = 0.9\,N/m$ and a viscosity of $\eta = 1000\,\text{Pa}\cdot\text{s}$. The pressure at the outer boundary is set to zero ($p_{out} = 0$). Therefore the theoretical value of the pressure inside the bubble is $p_{in}^{th} = 4.5\,\text{Pa}$. Figure 6.5 shows the relative error on the mean pressure inside the bubble $((p_{in}^{th} - p_{in})/p_{in}^{th})$ as a function of the square root of the number of nodes $N^{1/2}$. Four of these curves have been extracted from [Bordère *et al.* 2010]: results

5. Section 6.2.3.2 from the previous Chapter 5 where the mixed formulation $\kappa/\Delta_s\kappa$ was introduced.

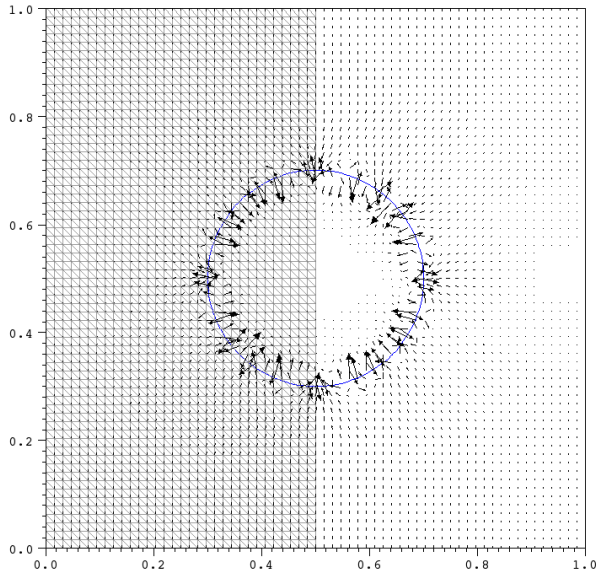

Figure 6.4: Parasitic currents in a static bubble simulation over a square computational domain of side 1 and element size $h = 1/64$ (left with mesh, right velocity only).

named "CSF" are computed by Brackbill et al. using the *Continuum Surface Force* Method [Brackbill *et al.* 1992] within a Eulerian VOF framework; Results named "HAREM" correspond to an augmented Lagrangian method combined with a VOF approach [Vincent *et al.* 2004]; the "Front Tracking" results correspond to a Level Set Finite Differences Method [Shin & Juric 2002]; and the "Monte Carlo" approach is based on energy potential including interface and volume energies [Bordère *et al.* 2010].

The fifth curve in Figure 6.5, referred to as "Pino et al." corresponds to the simulation carried out by using the direct computation of the curvature ($\kappa/\Delta_s\kappa$ - Section 6.2.3.2), and the SLR method (Section 6.2.3.1) for surface tension integral evaluation. For comparison, the sixth curve, referred to as "Pino et al. Dirac" is obtained in the same condition of curvature computation, but using an approximation of the Dirac delta function to compute the surface integral similarly to the "CSF" method (Section 6.2.3.1). Both simulations show a similar trend, with a first order spatial convergence, and can be compared with relevancy to the recent results obtained by Bordère et al. (2010) [Bordère *et al.* 2010], referred to as "Monte Carlo" in Figure 6.5. The mesh adaptation strategy presented in Chapter 4 (Section 4.4.4) has been used to perform the same simulation presented previously and the corresponding relative error on the mean pressure is also plotted in Figure 6.5 (referred to as "Pino et al. Adapt"). This mesh adaptation leads to a non uniform element size distribution which has an element size smaller close to the interface and a bigger one away from $\Gamma_{s/f}$. Compared with an structured

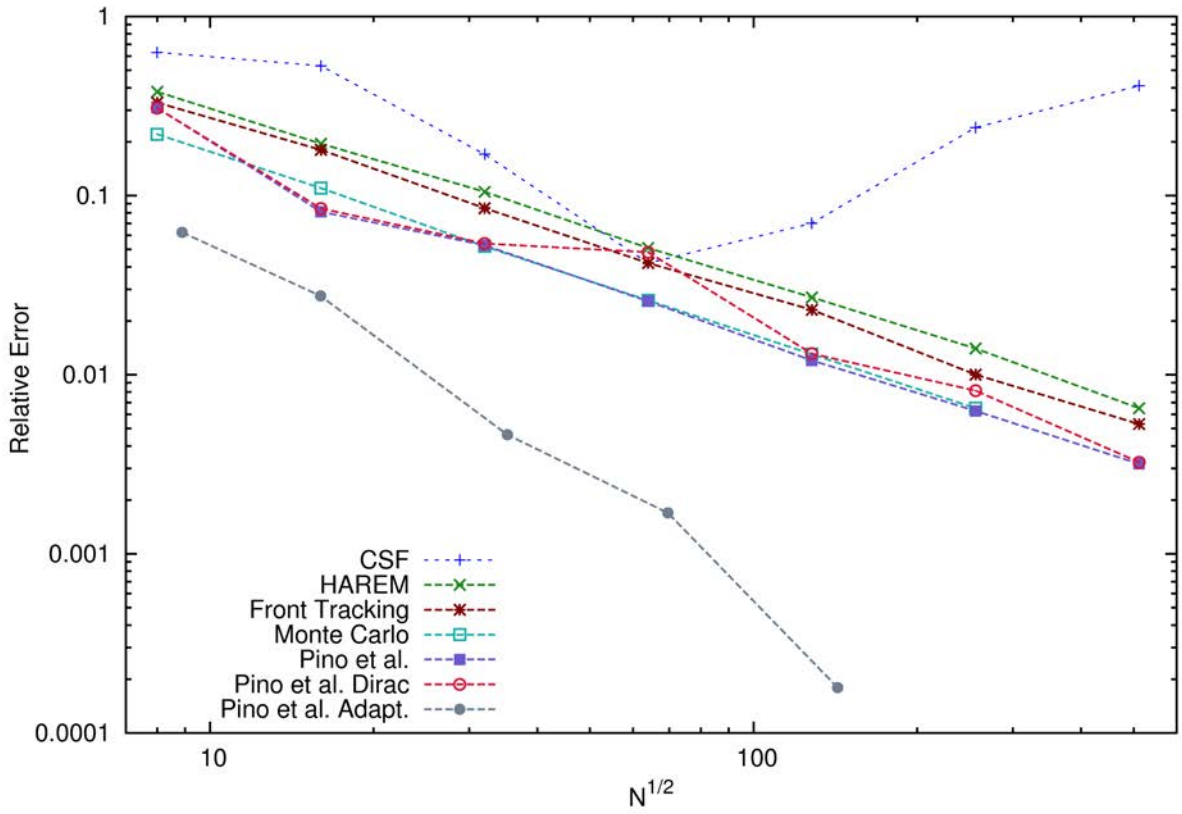

Figure 6.5: Relative error on the mean pressure computed inside the bubble.

mesh with the same number of nodes, the adaptated mesh has an element size that could be up to 20 times smaller that the structured one.

Finally a comparison between the two stabilized finite element methods used to solve the mechanical problem, that is $P1+/P1$ and ASGS, is reported in Table 6.2. For this comparison the same incompressible bubble inclusion simulation as described previously has been considered, using a structured mesh with an element size of 1/256. The curvature is computed in three different manners: in the first one ("Analytical") the curvature is replaced by its exact value $\kappa = 1/R$, the second method ("Direct") is the mixed solver $\kappa/\Delta_s\kappa$ described in Section 5.2.2, and the third way ("Tensorial") corresponds to the tensorial expression given in Section 6.2.3.2.

For this test case the best results are found by using a $P1+/P1$ stabilization whatever the curvature assessment procedure. Furthermore, it is an interesting fact to verify, like in [Fortin *et al.* 1998], that the result obtained by computing the curvature with the direct method allows us to get a result as accurate as in the case where the curvature is replaced by its

Stabilization \ Curvature	Analytical	Direct	Tensorial
ASGS	$1.72 \cdot 10^{-2}$	$1.72 \cdot 10^{-2}$	$1.73 \cdot 10^{-2}$
$P1+/P1$	$6.20 \cdot 10^{-3}$	$6.29 \cdot 10^{-3}$	$8.65 \cdot 10^{-3}$

Table 6.2: Relative error on the mean pressure as a function of the stabilized finite element and curvature computation methods.

exact analytical value. It is also important to highlight that the ASGS stabilization does not present any relevant dependence to the curvature computation method. However, it has to be underlined that $P1+/P1$ stabilization appears slightly better, for this case, than the ASGS method when the error is estimated with the mean pressure. If the error is now based on the maximum pressure value (*i.e.* L^∞-norm), the conclusions are different as shown in next section.

6.3.2 Fluid - elastic solid interaction

The mechanical monolithical formulation presented in Equations (6.20) and (6.21) will be used from now on to simulate the interaction between an incompressible fluid and a linear elastic solid with surface tension. This kind of interaction presents some new challenges such as coping with the high ratio between the mechanical properties of the two phases and the compressible nature of elastic solids.

6.3.2.1 Spherical elastic inclusion

This section focuses on the case of an elastic cylindrical 2D inclusion embedded into a Newtonian fluid matrix. Like in the previous section, the stress vector is set to $-p_{out}\underline{n}$ over the boundary of the computational domain. The mechanical properties of both phases, solid and fluid, are presented in table 6.3. This problem is solved under the plane strain hypothesis. The pressure inside the elastic inclusion depends on the curvature κ and surface tension coefficient γ_{sf}, but is also a function of the mechanical properties of the solid. The analytical solution of this problem is:

$$p_{in} = p_{out} + \frac{3K}{3K+\mu}\gamma_{sf}\kappa = p_{out} + \frac{2}{3}\gamma_{sf}\kappa\,(1+\nu) \tag{6.36}$$

where p_{in} is the pressure in the solid (Ψ_s), p_{out} is the pressure in the fluid (Ψ_f), and ν is the Poisson's ratio. In this case p_{out} is set to zero, and therefore the pressure inside the solid should be $p_{in} = 3.75\,\text{MPa}$ considering the mechanical properties in Table 6.3.

Elastic solid	
Properties	Value
μ	156 GPa
K	260 GPa
ν	0.25
γ_{sf}	0.9 J/m^2

Incompressible fluid	
Properties	Value
η	1 Pa·s

Table 6.3: Material properties of the solid and the fluid

Within the Eulerian approach used in this work, the surface tension at $\Gamma_{s/f}$ introduces a discontinuity of the normal stress, and therefore, a discontinuity of the pressure. However, the presented simulations have been carried out by approximating the pressure with a continuous piecewise linear function. With this continuous approximation, the pressure discontinuity and the material property discontinuity at the fluid - solid interface, generate some pressure oscillations that do not represent finely the physical nature of the problem. Nevertheless, continuous approximations remain popular and easy-to-implement methods to deal with two-phase problem [Brackbill *et al.* 1992, Lafaurie *et al.* 1994, Renardy & Renardy 2002, Smolianski 2005, Hysing 2006, Groß & Reusken 2007, Bordère *et al.* 2010, Hysing 2011], although other techniques as the Extended Finite Element Method, the Discontinuous Galerkin method, or a recent modified continuous Galerkin method [Ausas *et al.* 2010] exist and can be used.

Figure 6.6 shows the relative L^2-error on the pressure, as a function of the square root of the number of nodes. The surface integral has been evaluated by using the SLR method which was proved to yield the best results. The curvature can be computed into three different ways: the first one corresponds to its analytical value (solid line) and the two other ones are the direct formulation ($\kappa/\Delta_s\kappa$) (dotted line) and the tensorial method (dashed line) presented in Section 6.2.3.2. Both stabilization methods studied in this work are also plotted: the $P1+/P1$ stabilization (filled circles) and the ASGS method (filled triangles). It is important to note that the six first curves are obtained with structured meshes, and the last one (referred to as "Tensorial Curvature, ASGS Adapted") is obtained from an adapted unstructured mesh (Section 4.4.4).

It can clearly be seen that the surface tension term is not accurately computed by the tensorial method for structured meshes with less than 160^2 nodes (green curves). However, when the mesh size is small enough, the tensorial method leads to results with a relative error lower than 2%, which is of same order as the error obtained with the analytical value of the curvature, or obtained with the direct computation of the curvature. The stabilization method also has an effect on the relative error: with the structured meshes, the $P1+/P1$ stabilization seems to lead to slightly better result than the ASGS method. However, even

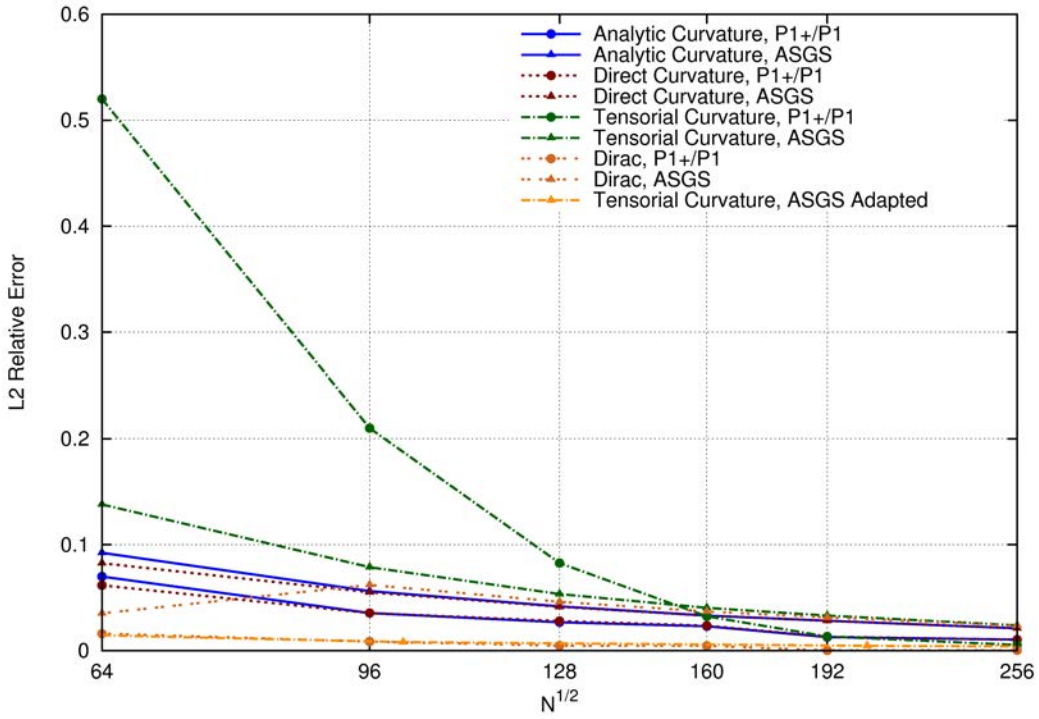

Figure 6.6: L^2-relative error on the pressure computed inside the elastic inclusion.

if the relative L^2-error on the pressure is better when using the $P1+/P1$ stabilization, the nonphysical oscillations of the pressure (L^∞-error) are significantly amplified when using the $P1+/P1$ stabilization, as it can be seen in Figure 6.7. Accordingly, the pressure analytical solution should be zero in the fluid, but as a result of the non physical oscillation of the pressure close to the interface this pressure is lower than zero and larger for the $P1+/P1$ case. However this oscillation is reduced by using the ASGS stabilization method. Since we seek the smoothest pressure distribution, especially for physical phenomena driven by pressure gradients, the following simulations are performed by using the ASGS method. The impact of the curvature computation method is discussed in the next section.

6.3.2.2 Two spherical particles with neck.

The case described in Figure 6.8 is now considered: two spherical elastic particles of radii R_1 and R_2, are connected by a neck of radius r as presented in Chapter 4 (Section 5.1). The analytical value of the curvature is known all over the surface: over the neck it is equal to $1/r$, over the surface of each particle it is equal to $1/R_1$ and $1/R_2$, respectively, and at the

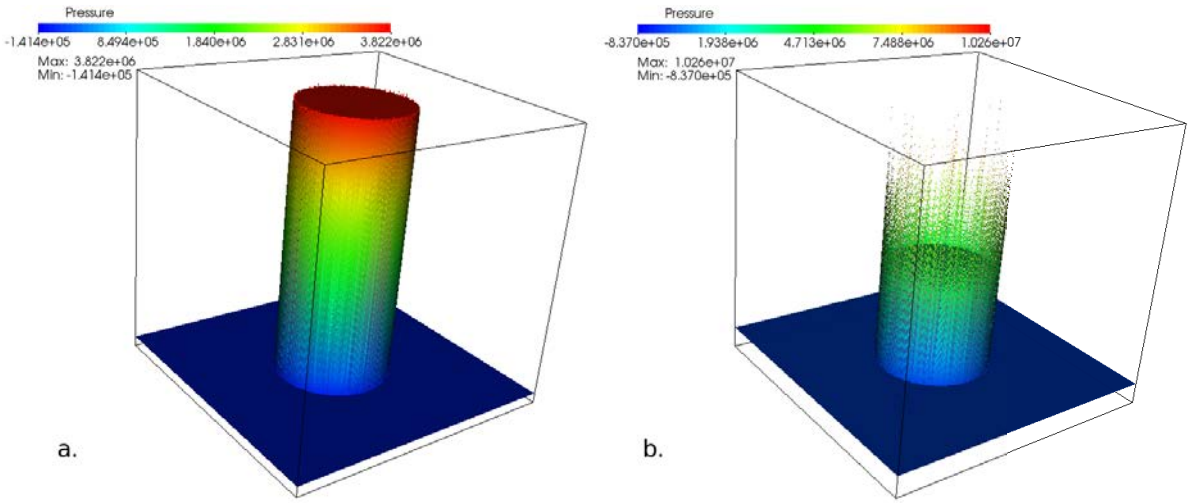

Figure 6.7: Oscillations of the pressure at the fluid - solid interface, using a. ASGS method and b. $P1+/P1$ stabilization.

inflection points (see Figure 6.8) the curvature is zero. A 2D simulation is carried out (plane strain assumption), for which the computational domain is the unit square, and the particles radii are $R_1 = 0.2\mu$m and $R_2 = 0.2\mu$m. The material properties of both fluid and solid phases are those given in Table 6.3.

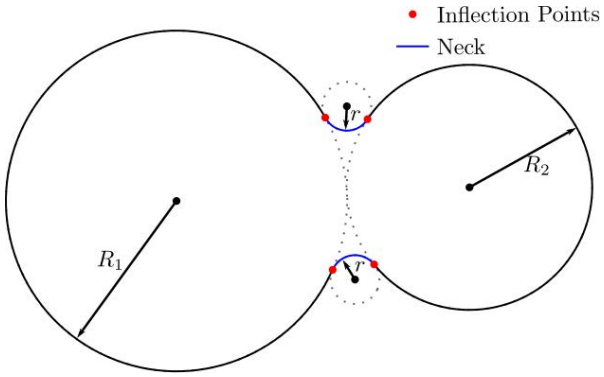

Figure 6.8: Inflection points (2D).

The results obtained with the approach presented in this work are compared with those obtained by performing the same simulation using *Abaqus 6.10* ®. Contrary to *CimLib*, the framework adopted in *Abaqus*® for the elastic analysis is a Lagrangian one. Consequently, the following comparison methodology has been used. First, the mesh of the computational domain is created using the *Gmsh* free mesher (see [Geuzaine & Remacle. 2009]), in such a way the fluid - solid interface is exactly represented by a set of interior element edges, as

shown in Figure 6.9. A Eulerian computation is then carried out with *CimLib*, using this mesh made up of ASGS-stabilized triangles, the SLR algorithm, and three methods for calculating the curvature: the analytical one, the "direct" one, and the "tensorial" one. A Lagrangian simulation is subsequently achieved with *Abaqus*®, using the particle's mesh, extracted from the previous fluid - solid mesh. Furthermore, the curvature is computed in two different ways to study the impact of slight curvature variations onto the mechanical equilibrium. The first method uses the analytical value of the curvature. The second one uses *CimLib* with the direct method to compute the curvature that is subsequently imported into *Abaqus*®. The Laplace's law (6.7) is then applied as a Neumann condition over the mesh boundary.

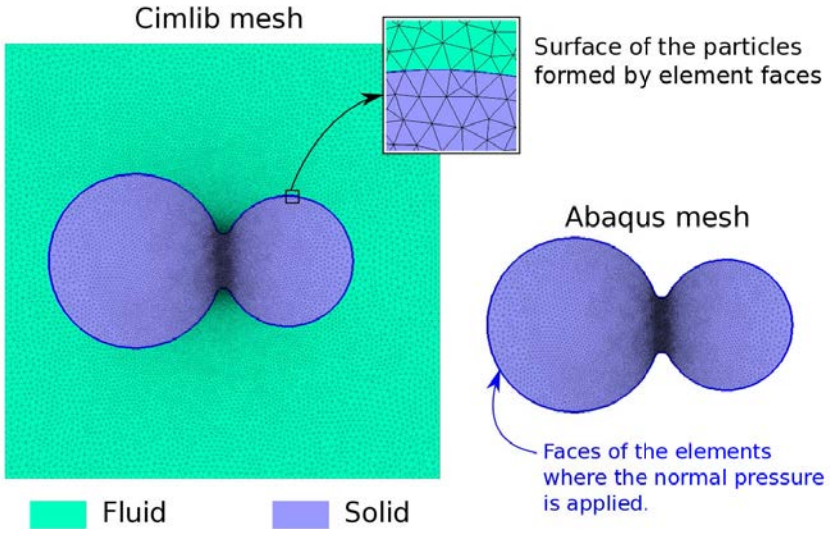

Figure 6.9: Both meshes used for the *CimLib* - *Abaqus*® comparison.

Figure 6.10 shows the variation of the computed pressure along the vertical line connecting both necks, as depicted in the sketch of the particles configuration. Note that the elastic analysis in *Abaqus*® is carried out with displacement based FE. The pressure field is then post-treated and equal to minus one-third the trace of the stress tensor. Looking at the *CimLib* and *Abaqus*® simulations using the analytical value of the curvature in Figure 6.10 ("Analytical Curvature"), an excellent agreement is found. The same kind of agreement is found regarding the *CimLib* and *Abaqus*® simulations using the direct method for computing the curvature ("Direct Curvature"). But a slight variation of the curvature (Analytical or Direct) has an impact on the pressure, which means that the mechanical problem itself is intrinsically very sensitive to slight curvature variations. Obviously the mechanical approach developed here also presents this sensitivity. Pressure obtained with *CimLib* using the tensorial method to

express the surface tension term is bounded by the pressure computed by using the Analytical and Direct method for the curvature, demonstrating the precision of this method for curvature computation even for a non-structured mesh.

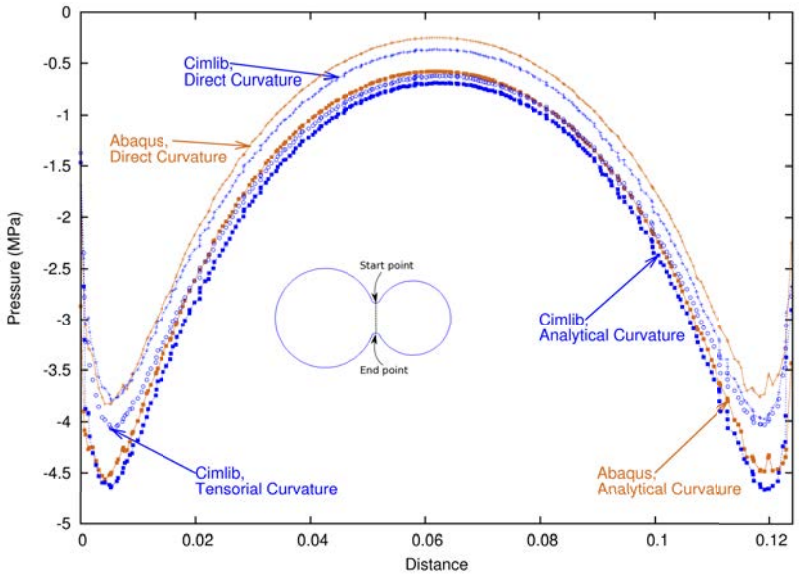

Figure 6.10: Comparison of the pressure along the vertical line drawn in the sketch below (left corner).

The tensorial method still yields good results, as it can be seen in Figure 6.11, where the pressure isovalues obtained with this approach under *CimLib* are compared to the *Abaqus*® results. Furthermore, two advantages have been found to the tensorial method compared with the direct curvature evaluation. First, in the limit case where the neck curvature tends to zero, the pressure field exhibits a better behavior when it is computed using the tensorial method. Second, when using an iterative method to solve the linear algebraic system obtained from the finite element discretization, the convergence is found to be better with this approach than when the curvature is computed. And finally, as the explicit curvature estimation is avoided, the computation time is reduced.

Finally, even if the variational formulation of the problem has been developed as a function of the velocity, the displacement inside the solid can be computed during the post-processing by using the Euler explicit scheme (Equation (6.19)). The Eulerian framework used can generate a rigid body displacement of the solid. In order to be able to establish a comparison between the results obtained from *Abaqus*® and *CimLib*, this rigid body displacement should be subtracted to match the Dirichlet boundary conditions applied to the *Abaqus*® simulation. Consequently,

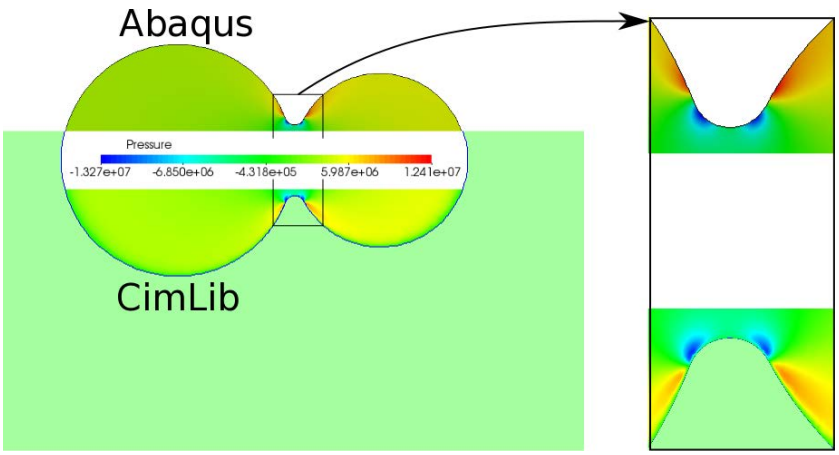

Figure 6.11: Comparison between the pressure field obtained with *Abaqus* using analytical curvature (upper) and *CimLib* using Tensorial curvature (lower).

a translation is applied to the solid in *CimLib* in order to set the displacement of point "A" in Figure 6.12 equal to zero. And finally, a rotation is applied to the solid to prescribe the displacement in the Y direction equal to zero at point "B" (Figure 6.12). After the post-processing, a comparison of the displacement magnitude between the results obtained from *Abaqus*® (upper) and *CimLib* is presented in Figure 6.12. A very good agreement between both simulations is found.

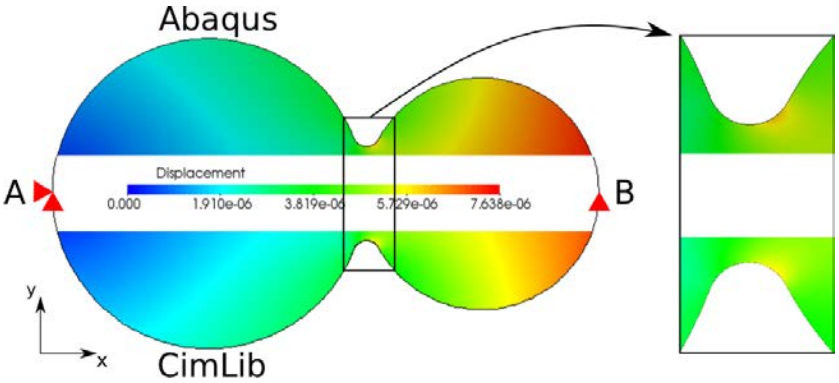

Figure 6.12: Comparison between the magnitude of the displacements obtained with *Abaqus* (upper) and *CimLib* (lower). $u_x = u_y = 0$ at point "A" and $u_y = 0$ at point "B". The analytical curvature (upper) and Tensorial curvature (lower) methods were used.

6.3.2.3 Multiples spherical particles in 3D.

To conclude this chapter, the simulation of a particle packing embedded into a Newtonian fluid is shown in Figure 6.13. Packing is made up of 178 elastic spherical particles, which can initially slightly intersect each other, with a uniform radius distribution ranging from 0.05μm to 0.1μm. The material properties of both fluid and solid phases are given in Table 6.3. The mesh has been adapted in the vicinity of the particles surface using the strategy presented in Section 4.4.4, in order to improve the description of the microstructure while keeping a reasonable number of elements. In the simulation shown in Figure 6.13 about 700,000 nodes and 4,000,000 elements has been used. The simulation has been performed using the SLR combined to the tensorial method, for computing the surface tension term, and the multiscale ASGS technique to stabilize the $P1/P1$ velocity - pressure formulation. Regarding Figure 6.13, the developed methodology allows the pressure field to be accurately computed in this particles compact, with limited oscillations at the fluid - solid interface.

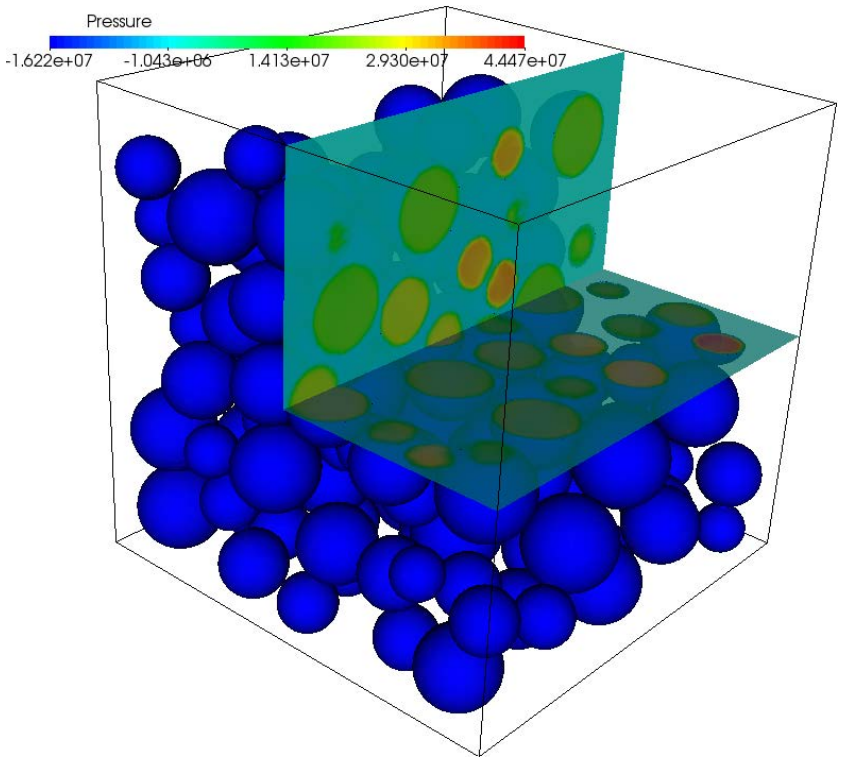

Figure 6.13: Pressure (Pa) field in a particle packing.

6.4 Conclusion

A numerical model for the simulation of the fluid - elastic solid coupling with surface tension, has been proposed in a fully Eulerian way. This approach is based on a mixed formulation in velocity - pressure of the coupled mechanical problem, first proposed in [Papadakis 2008], with a continuous and linear approximation of both pressure and velocity. A Level-Set method is used to capture the fluid - solid interface. The main drawback of this type of Eulerian approach is the spurious pressure oscillations which take place at the phase interface. The cause of these oscillations is first the discontinuity in the material properties, but also in the present case, the surface tension term. Three manners for reducing these oscillations have been investigated. First, two stabilized finite element formulations have been used: the $P1+/P1$ or MINI-element formulation, and the ASGS method, which belongs to the variational multiscale methods. Second, and it is more specific to the problems with surface tension, two ways to compute the surface integral in a Eulerian framework have been considered: in one hand, the classical Continuum Surface Force method consisting in turning the surface integral into a volume integral, and in the other hand the SLR consisting in a linear approximation of the surface. Finally, a tensorial formulation has been proposed to avoid the direct evaluation of the curvature. Different simulations have been carried out to test the efficiency and the accuracy of these methods and their combination: the evaluation of parasitic currents in a two-phase incompressible flow problem; the spherical elastic inclusion embedded into a Newtonian fluid, and the case of two spherical particles connected by a neck. In each of these simulations, numerical results obtained by combining the different methods were compared with analytical values when it is possible, or with results obtained in a Lagrangian context with *Abaqus®*. It has been found that the more efficient combination in terms of pressure oscillation reduction and convergence of the iterative linear solver is the ASGS method together with the SLR and tensorial methods. Finally, a 3D case related to the context of this work has been presented: a granular packing of elastic bodies embedded into a Newtonian fluid.

In the next Chapter 7, the numerical approach presented here will be used to perform simulation of sintering by volume diffusion.

6.5 Résumé en français : Problème mécanique

La prochaine étape est l'introduction de la diffusion volumique dans le cadre numérique présenté précédemment. Le flux de matière lié à la diffusion volumique est fonction du gradient de pression à l'intérieur des particules. Les particules ont été considérées comme un matériau linéaire élastique isotrope. Même si dans le cas du frittage naturel libre il n'y a pas d'efforts extérieurs appliqués pendant le procédé, le compact pulvérulent est soumis à des contraintes très élevées induites par la tension surfacique présente aux interfaces (surfaces des particules et joints des grains). Additionnellement, dans le cadre du calcul Eulérien fixé, le milieu environnant doit être pris en compte dans le calcul mécanique. Une première approche vise à la prise en compte des effets de la tension surfacique juste au niveau de la surface des particules. Une stratégie numérique pour la simulation de l'interaction entre un fluide incompressible et un solide élastique avec la tension surfacique est donc proposée.

Cette approche est basée sur une formulation mixte en vitesse - pression du problème mécanique, avec une approximation linéaire continue de la vitesse et de la pression. La fonction Level-Set est donc utilisée pour capturer l'interface entre les particules et le fluide. Le traitement numérique de problèmes mécaniques avec tension surfacique dans un contexte Eulerien en utilisant une formulation mixte en vitesse - pression mène à des oscillations de la pression qui ont lieu principalement autour de l'interface. Ces oscillations proviennent de la discontinuité des propriétés mécaniques et du terme de tension surfacique. Différentes méthodes ont été utilisées afin de réduire ces oscillations : deux méthodes différentes de stabilisation, deux méthodes différentes pour le calcul des intégrales surfaciques dans un contexte Eulerien et finalement deux méthodes différentes pour le calcul de la courbure. Les résultats obtenus avec cette approche numérique ont été validés en faisant des comparaisons avec des solutions analytiques, avec d'autres approches numériques et avec des logiciels de calcul commerciaux (Abaqus). Les combinaisons entre les différentes méthodes donnent un grand nombre de possibilités. Parmi ces options, il a été trouvé que la combinaison qui permet d'obtenir le moins d'oscillations de la pression ainsi qu'une bonne convergence au niveau du solveur itératif sont la méthode de stabilisation multi-échelle ASGS, la reconstruction local de l'interface (SLR) pour l'intégration surfacique et la méthode tensorielle pour le calcul de la courbure. Plusieurs cas test ont montré que cette approche numérique permet de calculer le champ de pression à l'intérieur des particules avec très peu d'oscillations de la pression sur des empilements granulaires en 2D et 3D.

Chapter 7

Sintering by volume diffusion

Contents

In this chapter the strategy for sintering simulation by volume diffusion is presented. This diffusion mechanism is modeled by using the Fick's first law, which relates the matter flux $\underline{j^v}$ to the gradient of pressure p:

$$\underline{j^v} = -A_1 \underline{\nabla p} \tag{7.1}$$

where $A_1 = (1-f)\, D_v/kT$ is a constant function of the volume diffusion coefficient D_v, the Boltzmann's constant k, the temperature T and the vacancies volume fraction f. Furthermore, it is possible to compute the normal velocity $\underline{v^v}$ due to the volume diffusion [1]:

1. see Figure 2.9 in Chapter 2 (page 18).

$$\underline{v^v} = v^v \underline{n} \qquad \text{with} \qquad v^v = \Omega \underline{j^v} \cdot \underline{n} \tag{7.2}$$

The numerical strategy presented in the previous Chapter 6 is used to compute the pressure field within the particles and the surrounding medium. At this point another challenge should be handled: the computation of the matter flux and the velocity induced by volume diffusion within the computational framework developed.

As discussed before, the surface tension induces a discontinuity of the normal stress across the interface between the particles and the surrounding fluid, and hence a the pressure field (formulation (6.20) and (6.21), in Chapter 6, page 90). Therefore the computation of the volume velocity $\underline{v^v}$ is not straightforward. Three different strategies for the computation of $\underline{v^v}$ are presented in Section 7.1. The impact of the volume velocity computation on the growth of the neck between two particles is also discussed in Section 7.1.

Within the context of volume diffusion, the strategy leading to volume conservation is presented in Section 7.2. Finally, some simulations of sintering by volume diffusion are presented in Section 7.3.

7.1 Volume velocity computation

The volume velocity $\underline{v^v}$ associated with the volume diffusion (Equation (7.2)) involves the evaluation of the pressure gradient over the particles surface. However, by virtue of the Laplace's law (Section 6.1, page 90), the normal stress is discontinuous across this interface $\Gamma_{s/f}$, and consequently the pressure gradient is not defined at this place. This means that in the particle, just under the particles surface, the pressure field is equal to the perticles pressure (driven by the curvature through the Laplace's law), while just over the surface, the pressure field is equal to the pressure of the surrounding medium. Consequently, pressure gradient, computed in a finite element sense, is not correct at the interface, because it takes into account the values of both, particles pressure and surrounding medium pressure. Furthermore, in a finite element framework, this problem does not occur only in the mesh elements crossed by the interface, but in a few layers of elements around the interface.

Figure 7.1a shows the pressure field on two particles during the first stages of the sintering process. The matter flux should induce a volume velocity $\underline{v^v}$ such that the neck joining the two particles grows. However if $\underline{v^v}$ is directly computed from the pressure field then the velocity is not computed properly, as it can be seen in Figure 7.1b. In this Figure 7.1b. the velocity field

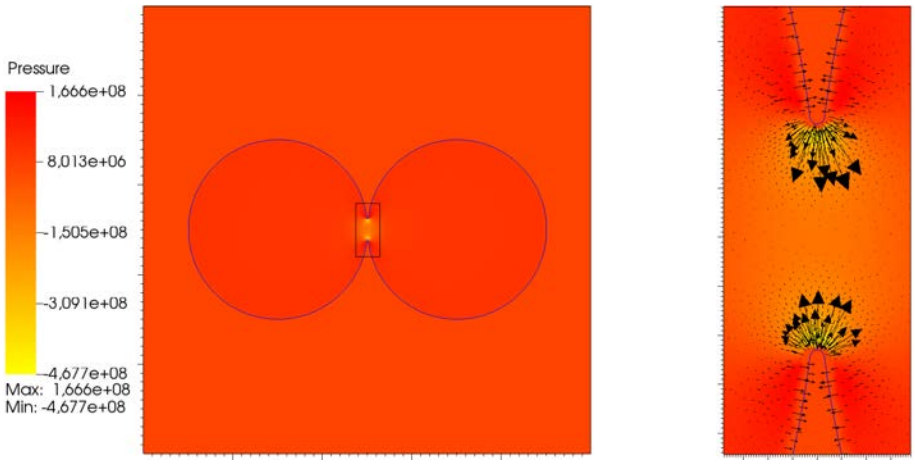

a. b.

Figure 7.1: Incorrect volume velocity computation $\underline{v^v} = -A_1 \underline{\nabla p}$: a. Pressure field ; b. Incorrect volume velocity over the rectangular region shown in a.

is pointing inside the particles, which means that the neck radius would decrease.

In order to overcome this difficulty, three different methods are proposed: the first method consists in a normal displacement of the particles surface, the second one is the convection of the normal velocity and the last one is inspired from the convection and consists in an instantaneous convection.

7.1.1 Particle surface shifting

This method has already been published by Bruchon *et al.* in [Bruchon *et al.* 2012]. The method is based on the metric properties of the level-set (or distance) function ϕ. Figure 7.2 shows the isovalues of the function ϕ in the vicinity of the interface, i.e. the lines described by $\{\phi = \beta\}$ for several values of β, $\| \beta \| \ll 1$. These lines can be considered, at least locally, as linear transformations (geometric expansions or contractions) of the surface $\{\phi = 0\}$ (the black solid line in Figure 7.2). Consequently, the curvature of these lines is approximatively equal to the curvature of the surface $\{\phi = 0\}$ when β is very small.

The numerical trick consists in solving the mechanical problem presented in the previous Chapter 6 (Equations (6.20) and (6.21), page 96) using a shifted level-set function, say $\phi' = \phi - \lambda$, with λ a positive constant parameter. In this way, the surface is shifted and becomes the dashed line in Figure 7.2. The pressure is then discontinuous over this virtual surface $\{\phi' = 0\}$, and remains continuous and differentiable over the true surface $\{\phi = 0\}$, where the pressure

gradient, the flux (Equation 7.1), and the velocity (Equation (7.2)) can now be numerically computed.

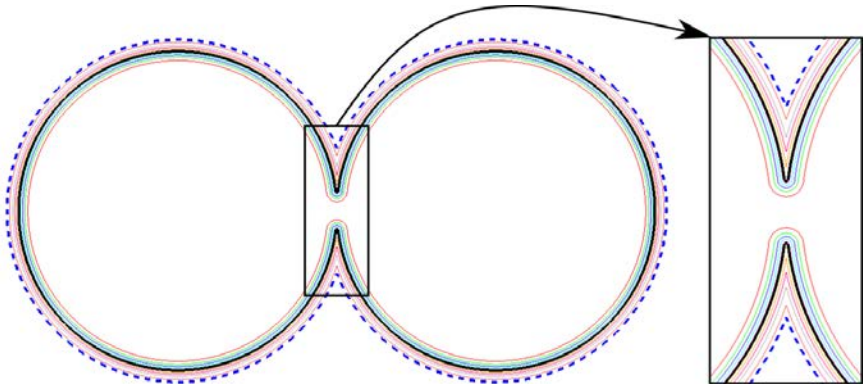

Figure 7.2: Isovalues of the level-set function ϕ in the vicinity of the interface. Black solid line: $\{\phi = 0\}$ (interface), dashed line: $\{\phi = 0.009\}$, or $\{\phi' = 0\}$ with $\phi' = \phi - \lambda$ and $\lambda = 0.009$.

From a practical point of view, the value of λ is chosen by a numerical test, as the smallest distance from the particles surface $\{\phi = 0\}$ at which the pressure and the gradient of pressure are found to be appropriate (the criterion is the sign of the normal component of the pressure gradient) when the Laplace's law is enforced over this surface. This choice provides a value of λ equal to twice or thrice the mesh size. The use of a mesh adaptation technique (Chapter 4) guarantees that this value is small when compared to the particles size.

This method allows to obtain good results as those published in [Bruchon *et al.* 2012]. The big advantage of this method is that it is computationally very cheap since no additional problem, other than the shifting of the level-set function, has to be solved. Furthermore it can be used to deal with problems in 2D and 3D without any modification. However, it also presents some drawbacks, the most important being that sometimes, depending on the configuration of the system, it is possible that the structure obtained with the shifted level-set function ($\phi' = \phi - \lambda$) is significantly different from the original. For example, this may occur when there are two particles that are very close but not in contact. In that case the two particles will be touching each other after the level-set function has been shifted and therefore the pressure field will be significantly different.

Figure 7.3 shows an example of how different the pressure field is when the shifting of the level-set function induces an important change in the topology of the structure. Figure 7.3a shows the initial geometry and its corresponding pressure field. Initially there are two particles that are very close but not yet in contact. However the shifting of the level-set function

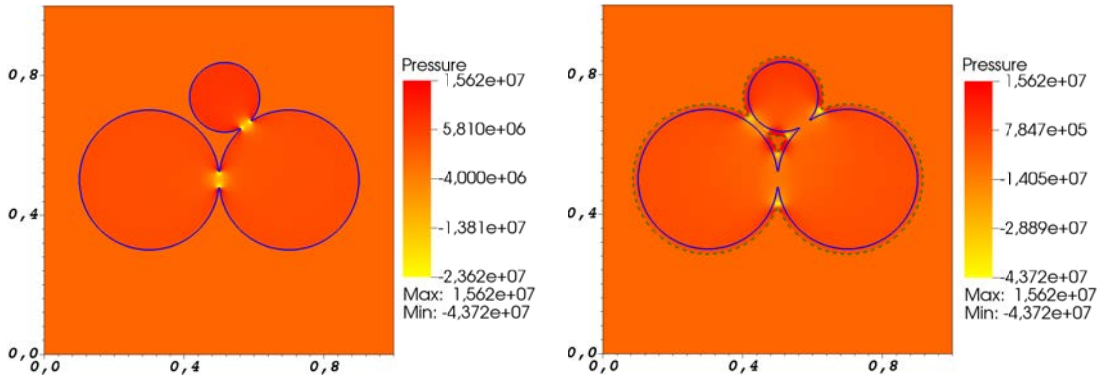

a. b.

Figure 7.3: a. Pressure field of three particles, the upper one is not in contact with the one on the left hand side; b. Pressure field of three particles after the level-set function was shifted, the three particles are in contact. The dashed green line is the shifted level-set function and the blue line is the original configuration.

($\phi' = \phi - \lambda$) will get those particles in contact as it can be seen in Figure 7.3b. Furthermore, when the contact between the two particles has been created there is a region of very high curvature that appears at the new contact point and this high curvature region leads to a pressure field that is very different from the original one. As the pressure field obtained with the shifted level-set function is used to compute the volume diffusion velocity on the initial configuration then this velocity will not correspond to the initial geometry.

In order to overcome this problem two methods of convecting the volume diffusion velocity are presented in Sections 7.1.2 and 7.1.3.

7.1.2 Velocity convection

In some physical problems involving interfaces, some quantities are only defined in a region of the computational domain or even sometimes only over the interfaces. In those cases a "classical" extension method is used [Osher & Sethian 1988, Peng *et al.* 1999, Tsai & Osher 2003, Salac & Lu 2008]. In the particular case of the volume diffusion, the velocity is well defined inside of the particles where $\phi < -\lambda$, and the goal of the velocity convection step is to compute a smooth extension, e.g. v^v on $\phi < -\lambda$ to a neighborhood of $\Gamma_{s/f}$ [Osher & Fedkiw 2001].

Let $v^v = \underline{v^v} \cdot \underline{n}$ be the scalar normal velocity, this normal velocity is extended out the region $\phi < -\lambda$ by solving the following equation:

$$\frac{\partial v^{ext}}{\partial \tau} + \underline{\nabla v^{ext}} \cdot \frac{\underline{\nabla \phi}}{\| \underline{\nabla \phi} \|} = 0, \quad \text{with } v^{ext}(\underline{x}, t) = v^v \quad \text{if } \phi(\underline{x}) < -\lambda \tag{7.3}$$

where v^{ext} is the extension velocity and τ is a non physical time. The previous Equation (7.3) is solved incrementally until the steady state: $\partial v^{ext}/\partial \tau = 0$. $\underline{\nabla \phi}/ \| \underline{\nabla \phi} \|$ corresponds to the outward normal to the particles surface, therefore Equation (7.3) is equivalent to the transport Equation (4.10) (Chapter 4, 51) and, in fact, Equation (7.3) represents the convection of v^{ext} out of $\phi < -\lambda$ with a convection velocity $\underline{\nabla \phi}/ \| \underline{\nabla \phi} \|$.

It is important to highlight that the volume diffusion velocity $\underline{v^v}$ must be computed from the pressure field, and then introduced into Equation (7.3). Indeed, this velocity is used as a Dirichlet boundary condition applied where $\phi(\underline{x}) < -\lambda$.

Equation (7.3) is very close to the level-set convection equation presented in Chapter 4 (Equation (4.10), page 51). Again, this equation should be solved using a SUPG stabilization method in order to avoid numerical oscillations of the solution (see Section 4.4.3, page 56 and [Brooks & Hughes 1982]).

After the velocity has been extended, the volume diffusion velocity $\underline{v^v}$ can be computed again:

$$\underline{v^v} = v^{ext} \underline{n} \tag{7.4}$$

7.1.3 Instantaneous convection

This method is inspired by the convection method presented previously (Section 7.1.2). The idea is to find a velocity field in the vicinity if the interface $\Gamma_{s/f}$ that does not change in the normal direction. This is equivalent to solve the following equation [Tsai & Osher 2003]:

$$\underline{\nabla v^{ext}} \cdot \frac{\underline{\nabla \phi}}{\| \underline{\nabla \phi} \|} = 0, \quad \text{with } v^{ext}(\underline{x}, t) = v^v \quad \text{if } \phi(\underline{x}) < -\lambda \tag{7.5}$$

As the previous Equation (7.5) is solved only once, therefore the volume diffusion velocity $\underline{v^v}$ can be directly introduced into the formulation. This would allow to directly compute v^v out of the pressure:

$$\begin{aligned} v^{ext} + \epsilon_{v^{ext}} \Delta v^{ext} &= -A_1 \Omega \underline{\nabla p} \cdot \frac{\underline{\nabla \phi}}{\| \underline{\nabla \phi} \|} && \text{if } \phi(\underline{x}) < -\lambda \\ \underline{\nabla v^{ext}} \cdot \frac{\underline{\nabla \phi}}{\| \underline{\nabla \phi} \|} + \epsilon_{v^{ext}} \Delta v^{ext} &= 0 && \text{if } \phi(\underline{x}) > -\lambda \end{aligned} \tag{7.6}$$

where the terms containing $\epsilon_{v^{ext}}$ (the regularization parameter) correspond to an elliptic regularization [Miller 1997]. At this point it is important to say that the elliptical regularization is strictly necessary when the filtered level-set function is used (Section 4.4.2, page 55). This is because the level-set function ϕ is constant outside of the filtering region and therefore the products $\underline{\nabla v^{ext}} \cdot \underline{\nabla \phi} / \| \underline{\nabla \phi} \|$ would be equal to zero.

The formulation (7.6) is also stabilized by using a SUPG method (see Section 4.4.3, page 56 and [Brooks & Hughes 1982]). The volume diffusion velocity is finally computed by using again Equation (7.4).

7.1.4 Comparison between the methods

The method of particle surface shifting presented in Section 7.1.1 could lead, in some cases, to a miss-computation of the velocity field and therefore this method will not be considered in this comparison. Though, some results concerning the sintering simulation by using this method have already published and are available in [Bruchon *et al.* 2012]. Instead, a comparison between the two methods involving convection (Sections 7.1.2 and 7.1.3) is presented.

In order to establish a comparison between those two different methods for the computation of the volume diffusion velocity $\underline{v^v}$ a system with two particles at a specific time step is considered. The initial geometry is the one shown in Figure 7.1a. Looking at the values of the gradient of the pressure, the value of λ in Equations (7.6) and (7.3) is set to be equal to $\lambda = 0.005\mu$m, which corresponds to 1/80 of the particles diameter. All the simulations in this section were carried out over a square computational domain of side 1μm and built-up of 50.000 elements. The simulations were performed by using a parallel computing strategy over 4 processors @ 2.66GHz.

It is important to recall that the level-set function has been filtered (Equation (4.20), page 55) over a narrow band of width $2E$ around the interface $\Gamma_{s/f}$. Furthermore the value of the normal defined as a function of the gradient of the level-set function is very close to zero outside of this narrow band. Considering this, the convection method (Section 7.1.2) has to be solved until the "steady state" has been reached inside this band which allows to reduce the computational time.

First some experiments have been conduced in order to identify the number of artificial time step needed to achieve this steady state. As it has been said before, the volume diffusion velocity has to be computed before the convection in order to be used as a Dirichlet boundary condition. In this way the velocity in the region where $\phi < -\lambda$ is computed directly from the pressure field as follows:

$$\underline{v^v} = v^v \underline{n} \qquad ; \qquad v^v = \begin{cases} -\Omega A_1 \underline{\nabla p} \cdot \underline{n} & \text{if } \phi < -\lambda \\ 0 & \text{if } \phi > -\lambda \end{cases} \tag{7.7}$$

The value of the volume diffusion velocity v^v present in convection Equation (7.3) is computed by using the previous Equation (7.7). The convection is carried out over an artificial time τ by using an artificial time step equal to the minimum element size: $\Delta\tau = h_{min}$. Figure 7.4 shows the convected velocity v^{ext} at different artificial time steps over a region near to the neck between the particles. The interface $\Gamma_{s/f}$ is plotted with the continuous black line and the isovalue $\phi = -\lambda$ is plotted with the dashed green line. In Figure 7.4a the result of Equation (7.7) is shown. Figures 7.4b, 7.4c and 7.4d show the convected velocity field at $\tau = 5\Delta\tau$, $\tau = 10\Delta\tau$ and $\tau = 100\Delta\tau$, respectively.

After performing some numerical experiments, it seems that the convected velocity does not change significantly after $10\Delta\tau$. Indeed, there is any important difference between the convected velocity obtained after $10\Delta\tau$ (Figure 7.4c) and the one obtained after $100\Delta\tau$ (Figure 7.4d). The number of artificial time step performed is an important parameter because the computational cost of the convection mainly depends on this parameter.

The convection of the volume diffusion velocity is computationally very expensive. For example each time step (Δt) the simulation shown in Figure 7.4 required about 48 seconds. The convection of the velocity over $\tau = 10\Delta\tau$ required, in average about 18.5 seconds, this means that more than 35% of the CPU effort during every time step Δt is used to perform the convection of the velocity.

Concerning the instantaneous convection method (Section 7.1.3), another parameter has to be set. This method uses an elliptic regularization which introduces a numerical parameter $\epsilon_{v^{ext}}$ (Equation (7.6)). The elliptic regularization generates a numerical diffusion of the quantity being convected. This numerical diffusion is controlled by the value of $\epsilon_{v^{ext}}$. If $\epsilon_{v^{ext}}$ is too high then the numerical diffusion induced is too strong and the obtained velocity is very different from the value of the velocity at the layer $\phi = -\lambda$. Yet, if the value of the regularization

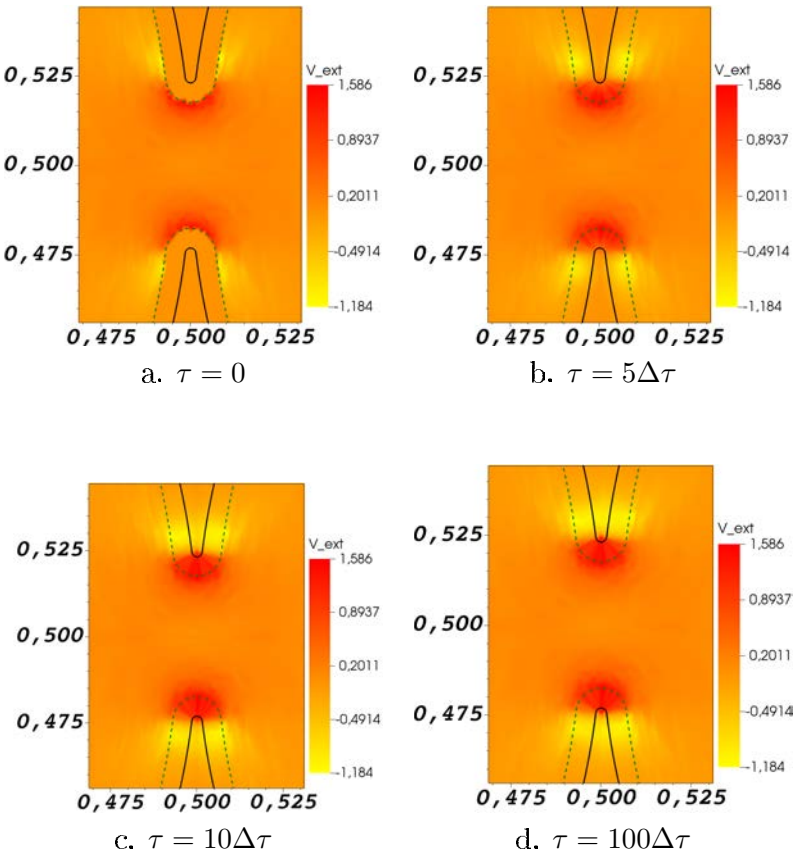

a. $\tau = 0$ b. $\tau = 5\Delta\tau$

c. $\tau = 10\Delta\tau$ d. $\tau = 100\Delta\tau$

Figure 7.4: Evolution of the convected velocity over the artificial time τ. The continuous black line corresponds to the interface $\Gamma_{s/f}$ and the dashed green line is the isovalue $\phi = -\lambda$.

parameter is too low then the numerical system can become ill-defined and the convergence of the numerical solver could be compromised[2].

The value of the regularization has been tuned by performing some numerical experiments. Figure 7.5 shows the convected velocity field for different values of $\epsilon_{v^{ext}}$. The classical convection method leads to values of the velocity near to the neck of about 1.5 μm/s. This value can be used to assess the proper computation of v^{ext}, and more precisely the effect of the stabilization parameter onto the final velocity in this region. It is possible to see that the numerical diffusion is too high for $\epsilon_{v^{ext}} = 2.5 \cdot 10^{-5}$ (Figure 7.5a). As the value of this parameter is lowered, the value of the convected velocity near to the neck get closer to the velocity obtained with the

2. At this point it is important to say that CimLib uses the "Portable, Extensible Toolkit for Scientific Computation" (PETSc) for the iterative resolution of the numerical systems [Balay *et al.* 1997].

classical velocity convection.

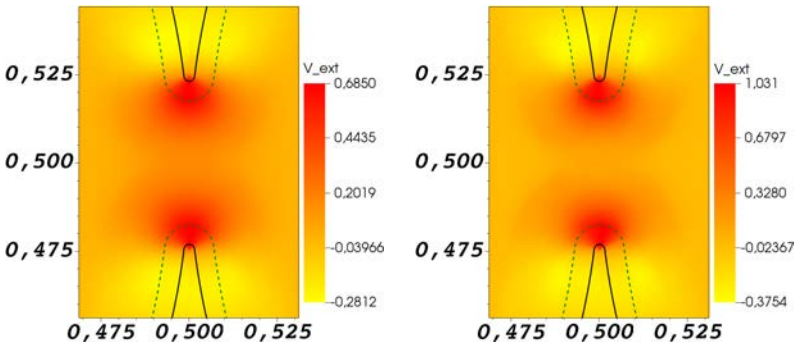

a. $\epsilon_{v^{ext}} = 2.5 \cdot 10^{-5}$ b. $\epsilon_{v^{ext}} = 8 \cdot 10^{-6}$

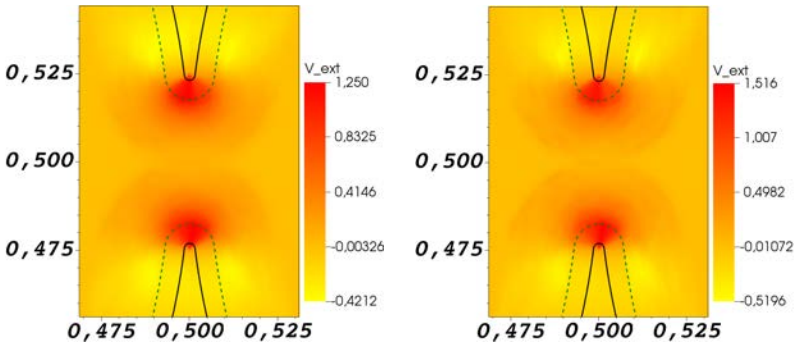

c. $\epsilon_{v^{ext}} = 4 \cdot 10^{-6}$ d. $\epsilon_{v^{ext}} = 2 \cdot 10^{-6}$

Figure 7.5: Velocity field for different values of the regularization parameter $\epsilon_{v^{ext}}$ for the instantaneous convection.

The value of the regularization parameter $\epsilon_{v^{ext}} = 2 \cdot 10^{-6}$ is the lowest value that can be used without losing too much of the convergence properties of the system (See Table 7.1). Table 7.1 presents the convergence of the solver corresponding to each value of $\epsilon_{v^{ext}}$. If $\epsilon_{v^{ext}} = 10^{-6}$ then the convergence of the system is very low and the computational time is very high. Nevertheless a value of $\epsilon_{v^{ext}} = 2 \cdot 10^{-6}$ allows to achieve a good convergence, the numerical diffusion is quite acceptable and the resolution of the system is not too expensive.

The velocity fields obtained by the classical convection method and the instantaneous convection are almost the same. However by using the instantaneous convection the time expended in the convection is almost a half of the time required by the classical convection method. For those reasons the instantaneous convection method will be used from now on to compute the volume diffusion velocity.

$\epsilon_{v^{ext}}$	Iterations required	Computational time (s)	Convergence
$2.5 \cdot 10^{-5}$	286	4.618	$4.419 \cdot 10^{-10}$
$8 \cdot 10^{-6}$	405	6.73	$1.14 \cdot 10^{-9}$
$4 \cdot 10^{-6}$	536	8.42	$3.14 \cdot 10^{-9}$
$2 \cdot 10^{-6}$	972	10.52	$8.72 \cdot 10^{-8}$
10^{-6}	3000	52.10	$4.42 \cdot 10^{-2}$

Table 7.1: Computational elapsed time as a function of $\epsilon_{v^{ext}}$.

7.2 Volume conservation enforcement

Another issue has to be handled concerning the volume conservation. As it has been discussed in Chapter 5 (page 70), during the sintering process the density of the material remains constant and since the mass of the compact powder is also constant, the volume of the solid phase must be conserved throughout the whole simulation if not external load is applied.

Considering the volume diffusion velocity $\underline{v^v}$, the volume of the solid phase at a given time step is conserved if the following expression is satisfied [Brenner 2005]:

$$\int_{\Gamma_{s/f}} \underline{v^v} \cdot \underline{n} dS = 0 \tag{7.8}$$

By using the divergence theorem, the previous volume integral can be rewritten as a volume integral[3]:

$$\int_{\Upsilon_s} \underline{\nabla} \cdot \underline{v^v} dV = 0 \tag{7.9}$$

where Υ_s is the solid phase computational domain. As the previous Equation (7.9) should be satisfied for any volume Υ_s, then the following expression holds:

$$\underline{\nabla} \cdot \underline{v^v} = 0 \tag{7.10}$$

Since the volume diffusion velocity $\underline{v^v}$ can be computed as a function of the pressure, then it is possible to write a constraint that the pressure field should fulfill in order to satisfy Equation (7.10). This constraint is found by replacing expression of normal velocity as a function of the flux (7.2) into the previous Equation (7.10):

3. From the Chapter 6 (Page 90) the boundary of the solid phase $\partial\Upsilon_s$ is the interface between the solid and the fluid $\Gamma_{s/f}$

$$\begin{aligned} \underline{\nabla} \cdot \underline{v^v} &= \underline{\nabla} \cdot \left(-A_1 \Omega \underline{\nabla p}\right) &= 0 \\ &= -A_1 \Omega \Delta p &= 0 \\ \\ &\Leftrightarrow \Delta p \equiv 0 \end{aligned} \tag{7.11}$$

The material has been considered to respond as a linear isotropic elastic material. Then when the momentum conservation equation (6.1) is solved, in general, the pressure field does not satisfy the constraint (7.11). Therefore if any other additional velocity is locally added, then the volume of the solid phase will be modified throughout the sintering simulation.

This problem is also present when the grain boundary diffusion is considered. In literature different solutions are proposed, for example by Pan J. [Pan *et al.* 1997, Pan *et al.* 1998, Kucherenko *et al.* 2000, Ch'ng & Pan 2004, Ch'ng & Pan 2005, Pan *et al.* 2005], some additional degrees of freedom are added to each particle corresponding to the translational and rotational velocities of a rigid body motion, in such a way that the volume of the particles is conserved. Another solution considering the sintering by surface and grain boundary diffusions of two particles of the same size [Wakai & Brakke 2011], consists in the addition of a relative velocity between the two particles to represent the effect of the grain boundary diffusion and at the same time establish the coupling between the two diffusion mechanisms.

7.2.1 Artificial volume conservation velocity

Those solutions are more adapted for Lagrangian approaches where the nodes of the mesh are placed over the surface of the particles and the grain boundaries and mainly used in 2D problems. It would be complex to integrate them within the level set approach presented in this work as the velocity field should be computed over the vicinity of the interface and not only at the interface and also their extension to 3D problems raises some additional challenges.

Another solution is proposed here, the idea consists in adding an artificial volume conservation velocity intended to recover the volume loss/gain (ΔV) due to the diffusion phenomena. This artificial volume conservation velocity $\underline{v^{avc}}$ is defined in such a way that its magnitude is constant over all the computational domain and it is oriented in the local normal direction of the particles surface:

$$\underline{v^{avc}} = v^{avc} \underline{n} \tag{7.12}$$

Furthermore, if the level-set function is transported by using this artificial volume conservation velocity $\underline{v^{avc}}$ over an artificial time step set as $\Delta\tau = \Delta t$, the volume of the solid phase Υ_s would change of $\Delta\tilde{V}$:

$$\Delta\tilde{V} = \Delta\tau \int_{\Upsilon_s} \underline{\nabla} \cdot \underline{v^{avc}} dV + \mathcal{O}(\Delta t) \tag{7.13}$$

By using the divergence theorem, the previous expression can be rewritten as follows:

$$\begin{aligned}
\Delta\tilde{V} &= \Delta\tau \int_{\Gamma_{s/f}} \underline{v^{avc}} \cdot \underline{n} dS + \mathcal{O}(\Delta t) \\
&= \Delta\tau \int_{\Gamma_{s/f}} v^{avc} \underline{n} \cdot \underline{n} dS + \mathcal{O}(\Delta t) \\
&= v^{avc} \Delta\tau \int_{\Gamma_{s/f}} \underline{n} \cdot \underline{n} dS + \mathcal{O}(\Delta t)
\end{aligned}$$

$$\Delta\tilde{V} \approx v^{avc} \Delta\tau S \tag{7.14}$$

where S is the area of the interface $\Gamma_{s/f}$.

Now the artificial volume conservation velocity $\underline{v^{avc}}$ will be related to the real change in the volume ΔV induced by the diffusion phenomena after a time step. Let V_0 be the initial volume of the solid phase $\Upsilon_s|_{t_0}$:

$$V_0 = \int_{\Upsilon_{s|_{t_0}}} dV \tag{7.15}$$

Considering the actual configuration, the related mechanical problem is solved and the pressure field found is used to compute [4] the volume diffusion velocity $\underline{v^v}$. After a time step Δt, this volume velocity $\underline{v^v}$ will induce a change on the volume of the solid phase given by :

$$\Delta V = \int_{\Upsilon_{s|_{t_0+\Delta t}}} dV - V_0 \tag{7.16}$$

As $\underline{v^{avc}}$ is intended to recover the volume loss (or gain), then $\Delta\tilde{V} \equiv -\Delta V$. In this way, Equations (7.14) and (7.16) allow to find an expression for the artificial volume conservation velocity $\underline{v^{avc}}$:

4. This computation includes the extension procedure presented in Section 7.1

$$v^{avc} = -\frac{\Delta V}{\Delta \tau S} \tag{7.17}$$

Considering this volume conservation velocity, some numerical tests are carried out in Section 7.3.1.

7.2.2 Volume diffusion time stepping algorithm

Algorithm 4 presents the procedure used to perform the simulation by volume diffusion. This Algorithm shows that in order to perform a simulation of sintering by volume diffusion several challenges must be handled. First the mechanical problem has to be solved, this requires the use of the numerical strategy presented in Chapter 6. Even after the pressure field has been computed, the computation of the volume diffusion velocity is still a challenging task. The instantaneous convection is used to find the volume diffusion field. This velocity is used to make evolve the structure and then the artificial volume conservation velocity is used to recover the initial volume of the structure. Finally at this point it is possible to start over at the next time step.

Algorithm 4 Time stepping algorithm for the volume diffusion strategy developed.

$\phi_h^0 \leftarrow$ From Algorithm 2 (page 70) for a given geometry at $t = 0$.
$\mathcal{T}_h(\Upsilon)$: Initial mesh adaptation by using ϕ_h^t at $t = 0$
$V_0 \leftarrow$ From Equation (7.15)
for $t = 0 \rightarrow (t_f - \Delta t)$ with ϕ_h^t known at the current time t **do**
  $(\underline{v_h}, p_h) \leftarrow$From the resolution of the mechanical problem (system (6.20) and (6.21))
  $\underline{v^v} \leftarrow$Volume diffusion velocity (From Equation (7.6))
  $\phi_h^{t+\Delta t} \leftarrow$From the resolution of the convective-reinitialization Equation (4.19) [a]
  $\Delta V \leftarrow$Volume change induced by the volume diffusion velocity (From Equation (7.16))
  $\underline{v^{avc}} \leftarrow$Artificial volume conservation velocity (From Equations (7.12) and (7.17))
  $\phi_h^{t+\Delta t} \leftarrow$From the resolution of the convective-reinitialization Equation (4.19) [b]
  $t \leftarrow t + \Delta t$
  $\mathcal{T}_h(\Upsilon) \leftarrow$Remeshing step every f_{rem} time steps.
end for
$\phi_h^{t_f} \rightarrow$ Output of the simulation at $t = t_f$.

a. The level-set function ϕ_h^t is transported by using the volume diffusion velocity, which induces a change on the volume of the structure that is later corrected.

b. The volume change induced by the volume diffusion velocity is recovered by transporting again $\phi_h^{t+\Delta t}$ with the artificial volume conservation velocity $\underline{v^{avc}}$ over an artificial time step $\Delta\tau = \Delta t$.

7.3 Numerical simulations

All the simulations were performed by considering that the computational domain Υ is a square (2D) or a cube (3D) of side 1μm. One of the most important step on the simulation of the sintering by volume diffusion consists in solving the mechanical problem. The numerical approach presented in Chapter 6 is used and the mechanical properties of the solids and the surrounding medium are presented in Table 7.2.

It is important to recall that the role of the surrounding medium is to transmit the stress applied on the boundary of the computational domain to the particles. Therefore an accurate description of the dynamics of this medium is not required. Furthermore, the mechanical properties of the fluid have been chosen in such a way that the stress (pressure field) on the particles is not perturbed.

The diffusion related properties are also presented in Table 7.2. The timescale is set through the parameter $A_1 = (1-f)\, D_v/kT$, more exactly through the volume diffusion coefficient D_v. In this work time is given in seconds.

Property	Value
μ	156 GPa
K	260 GPa
ν	0.25
γ_{sv}	0.9 J/m^2
η	1 Pa·s
ΩA_1	0.013m^4/(s·N) Pa·s

Table 7.2: Material properties of the solid and the fluid.

Like in Chapter 5, the diffusion related properties used are significantly bigger than real properties of the material. However, and as stated before, the use of larger diffusion coefficients does not have an effect on the kinectics of the diffusion mechanism.

7.3.1 Effect of the artificial volume conservation velocity

As stated before, the volume diffusion simulation does not lead naturally to the conservation of the volume of the particles. Therefore a supplementary procedure intended to ensure the volume conservation has been added to the algorithm (See Algorithm 4). As an artificial velocity ($\underline{v^{avc}}$) is added to the simulation, the evolution of the structure is modified along, but as it will be shown, the volume is conserved throughout the whole simulation.

Figure 7.6 shows the effect of the procedure of volume conservation. Two simulations are performed, one without the artificial volume conservation velocity $\underline{v^{avc}}$ and the second one with

volume conservation. The initial geometry used for both simulations and the corresponding pressure field are shown in Figure 7.6a. The structure evolves differently if the volume conservation procedure is whether or not applied. Figures 7.6c and 7.6d show the structure after $200\Delta t$ and $650\Delta t$, respectively. In those figures, the initial geometry is plotted in blue, the simulation without volume conservation is plotted with a dashed green line and the continuous red line corresponds to the simulation with volume conservation. When the volume conservation strategy is not used, the structure becomes significantly bigger than the initial geometry (dashed green line and blue line, respectively, in Figures 7.6c and 7.6d). After $650\Delta t$ the two particles have become about 12% bigger (7.6b). Nevertheless, this behavior is corrected by using the artificial volume conservation velocity as it can be seen in Figure 7.6b, where the volume change is lower than 0.01%.

It is important to note that the change of volume ΔV can depend on the strategy used to compute the volume diffusion velocity (methods presented in Section 7.1), but independently on the method, the artificial volume conservation strategy allows to successfully ensure a very low change on the volume. In 2D the change of volume is usually lower than the corresponding 3D problem. In order to use the same strategy when dealing with 2D or 3D problems, the volume conservation procedure will be used for all kind of simulations.

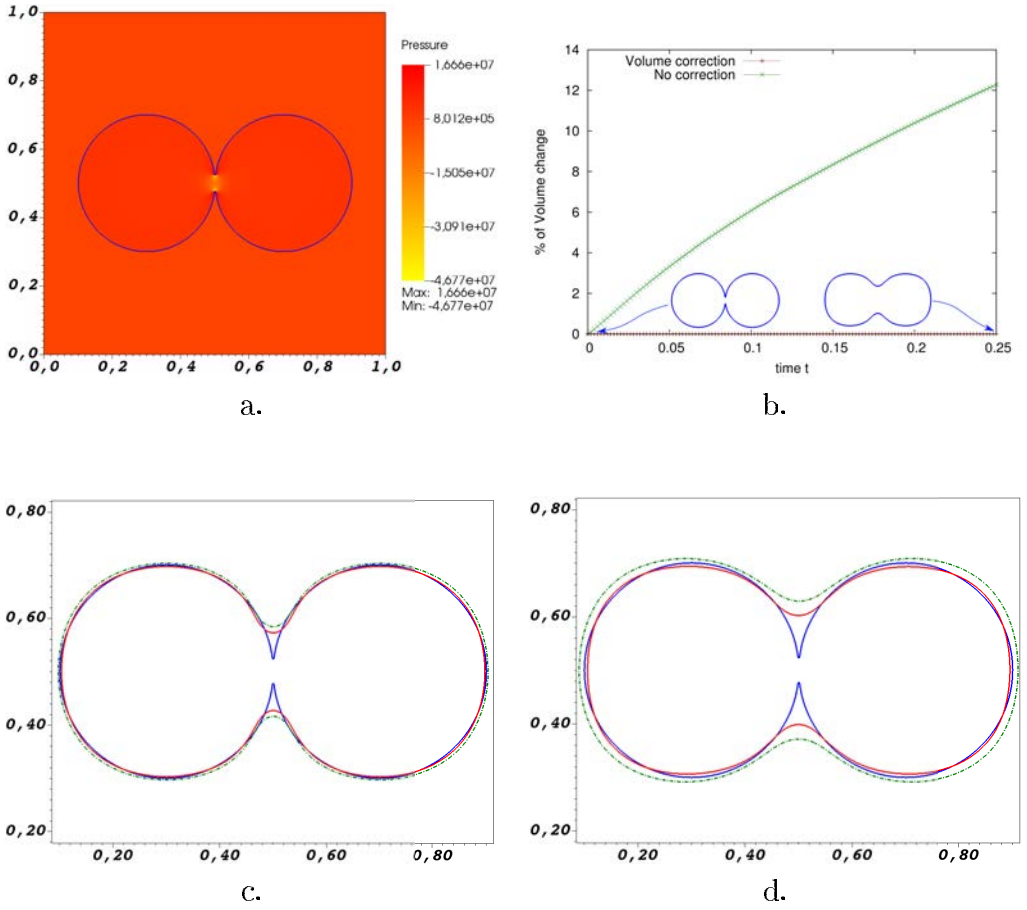

Figure 7.6: a. Pressure field of two particles sintering at $t = 0$; b. Volume change percent without volume correction (green line) and with correction (Red line over superimposed with the time axis) over the time; c. and d. Structure at $t = 200\Delta t$ and $t = 650\Delta t$, respectively, the blue line is the initial geometry, the dotted green line is obtained without volume correction and the continuous red line is obtained with volume conservation.

7.3.2 Two spherical particles

As in Chapter 5, this example aims to establish a comparison between the numerical approach developed and the analytical model of volume diffusion presented in Section 3.1. The first case involves two particles of radii R as presented previously in Figure 7.6a. As before the analytical model for the growth of the neck between the particles presented in Chapter 3 (Table 3.2, page 28) can be rewritten as follows:

$$\begin{aligned} \frac{x(t)}{R} &= \left(\frac{16 D_v \gamma_{sv} \Omega}{kT} \frac{t}{R^3} \right)^{1/5} \\ \frac{x(t)}{R} &= (16\, t')^{\,1/5} \end{aligned} \tag{7.18}$$

where $t' = D_v \gamma_{sv} \Omega t / kTR^3$ the adimensional time. The exponent 1/5 present in the previous Equation (7.18) is found by making some geometrical hypothesis, but it is possible to obtain exponents ranging between 1/5 and 1/4 (See Chapter 3, page 24).

Figure 7.7 shows the growth of the dimensionless neck radius x/R versus t', computed by finite element for a particle radius ranging from 0.1 to 0.4 μm. The best curve fitting these data, obtained by a least-square approximation of the numerical results, is $x/R = 0.36t'^{1/5.6}$ and is referred to as "$n = 5.6$". Once again this value, which is slightly larger than the upper bound predicted by the theory, represents a kind of mean value that takes into account the different stages of the sintering. However, when these simulations are examined individually, the coefficient n is shown to depend on the particles size and to vary slightly into each simulation. More precisely, the simulations provide a coefficient n that decreases when the particles size increases: n is equal to 4.85 when $R = 0.1\mu$m, to 4.23 when $R = 0.2\mu$m, to 4.14 when $R = 0.3\mu$m and to 3.88 when $R = 0.4\mu$m. Understanding in details this dependency requires deeper investigations which are still to be done.

Figure 7.8 presents the evolution, by volume diffusion, of two spherical particles of different sizes. This simulation has been performed in 2D and the plane strain assumption is considered. The initial radii of the two particles are 0.25μm and 0.1μm, respectively. The mesh adaptation strategy discussed in Chapter 4 (Section 4.4.4, page 59) is used to refine the mesh over a narrow band around the interface $\Gamma_{s/f}$, as shown in Figures 7.8a and 7.8c. The mesh is built up of about 55,000 elements.

The pressure field computed at the initial configuration is shown in Figure 7.8a. After $t = 250\Delta t$ the pressure field is shown in Figures 7.8b and 7.8c. At that time step ($t = 250\Delta t =$

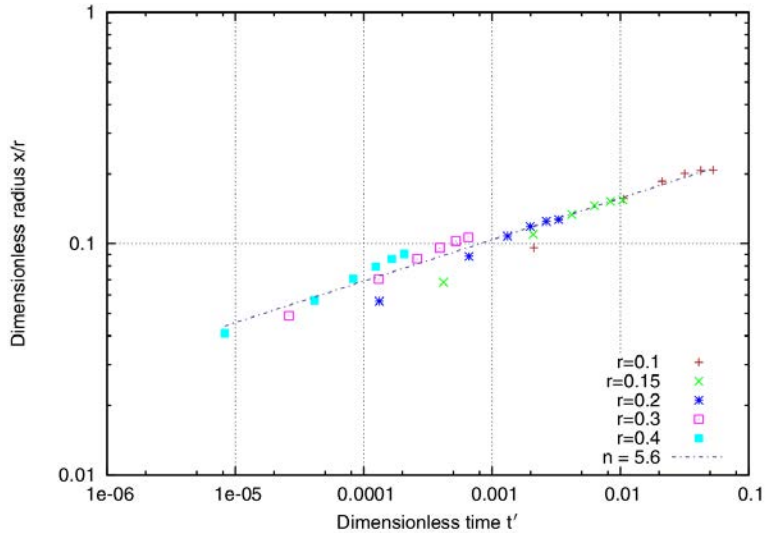

Figure 7.7: Growth by volume diffusion of the dimensionless neck x/R over the adimensional time t' in logarithmic scale for different values of R.

$0.1s$) the neck between the particles is about 87% of the radius of the smaller particle and as the curvature is lower then, as expected, the pressure is not as strong as it was at the beginning (Figure 7.8a).

It is important to highlight that the change on the volume[5] during the whole simulation is just about $2.2 \cdot 10^{-6}$% which can be considered as zero.

7.3.3 Particle packing sintering

One of the most important advantages of the numerical strategy presented here is related to its capability to handle very complex geometries and strong topological changes. In this section a 3D simulation of the sintering of a particle packing is presented. The computational domain is a cube of side 1μm. The stack of articles is built-up of about 150 particles with an uniform radii distribution ranging from 0.063μm to 0.079μm. The mesh adaptation strategy presented in Section 4.4.4 (page 59) has been used and the mesh can be seen in Figure 7.9a. The mesh is built-up of about ten millions of tetrahedra and about two millions of nodes and an element h size ranging between $1.2 \cdot 10^{-3}$ μm and $1.5 \cdot 10^{-1}$ μm . The time step ranges from $\Delta t = 4 \cdot 10^{-4}$s to $\Delta t = 6.4 \cdot 10^{-3}$s. The value of the parameter λ used to extend the velocity out of the solid is $\lambda = 0.005\mu$m. The simulation involving 570 time steps has been carried out within a parallel computing framework using 24 cores @ 2.66 GHz in about 200h.

5. Which in this 2D simulation is equivalent to the area of the particles.

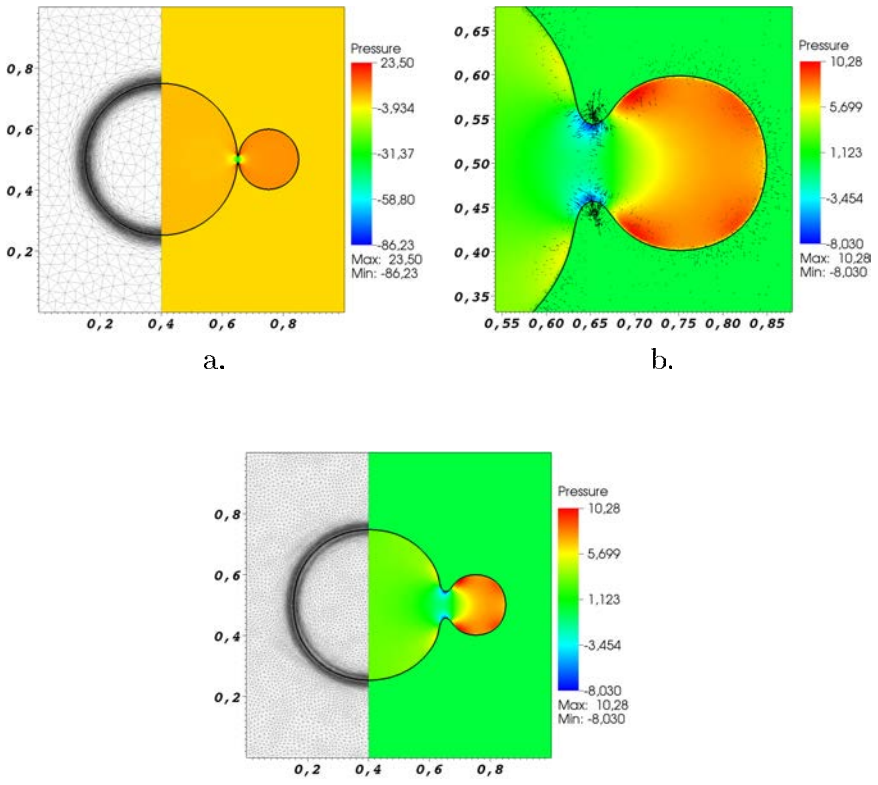

Figure 7.8: 2D simulation, under plane-strain assumption, of volume diffusion for two cylindrical particles of different size: (a) and (c) mesh refined around the interface and pressure isovalues (MPa), respectively on the initial configuration and after 250 computation increments; (b) pressure field (MPa) and induced diffusion velocity after 250 computation increments.

Figure 7.9a shows the initial geometry of the powder packing. In order to successfully perform this kind of simulations, several challenges must be handled: the mechanical problem should be solved by taking into account the surface tension at the surface of the particles, the volume diffusion velocity has to be computed only inside of the particles and extended over a region around the interface and the volume of the compact powder must remain constant. Additionally, all those operations have to be performed over a very complex geometry with a very high ratio between the mechanical properties of the phases. Considering all those challenges, at least to the authors knowledge, this work represents the first successful attempt to simulate the sintering by volume diffusion of a particles packing in 3D.

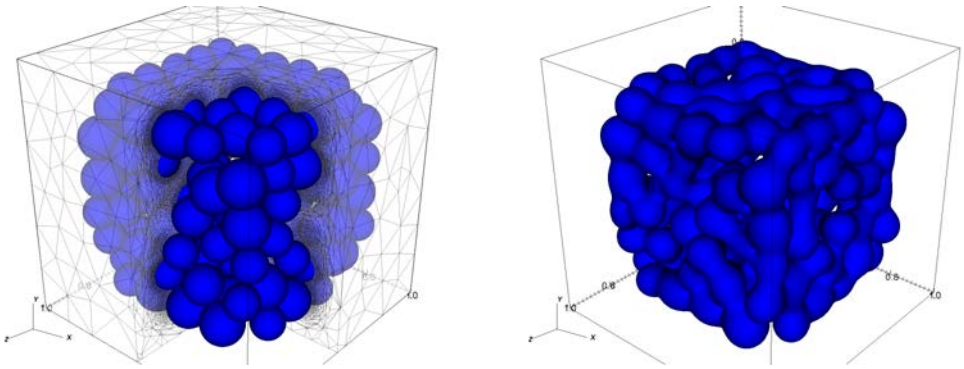

a. $t = 0$s b. $t = 0.08$s

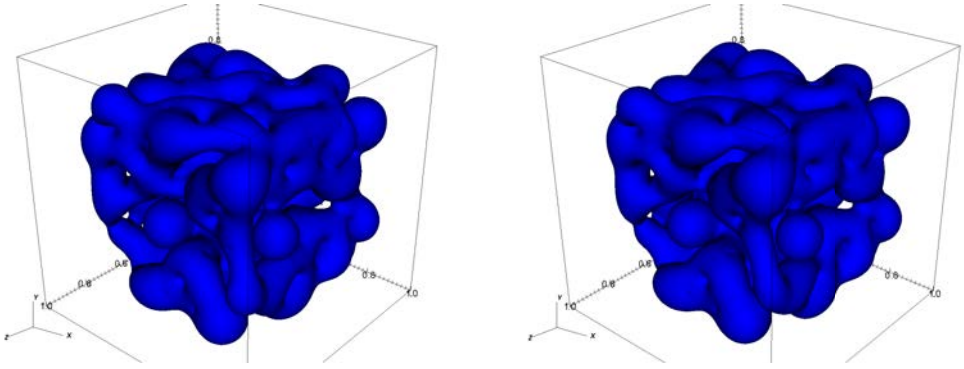

c. $t = 1.08$s d. $t = 1.624$

Figure 7.9: Evolution of a structure built-up of about 150 particles at different time steps: a. $t = 0$s (the adapted mesh is also plotted); b. $t = 0.08$s; c. $t = 1.08$s; d. $t = 1.624$s.

Figures 7.9b, 7.9c and 7.9d show the structure of the compact powder at $t = 0.08$s, $t = 1.08$s and $t = 1.624$s, respectively. It can be seen that the structure undergoes strong topological

changes. The total surface of the particles represents a part of the free energy of the system, therefore a easy way to quantity the reduction of this energy is to measure the total surface of the powder compact. Figure 7.10 shows how the total surface of the system decreases as the volume diffusion takes place. The total volume of the powder compact was, at the beginning of the simulation, $0.2272\mu\text{m}^3$ and after $t = 1.624$s the volume increased of about $1.17 \cdot 10^{-3}\% \approx 2.66 \cdot 10^{-4}\mu\text{m}^3$. The total volume of the compact powder can be considered to be conserved and the total surface of the particles decreases of about 30% as it can be seen in Figure 7.10.

Even if the evolution of the structure seems to be in agreement with the kinetics of the process, it is very difficult to validate the numerical result as there is no experimental data. However the capabilities of the method to simulate the sintering process by volume diffusion over realistic 3D powder compacts has been demonstrated with this example.

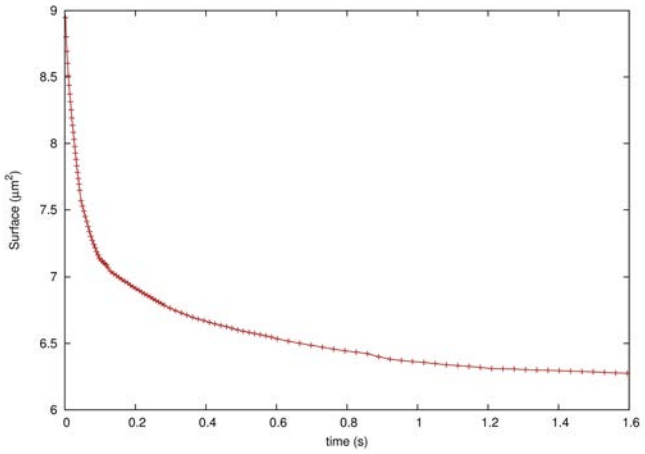

Figure 7.10: Evolution of the total surface of the system over the time.

7.4 Conclusions

The numerical approach presented in this chapter allows to perform simulations of sintering by volume diffusion without any restriction regarding the shape or the geometry of the compact powder. The artificial volume conservation procedure allows to successfully ensure the conservation of volume of the particles throughout the whole simulation for 2D and 3D problems. The growth of the neck between two particles by volume diffusion has been compared with the analytical models presented in Chapter 3 and the approach developed for the volume diffusion path leads to a good simulation of the process kinetics.

Even if the experimental validation of this kind of simulation is very complicated and probably not even possible as for today, the results of this work can be used to feed other models that would allow to enhance the understanding the underlying physical phenomena. In the next chapter, an approach for the coupling between the volume diffusion and the surface diffusion is presented, and at the same time, the numerical strategy for the integration of the grain boundary diffusion into the computational framework will be established.

7.5 Résumé en français : Frittage par diffusion volumique

Une stratégie numérique pour le calcul de la pression ayant été fixée, une méthode pour la simulation du frittage par diffusion volumique peut être proposée dans ce chapitre. Une fois le champ de pression calculé, le flux de matière et la vitesse de diffusion volumique doivent être calculés, ce qui soulève des nouvelles difficultés. La tension surfacique induit une discontinuité de la contrainte normale. Cette discontinuité est aussi présente dans le champ de pression à travers la surface des particules. Cependant, le gradient de la pression doit être calculé à la surface des particules justement où ce gradient n'est pas défini. Or, dans le cadre Level-Set présenté, la vitesse doit être calculée des deux cotés de l'interface.

Afin de résoudre ce problème, trois approches numériques ont été proposées. Ces trois approches sont basées sur une seule idée : utiliser la vitesse calculée sur une couche légèrement à l'intérieur des particules et ensuite étendre cette vitesse à l'extérieur de la surface des particules. Des comparaisons entre ces approches ont été faites et la convection instantanée de la vitesse a montré qu'elle permet d'obtenir des très bons résultats avec des temps de calculs acceptables.

Le volume de mati1ere du compact pulvérulent doit rester constant pendant le procédé de frittage. Cependant, la vitesse induite par la diffusion volumique mène à un changement du volume au cours du temps. Il est possible de trouver dans la littérature quelques méthodes qui permettent d'assurer la conservation du volume, mais la plupart de ces méthodes sont limitées à des cas 2D ou bien leur application à des problèmes 3D est très complexe. Pour cette raison une méthode alternative, dans laquelle une vitesse artificielle est ajoutée, a été developpée. Cette méthode permet de garantir la conservation du volume pendant toute la simulation du frittage en 2D et 3D.

En utilisant toutes ces approches numériques, pour le calcul de la pression, le calcul de la vitesse et la conservation du volume, il a finalement été possible de réaliser des simulations du frittage par diffusion volumique. Comme première validation, la croissance du cou entre deux particules de la même taille a été comparée avec succès aux prédictions données par les modèles analytiques. Par contre la validation des résultats sur des empilements de particules plus proches de la réalité est très compliquée car aucun résultat expérimental n'est disponible. Les résultats obtenus représentent, au moins à la connaissance des auteurs, la première tentative réussie de simulation du frittage par diffusion volumique en 3D.

Chapter 8

Toward a full sintering simulation

Contents

Sintering is a very complex process and the microstructural evolution of the system is thermo-physically controlled by the diffusion phenomena which will lead to reduction of free energy. During sintering different diffusion mechanisms (surface, volume, grain boundary, etc...) take place at the same time, therefore it is necessary to establish a coupling between the different diffusion mechanisms in order to simulate the complete process of sintering. So far the grain boundary diffusion has not been tackled, however the coupling between surface and volume diffusions represents a further step toward the complete sintering simulation. In this chapter a way to couple the surface (Chapter 5) and volume (Chapter 7) diffusions is presented in Section 8.1 and the numerical results obtained by using this approach are discussed in Section 8.2.

The grain boundary diffusion remains a very important mechanism, therefore the bases for the introduction of this diffusion path are set. As a first step toward the sintering simulation by grain boundary diffusion, the surface tension that is present over the grain boundary between the particles has to be considered in the mechanical problem. A strategy allowing to take into

account this grain boundary surface tension is presented in Section 8.3. Finally the conclusions are discussed in Section 8.4.

8.1 Coupled velocity computation

In order to establish a coupling method for those two diffusion paths, some hypotheses have to be made. The surface diffusion matter flux $\underline{j^s}$ and the volume diffusion matter flux $\underline{j^v}$ are assumed to be independent and therefore the corresponding velocities are also independent. Additionally, the two diffusion mechanisms are supposed to occur simultaneously. In fact, as it has been shown in Chapters 5 and 7, those diffusion fluxes mainly depend on the geometry of the structure and more precisely on the curvature κ. The surface diffusion matter flux $\underline{j^s}$ is directly proportional to the surface gradient of the curvature and the volume diffusion matter flux is proportional to the pressure gradient which also depends on the curvature through Laplace's law. Therefore by considering the structure at a time t, it is possible to compute the matter flux corresponding to each diffusion path at t:

$$\underline{j^s} = -A_0 \underline{\nabla_s \kappa} \tag{8.1}$$

$$\underline{j^v} = -A_1 \underline{\nabla p} \tag{8.2}$$

where $A_0 = \frac{D_s \gamma_{sv}}{kT}$, $A_1 = (1-f)\, D_v / kT$ and p is the pressure.

In Chapter 2 (Section 2.2.5), the diffusion induced velocities $\underline{v^s}$ and $\underline{v^v}$ were shown to be oriented in the normal direction:

$$\underline{v^s} = \Omega A_0 \Delta_s \kappa \underline{n} \tag{8.3}$$

$$\underline{v^v} = -\Omega A_1 \underline{\nabla p} \cdot \underline{n}\, \underline{n} \tag{8.4}$$

with Ω the atomic volume and $\underline{n}$ the outward normal.

As both diffusion paths take place simultaneously, a very simple way to establish a coupling between the two diffusion paths consists in computing the coupled velocity $\underline{v^{coupled}}$ as the result of the vectorial addition of each individual diffusion velocity:

$$\begin{aligned} \underline{v}^{coupled} &= \underline{v^s} + \underline{v^v} \\ \Rightarrow \quad \underline{v}^{coupled} &= \Omega \left(A_0 \Delta_s \kappa - A_1 \underline{\nabla p} \cdot \underline{n} \right) \underline{n} \end{aligned} \tag{8.5}$$

Figure 8.1 shows a schematic example of a region of a particle under surface and volume diffusions. Each diffusion mechanism induces its corresponding diffusion velocity, $\underline{v^s}$ and $\underline{v^v}$. The coupled diffusion velocity is given by Equation (8.5) and corresponds to the purple vector shown in Figure 8.1.

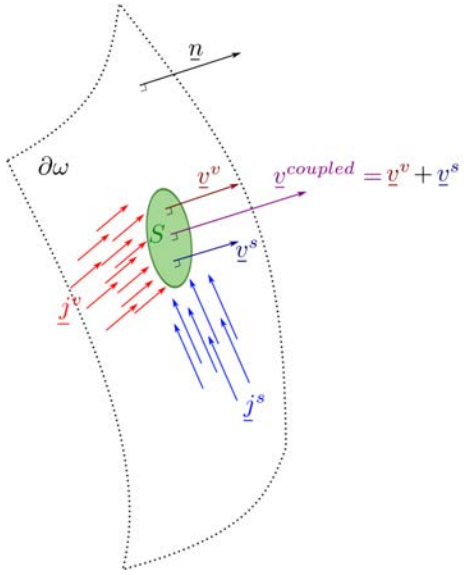

Figure 8.1: Schematic representation of simultaneous surface and volume diffusions inducing a coupled diffusion velocity $\underline{v}^{coupled}$.

In the next section, the time stepping algorithm and some numerical examples of coupling between those two diffusion mechanisms are presented.

8.2 Numerical results

Algorithm 5 is used to simulate the sintering by coupled diffusion. In fact, this algorithm is a combination of Algorithms 3 and 4 for surface diffusion and volume diffusion, respectively.

The coupled diffusion velocity $\underline{v}^{coupled}$ is the results of two different diffusion velocities: $\underline{v^s}$ and $\underline{v^v}$. It has been shown previously in Chapter 5, that the velocity induced by surface

Algorithm 5 Time stepping algorithm for the coupled diffusion strategy developed.

$\phi_h^t \leftarrow$ From Algorithm 2 (page 70) for a given geometry at $t = 0$.
$\mathcal{T}_h(\Upsilon)$: Initial mesh adaptation by using ϕ_h^t at $t = 0$
$V_0 \leftarrow$ From Equation (7.15)
for $t = 0 \rightarrow (t_f - \Delta t)$ with ϕ_h^t known at the current time t **do**
  $(\underline{v_h}, p_h) \leftarrow$From the resolution of the mechanical problem (system (6.20) and (6.21))
  $\underline{v^v} \leftarrow$Volume diffusion velocity (From Equation (7.6))
  $\underline{v^{st}} \leftarrow$From Equations (5.9) and (5.15)
  $\underline{v^{coupled}} \leftarrow$From Equation (8.5)
  $\phi_h^{t+\Delta t} \leftarrow$From the resolution of the convective-reinitialization Equation (4.19)
  $\Delta V \leftarrow$Volume change induced by the volume diffusion velocity (From Equation (7.16))
  $\underline{v^{avc}} \leftarrow$Artificial volume conservation velocity (From Equations (7.12) and (7.17))
  $\phi_h^{t+\Delta t} \leftarrow$From the resolution of the convective-reinitialization Equation (4.19) [a]
  $t \leftarrow t + \Delta t$
  $\mathcal{T}_h(\Upsilon) \leftarrow$Remeshing step every f_{rem} time steps.
end for
$\phi_h^{t_f} \rightarrow$ Output of the simulation at $t = t_f$.

a. Volume conservation enforcement.

diffusion ($\underline{v^s}$) does not lead to a change of the volume of the compact powder. However, the induced volume diffusion velocity ($\underline{v^v}$) can lead to a change of the volume of the particles. For this reason, when the coupled surface and volume diffusions are considered, it is necessary to add a step aiming at the volume conservation. This volume conservation step is performed by using the same approach presented for the volume diffusion in Section 7.2. In this case, the artificial volume conservation velocity $\underline{v^{avc}}$ is computed after the transport of the level set function under the coupled velocity ($\underline{v^{coupled}}$) has been performed.

The material properties used in the following simulations correspond to the properties of Alumina (Al_2O_3) and are summarized in Table 8.1. It is important to recall that the diffusion related properties are significantly larger than the real properties of the material, but this does not have an impact on the kinectics of the phenomena.

Property	Value	Units
$D_s\Omega\gamma_{sf}\delta_s/kT$	$1{\cdot}10^{-7}$	m mol/s
$D_v\Omega\left(1-f\right)/kT$	55.16	m mol/N s
K	260	GPa
μ	156	GPa
η	1e-3	Pa/s
γ_{sf}	0.9	N/m
Ω	$8.55{\cdot}10^{-6}$	m^3/mol

Table 8.1: Material properties used.

8.2.1 Two particles

Surface and volume diffusions are coupled to simulate the sintering of two particles by these two diffusion mechanisms. Figure 8.2 shows the evolution of two particles as they sinter together by surface and volume diffusions. Figure 8.2a presents the initial state of the particles, they are set to be quasi-tangent. After 50 time steps, the neck between the particles is about 30% of the particle radius, as it is shown in Figure 8.2b. The power laws presented in Section 3.1 (page 24) can be used for values of the neck radius $X < 0.3R$. It is interesting to see how the two particles evolve beyond this limit (Figure 8.2c), they can no longer be considered to remain spherical.

a. t_0 b. t_1 c. t_2

Figure 8.2: Two particles sintering by coupled surface and volume diffusion at: a. $t = 0$, b. $t = 50\Delta t$ and c. $t = 100\Delta t$.

In Chapter 5 it was highlighted that the velocity induced by surface diffusion should lead to the conservation of the volume of the compact powder. However, because of the numerical approach, the volume of the particles changes, in a very slight way but it still changes. In the coupled case, the change of the volume of the compact powder is mainly due to the volume diffusion velocity, but the surface diffusion velocity is still responsible for a small fraction of this volume change. The introduction of the artificial volume conservation velocity $\underline{v^{avc}}$ allows to recover the change of the volume induced for both diffusion paths. Considering the case of two particles sintering by coupled diffusion, the maximum change in the volume of the particles after volume conservation recovery is about 0.0035%. For this reason, volume can be considered to remain constant.

When the surface and volume diffusions mechanisms were presented (Chapters 5 and 7, respectively), the case of two particles was used to validate the results obtained. The analytical models for the growth of the neck between the particles presented in Chapter 3 (Table 3.2) can be written, in a general way for any diffusion mechanism, as follows:

$$\frac{x}{R} = B(R)\, t^{1/n} \tag{8.6}$$

where $B(R)$ is a constant that depends on the particles radius R and the diffusion properties of the materials. The exponent n is the parameter that describes the kinetics of the concerned diffusion paths. The evolution of the adimensional neck radius x/R for two particles of radius $R = 0.2\mu$m is considered. First, the surface and the volume diffusion were considered alone. The evolution of the adimensional neck radius x/R for these two diffusion mechanisms is plotted in Figure 8.3, where the red and the green lines correspond to the surface and volume diffusions, respectively. As stated in the previous Chapters 5 and 7, the kinectics of these two diffusion mechanisms is well represented by the numerical approach developed. The evolution of the adimensional neck radius x/R for the coupled diffusion is also plotted in Figure 8.3 with a blue line. As expected the neck growth is significantly faster when the coupled diffusion is considered. By using a least squares interpolation of the obtained data, the exponent corresponding the coupled diffusion is $n = 3.29$. Validation of this coupling is very complex since analytical models for the neck growth are not available for these two mechanisms working simultaneously. However, by considering the kinetics obtained, it is possible to say that the results are qualitatively correct.

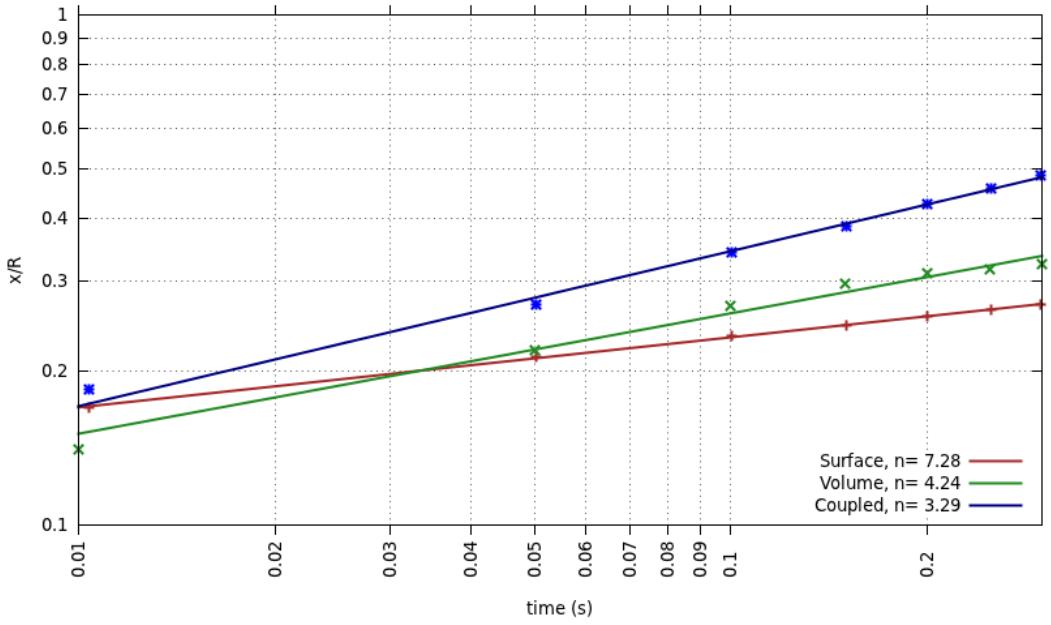

Figure 8.3: Evolution of the adimensional neck radius x/R over the time t (logarithmic scale.

It is possible to compare the neck growth obtained with each mechanism individually and the growth obtained with the coupled approach. The same simulation shown in Figure 8.2 was performed in three different ways: by using only the surface diffusion, then by using volume

diffusion alone and finally with the coupled approach. The results of the three simulations are shown in Figure 8.4. As expected, the neck grows significantly faster when surface and volume diffusion take place simultaneously.

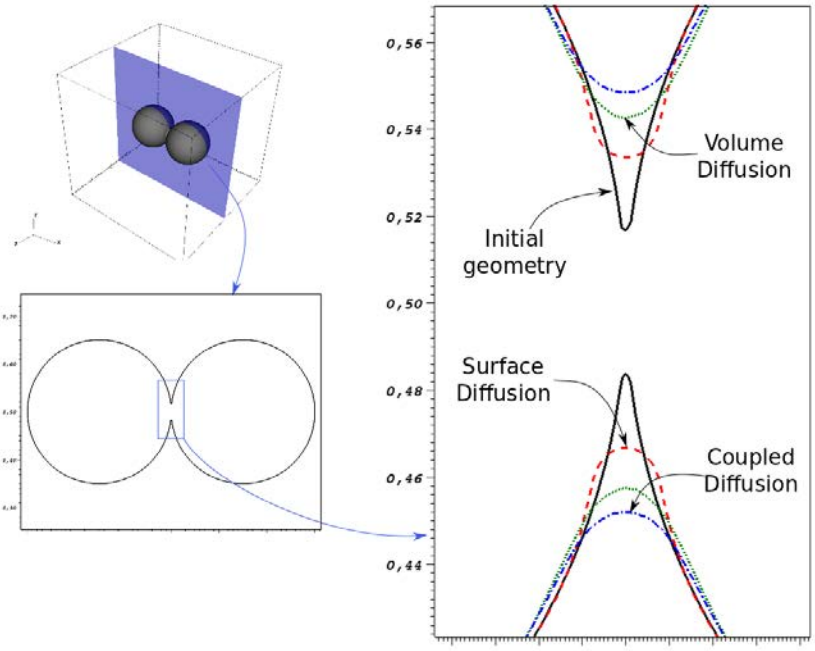

Figure 8.4: Geometry of the neck between the particles after 65 time steps.

8.2.2 Particles packing sintering

A sintering simulation by coupled surface and volume diffusions over a more realistic particles packing is presented. A set of 154 particles with radii ranging from 0.0633 μm to 0.0797 μm is embedded into a computational domain given by a cube of side 1.2 μm. The material properties used are presented in Table 8.1. Figure 8.5a shows the initial particles packing as well as a cut of the refined mesh that is made up of about 2 millions nodes and about 11 millions tetrahedral elements.

The evolution of the structure is shown in Figures 8.5a to 8.5d. In the initial geometry (Figure 8.5a) particles are set to be quasi-tangent. As the volume diffusion takes place, the necks between the particles grow up to a point (Figure 8.5d) where the particles can not be distinguished any more.

One of the most important advantages of the numerical approach developed in this work is related to its capability to supply information about the local state of the structure at any

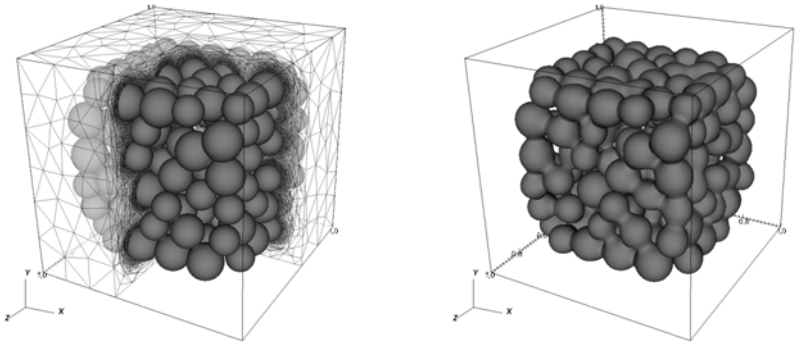

a. $t = 0$ & Adapted mesh

b. $t = 65\Delta t$

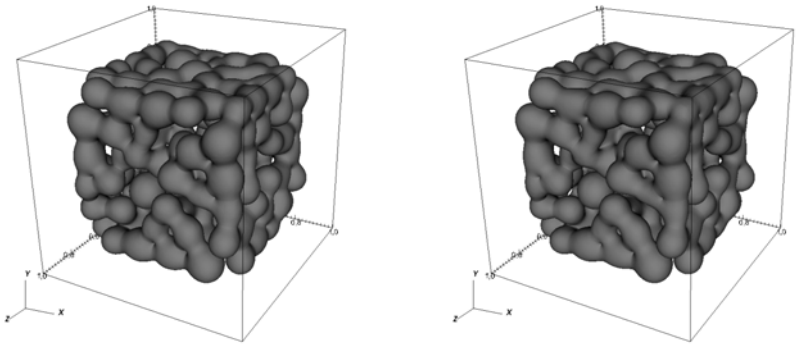

c. $t = 130\Delta t$

d. $t = 170\Delta t$ (All the pores)

Figure 8.5: Evolution of a particle packing through the time.

time step. Furthermore, as the surface and volume diffusions are coupled together, the results obtained should get closer to the microstructures that can be obtained in real experiments, but still important differences are present. Specially, the grain boundary diffusion mechanism has a huge contribution among the diffusion paths and therefore it is not yet possible to make qualitative comparisons with the results available experimentally where all the diffusion mechanisms are activated. Nevertheless, important information can be extracted of this kind of simulation.

For example the particles packing presented in Figure 8.5a was initially formed by a set of 154 particles with no closed porosity. As coupled diffusion takes place, the structure evolves and closed porosity appears after about 250 time steps ($t \approx 0.2$s). Figure 8.6a shows the first pore that appeared inside the compact powder. In fact this pore evolves until a roughly

spherical shape is reached (Figures 8.6a, 8.6b and 8.6c). The structure continues evolving and after $520\Delta t$ it is possible to identify multiple pores of different sizes inside the compact powder, as it can be seen in Figure 8.6d.

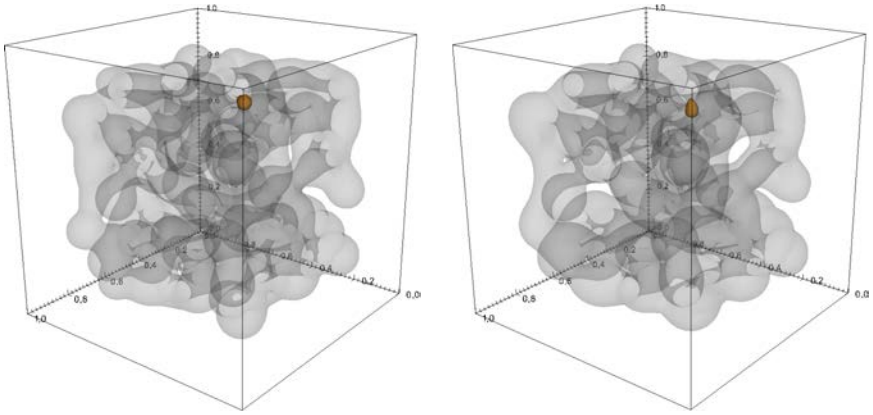

a. $t = 270\Delta t$ b. $t = 350\Delta t$

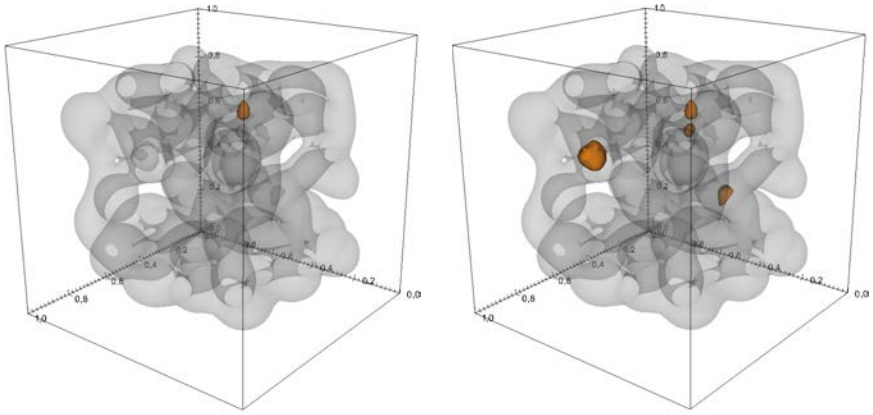

c. $t = 520\Delta t$ d. $t = 520\Delta t$ (All the pores)

Figure 8.6: Closed porosity at different time steps: a. $t = 270\Delta t$, b. $t = 350\Delta t$ and c. $t = 520\Delta t$. All the pored developed d.

As stated previously, neither the mass nor the density of the particles change during the sintering process, the volume of the particles must remain constant. Considering the simulation shown in Figure 8.5, the change of total volume of the particles after 200 time steps is about 0.12%, which is negligible. This simulation involves 550 time steps and has been performed in about 245h by using a parallel computing strategy on 24 cores.

8.3 Toward the grain-boundary diffusion

The chemical potential associated with grain boundary diffusion is proportional to the normal stress σ_{nn}. Furthermore, the velocity induced by the grain boundary matter flux is function of the second derivative of this normal stress. The first step toward the sintering simulation by grain boundary diffusion therefore consists in developing a strategy able to solve the mechanical problem by taking into account, in addition to the surface tension at the free surface of the particles, the surface tension present at the grain boundary.

In this way another challenge has to be handled in order to introduce the grain boundary diffusion mechanism into the numerical approach presented here. In fact, when the grain boundary is considered, an additional term has to be added to the formulation of the mechanical problem. This additional term corresponds to the surface tension present over the grain boundary. Therefore, the numerical approach used to solve the mechanical problem (Chapter 6) has to be modified in order to take into account both surface tensions.

In this work, a numerical strategy taking into account the surface tension over the grain boundary is proposed. The approach is intended to be used within the context of grain boundary diffusion. However the numerical strategy concerning this diffusion path will be developed in a forthcoming work.

8.3.1 Surface tension at the grain boundary

In order to introduce the formulation of the mechanical problem containing the grain boundary surface tension term, consider two solids (two particles) Ψ_s^1 and Ψ_s^2. Both particles are in contact, therefore a section of their surface is shared which forms the grain boundary $\Gamma_{s/s}$. Figure 8.7 shows the two solids Ψ_s^1 and Ψ_s^2 and the grain boundary $\Gamma_{s/s}$ formed between them.

The mechanical problem that has to be solved corresponds, again, to the momentum conservation which can be expressed as follows:

$$\begin{aligned} \underline{\nabla} \cdot \underline{\underline{\sigma}} &= \underline{0} && \text{in } \Psi, \\ \underline{\underline{\sigma}} \cdot \underline{n^f} &= -p_e \, \underline{n^f} && \text{in } \Sigma_t, \\ \underline{v} &= \underline{v_c} && \text{in } \Sigma_v \end{aligned} \tag{8.7}$$

where $\underline{\underline{\sigma}}$ is the *Cauchy* stress tensor for the solids or the fluid. p_e is the pressure applied on the outer boundary Σ_t, $\underline{n^f}$ is the outward normal to Σ_t and velocity $\underline{v}$ is equal to $\underline{v_c}$ over Σ_v. The

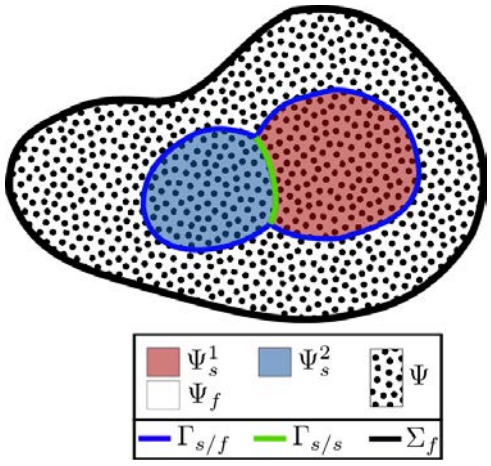

Figure 8.7: Schematic representation of the computational domain containing the surrounding medium Ψ_f and two solids (Ψ_s^1 and Ψ_s^2). $\Gamma_{s/s}$ corresponds to the grain boundary between the particles.

procedure used to obtain the mixed formulation containing the grain boundary surface tension is very similar to the one presented in Chapter 6, therefore here only an overview is developed.

Both solids are considered to be linear elastic materials like in Chapter 6 (Section 6.1). The *Cauchy* stress tensor $\underline{\underline{\sigma}}^s$ and the mass conservation Equations are given by:

$$\underline{\underline{\sigma}}^s(\underline{u}) = 2\mu\underline{\underline{\epsilon}}(\underline{u}) - \left(1 - \frac{2}{3}\frac{\mu}{K}\right) p\underline{\underline{\mathcal{I}}} \tag{8.8}$$

$$\operatorname{div}\underline{u} + \frac{p}{K} = 0 \tag{8.9}$$

On the other hand, the *Cauchy* stress tensor $\underline{\underline{\sigma}}^f$ and the mass conservation for the fluid phase (incompressible Newtonian fluid) are given by:

$$\underline{\underline{\sigma}}^f(\underline{v}) = 2\eta\underline{\underline{\dot{\epsilon}}}(\underline{v}) - p\underline{\underline{\mathcal{I}}} \tag{8.10}$$

$$\operatorname{div}\underline{v} = 0 \tag{8.11}$$

As stated previously, there are two interfaces where the surface tension phenomena are present: the solid/fluid interface $\Gamma_{s/f}$ and the solid/solid interface $\Gamma_{s/s}$. The jump of the stress vector $\underline{\underline{\sigma}} \cdot \underline{n}$ is given by:

$$\left[\,(\underline{\underline{\sigma}}\cdot\underline{n})\,\right]|_{\Gamma_{s/f}} = \gamma_{sf}\kappa\underline{n} + \underline{\nabla}_s\gamma_{sf} \tag{8.12}$$

$$\left[\,(\underline{\underline{\sigma}}\cdot\underline{n})\,\right]|_{\Gamma_{s/s}} = \gamma_{ss}\kappa\underline{n} + \underline{\nabla}_s\gamma_{ss} \tag{8.13}$$

where γ_{ss} is the surface tension coefficient at the interface between the two particles. As before, the surface tension coefficients γ_{sf} and γ_{ss} are assumed to be constant and the previous expressions (8.12) and (8.13) write:

$$\left[\,(\underline{\underline{\sigma}}\cdot\underline{n})\,\right]|_{\Gamma_{s/f}} = \gamma_{sf}\kappa\underline{n} \tag{8.14}$$

$$\left[\,(\underline{\underline{\sigma}}\cdot\underline{n})\,\right]|_{\Gamma_{s/s}} = \gamma_{ss}\kappa\underline{n} \tag{8.15}$$

Because of mass conservation across the interface, the normal velocity has to be continuous across those interfaces:

$$[\underline{v}\cdot\underline{n}]|_{\Gamma_{s/f}} = 0 \tag{8.16}$$

$$[\underline{v}\cdot\underline{n}]|_{\Gamma_{s/s}} = 0 \tag{8.17}$$

The mixed variational formulation of Equation (8.7) for the elastic solid Ψ_s^1 consists in finding $(\underline{u}, p)$ in $(V(\Psi_s^1)^d \times Q(\Psi_s^1))$ such that [1]:

$$\int_{\Psi_s^1} 2\mu_1\underline{\underline{\epsilon}}(\underline{u}) : \underline{\underline{\epsilon}}(\underline{w})\,dV - \int_{\Psi_s^1}\left(1-\frac{2}{3}\frac{\mu_1}{K_1}\right)p\,\mathrm{div}(\underline{w})\,dV = \underbrace{\int_{\Gamma_{s/f}}(\underline{\underline{\sigma}}^s\cdot\underline{n}_1^s)\cdot\underline{w}\,dS}_{\text{Stress vector at }\Gamma_{s/f}} + \underbrace{\int_{\Gamma_{s/s}}(\underline{\underline{\sigma}}^s\cdot\underline{n}_1^s)\cdot\underline{w}\,dS}_{\text{Stress vector at }\Gamma_{s/s}} \tag{8.18}$$

$$\int_{\Psi_s^1}\mathrm{div}(\underline{u})q\,dV + \int_{\Psi_s^1}\frac{p}{K_1}q\,dV = 0 \tag{8.19}$$

where $\underline{n}_1^s$ is the unit normal pointing outward the solid Ψ_s^1, μ_1 and K_1 are the shear modulus and the bulk modulus of the solid Ψ_s^1.

In the same way, the mixed variational formulation of Equation (8.7) for the elastic solid

1. $(V(\Psi_s^1)^d$ and $Q(\Psi_s^1))$ correspond to the functional spaces defined in Section 6.1.4 (page 93).

Ψ_s^2 is given by:

$$\int_{\Psi_s^2} 2\mu_2 \underline{\underline{\epsilon}}(\underline{u}) : \underline{\underline{\epsilon}}(\underline{w})\, dV - \int_{\Psi_s^2} \left(1 - \frac{2}{3}\frac{\mu_2}{K_2}\right) p \,\mathrm{div}(\underline{w})\, dV = \underbrace{\int_{\Gamma_{s/f}} (\underline{\underline{\sigma}}^s \cdot \underline{n}_2^s) \cdot \underline{w}\, dS}_{\text{Stress vector at } \Gamma_{s/f}} + \underbrace{\int_{\Gamma_{s/s}} (\underline{\underline{\sigma}}^s \cdot \underline{n}_2^s) \cdot \underline{w}\, dS}_{\text{Stress vector at } \Gamma_{s/s}} \tag{8.20}$$

$$\int_{\Psi_s^2} \mathrm{div}(\underline{u}) q\, dV + \int_{\Psi_s^2} \frac{p}{K_2} q\, dV = 0 \tag{8.21}$$

with $\underline{n}_2^s$ the unit normal pointing outward the solid Ψ_s^2, μ_2 and K_2 are the shear modulus and the bulk modulus of the solid Ψ_s^2.

Finally, the mixed variational formulation for an incompressible fluid is given by:

$$\int_{\Psi_f} 2\eta \dot{\underline{\underline{\epsilon}}}(\underline{v}) : \underline{\underline{\epsilon}}(\underline{w})\, dV - \int_{\Psi_f} p \,\mathrm{div}(\underline{w})\, dV = \int_{\Sigma_t} (-p_e \underline{n}^f) \cdot \underline{w}\, dS + \underbrace{\int_{\Gamma_{s/f}} (\underline{\underline{\sigma}}^f \cdot \underline{n}^f) \cdot \underline{w}\, dS}_{\text{Stress vector at } \Gamma_{s/f}} \tag{8.22}$$

$$\int_{\Psi_f} \mathrm{div}(\underline{v})\, q\, dV = 0 \tag{8.23}$$

The numerical strategy used to integrate Equations (8.18) to (8.23) into a single monolithical mixed formulation is presented in the next section.

8.3.2 Numerical strategy

The level-set method used has shown its capability to handle strong topological changes over complex geometries in 2D and 3D. However, when a single level-set function ϕ is used, it is only possible to track one interface separating two different phases. If the grain boundary is introduced, different solids (particles) have to be described and multiple interfaces can appear (free surfaces and grain boundaries). Considering this, it is not longer possible to track either the free surface $\Gamma_{s/f}$ and the grain boundary $\Gamma_{s/s}$ by using a single level set function ϕ. In fact, this problem contains at least three different phases therefore at least two different level set fuctions are required.

The approach proposed here consists in using at least two level set functions. Indeed, the

number of level set function required can be different according to the number of particles to be tracked. The simplest solution is to use one level set function for each particle, however this solution is computationally very expensive. Another solution consists in describing multiple particles with one level set, this method is called coloration algorithm (see [Hitti 2011]). In that case, the choice of the particles belonging to the same level set function has to be made in such a way that they do not get in contact throughout the whole simulation. In fact, if two particles described by the same level set get in contact, no grain boundary would be created and the two particles would become a single one.

For example, two level set functions ϕ_1 and ϕ_2 are used to track the surface of the particles Ψ_s^1 and Ψ_s^2 respectively (Figure 8.7). ϕ_1 and ϕ_2 are given by:

$$\phi_1(\underline{x}) = \begin{cases} -\text{dist}\left(\underline{x}, \partial\Psi_s^1\right) & \text{if } \underline{x} \in \Psi_s^1 \\ \text{dist}\left(\underline{x}, \partial\Psi_s^1\right) & \text{if } \underline{x} \notin \Psi_s^1 \\ 0 & \text{if } \underline{x} \in \partial\Psi_s^1 \end{cases} \quad ; \quad \phi_2(\underline{x}) = \begin{cases} -\text{dist}\left(\underline{x}, \partial\Psi_s^2\right) & \text{if } \underline{x} \in \Psi_s^2 \\ \text{dist}\left(\underline{x}, \partial\Psi_s^2\right) & \text{if } \underline{x} \notin \Psi_s^2 \\ 0 & \text{if } \underline{x} \in \partial\Psi_s^2 \end{cases} \tag{8.24}$$

In this way, the grain boundary $\Gamma_{s/s}$ is defined by the surface where both level set functions are equal to zero (Equation (8.26)). The solid/fluid interface $\Gamma_{s/f}$ is defined by the surface where only one of the level set functions is equal to zero:

$$\Gamma_{s/f} = \{\underline{x} \in \mathcal{R}^n, [\phi_1(\underline{x}, t) = 0) \cap \phi_2(\underline{x}, t) \neq 0] \cup [\phi_1(\underline{x}, t) \neq 0) \cap \phi_2(\underline{x}, t) = 0]\} \tag{8.25}$$

$$\Gamma_{s/s} = \{\underline{x} \in \mathcal{R}^n, [\phi_1(\underline{x}, t) = 0) \cap \phi_2(\underline{x}, t) = 0]\} \tag{8.26}$$

In the mechanical problem presented in Chapter 6, there were only two phases: the solid and the surrounding medium. However as the grain boundary is introduced more phases have to be handled (multiple solids and the surrounding medium). For this reason it is also necessary to define a Heaviside function associated with each level set function used. Considering the case of two level set functions (ϕ_1 and ϕ_2), three Heaviside functions are defined:

$$H_s^1(\phi_1) = \begin{cases} 1 & \text{if } \phi_1 \leq 0 \\ 0 & \text{if } \phi_1 > 0 \end{cases} \tag{8.27}$$

$$H_s^2(\phi_2) = \begin{cases} 1 & \text{if } \phi_2 \leq 0 \\ 0 & \text{if } \phi_2 > 0 \end{cases} \tag{8.28}$$

$$H_f(\phi_1, \phi_2) = 1 - H_s^1(\phi_1) - H_s^2(\phi_2) \tag{8.29}$$

where H_s^1, H_s^2 and H_f are respectively the Heaviside functions associated with Ψ_s^1, Ψ_s^2 and Ψ_f (see Figure 8.7).

Again, by using the same time discretization such as presented in Chapter 6 (Section 6.2.1), the mixed weak formulations of the solids Ψ_s^1 and Ψ_s^2 (Equations (8.18) to (8.21)) are written in terms of velocity $\underline{v}$ and pressure p:

$$\begin{aligned} \int_\Psi 2\left(H_s^1\mu_1\Delta t + H_s^2\mu_2\Delta t + H_f\eta\right)\underline{\underline{\dot{\epsilon}}}(\underline{v}) : \underline{\underline{\dot{\epsilon}}}(\underline{w})\, dV - \\ \int_\Psi \left(H_s^1\left(1 - \frac{2}{3}\frac{\mu_1}{K_1}\right) + H_s^2\left(1 - \frac{2}{3}\frac{\mu_2}{K_2}\right) + H_f\right) p\,\mathrm{div}(\underline{w})\, dV = \\ \underbrace{\int_{\Gamma_{s/f}} \gamma_{sf}\kappa\underline{n}\cdot\underline{w}\, dS}_{\text{Surface tension over } \Gamma_{s/f}} + \underbrace{\int_{\Gamma_{s/s}} \gamma_{ss}\kappa\underline{n}\cdot\underline{w}\, dS}_{\text{Surface tension over } \Gamma_{s/s}} + \\ \int_{\Sigma_f} (-p_e\,\underline{n}^f)\cdot\underline{w}\, dS - \int_\Psi 2H_s(\phi)\mu\underline{\underline{\epsilon}}(\underline{u}^{t-\Delta t}) : \underline{\underline{\epsilon}}(\underline{w})\, dV \end{aligned} \tag{8.30}$$

$$\begin{aligned} \int_\Psi \mathrm{div}(\underline{v}) q\, dV + \int_\Psi \left(H_s^1\frac{p}{K_1\Delta t} + H_s^2\frac{p}{K_2\Delta t}\right) q\, dV = \\ -\int_\Psi \left(\frac{H_s^1}{\Delta t} + \frac{H_s^2}{\Delta t}\right)\mathrm{div}(\underline{u}^{t-\Delta t}) q\, dV \end{aligned} \tag{8.31}$$

The numerical approach used to solve the mixed formulation (8.30) and (8.31) is exactly the same presented in Chapter 6. The Surface Local Reconstruction method (SLR, Section 6.2.3.1) is used to perform the integration over both interfaces $\Gamma_{s/f}$ and $\Gamma_{s/s}$. However special attention has to be paid to the element containing the triple point shown in Figure 8.8a.

In fact, the triple point will be placed by contruction of the intersection of the level set functions over an edge of an element as shown in Figure 8.8a. Therefore there will be an element containing three phases: the two solids and the surrounding medium. Then, the numerical computation of the volume integrals of the mixed formulation (8.30) and (8.31) can

be tricky, specially in 3D. Furthermore, it would be necessary to develop a special routine to deal with the elements containing the triple points.

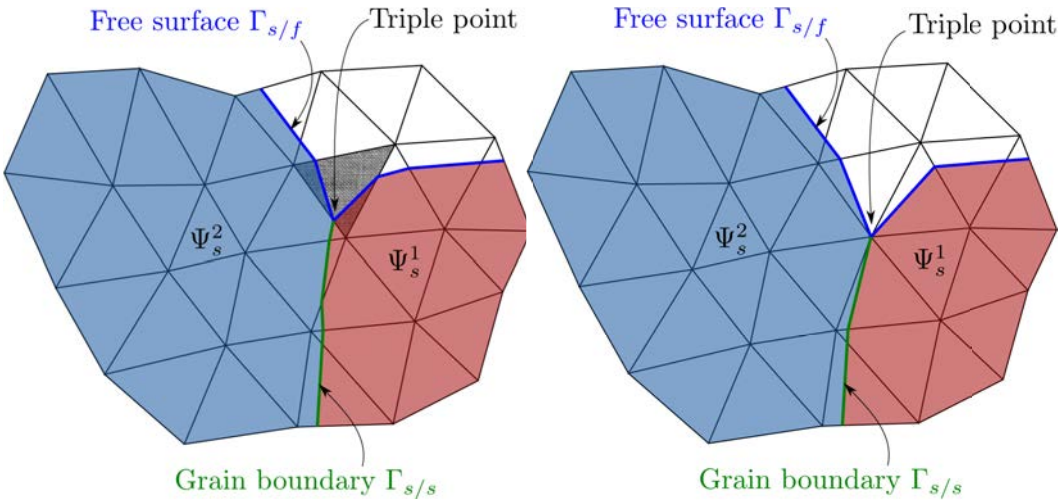

a. Original geometry b. Translated triple point

Figure 8.8: Schematic representation of a mesh containing two solids Ψ_s^1 and Ψ_s^2. a. General geometry of the structure near to the triple point (the shaded element corresponds to the element containing the triple point.) b. Geometry of the structure after the triple point is translated.

In order to avoid those numerical difficulties, another solution is proposed. The idea is to translate the triple point in such a way that it is placed on a node where the level set functions are strictly defined. The new position of the triple point is given by the closest node to the original triple point. Figure 8.8b shows how the original triple point (Figure 8.8a) has been translated to the closest node. Considering that the simulation are carried by using a mesh adaptation strategy (Section 4.4), the change of the structure induced by the translation of the triple point can be considered as negligible.

8.3.3 Results

The numerical strategy for the mechanical problem presented in Chapter 6 is modified to take into account the surface tension at the grain boundary. The surface tension present over the grain boundary induces a discontinuity of the normal stress that is proportional to the curvature of the interface, in this case the curvature of the grain boundary. Therefore, in order to obtain a jump of the normal stress across the grain boundary, the grain boundary can not

be flat (i.e., it must have a curvature different from zero).

As a simple example, two spherical particles with the same radii R were considered. The two particles were placed inside the computational domain in such a way that the distance between the centers of the particles was smaller than $2R$. The intersection of both particles is removed from one of them and, in this way a grain boundary with a constant curvature $\kappa_{gb} = 1/R$ is created. Figure 8.9a shows the pressure field computed by taking into account both surface tension at the free surface Γ_{sf} and surface tension at the grain boundary Γ_{gb}.

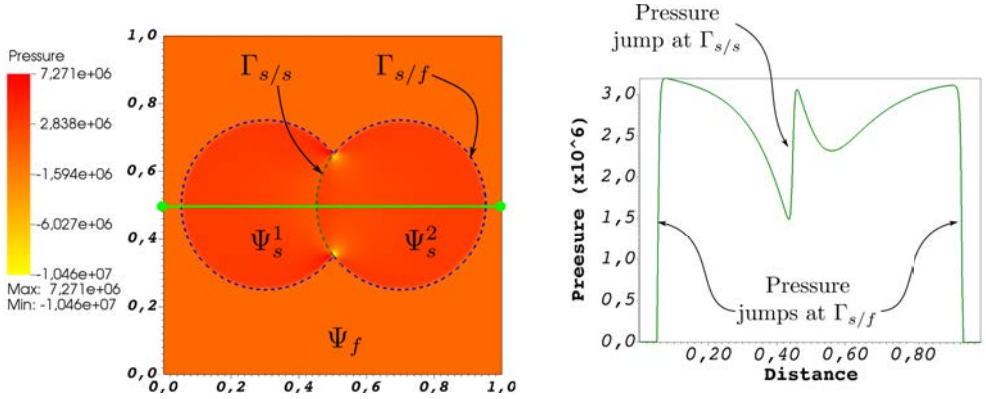

Figure 8.9: (a) Pressure field (Pa) computed by taking into account the surface tension over $\Gamma_{s/f}$ and $\Gamma_{s/s}$. (b) the jumps of the pressure across the interfaces $\Gamma_{s/f}$ and $\Gamma_{s/s}$ along the green line shown in a.

As the grain boundary between the particles is not flat, the grain boundary surface tension induces a discontinuity of the normal stress. This discontinuity is also present on the pressure field and therefore there is a jump of the pressure field across the grain boundary. The analytical solution of this kind of problem is not available, at least to the authors knowledge, then it is complex to validate this kind of approach. The normal stress was computed and its jump across $\Gamma_{s/s}$ was very close to the analytical value of the jump $\kappa_{gb}\gamma_{ss}$.

The numerical strategy allowing to compute the velocity due to grain boundary diffusion is yet to be developed. In fact, the introduction of this diffusion path into the numerical approach is not an easy task. The normal stress, that is discontinuous across the grain boundary, has to be used to compute the grain boundary diffusion velocity. This velocity depends on the surface laplacian of the normal stress, and therefore the normal stress must be computed in a very precise way which, at this moment, can not be achieved with the numerical approach proposed. Additionally, all the level set functions have to be transported, by using the grain

boundary diffusion velocity, in such a way that there is no overlapping or creation of voids over the grain boundary between the different level set functions. Nevertheless, the strategy presented for the mechanical problem with surface tension on the free surface and the grain boundary is an important step toward the sintering simulation by grain boundary diffusion.

8.4 Conclusions

A simple numerical strategy for the coupling between the surface diffusion and the volume diffusion has been presented. The basic idea is to compute individually the velocities induced by those mechanisms, and the create a coupled diffusion velocity given by the vectorial sum of each individual velocity. Even if at first sight this approach could seem to be very simple, the hypotheses made are in agreement with the hypotheses required by each diffusion mechanism. In fact, the both diffusions are driven by the geometry of the structure, in one hand the surface diffusion is driven by the surface laplacian of the curvature and, on the other hand, the volume diffusion is driven by the pressure gradient which also depends on the curvature. Considering this, the addition of both diffusion velocities is a good choice.

Even if it is very complex to make a validation of the obtained results, as there are no analytical models coupling those two diffusion mechanisms, the results obtained with the approach are qualitatively correct. Considering the case of two particles sintering by coupled surface and volume diffusions, the growth of the neck between the particles is significantly faster compared with the growth obtained with either of the mechanisms alone.

This coupling allows to perform more realistic simulations, however the lack of the grain boundary does not allow to fully simulate the sintering of a material. In order to introduce the grain boundary diffusion into the numerical approach presented, a method allowing to solve the mechanical problem considering the surface tension over the free surface and the grain boundary has been presented. The results obtained are promising, however further developments are yet to be done, including the approach allowing to compute the matter flux by grain boundary diffusion.

8.5 Résumé en français : Vers la simulation complète du frittage

Le frittage est le résultat de plusieurs mécanismes de diffusion agissant de façon simultanée par la diminution de l'énergie totale libre du système. Afin de pouvoir faire une simulation complète du procédé de frittage, il est donc nécessaire d'établir un couplage entre les différents chemins de diffusion. Pour cette raison, une stratégie numérique pour le couplage entre la diffusion surfacique et la diffusion volumique est présentée. L'idée consiste à calculer la vitesse couplée comme la somme vectorielle de chaque vitesse (surfacique et volumique). La validation de cette approche est très complexe car il n'existe pas de modèle analytique pour prédire la croissance du cou entre deux particules de la même taille par diffusion couplée. Cependant, des simulations de frittage entre deux particules ont montré que le cou entre les particules se développe beaucoup plus rapidement lorsque le couplage est considéré que lorsque chaque mécanisme est pris individuellement. La validation de simulations plus réalistes n'est pas non plus possible, mais l'évolution du système semble être correcte.

Le fait de ne pas avoir pris en compte les joints des grains ne permet pas de faire de simulation complète du frittage (ce dernier mécanisme restant essentiel). Afin d'introduire la diffusion aux joints de grains dans le cadre numérique présenté, le calcul de la pression doit prendre en compte la tension surfacique présente aux joints de grains entre les particules. Une méthode pour résoudre le problème mécanique avec la prise en compte de la tension surfacique sur la surface des particules et aux joints de grains est donc présentée. La méthode est basée sur l'approche numérique utilisée pour le calcul de la pression dans le cadre de la diffusion volumique. La principale différence est liée à l'introduction de plusieurs fonctions Level-Set requises pour pouvoir identifier chaque particule individuellement ainsi que les joints de grains. Avec cette méthode, il est possible de résoudre le problème mécanique en 2D en tenant en compte des deux termes de tension surfacique et les résultats sont très encourageants. Cependant, un long travail reste à réaliser afin d'arriver à faire des simulations de frittage par diffusion aux joints de grains.

Chapter 9

Conclusions

Sintering is a very complex process involving several multiphysics phenomena. From a practical point of view there are many variables that have to be controlled in order to obtain the desired properties of the final product. Because of these many variables and their interdependency, it is difficult to extract useful information from experimental data. Therefore numerical simulations represent a powerful tool that can provide meaningful information about this phenomena.

Considering the numerical tools available aiming at the simulation of the sintering process at the particle scale, a lack of a numerical approach able to handle the different diffusion mechanisms, complex geometries, and strong topological changes in 2D and even more drastically in 3D became evident. In this work was developed a numerical approach able to integrate efficient simulations of sintering by multiple diffusion mechanisms at the particles scale, allowing to study the microstructural evolution of the compact powder. The level set method, which is a Eulerian approach, was chosen because of its capability to handle strong topological changes in 2D and specially in 3D without any kind restriction concerning the geometry and the evolution of the system.

A level set finite element approach has been used to integrate the surface and volume diffusions, and partially the grain boundary diffusion, into a continuum mechanics framework. In order to achieve the goal, several challenges had to be overcome. Considering the surface diffusion, the induced velocity is proportional to the second-order spatial derivative of the curvature and therefore to the fourth-order spatial derivative of the level set function ($v^s \propto \Delta_s \kappa$) which is interpolated by using piecewise linear functions. In order to overcome this problem, a stabilized finite element mixed formulation curvature/surface laplacian of the curvature was proposed. In fact, the numerical approach showed its capability to keep very reduced spurious oscillations of the curvature. The stability and the convergence of the numerical method was also tested.

Concerning the volume diffusion, the associated velocity is proportional to the gradient of pressure $v^v \propto \underline{\nabla p} \cdot \underline{n}$. Therefore, the momentum conservation equation must be solved in order to compute the volume diffusion velocity. The issue, in the Eulerian framework used, being that the mechanical behavior of both, the compact powder and the surrounding medium, has to be taken into account along with the surface tension present at the particle surface. This surface tension induces a discontinuity of the normal stress and very often leads to unphysical oscillations of the pressure. The high ratio between the mechanical properties of both phases (particles and surrounding medium) represents another source of pressure oscillations.

A finite element mixed formulation pressure/velocity was proposed to solve the mechanical problem. This formulation, despite the multiple sources of spurious oscillations, allowed to obtain "smooth" pressure fields. And additionally, this method represents, at least to the authors knowledge, the first successful approach for the treatment of the fluid - elastic solid interaction with surface tension. This specific issue is in press in [Pino Muñoz *et al.* 2012].

However, even if a "smooth" pressure fields can be obtained, the computation of the volume diffusion velocity, which depends on the pressure gradient, is still complex. In fact, the normal stress discontinuity also induces a discontinuity of the pressure field, therefore the computation of the pressure gradient is not straightforward. The proposed solution consisted in computing the pressure gradient, and hence the volume diffusion velocity, over a layer slightly below the particles surface and then to extend this volume diffusion velocity beyond the interface. To do so, an efficient numerical approach capable of computing a volume diffusion velocity over a region around the particles surface was proposed. Additionally, a method for the enforcement of conservation of the particles volume was also proposed.

By combining all those numerical methods, a method for the simulation of sintering by volume diffusion was proposed. The results obtained were successfully compared with analytical models and it was also shown that this approach allows to cope with the severe topological changes and complex geometries that characterize the sintering process. Again, this method represents the first successful attempt to simulate the sintering by volume diffusion of a particles packing in 3D.

It is important to highlight that this kind of simulations are computationally very expensive, specially in 3D. In fact, the 3D simulations of the 150 particles packing sintering were performed by using a mesh built-up of about ten millions of elements and 24 processors were used, which required a computational time of about 200h.

The numerical framework developed, allowed to establish a coupling between surface and

volume diffusions. Even if the validation of this coupling is not yet possible, the results are promising and the kinetics of the surface area reduction, related to the surface free energy, seems to be correct. The next step toward the full sintering simulation, consists in adding the grain boundary diffusion. Aiming at this goal, the grain boundary surface tension has to be taken into account in the momentum conservation equation. Therefore, a numerical strategy to solve this new mechanical problem using multiple level set functions was proposed. This numerical strategy led to a first numerical approach allowing to compute the stress state of a system considering the surface tension over the free surface and the grain boundary. This approach sets the bases for the simulation of the sintering by grain boundary diffusion.

Several outlooks can be drawn from this work. Since the framework for the simulation of the grain boundary diffusion path has already been fixed, the most straight outlook is the introduction of this diffusion mechanism into the numerical approach. However, this represents a challenging task since the transport of multiple level set functions has to be handled and the normal stress over the grain boundary has to be computed in a more accurate way. Coupling between those three main diffusion mechanisms (surface, volume and grain boundary) could lead to comparisons with experimental data and calibrated powder compact sintering. Moreover, the microstructural evolution of the compact powder could be embedded into macroscopic models.

As for today, considering that this numerical tool allows to obtain the geometry of a powder compact at any time, it could be possible to study the effect of electromagnetic waves during the microwave sintering. Additionally, this numerical tool would also allow to deal with the sintering of multi-materials or the study of the sintering of doped powders. In fact, all the diffusion mechanisms are numerically controlled by the value of the material properties, i.e. diffusion coefficients, mechanical properties, surface tension coefficients, therefore it would be possible to evaluate different material properties from physical considerations to represent the multi-materials sintering or the sintering of doped powders. This corresponds to the subject of an undergoing PhD thesis (Howatchinou Tossoukpè), which is expected to be defended by the end of 2013.

Bibliography

[Adalsteinsson & Sethian 1995] D. Adalsteinsson and J. A. Sethian. *A Fast Level Set Method for Propagating Interfaces.* Journal of Computational Physics, vol. 118, no. 2, pages 269–277, 1995. (Cited in pages 54 and 55.)

[Al-Raoush & Alsaleh 2007] R. Al-Raoush and M. Alsaleh. *Simulation of random packing of polydisperse particles.* Powder technology, vol. 176, no. 1, pages 47–55, 2007. (Cited in page 69.)

[Arnold *et al.* 1984] D. N. Arnold, F. Brezzi and M. Fortin. *A stable finite element for the Stokes equations.* Calcolo, vol. 21, no. 4, pages 337–344, 1984. (Cited in page 97.)

[Ashby 1974] M. F. Ashby. *First report on sintering diagrams.* Acta Metallurgica, vol. 22, no. 3, pages 275–289, 1974. (Cited in pages 7 and 10.)

[Aulisa *et al.* 2007] E. Aulisa, S. Manservisi, R. Scardovelli and S. Zaleski. *Interface reconstruction with least-squares fit and split advection in three-dimensional Cartesian geometry.* Journal of Computational Physics, vol. 225, no. 2, pages 2301–2319, 2007. (Cited in pages 100 and 106.)

[Ausas *et al.* 2010] R. F. Ausas, F. S. Sousa and G. C. Buscaglia. *An improved finite element space for discontinuous pressures.* Computer Methods in Applied Mechanics and Engineering, vol. 199, no. 17-20, pages 1019–1031, 2010. (Cited in pages 99 and 110.)

[Badia & Codina 2009] S. Badia and R. Codina. *Unified Stabilized Finite Element Formulations for the Stokes and the Darcy Problems.* SIAM Journal on Numerical Analysis, vol. 47, no. 3, pages 1971–2000, 2009. (Cited in page 97.)

[Badia & Codina 2010] S. Badia and R. Codina. *Stabilized continuous and discontinuous Galerkin techniques for Darcy flow.* Computer Methods in Applied Mechanics and Engineering, vol. 199, no. 25-28, pages 1654–1667, 2010. (Cited in page 99.)

[Balay *et al.* 1997] Satish Balay, William D. Gropp, Lois Curfman McInnes and Barry F. Smith. *Efficient Management of Parallelism in Object Oriented Numerical Software Libraries.* In E. Arge, A. M. Bruaset and H. P. Langtangen, editeurs, Modern Software Tools in Scientific Computing, pages 163–202. Birkhäuser Press, 1997. (Cited in page 127.)

[Bänsch *et al.* 2005] E. Bänsch, P. Morin and R. H. Nochetto. *A finite element method for surface diffusion: the parametric case.* Journal of Computational Physics, vol. 203, no. 1, pages 321–343, 2005. (Cited in pages 72 and 76.)

[Bernoff *et al.* 1998] A. J. Bernoff, A. L. Bertozzi and T. P. Witelski. *Axisymmetric surface diffusion: dynamics and stability of self-similar pinchoff.* Journal of statistical physics, vol. 93, no. 3, pages 725–776, 1998. (Cited in page 71.)

[Bordère *et al.* 2010] S. Bordère, S. Vincent and J. P. Caltagirone. *Stochastic energetic approach devoted to the modeling of static two-phase problems dominated by surface tension.* Computers & Fluids, vol. 39, no. 3, pages 392–402, 2010. (Cited in pages 100, 106, 107 and 110.)

[Brackbill *et al.* 1992] J. U. Brackbill, D. B Kothe and C. Zemach. *A continuum method for modeling surface tension.* Journal of Computational Physics, vol. 100, no. 2, pages 335–354, 1992. (Cited in pages 100, 106, 107 and 110.)

[Braginsky *et al.* 2005] M. Braginsky, V. Tikare and E. Olevsky. *Numerical simulation of solid state sintering.* International journal of solids and structures, vol. 42, no. 2, pages 621–636, 2005. (Cited in page 29.)

[Brenner 2005] H. Brenner. *Kinematics of volume transport.* Physica A: Statistical Mechanics and its Applications, vol. 349, pages 11–59, 2005. (Cited in page 129.)

[Brooks & Hughes 1982] A. N. Brooks and T. J. R. Hughes. *Streamline upwind/Petrov-Galerkin formulations for convection dominated flows with particular emphasis on the incompressible Navier-Stokes equations.* Computer methods in applied mechanics and engineering, vol. 32, no. 1, pages 199–259, 1982. (Cited in pages 58, 124 and 125.)

[Bross & Exner 1979] P. Bross and H. E. Exner. *Computer simulation of sintering processes.* Acta Metallurgica, vol. 27, no. 6, pages 1013–1020, 1979. (Cited in pages 31 and 32.)

[Bruchon *et al.* 2010] J. Bruchon, D. Pino-Muñoz, F. Valdivieso, S. Drapier, G. Pacquaut*et al.* *3D simulation of the matter transport by surface diffusion within a Level-Set context.* European Journal of Computational Mechanics, vol. 19, pages 281–292, 2010. (Cited in page 65.)

[Bruchon *et al.* 2011] J. Bruchon, S. Drapier and F. Valdivieso. *3D finite element simulation of the matter flow by surface diffusion using a level set method.* International Journal for Numerical Methods in Engineering, vol. 86, no. 7, pages 845–861, 2011. (Cited in pages 65, 71, 74, 78, 79, 80, 81, 82, 83 and 90.)

[Bruchon *et al.* 2012] J. Bruchon, D. Pino-Muñoz, F. Valdivieso and S. Drapier. *Finite element simulation of mass transport during sintering of a granular packing. Part I. Surface and lattice diffusion.* Journal of the American Ceramic Society, vol. 95, no. 8, pages 2398–2405, 2012. DOI: 10.1111/j.1551-2916.2012.05073.x. (Cited in pages 121, 122 and 125.)

[Burger *et al.* 2007] M. Burger, F. Haußer, C. Stöcker and A. Voigt. *A level set approach to anisotropic flows with curvature regularization.* Journal of computational physics, vol. 225, no. 1, pages 183–205, 2007. (Cited in page 72.)

[Cervera *et al.* 2010] M. Cervera, M. Chiumenti and R. Codina. *Mixed stabilized finite element methods in nonlinear solid mechanics: Part I: Formulation.* Computer Methods in Applied Mechanics and Engineering, vol. 199, no. 37-40, pages 2559–2570, 2010. (Cited in page 98.)

[Chen *et al.* 1990] I. W. Chen, G. N. Hassold and D. J. Srolovitz. *Computer Simulation of Final-Stage Sintering: II, Influence of Initial Pore Size.* Journal of the American Ceramic Society, vol. 73, no. 10, pages 2865–2872, 1990. (Cited in page 29.)

[Chen 2002] L. Q. Chen. *Phase-field models for microstructure evolution.* Annual review of materials research, vol. 32, no. 1, pages 113–140, 2002. (Cited in pages 31 and 36.)

[Chiumenti *et al.* 2002] M. Chiumenti, Q. Valverde, C. Agelet de Saracibar and M. Cervera. *A stabilized formulation for incompressible elasticity using linear displacement and pressure interpolations.* Computer Methods in Applied Mechanics and Engineering, vol. 191, no. 46, pages 5253–5264, 2002. (Cited in page 97.)

[Ch'ng & Pan 2004] H. N. Ch'ng and J. Pan. *Cubic spline elements for modelling microstructural evolution of materials controlled by solid-state diffusion and grain-boundary migration.* Journal of Computational Physics, vol. 196, no. 2, pages 724–750, 2004. (Cited in pages 35, 36 and 130.)

[Ch'ng & Pan 2005] H. N. Ch'ng and J. Pan. *Modelling microstructural evolution of porous polycrystalline materials and a numerical study of anisotropic sintering.* Journal of computational physics, vol. 204, no. 2, pages 430–461, 2005. (Cited in pages 35 and 130.)

[Chopp & Sethian 1999] D. L. Chopp and J. A. Sethian. *Motion by intrinsic Laplacian of curvature.* Interfaces and Free Boundaries, vol. 1, no. 1, pages 107–123, 1999. (Cited in pages 77 and 78.)

[Coupez 2006] T. Coupez. *Réinitialisation convective et locale des fonctions Level Set pour le mouvement de surfaces et d'interfaces.* Journées Activités Universitaires de Mécanique-La Rochelle, 31 août et 1er septembre 2006, 2006. (Cited in pages 54 and 55.)

[Coyajee 2007] E. R. A. Coyajee. *A front-capturing method for the numerical simulation of dispersed two-phase flow.* PhD thesis, Delft University of Technology, 2007. (Cited in page 42.)

[Daly & Pracht 1968] B. J. Daly and W. E. Pracht. *Numerical Study of Density-Current Surges.* Physics of Fluids, vol. 11, page 15, 1968. (Cited in page 44.)

[Digonnet *et al.* 2007] H. Digonnet, L. Silva and T. Coupez. *Cimlib: a fully parallel application for numerical simulations based on components assembly.* In Materials Processing and Design: Modeling, Simulation and Applications; Part One(AIP Conference Proceedings Volume 908), volume 908, pages 269–274. American Institute of Physics, 2 Huntington Quadrangle, Suite 1 NO 1, Melville, NY, 11747-4502, USA„ 2007. (Cited in pages 59 and 105.)

[Djohari & Derby 2009] H. Djohari and J. J. Derby. *Transport mechanisms and densification during sintering: II. Grain boundaries.* Chemical Engineering Science, vol. 64, no. 17, pages 3810–3816, 2009. (Cited in page 32.)

[Djohari *et al.* 2009] H. Djohari, J. I. Martínez-Herrera and J. J. Derby. *Transport mechanisms and densification during sintering: I. Viscous flow versus vacancy diffusion.* Chemical Engineering Science, vol. 64, no. 17, pages 3799–3809, 2009. (Cited in page 32.)

[Escher *et al.* 1998] J. Escher, U. F. Mayer and G. Simonett. *The surface diffusion flow for immersed hypersurfaces.* SIAM journal on mathematical analysis, vol. 29, no. 6, pages 1419–1433, 1998. (Cited in page 71.)

[Exner *et al.* 1996] H. E. Exner, E. Arzt, Robert W. Cahn and P. Haasen. *Sintering Processes.* In Physical Metallurgy (Fourth Edition), pages 2627–2662. North-Holland, Oxford, 1996. (Cited in pages 3, 8, 10, 27 and 28.)

[Fortin *et al.* 1998] A. Fortin, A. Béliveau and Y. Demay. *A Two-dimensional Numerical Method for the Deformation of Drops with Surface Tension.* International Journal for Numerical Methods in Fluids, vol. 10, no. 3, pages 225–240, 1998. (Cited in pages 95, 103, 105 and 108.)

[Garikipati *et al.* 2001] K. Garikipati, L. Bassman and M. Deal. *A lattice-based micromechanical continuum formulation for stress-driven mass transport in polycrystalline solids.* Journal of the Mechanics and Physics of Solids, vol. 49, no. 6, pages 1209–1237, 2001. (Cited in page 12.)

[Gerlach *et al.* 2006] D. Gerlach, G. Tomar, G. Biswas and F. Durst. *Comparison of volume-of-fluid methods for surface tension-dominant two-phase flows.* International Journal of

Heat and Mass Transfer, vol. 49, no. 3-4, pages 740–754, 2006. (Cited in pages 99, 100 and 106.)

[German 1996] R. M. German. Sintering theory and practice. Wiley (New York), 1996. (Cited in page 8.)

[Geuzaine & Remacle. 2009] C. Geuzaine and J.-F. Remacle. *Gmsh: a three-dimensional finite element mesh generator with built-in pre- and post-processing facilities.* International Journal for Numerical Methods in Engineering, vol. 79, no. 11, pages 1309–1331, 2009. (Cited in page 112.)

[Gibbs 1928] J. W. Gibbs. The collected works of J. Willard Gibbs, volume 1. Longmans, Green, 1928. (Cited in pages 14 and 16.)

[Groß & Reusken 2007] S. Groß and A. Reusken. *An extended pressure finite element space for two-phase incompressible flows with surface tension.* Journal of Computational Physics, vol. 224, no. 1, pages 40–58, 2007. (Cited in pages 100, 106 and 110.)

[Han *et al.* 2005] K. Han, Y. T. Feng and D. R. J. Owen. *Sphere packing with a geometric based compression algorithm.* Powder Technology, vol. 155, no. 1, pages 33–41, 2005. (Cited in page 69.)

[Harlow *et al.* 1965] F. H. Harlow, J. E. Welch*et al.* *Numerical calculation of time-dependent viscous incompressible flow of fluid with free surface.* Physics of fluids, vol. 8, no. 12, page 2182, 1965. (Cited in page 43.)

[Hassold *et al.* 1990] G. N. Hassold, I. W. Chen and D. J. Srolovitz. *Computer Simulation of Final-Stage Sintering: I, Model Kinetics, and Microstructure.* Journal of the American Ceramic Society, vol. 73, no. 10, pages 2857–2864, 1990. (Cited in page 29.)

[Herring 1951] C. Herring. *Surface tension as a motivation for sintering.* The physics of powder metallurgy, vol. 27, no. 2, pages 143–179, 1951. (Cited in pages 8, 10, 11, 12, 13, 14, 15, 16 and 17.)

[Hirt & Nichols 1981] C. W. Hirt and B. D. Nichols. *Volume of fluid (VOF) method for the dynamics of free boundaries.* Journal of computational physics, vol. 39, no. 1, pages 201–225, 1981. (Cited in page 46.)

[Hitti *et al.* 2011] K. Hitti, P. Laure, T. Coupez, L. Silva and M. Bernacki. *Fast generation of complex statistical Representative Elementary Volumes (REVs) in a finite element context.* submitted to Journal of Computational Physics, 2011. (Cited in page 69.)

[Hitti 2011] K. Hitti. *Direct numerical simulation of complex Representative Volume Elements (RVEs): Generation, Resolution and Homogenization.* PhD thesis, Ecole Nationale Supérieure des Mines de Paris, 2011. (Cited in pages 69 and 156.)

[Hoge & Pask 1977] C. E. Hoge and J. A. Pask. *Thermodynamic and geometric considerations of solid state sintering.* Ceramurgia International, vol. 3, no. 3, pages 95–99, 1977. (Cited in page 8.)

[Holm *et al.* 1991] E. A. Holm, J. A. Glazier, D. J. Srolovitz and G. S. Grest. *Effects of lattice anisotropy and temperature on domain growth in the two-dimensional Potts model.* Physical Review A, vol. 43, no. 6, page 2662, 1991. (Cited in page 29.)

[Howard & Lidiard 1964] R. E. Howard and A. B. Lidiard. *Matter transport in solids.* Reports on progress in Physics, vol. 27, page 161, 1964. (Cited in pages 9 and 10.)

[Hughes & Sangalli 2007] T. J. R. Hughes and G. Sangalli. *Variational Multiscale Analysis: the Fine-scale Green's Function, Projection, Optimization, Localization, and Stabilized Methods.* SIAM Journal on Numerical Analysis, vol. 45, no. 2, pages 539–557, 2007. (Cited in page 97.)

[Hughes 1987] T. J. R. Hughes. *Recent progress in the development and understanding of SUPG methods with special reference to the compressible Euler and Navier-Stokes equations.* International Journal for Numerical Methods in Fluids, vol. 7, no. 11, pages 1261–1275, 1987. (Cited in page 58.)

[Hysing 2006] S. Hysing. *A new implicit surface tension implementation for interfacial flows.* International Journal for Numerical Methods in Fluids, vol. 51, no. 6, pages 659–672, 2006. (Cited in pages 100, 106 and 110.)

[Hysing 2011] S. Hysing. *Mixed finite element level set method for numerical simulation of immiscible fluids.* International Journal for Numerical Methods in Fluids, 2011. Submitted. (Cited in pages 95, 100, 106 and 110.)

[Jerier *et al.* 2010] J. F. Jerier, V. Richefeu, D. Imbault and F. V. Donzé. *Packing spherical discrete elements for large scale simulations.* Computer Methods in Applied Mechanics and Engineering, vol. 199, no. 25, pages 1668–1676, 2010. (Cited in page 69.)

[Job & Herrmann 2006] G. Job and F. Herrmann. *Chemical potential: a quantity in search of recognition.* European journal of physics, vol. 27, page 353, 2006. (Cited in page 12.)

[Kucherenko *et al.* 2000] S. Kucherenko, J. Pan and J. A. Yeomans. *A combined finite element and finite difference scheme for computer simulation of microstructure evolution and*

its application to pore–boundary separation during sintering. Computational materials science, vol. 18, no. 1, pages 76–92, 2000. (Cited in pages 35, 71 and 130.)

[Kuczynski 1949] G. C. Kuczynski. *Self-diffusion in sintering of metallic particles.* Transactions of the AIME, vol. 185, pages 169–178, 1949. (Cited in pages 10 and 25.)

[Lafaurie *et al.* 1994] B. Lafaurie, C. Nardone, R. Scardovelli, S. Zaleski and G. Zanetti. *Modelling merging and fragmentation in multiphase flows with SURFER.* Journal of Computational Physics, vol. 113, no. 1, pages 134–147, 1994. (Cited in pages 95, 100, 105, 106 and 110.)

[Landau & Lifshits 1959] L. D. Landau and E. M. Lifshits. Fluid mechanics. Pergamon Press, 1959. (Cited in page 92.)

[Merriman *et al.* 1994] B. Merriman, J. K. Bence and S. Osher. *Motion of multiple junctions: A level set approach.* Journal of Computational Physics, vol. 112, no. 2, pages 334–363, 1994. (Cited in page 52.)

[Mesri *et al.* 2008] Y. Mesri, W. Zerguine, H. Digonnet, L. Silva and T. Coupez. *Dynamic parallel adaption for three dimensional unstructured meshes: Application to interface tracking.* Proceedings of the 17th International Meshing Roundtable, pages 195–212, 2008. (Cited in page 59.)

[Miller 1997] K. Miller. *Elliptic versus parabolic regularization for the equation of prescribed mean curvature.* journal of differential equations, vol. 137, pages 1–53, 1997. (Cited in pages 73 and 125.)

[Nichols & Mullins 1965] F. A. Nichols and W. W. Mullins. *Morphological Changes of a Surface of Revolution due to Capillarity-Induced Surface Diffusion.* Journal of Applied Physics, vol. 36, pages 1826–1835, 1965. (Cited in page 31.)

[Noh & Woodward 1976] W. Noh and P. Woodward. *SLIC (simple line interface calculation).* In Proceedings of the Fifth International Conference on Numerical Methods in Fluid Dynamics June 28–July 2, 1976 Twente University, Enschede, pages 330–340. Springer, 1976. (Cited in page 46.)

[Osher & Fedkiw 2001] S. Osher and R. P. Fedkiw. *Level set methods: an overview and some recent results.* Journal of Computational physics, vol. 169, no. 2, pages 463–502, 2001. (Cited in pages 47, 48, 51, 95 and 123.)

[Osher & Sethian 1988] S. Osher and J. A. Sethian. *Fronts propagating with curvature-dependent speed: algorithms based on Hamilton-Jacobi formulations.* Journal of computational physics, vol. 79, no. 1, pages 12–49, 1988. (Cited in pages 47, 51 and 123.)

[Pan & Cocks 1995] J. Pan and A. C. F. Cocks. *A numerical technique for the analysis of coupled surface and grain-boundary diffusion.* Acta metallurgica et materialia, vol. 43, no. 4, pages 1395–1406, 1995. (Cited in pages 17, 31, 32, 33, 34 and 35.)

[Pan *et al.* 1997] J. Pan, A. C. F. Cocks and S. Kucherenko. *Finite element formulation of coupled grain-boundary and surface diffusion with grain-boundary migration.* Proceedings of the Royal Society of London. Series A: Mathematical, Physical and Engineering Sciences, vol. 453, no. 1965, pages 2161–2184, 1997. (Cited in pages 35, 36, 71 and 130.)

[Pan *et al.* 1998] J. Pan, H. Le, S. Kucherenko and J. A. Yeomans. *A model for the sintering of spherical particles of different sizes by solid state diffusion.* Acta materialia, vol. 46, no. 13, pages 4671–4690, 1998. (Cited in pages 35 and 130.)

[Pan *et al.* 2005] J. Pan, H. N. Ch'ng and A. C. F. Cocks. *Sintering kinetics of large pores.* Mechanics of materials, vol. 37, no. 6, pages 705–721, 2005. (Cited in pages 35 and 130.)

[Papadakis 2008] G. Papadakis. *A novel pressure-velocity formulation and solution method for fluid-structure interaction problems.* Journal of Computational Physics, vol. 227, no. 6, pages 3383–3404, 2008. (Cited in pages 96 and 117.)

[Peng *et al.* 1999] D. Peng, B. Merriman, S. Osher, H. Zhao and M. Kang. *A PDE-based fast local level set method.* Journal of Computational Physics, vol. 155, no. 2, pages 410–438, 1999. (Cited in pages 48, 51, 52, 95 and 123.)

[Pino Muñoz *et al.* 2012] D. Pino Muñoz, J. Bruchon, S. Drapier and F. Valdivieso. *A finite element-based Level-Set method for fluid - elastic solid interaction with surface tension.* International Journal for Numerical Methods in Engineering, vol. In press, 2012. (Cited in pages 90 and 164.)

[Popinet & Zaleski 1999] S. Popinet and S. Zaleski. *A front-tracking algorithm for accurate representation of surface tension.* International Journal for Numerical Methods in Fluids, vol. 30, no. 6, pages 775–793, 1999. (Cited in page 42.)

[Puaux *et al.* 2010] G. Puaux, L. Silva, P. Laure, M. Vincent and T. Coupez. An immersed finite element method for permeability determination of a porous media. To appear in *Int J Numer Meth Fl*, 2010. (Cited in page 99.)

[Qiu *et al.* 2008] F. Qiu, T.A. Egerton and I. L. Cooper. *Monte Carlo simulation of nanoparticle sintering.* Powder Technology, vol. 182, no. 1, pages 42–50, 2008. (Cited in pages 29 and 31.)

[Rahaman 1995] M. N. Rahaman. Ceramic processing and sintering. Marcel Dekker, 1995. (Cited in pages 4, 5, 7, 9, 10, 11, 16, 25 and 84.)

[Renardy & Renardy 2002] Y. Renardy and M. Renardy. *PROST: A Parabolic Reconstruction of Surface Tension for the Volume-of-Fluid Method.* Journal of Computational Physics, vol. 183, no. 2, pages 400–421, 2002. (Cited in pages 100, 106 and 110.)

[Rider & Kothe 1998] W. J. Rider and D. B. Kothe. *Reconstructing volume tracking.* Journal of computational physics, vol. 141, no. 2, pages 112–152, 1998. (Cited in page 46.)

[Riedel *et al.* 1994] H. Riedel, H. Zipse and J. Svoboda. *Equilibrium pore surfaces, sintering stresses and constitutive equations for the intermediate and late stages of sintering–II. Diffusional densification and creep.* Acta metallurgica et materialia, vol. 42, no. 2, pages 445–452, 1994. (Cited in page 32.)

[Roberts & Thomas 1987] J. Roberts and J. M Thomas. *Mixed and hybrid finite element methods.* Rapport technique, Institut National de Recherche en Informatique et en Automatique (INRIA), 1987. (Cited in page 97.)

[Rudman 1997] M. Rudman. *Volume-tracking methods for interfacial flow calculations.* International journal for numerical methods in fluids, vol. 24, no. 7, pages 671–691, 1997. (Cited in pages 43, 46 and 47.)

[Salac & Lu 2008] D. Salac and W. Lu. *A local semi-implicit level-set method for interface motion.* Journal of Scientific Computing, vol. 35, no. 2, pages 330–349, 2008. (Cited in page 123.)

[Shin & Juric 2002] S. Shin and D. Juric. *Modeling three-dimensional multiphase flow using a level contour reconstruction method for front tracking without connectivity.* Journal of Computational Physics, vol. 180, no. 2, pages 427–470, 2002. (Cited in page 107.)

[Siiriä & Yliruusi 2007] S. Siiriä and J. Yliruusi. *Particle packing simulations based on Newtonian mechanics.* Powder technology, vol. 174, no. 3, pages 82–92, 2007. (Cited in page 69.)

[Smolianski 2005] A. Smolianski. *Finite-element/level-set/operator-splitting (FELSOS) approach for computing two-fluid unsteady flows with free moving interfaces.* International Journal for Numerical Methods in Fluids, vol. 48, no. 3, pages 231–269, 2005. (Cited in pages 95, 100, 106 and 110.)

[Sussman *et al.* 1994] M. Sussman, P. Smereka and S. Osher. *A level set approach for computing solutions to incompressible two-phase flow.* Journal of Computational Physics;(United States), vol. 114, no. 1, 1994. (Cited in pages 52 and 95.)

[Tikare *et al.* 2003] V. Tikare, M. Braginsky and E. A. Olevsky. *Numerical Simulation of Solid-State Sintering: I, Sintering of Three Particles.* Journal of the American Ceramic Society, vol. 86, no. 1, pages 49–53, 2003. (Cited in page 29.)

[Tikare *et al.* 2010] V. Tikare, M. Braginsky, D. Bouvard and A. Vagnon. *Numerical simulation of microstructural evolution during sintering at the mesoscale in a 3D powder compact.* Computational Materials Science, vol. 48, no. 2, pages 317–325, 2010. (Cited in page 29.)

[Tsai & Osher 2003] R. Tsai and S. Osher. *Review article: Level set methods and their applications in image science.* Communications in Mathematical Sciences, vol. 1, no. 4, pages 1–20, 2003. (Cited in pages 123 and 124.)

[Uskoković & Exner 1977] D. P. Uskoković and H. E. Exner. *Kinetics of contact formation during sintering by diffusion mechanisms.* Science of Sintering, vol. 9, no. 3, pages 265–303, 1977. (Cited in pages 24 and 26.)

[Ville *et al.* 2011] L. Ville, L. Silva and T. Coupez. *Convected level set method for the numerical simulation of fluid buckling.* International Journal for numerical methods in fluids, vol. 66, no. 3, pages 324–344, 2011. (Cited in pages 51, 55, 56, 58, 59, 77 and 78.)

[Vincent *et al.* 2004] S. Vincent, J. P. Caltagirone, P. Lubin and T. N. Randrianarivelo. *An adaptative augmented Lagrangian method for three-dimensional multimaterial flows.* Computers & Fluids, vol. 33, no. 10, pages 1273–1289, 2004. (Cited in page 107.)

[Wakai & Brakke 2011] F. Wakai and K. A. Brakke. *Mechanics of sintering for coupled grain boundary and surface diffusion.* Acta materialia, vol. 59, no. 14, pages 5379–5387, 2011. (Cited in pages 17, 31, 32, 37, 71 and 130.)

[Wang 2006] Y. U. Wang. *Computer modeling and simulation of solid-state sintering: A phase field approach.* Acta materialia, vol. 54, no. 4, pages 953–961, 2006. (Cited in pages 36, 37 and 39.)

[Weaire *et al.* 1986] D. Weaire, J. P. Kermode and J. Wejchert. *On the distribution of cell areas in a Voronoi network.* Philosophical Magazine B, vol. 53, no. 5, pages 101–105, 1986. (Cited in page 29.)

[Williams *et al.* 1998] M. W. Williams, D. B. Kothe and E. G. Puckett. *Accuracy and convergence of continuum surface tension models.* Fluid Dynamics at Interfaces, Cambridge University Press, Cambridge, pages 294–305, 1998. (Cited in pages 100, 101 and 106.)

[Wu 1983] F. Y. Wu. *Erratum: The Potts model.* Reviews of Modern Physics, vol. 55, no. 1, page 315, 1983. (Cited in page 29.)

[Youngs 1982] D. L. Youngs. *Time-dependent multi-material flow with large fluid distortion.* Numerical methods for fluid dynamics, vol. 24, pages 273–285, 1982. (Cited in page 46.)

École Nationale Supérieure des Mines
de Saint-Étienne

NNT : 2012 EMSE 0669

Daniel Humberto PINO MUÑOZ

High performance computing of sintering process at particle scale

Speciality : Mechanics and Engineering

Keywords : Sintering, Diffusion phenomena, Level-set method, Surface tension, Finite elements, Parallel computing.

Abstract :

Within the general context of solid-state sintering process, this work presents a numerical modeling approach, at the particle scale, of ceramic particle packing consolidation. Typically, the sintering process triggers several mass transport paths that are thermally activated. Among those diffusion paths, the most important ones are: surface diffusion, grain boundary diffusion and volume diffusion. Including this physics into a high-performance computing framework would permit to gain precious insights about the driving mechanisms which are seldom accessible at this scale.
The aim of the present work is to develop a model and a numerical strategy able to integrate the different diffusion mechanisms into continuum mechanics framework. In the cases of surface diffusion and volume diffusion, the mass flux is calculated as a function of the surface curvature Laplacian and the hydrostatic pressure gradient, respectively. The physical model describing these two transport mechanisms is first presented within the framework of continuum mechanics. Then the numerical strategy developed for the simulation of the sintering of many particles is detailed. This strategy is based on a discretization of the problem by using a finite element approach. In order to be able to take into account all the different topological changes that can appear in the structure during the sintering process (neck formation between the particles, open and closed pores, pores elimination, etc), the grains are described through an Eulerian approach. More precisely, a Level-Set method is used to describe the particles free surface. This versatile strategy allows us to perform simulations involving a relatively large number of particles. Particles are chosen to be tangential spheres at the beginning of the simulation. Then, due to surface diffusion, necks are quickly formed between the particles. The subsequent change leads the system towards an equilibrium state, it is driven solely by the mass and momentum balance equations combined with diffusion equations. Furthermore, a mesh adaptation technique allows the particles surface description to be improved, while the number of mesh elements is kept reasonable. Several 3D simulations, performed in a parallel computing framework, show the changes occurring in the structure of 3D granular stacks.

École Nationale Supérieure des Mines
de Saint-Étienne

NNT : 2012 EMSE 0669

Daniel Humberto PINO MUNOZ

Calcul intensif en simulation de frittage à l'échelle des particules.

Spécialité: Mécanique et Ingénierie

Mots clefs : Frittage, Phenomènes de diffusion, Méthode Level-Set, Tension surfacique, Eléments finis, Calcul intensif.

Résumé :

Dans le cadre général de la simulation du procédé de frittage en phase solide, ce travail propose une approche numérique, à l'échelle des particules, de la consolidation d'un compact pulvérulent céramique. Le frittage est un procédé mettant en jeu plusieurs chemins de diffusion activés thermiquement. Parmi ces chemins de diffusion, les plus importants sont : la diffusion surfacique, la diffusion aux joints des grains et la diffusion volumique. La mise en place de cette physique dans un cadre de calcul intensif doit permettre de mieux comprendre ces mécanismes de diffusion ainsi que leur influence sur l'évolution de la microstructure dont la caractérisation expérimentale directe, à cette échelle, est quasiment irréalisable.

Le but de ce travail consiste à développer un modèle ainsi qu'une stratégie numérique capable d'intégrer les différents mécanismes de diffusion dans un cadre de calcul intensif. Le flux de matière est calculé en fonction du Laplacien de la courbure dans les cas de la diffusion surfacique, tandis que pour la diffusion volumique ce flux est proportionnel au gradient de la pression hydrostatique. Le modèle physique, qui décrit ces deux mécanismes de transport, est tout d'abord présenté dans le cadre de la mécanique des milieux continus. Ensuite, la stratégie numérique développée pour la simulation du frittage d'un empilement granulaire est détaillée. Cette stratégie est basée sur une discrétisation du problème par des éléments finis stabilisés. Afin de pouvoir traiter tous les changements topologiques qui peuvent avoir lieu pendant le frittage (formation des cous entre les particules, pores ouverts et fermés, élimination de pores, etc.), les particules sont décrites à l'aide d'une méthode eulérienne. Plus précisément, une méthode Level-Set est utilisée pour décrire la surface libre des particules. Cette stratégie nous permet de faire des simulations avec un "grand" nombre de particules. Les particules sont sphériques et tangentes en début de simulation. Ensuite, et grâce à la diffusion surfacique, les cous entre les particules se forment très rapidement. Par la suite le système évolue vers un état d'équilibre, qui est contrôlé uniquement par les équations de la conservation de la masse et de la quantité de moment couplées avec les équations de la diffusion. En complément, une technique d'adaptation de maillage permet d'améliorer la description de la surface des particules, tout en gardant un nombre raisonnable d'éléments. Plusieurs simulations en 3D, menées dans un cadre de calcul parallèle, montrent l'évolution qui a lieu sur un empilement granulaire réaliste.